

## ENTREPRENEURIAL ATTITUDE AND LIFE COPING SKILLS OF RURAL WOMEN ENTREPRENEURS OF SELF HELP GROUPS IN DHARMAPURI DISTRICT OF TAMILNADU, INDIA

**SHANMUGAM. D**, Research Scholar, Presidency College Chennai,  
**ROBERT RAMESH BABU P**, Research Scholar, Central University of Tamilnadu, Tiruvarur,  
**Dr. JOHN XAVIER Ph.D**, Associate Professor.

### **ABSTRACT**

#### **Background**

Women self help groups have emerged as one of the greatest phenomena of this century in empowering the rural poor with self dignity and authority over their life situations. However, women entrepreneurs in rural areas undergo several problems due to different role they carry on in their homes as well as in the society. The demands of the new entrepreneurship without much experience and skill make them stressful and put them all into a dangerous position. This paper intends to identify the problems related to life coping strategies of women self help group members.

#### **Aim**

The aim of the study is to find out the entrepreneurial attitude and life coping skills of the rural women self help group members those who have emerged as entrepreneurs in rural areas.

#### **Research method**

This study has used non-experimental descriptive research design in order to recognize the types of problems and coping behavior of women rural entrepreneurs and their entrepreneurial attitude in Dharmapuri District. Primary data was collected from 200 respondents by using a structured questionnaire method administered among the randomly selected 200 women self help group entrepreneurs, who come under the age groups of 18 – 60 years. Hypothesis were tested with the application of descriptive and inferential statistics.

#### **Findings**

The overall entrepreneurial attitude of 200 respondents is that High (15%), Average (61%) and low (24%). Most of the respondents have an average level of life coping skills.

#### **Implications**

Results of this study aptly suggests that it is one of good references for carrying out future studies and could be interrelated with other variables, which can be quoted as a reference in terms of entrepreneurial attitude and also identifying the causes of stress and life coping strategies of women entrepreneurs in rural areas. This would suggest better solutions to reduce the stress level and increase the coping mechanism of the women entrepreneurs.

**Keywords:** Entrepreneurial attitude, women entrepreneurs, life coping skills, entrepreneurship, rural women, self-help groups.

### **1.1. Introduction**

Women are the growing part of a present day human resources. The development would be imperfect if this section of the population is not given opportunities to prove their capabilities. It was in the ancient period women were recognized equally with men and in fact they were the head of the households and participated equally in decision making like men. The gender disparity prevailed in various areas including literacy, education, nutrition and health, employment, decision making, participation in politics and executive positions, property rights, etc.

This discrimination has been the outcome of the gender division of labour making the men to go out and market their services and so also act as the head of the household, decision-maker etc. On the other hand, making women to remain at home to continuously perform the domestic activities such as taking care of the children, cook and wash for the family which have not been recognized as work till 1981 Census in India. As a result of making the men as breadwinners of the family, the female members also started assigning themselves a secondary role next only to men and as such they are treated as secondary citizen in the society.

Women form a vital part of the Indian Economy, who constitute one third of the labour resource, and primary member contributing in the survival of the family. It is true that women form the backbone of agriculture sector, comprising the majority of agricultural labourers in India. Gender divisions in agriculture are stark with all activities involving manual labour assigned to women. While all operations involving machinery and drought animals generally performed by men.

Female agricultural laborers are among the poorest sections of Indian society. Agricultural wages for women are on an average 30-50 percent less than those for men. The greater is dependence on women's income. Despite several progresses made since independence in the lives of women, a gender analysis of most social and economic data demonstrates that women in India continue to be relatively disadvantaged in matters of survival, health, nutrition, literacy and productivity.

## **Review of literature**

### **1.2. Micro Finance and Rural Poor**

The micro finance and the micro credit and lending had been in practice since man started trade. The micro credit, which is claimed to be contributing to women through SHGs, was in existence prior to it in the name of IRDP, DWCRA etc. Finance has been the central focus in all these programmes. Given that finance is backbone of all economic activities, in alleviating poverty. They play a significant role in transferring funds from surplus to deficit sectors but hardly the formal banks concentrate on rural poor borrower particularly in backward areas.

It was felt by the women's associations and other organizations, that there is a need to mainstreaming of women. So that the human resource development would be complete and the economic development would be better with the contribution of the other half of the human resource and also the gender disparity will be reduced. However, till in year 1970 the organized efforts have not made to mainstream women by extending equal opportunities in education, nutrition and health, economic participation country right access to credit and decision-making practices both at the household and community.

Since 1975 with the United Nation's declarations of Women Empowerment Decade, every effort towards ensuring gender equality was recognized everywhere. In present days several approaches have been followed to empower women and address the gender disparities in the society. At the beginning stages in India the efforts taken to support women were related to welfare programmes in which the women were treated as beneficiaries. As a next stage equity approach was followed in which women were facilitated to be equal citizens in the field of economic participation.

Later the equity approach was replaced by empowerment approach, which emphasized that the women must be given equal power and must come to the mainstream to prove their capabilities. Then there is a paradigm shift in the development processes by incorporating the gender concerns as an important element of development strategy. Government of Andhra Pradesh has taken up women empowerment as

one of the two agenda items recognizing the importance and involvement of women to tackle rural poverty and socio-economic issues.

### 1.3.1 Indian Scenario

While accessing the credit, the women folk of the rural areas face myriad problems in the areas of collateral security, cultural distance between rural women and nationalized banks, high transaction cost, restricted and fixed banking hours, inflexibility in quantum and purpose of credit, inconvenient repayment schedule, cumbersome procedure and exploitation by the intermediaries. Dissatisfaction with the result of many provides affective financial service to the rural people, particularly to the rural women.

Taking a leaf out of the book of developing countries like Bangladesh, Indonesia, Bolivia and Philippines where the combination of the combine efforts of formal and informal finances provide sustainable and valuable services to the poor. Few NGOs in India have started experimenting on innovative schemes of Self Help Group.

The member's problems and satisfaction is the aside test for the success of efficiency of any women development programme. The "Member-Beneficiaries" of SHG groups are the key members of any rural development and women welfare network. The members who are enrolled in SHG programmes as members possess and came to equip with the given financial potency to invest on their income generating activities in order to keep away from the exploitation of the money lenders. Even though the government of India has been launching various schemes and providing subsidies, due to poor socio-economic background, these women are not able to generate sufficient income from various programmes.

The brief overview of the demand for micro-financial services suggests the huge challenges and the opportunities the Indian market presents. Protective financial services may be critical for poverty alleviation, but they do little for helping people out of poverty. Hence, promotional financial services are required, primarily for enhancing livelihood among poor people. It is said that micro-finance can also harm poor people.

The increase in income of micro-credit borrowers is directly proportional to their starting level of income – the poorer they were to start with, the less is the impact of the loan. Secondly, poor borrowers from Micro-financing organizations often do not graduate to higher and higher loans, and consequently to productive small enterprises. While credit may initially be the ruling constraint for micro enterprises, to grow beyond a certain size, other constraints come into play.

Livelihood promotion is complex, opening up multiple potential goals and interventions and demanding an understanding of individual household and enterprise as well as the economic systems or sub-sectors in which they operate. Intervening in livelihood promotion is far more challenging developing the efficient delivery of financial services.

The SHG has, in fact, moved away from livelihood Promotion. Using micro-credit to promote livelihood may not be feasible with such a strategy. As autonomous organization, SHG's share the challenges and dynamics of other small organizations. Forming new groups requires significant energy and the necessary group. Processes, Governments, donors, policy makers and resource providers need to be

aware of the dynamics involved in these small organizations. The institutional challenges in SHGs are three fold:

### 1.4.1. Life Coping or Adjustment Skills

Present study deals with Life Coping Skills otherwise known as Life Adjustment Skills. Coping skills refers to the behavioral process of balancing conflicting needs, or needs against obstacles the problems caused by environmental factors. Coping skills is otherwise called as specific psychological skills required to problem-solving.

Lazarus (2001)<sup>1</sup> defined that Coping skills or the Adjustment skills as a ways of managing and consists of coping with various demands and process of life. Good (1959)<sup>2</sup> state that adjustment is the process of finding and adopting modes of behavior suitable to the environment or the changes is the environment. Parammeswaran & Beena (2004)<sup>3</sup> defined adjustment is a process which a living organism acquires in a particular way of acting or behaving or changes an existing form of behavior or action. `

Coping is an important psychological activity of human being. Life is a process of life coping and adjustment. Coping is a persistent feature of human personality. If a person is not able to adjust himself to the environment he/she cannot develop his/her wholesome personality. A person with coping skills can lead a cheerful and wholesome life but a less adjusting person is prone to lead a depressed and unhealthy life. Adjustment is a process by which an individual learns certain ways of behavior to cope with the situation which he/she attains through harmony with his/her environment.

### 1.4.2. Areas of Coping (Adjustment) Skills

**Emotional:** Traditionally, women undergo various emotional changes due to varied responsibilities and roles they play in a family and in a society. Women as an entrepreneur from a rural areas even undergo more stressful situation due to lack of skills and experiences. The financial constrains, the business, the family demand and social ethos all contribute to the heightened level of stress and emotional imbalances.

**Health:** Good health contributes to good life-adjustment and in turn to good physical and mental health. Poor health and illness on the other hand, adversely affect personality through the unfavorable effects they have on social and personal adjustment. Poor adjustments often predispose the person.

**Home:** A certain degree of tension in the home life is normal during family life Furthermore, such feelings sometimes have strong motivating effects upon the individual and stimulate them into achieve something they do not have. It is only when these feelings become intense and persistent over a considerable period of time that they have seriously distressing influence on the overall adjustment.

**Social:** One of the most difficult developmental tasks women relates to social adjustments. These adjustments must be made with members of the opposite sex a relationship that never existed before and to adults outside the family and school environments. Early adults are a period of social expansion and development.

**Educational:** Young adolescents complain about school in general and about restriction, homework required courses, food in the cafeteria, and the way the school is run. They are critical of their teachers and the way they teach. This is the “thing to do.” A young adolescent who wants to be popular with their peers must avoid creating the impression that they are “brains.” This is even more important for girls

than for boys because less prestige is associated with academic achievement among girls than among boys.

### 1.4.3. Need of the study

#### **Psychological problems faced by the members of the self help group members,**

The rural women mostly undergo the following problems in their lives: Adjustment (53%), Jealousy (16%), Egoism (18%) and Self centeredness (11%).

Common Problems faced by the Self help group members

1. Lack of numerical skills (44%)
2. Income problems (83%)
3. Group conflict (43%)
4. Migration for employment (25%)
5. Lack of proper planning and management (35%)
6. High incident of defunct (16%)
7. Political inference (37%)
8. Unhealthy competition among the groups (42%)
9. Different attitude of banks (29%)
10. Lack of marketing of products (78%)

### 1.4.4. General Objectives:

The primary objective of the research is to study the Life coping skills of women entrepreneurs in Dharmapuri district of Tamil Nadu.

### 1.4.5. Specific Objectives:

1. To know the socio-economic conditions of women entrepreneurs.
2. To find out the entrepreneurial attitudes of women entrepreneurs
3. To explore the differences, association and correlations of selected independent variables of women entrepreneur with their overall life coping skills
4. To suggest measures for improving the development of women entrepreneurs in the study area based upon the findings of the present study.

### 1.4.6. HYPOTHESIS

1. There is significant relationship between the community and their life coping skills
2. There is significant difference between the educational qualification and their life coping skills
3. There is significant association between religion and their life coping skills
4. There is significant relationship between educational qualification and their life coping skills.
5. There is significant difference between the types of families and their life coping skills.
6. There is significant difference between different jobs of the women and their life coping skills.

### 1.4.7. FIELD OF STUDY

The women who have been doing entrepreneurship in rural areas of Dharmapuri district of Tamilnadu. India was studied. Dharmapuri is one of the drought affected district of Tamilnadu. The normal rainfall is very low. The people mainly depend on the agro based products for their living. The recent phenomenon of self help group movements has accelerated the rural poor to be self reliant and decision makers. This has given them varied opportunities to exercise their entrepreneurship skills with small amount.

### 1.4.8. RESEARCH DESIGN

The researcher has adopted a descriptive research design for this study. The researcher has explored the relationship between different variables like educational qualification, religion, community, type of family and life coping skills of women entrepreneurs. Moreover, this research explained the factors

responsible for the women becoming entrepreneurs; problems encountered by them and also described the psychological attitudes especially the home, educational, social, health and emotional status of women entrepreneurs.

**Life Coping (Adjustment) Scale:** The “Adjustment Inventory” is developed by A.K.P.SINHA and R.P.SINHA. This scale contains 102 items of which Home -16, Health -17, Social -22, Emotional -29 and Educational -18 items are randomly distributed on the scale. The scale gives a Holistic estimate of adjustment of an individual. The subjects can be classified into five categories in accordance with the raw scores obtained by them on the inventory. The five different categories of adjustment are: A = Excellent, B = Good, C =Average, D = Unsatisfactory, E = Very unsatisfactory adjustment.

## 1.4.9. FINDINGS

### DEMOGRAPHIC CHARACTERISTICS

#### Independent variables:

Age is an important variable which determines the vigor of entrepreneurship. According to this study 44% of the respondents come under the age group between 26 to 40 and others as follows : Below 25 (36%) and 41 to 60 (20%). Almost half of the respondents belong to the middle age group.

The educational qualifications also contribute much to the entrepreneurship attitude. Nearly 59% of the respondents are illiterates and have done only under 10<sup>th</sup> standard. Illiterates (27%), Below 10<sup>th</sup> (32%), Higher secondary (10%), Graduation (15%), Post graduation (6%), Technical (3%) and other (4%)

In India, Religion plays a vital role in deciding ones character and their social actions.

Marriage status of the respondents has a very crucial in determining the entrepreneurial attitude. Married (68%), Unmarried (19%), Divorced (1%) and separated (2%)

The Monthly income of the respondents are : Below 1000 (25%), 1001 to 5000 (53.5 %), 5001 to 10,000 (14%), 10,000 to 15000 (7%). Caste is an inseparable factor to be studied in the Indian sociological context. According to this sample taken : FC (1%), MBC (79%), BC (11%) and SC (9%). Total number of years residing in one place : One year (20%), Two years (21%), 3Three years (47%), Four years (8%) and 5 years 4%). Studies on women entrepreneurs show that the single women are more successful in running their concerns. This study collected the samples from Nuclear (62%) Joint (38%) families.

The total number of family members : 1 to 5 (60%), 6 to 10 ( 38%) , 11 and above (2%). Family occupation : Entrepreneurial ( 80%) Non entrepreneurial (20%). The Yearly income of the family is : 1 to 5000 ( 37%), 5001 to 10,000 (28%), 10001 to 20,000 ( 26%), 20001 to 50,000 (8%) , 50001 and above ( 1%). Many of the women entrepreneurs run their operation as their family business . according to this sample 53% run this as their family business.

The Starting capital of the business varies from person to person: Below 5000 ( 28%), 5000 to 10,000 ( 24%), 10001 to 15,000 (12%), 150001 to 20,000 ( 5%), 20001 to 25,000 (7%), 25001 to 30,000 (4%), 30001 to 35,000 ( 7%), 40001 to 45 000 (9%), 45001 to 50,000 ( 1%) and 50001 and above ( 11%).

The most important factor of the SHS's are its savings : Below 5000 (5%), 5001 to 10000 ( 25%), 10001 to 20000 (58%), 20001 to 50000 (7%) and 50000 and above (5%). The duration of doing business : 1year (48%), 2 years (45%), 3 years (2%), 4 years (1%) and 5 years (4%).

The Persons behind the start of the business : Self interest (34%), Parents (22%), Both parents and self (9%), Friends and self (22%) and others (8%). The different reasons for starting the buisiness:

It is a family members business (32%), Inspired by the success of the friends and relatives (13%), Desire to become an entrepreneur (95%), Unemployment (11%), Realization of own ideas (11%), dissatisfaction with the previous employment (9%), To do self employed (12%), Availability of finance and technical aspects (4%), Let me try or accidental (5%) Flexibile working time and location (2%). Regarding the Entrepreneurial aspects of the respondents 18% posses the quality and 82% do not posses the entrepreneurial skill.

Duration of the trainings attended : IVDP (24%, Madhampatti (1%) and Velli santhai (1%). The Names of the business run by the respondents: Cool drinks shop (7%), Fancy shop (4%), Fruit shop (4%), Goat rearing (10%), Milk selling (30%), Petty shop (15%), vegetable shop (19%), Water business (4%)

The status of the business: Sole ownership (87%) and Informal (7%). The present condition of the business: Growth with good income (22%), Moderate (59%) and Critical (15%). The Number of hours devoted for the business: Less than 5 hours (25%), between 5 to 10 (62%), Between 11 hrs to 15 hrs (7%) and Over 15 hours (1%). The Method of marketing : Retail (94%), others (6%).

Regarding the Competitors for the business : 100% there is no one exist in this district. The Role model to their business: Friends (7%), Husband (30%), Relatives (10%), SHG Members (32%) and Villagers (15%).

The Present Business condition : Very good 98%), Good (46%), Satisfactory (46%). Regarding their Leisure time activities: Outdoor (43%) and Indoor (57%). Regarding their Social participation: Membership in an association (31%), SHG members (56%) and Any other (6%)

Family members opinion about the business: Very good (77%), Good (20%) satisfactory (2%) and Bad (1%). The Relatives opinion on the business : Very good (22%), Good (65%) satisfactory (8%) and Bad (5%). Friends opinion their buisiness: Very good (34%), Good (29%) satisfactory (29%),Bad (6%) and very bad (2%). The SHG group members opinion: Very good (47%), Good (35%) satisfactory (16%) and Bad (2%). The Opinion of the Youth group leaders : Very good (35%), Good (37%) satisfactory (17%) and Bad (6%) and very bad (5%). The Opinion of the Local association leaders: Very good (23%), Good (40%) satisfactory (21%) and Bad (13%) and very bad (3%). The Opinion of the Political leaders: Very good (17%), Good (28%) satisfactory (31%) and Bad (16%)and very bad (8%) and the Opinion of the other Entrepreneurs: Very good (22%), Good (28%) satisfactory (22%) and Bad (14%) and very bad 14%)

Customers satisfaction of the business they run: Very good (25%), Good (34%) satisfactory (30%) and Bad (7%)and very bad (4%). The opinions of the Financial institutions': Very good (25%), Good (22%) satisfactory (15%) and Bad (14%)and very bad (4%). The Mentors opinion Very good (34%), Good (26%) satisfactory (28%) and Bad (9%) and very bad (3%). The other community people's opinion on the business: Very good (21%), Good (43%) satisfactory (20%) and Bad (12%) and very bad (4%).

Participation of women in politics; especially from rural areas, considered to be one of the indicators of women development. 18% the respondents do participate in the politics, 38% don't involve themselves and 35% were Unable to commend.

Following are the habits practiced by the respondents:

Chewing the pawn: Always (12%), Occasionaly (9%), Never (79%)

Drinking habit : Always (2%), Occasioionaly (14%), Never (83%)

Gambling: Always (2%), Occasionally (9%), Never (89%)

Dept and money lending: Always (15%), occasionally (26%), Never (59%)

**Table : 1 Life Coping Skill**

Factors of Life coping skill	High	Average	Low	Total
Emotional	25 (13%)	145 (73%)	30 (14%)	200 (100%)
Health	40 (20%)	130 (65%)	30 (15%)	200 (100%)
Home	20 (10%)	120 (60%)	60 (30%)	200 (100%)
Social	38 (19%)	106 (53%)	56 (28%)	200 (100%)
Educational	32 (16%)	105 (52%)	63 (32%)	200 (100%)
TOTAL	15%	61%	24%	100%

The overall entrepreneurial attitude of 200 respondents is that High (15%), Average (61%) and low (24%). The Life coping skills of the respondents trait wise: Emotional : High (13%), Average (73%) and Low (14%), Health : High (20%), Average (65%) and Low (15%), Home: High (10%), Average (60%) and Low (30%), Social : High (19%), Average (53%) and Low (28%) and Educational : High (16%), Average (61%) and low (32%).

The respondents have more of high level attitude in Health, more of average level in emotional, and more of low level in Educational attitudes.

The respondents have more of less level among the high level group is Home, Educational among average and emotional among the low level groups.

### **Anova**

5% level of significant differences are observed among the independent variables with the overall life coping skills. Yearly income (0.019\*), Religion (0.033\*), Family occupation (0.042\*) and year of residing in that place (0.29\*)

No significant differences exists among the independent variables with the overall life coping skills such as method of marketing, Number of hours devoted for business, Present status of the business, Reasons for starting the business, Persons behind start of the business, Number of years doing the business, Personal savings, Operation as family business, Yearly income, Family type, Different castes, Monthly income, Religion, Educational qualifications and age groups. Marital status of the respondents, Family Income, Starting capital of the business and Loan sources

### **Chi square test**

There is 5% level of association exist between the following independent variables with the overall entrepreneurial attitude.

The independent variable Religion (0.043\*) has got 5% level of association with the overall life coping skill.



There is no association exists between the following independent variables with the overall life coping skills: Castes, sub-castes, Migratory status, Year of residing in a place, Family type, Total no of family members, Family occupations, Family income, Starting capital, sources of loans savings, Number of years involved in the business,, persons behind business, Reasons for starting, Marital status, Names of business, Monthly income, Number of hours devoted for work, Method of marketing, Role model.,

## CORRELATIONS

1% level of correlation is observed between the following Independent variables with the overall life coping skill: Marital status (0.004\*\*)

5% level of correlation is observed between the following Independent variables with the overall life coping skill. age (0.013\*), Income (0.011\*), Persons who inspired the business (0.033\*) and Loan sources (0.021\*)

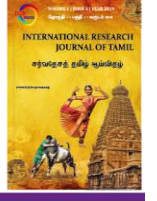
There is no correlations established between these following independent variables with the overall entrepreneurship : Religions, age, Monthly income, castes, total number of years residing in one place, Family type, Educational qualification, , Business as family operation, starting capital, savings, Number of years involved in the business and reasons behind the business. Present status of business

## 1.4.10. SUGGESTIONS

Almost all the respondents have only the average levels of entrepreneurships. Therefore, it is very important to arrange trainings on life coping and life management skills. The respondents are more in low level of educational attitudes. It is very important to improve the educational knowledge. Formal and informal educational programs, skill training on life skill and stress coping skills are very essential.

## REFERENCES

- Augustine, L. F., Vazir, S., Rao, S. F., Rao, M. V., Laxmaiah, A., & Nair, K. M. (2011). Perceived stress, life events & coping among higher secondary students of Hyderabad, India: A pilot study. *Indian Journal of Medical Research, 134*(1), 61-68.
- Chaudhary, S., & Joseph, P. M. (2010). Adolescents' Perceptions about Coping with Stress: A Qualitative View from India. *International Journal of the Humanities, 7*(11), 87-109.
- Deepshikha, & Bhanot, S. (2011). Role of Family Environment on Socio-emotional Adjustment of Adolescent Girls in Rural Areas of Eastern Uttar Pradesh. *Journal of Psychology, 2*(1), 53-56.
- Dhal, A., Bhatia, S., Sharma, V., & Gupta, P. (2007). Adolescent Self-Esteem, Attachment and Loneliness. *Journal of Indian Association for Child and Adolescent Mental Health, 3*(3), 61-63.
- Ganesh, K., & Vathsala, S. (2017). Pattern of Stress, Coping Strategies and Suicidal Ideation among women in Southern India. *Pattern of Stress, Coping Strategies and Suicidal Ideation among Adolescents in Southern India, 7*(1), 22-30.
- Lee, R. M., Jenny, S., & Yoshida, E. (2005). Coping with intergenerational family conflict among Asian American. *Journal of Counseling Psychology, 52*(3), 389-399.
- Mathew, A., & Nanoo, S. (2013, Jan-Mar). Psychosocial Stressors and Patterns of Coping in Adolescent Suicide Attempters. *Indian Journal of Psychological Medicine, 35*(1), 39-46.
- Parameswari, J. (2011, Jul-Dec). Self-Esteem and Life Coping among Adolescents. *Journal of Psychological Research, 6*(2), 257-264.
- Upadhayay, B. K., & Khokhar, C. P. (2006). Personality Traits And Feeling Of Loneliness In Unemployed Youths. *Europe's Journal of Psychology, 2*(4). Retrieved from Europe's Journal of Psychology: <https://ejop.psychopen.eu/article/view/288/html>



## நம்பியகப்பொருள் காட்டும் வாழ்க்கை நெறி மு.சென்னப்பன் அ.\*

அ\* தமிழ்த்துறை, அரசு கலைக்கல்லூரி, தருமபுரி-636705, தமிழ்நாடு, இந்தியா.

### The way of life that shows Nambiyaga Porul

M. Chennappan a,\*

<sup>a</sup> Department of Tamil, Government Arts College, Dharmapuri-636705, Tamil Nadu, India.

\* Corresponding Author:  
[anbiniyanthinai@gmail.com](mailto:anbiniyanthinai@gmail.com)

Received: 15-03-2021  
Revised: 30-06-2021  
Accepted: 06-07-2021  
Published: 26-07-2021



#### ABSTRACT

The development of grammatical literature is constantly changing according to the context in which it appears. On that basis, each of the Tamil grammar books records the biographical elements of the people who lived in the respective period. Nambiyaga Porul is the book that expands the internal grammar after the Iraiyanar Kalaviyalurai who gives grammar to the internal subject in the line of grammar. In that sense, the autobiographical grammar of Tholkappiyar grammar and Chandor's literature, which adapts it, expands the internal grammar and sets it up as a story show, showing new developments. The description of the inner branch was first known in this book. Karuporul ettu. He was fourteen. He also mentions the events leading up to the marriage in the area of handwriting and drawing people. The description of the inner branch was first known in this book. The karpial nattraai thirteen people were found to have marked the day along with the learner. It is the only object of faith in grammar texts that standardize internal traditions and describe them as fields. Tholkappiyar refers to events only as claims. Theft classification has been categorized as possible up to chastity and has been divided into various claims in 32 fields. Theft and chastity have been categorized and elaborated, and charitable standing has been summarized into seven categories, which have been extensively discussed in two areas, internal and graphical. Beliefs such as the Tholkappiyam have five physical distinctions: introspection, theology, graphics, pedagogy, and annihilation. The grammatical definition of thirukkovaayar is also interpreted as the concept of intuition. The text is based on the amount, type, and spread. Literary songs such as Thanjai Vanan Kovai songs, Sangam literary songs, Thinaimozhi lym padhu, Thinaimaalai Nootruyimpadhu, thirukkovaayar have also been taken as evidence songs. It explores lifestyles that show a special optimism with a theatrical style and literary style that arose from the old and new tradition.

**Keywords:** Tholkappiyam, Tamil Grammar, Nambiyaga Porul, Iraiyanar.

#### முன்னுரை

உலகியல் வழக்கு, செய்யுள் வழக்கு எனும் இவ்வழக்கின்கண் மொழியினை ஒழுங்குபடுத்தப் பேரறிஞர்கள் தமிழ்மரபிற்கேற்ப வகுத்த நெறிமுறையே இலக்கணமாகும். பேச்சுமொழி எப்பொழுது ஒழுங்கு பெற்றதோ அப்பொழுதே இலக்கணம் தோன்றிவிட்டது என கருதலாம். ஆக, “ஒரு மொழியைப் பிழையறப் பேசவும் எழுதவும் உதவுவது இலக்கணம்” என்ற பொதுவான கூற்று மெய்பிக்கின்றது. (Veluppillai, 2002) எனவே தமிழ் அகப்பொருள் இலக்கணங்களான தொல்காப்பியம், இறையனார் அகப்பொருள், தமிழ்நெறி விளக்கம்,

வீரசோழியம், நம்பியகப்பொருள், களவியற்காரிகை, மாறனகப்பொருள், இலக்கணவிளக்கம், தொன்னூல்விளக்கம், முத்துவீரியம், சுவாமிநாதம், அறுவகை இலக்கணம் ஆகியவற்றுள் பல அக மரபு மாற்றங்கள் நிகழ்ந்துள்ளன. இலக்கண நூல் வரிசையில் அகப்பொருளுக்கு இலக்கணம் கூறும் இறையனார் களவியலுரையை அடுத்து அக இலக்கணத்தை விரித்துக்கூறும் நூலாக இருப்பது நம்பியகப்பொருள் என்னும் நூலாகும். நம்பியகப்பொருள் இலக்கண நூலில், நிகழ்ந்த அகமரபு வளர்ச்சி பற்றி ஆராய்ந்து விளக்குவதே இக்கட்டுரையின் நோக்கமாகும்.

## நம்பியகப்பொருள்

நாற்கவிராச நம்பியரால் கி.பி.12-ஆம் நூற்றாண்டில் இயற்றப்பட்ட இலக்கணம். இது “தொல்காப்பியத்தின் அகப்பொருள் இலக்கணத்தையும், சான்றோரின் இலக்கியத்தையும் தழுவி இயற்றப்பட்டது. செப்பமுற விளங்குகிறது. நூற்பாக்கள் எளிமையுடையன; மனப்பாடம் செய்வதற்கு ஏற்றன; வேண்டியாங்கு விரித்துக் கூறப்பெறும் கருத்துக்களை விரிதும், அடுக்கிக் கூற வேண்டியவற்றைச் சுருக்கியும் கூறுகின்றது” என சோம.இளவரசு கூறுவர் (Ilavarasu, 2010). இந்நூல் ஐந்து இயல்களையுடையது. அகத்திணையியல்-116, களவியல்-54, வரைவியல்-29, கற்பியல்-10, ஒழிபியல்-43 என மொத்தம் 252 நூற்பாக்களையும் கொண்டுள்ளது. திருக்கோவையாரின் இலக்கண வரைமுறை அகப்பொருண்மைக் கருத்துக்களையும் நம்பியகப்பொருள் விளக்குகிறது. இந்நூல் கிளவிகள், தொகை, வகை, விரி என்கிற அடிப்படையில் அமைந்துள்ளன. தஞ்சைவாணன் கோவைப் பாடல்கள், சங்க இலக்கியப்பாடல்கள், திணைமொழிஐம்பது, திணைமாலை நூற்றைம்பது, திருக்கோவையார் போன்ற இலக்கியப் பாடல்களும் சான்றுப் பாடல்களாக எடுத்தாளப்பட்டிருக்கின்றன. ‘இலக்கியம் கண்டதற்கு இலக்கணம் இயம்பல்’ என்ற நெறி காலங்காட்டும் வளர்ச்சியில் மாறி இலக்கணம் கண்டதற்கு இலக்கியம் இயம்பும் முயற்சிகள் தோன்றின. இம்முயற்சிகளில் முதல் நூல் தஞ்சைவாணன் கோவையாகும்.

## மரபு

மரபு என்பது நம் முன்னோர்கள் விட்டுச்சென்ற எச்சங்களை காலம் காலமாகக் கடைப்பிடித்து வருபவை. காலச்சூழலுக்கு ஏற்ப சில மாற்றங்களும் நிகழ்வதற்கு வாய்ப்புண்டு. “ஒரு காலத்தில் சமூக வழக்கில் இருந்த ஒரு மரபு, எல்லாக் காலத்திலும் ஏற்கப் பெற்றிருக்கவேண்டும் என்ற கட்டாயம் இல்லை. கள்ளுண்ணுதல் சங்க கால மரபாக இருந்துள்ளது. ஒரு மரபு பிறிதொரு காலத்தில் வீழ்ச்சியடைந்த பிறகு அது மீண்டும் மறுமலர்ச்சி அடைய வாய்ப்பு உண்டு, அவ்வாறு அது மறுமலர்ச்சி அடையும்போது பண்டைக்கால உருவு இழந்து நடப்புக் காலத்திற்கு ஏற்ப மாற்றம் பெற்றே வழக்கு வரும் அல்லது சமகால சமூகத்தின் ஏற்புரிமை பெற்றே வழக்கு வரும்” என்கிறார் சிலம்பு நா. செல்வராசு (Selvarasu, 1998). மரபு என்பது விதியாக, அறமாக, கட்டுப்பாடாக, கட்டமைப்பாக அமைப்பொழுங்களாகச் சமூகத்தில் நிலவி வருகின்றது. “தொல்காப்பிய மரபியலில் உள்ள ‘மரபு’ என்ற சொல்லுக்கும் ‘நூன்மரபு’, ‘மொழிமரபு’ ஆகியவற்றிலுள்ள மரபு என்ற சொல்லுக்கும் பொருள் வேறுபாடு உண்டு. நன்னூலில் வரும் மரபு, மரபு வழுவமைதி ஆகியன குறிப்பதும் மேலே தொல்காப்பியத்தில் வரும் மரபு என்ற சொல்லும் ஒரு பொருள் தருவன அல்ல” என்று சீனிவாசன் குறிப்பிடுகிறார் (Kumarakuruparan, 2005). இப்பரிமாணங்களில் மரபு என்ற சொல்லாட்சியைப் பல பொருண்மைகளில் தொல்காப்பியர் பயன்படுத்தி இருப்பதைக் கொண்டு மரபின் தொன்மையை உணரமுடிகிறது. முந்தைய தலைமுறை வாழ்வியலோடு தொடர்புடைய வாழ்வியல் எச்சங்கள் தற்கால பயன்பாட்டிற்கு வழங்கும் எதுவும் மரபேயாகும்.

## அகப்பாட்டு உறுப்புகள்

செய்யுள் உறுப்புகளைப் பொதுவாகவே குறிப்பிடுகின்றார் தொல்காப்பியர். ஆனால் அகப்பாட்டு உறுப்புகள் இவை தான்.

“திணையே கைகோள் கூற்றே கேட்போர்

இடனே காலம் பயனே முன்னம்

மெய்ப்பாடெச்சம் பொருள் வகை துறையென்று

அப்பால் ஆறிரண்டகப்பாட் டுறுப்பே” (Thamizhannal, 2005)

என்று நாற்கவிராச நம்பி வரையறை செய்கிறார்.

### கைக்கிளை, பெருந்திணை

இலக்கணங்களை வரையறை செய்யும் பாங்கு தொல்காப்பியத்தைவிட நம்பியகப்பொருளில் மேலோங்கிக் காணப்படுகின்றன. கைக்கிளை, பெருந்திணை குறிப்பு (தொல்.அகத்.53,54) தொல்காப்பியர் கூறுவதை இவர் கைக்கிளையுடைய தொருதலைக் காமம் (நம்பி.நூ.3) பெருந்திணையென்பது பொருந்தாக்காமம் (நம்பி.நூ.5) என இலக்கணம் வகுக்கிறார் அகக்கைக்கிளை, அகப்பெருந்திணை, அகப்புறக் கைக்கிளை, அகப்புறப் பெருந்திணை எனவும் விரித்துக் காட்டுகின்றார்.

‘காமஞ்சால இளமையோள்’ எனத் தொல்காப்பியர் கைக்கிளைத் தலைவியைக் கூற, நாற்கவிராச நம்பி ‘காமஞ்சான்ற இளையோள்’ (ந.அ.நூ.29) எனக் கூறுவதினால் அகப்புறக் கைக்கிளைக்கு விளக்கம் முதலில் இந்நூலில்தான் அறியமுடிகிறது. பொருந்தாக்காமத்தை அகத்திணையில் கூறி இதன் விளக்கத்தை ஒழிப்பியலில் இருவகையாக அகப்பொருட்பெருந்திணை, அகப்புறப் பெருந்திணை என விவரித்துள்ளார். “அகன்றுழிக் கலங்கல், மடற்கூற்று, குறியிடையீடு, தெளிவிடை விலங்கல், வெறிகோள் வகை, உடன்போக்கு, பூப்பியலுரைத்தல், பொய்ச்சூளுரை, தீர்ப்பில் ஊடல், போக்கமுங்கியல்பு, பாசறைப் புலம்பல், பருவ மாறுபடுதல், வன்புறையெதிர்த்து மொழிதல், அன்புறு மனைவியும்தானும் வனமடைந்து நோற்றல்” (தமிழண்ணல், 2005) ஆகியவை அகப்பொருட் பெருந்திணை ஆகும். “மடலேறுதல், விடைதழால், குற்றிசை, குறுங்கலி, சுரநடை, முதுபாலை, தாபதநிலை, தபுதாரநிலை” (Thamizhannal, 2005) ஆகியவை அகப்புறப் பெருந்திணை ஆகும். இவற்றுள் நாற்கவிராசநம்பியார் காட்டிய பெருந்திணைப் பாசுப்பாடுகள் தெளிவிண்மை. இப்பாசுபாட்டைப் “பிழையான இலக்கண வரலாறு” (Manickam, 2009) என்று கூறும் வ.சுப. மாணிக்கம் அவர்களின் கருத்து சிந்தனைக்குரியதாகும்.

### அன்பின் ஐந்திணை

அன்பின் ஐந்திணையை ‘அன்புடைக் காமம்’ என்பதோடு அதனுடைய முப்பொருள்கள் குறித்த விளக்கமும் தொல்காப்பியரை அடியொற்றியே விளக்கி அதற்குரிய களவியல், வரைவியல், கற்பியல் என துறைகள் வைத்துக் கூறுகின்றார்.

கைகோள்

“அளவில் இன்பத் தைந்திணை மருங்கிற்

களவுகற் பெனவிரு கைகோள் வழங்கும்” (Thamizhannal, 2005)

என கைகோளுக்குரியதாகக் கூறுகின்றார்.

இயற்கைப்புணர்ச்சி, இடந்தலைப்பாடு, பாங்கற்கூட்டம், பாங்கியற்கூட்டம் ஆகியவற்றைத் தொல்காப்பியத்தைப் போல் (தொல்.நூ.487), களவுப்புணர்ச்சியில் வைக்கின்றார். மறைவெளிப்படுதல், தமரிற்பெறுதல் என கற்பிற் புணர்ச்சியில் (தொல்.நூ.488) தொல்காப்பியர் கூற, நம்பியகப்பொருள் குரவறிப்புணர்ச்சி, வாயிற் கூட்டம் இந்த இரண்டும் காட்டுகின்றன. பொருள் அடிப்படையில் மாற்றம் ஏதும் இல்லை.

### களவியல் துறைகள்

களவியலைப் பதினேழு துறைகளாகவும், கற்பியலை ஏழுதுறைகளாகவும், வரைவியலை எட்டுத்துறைகளாகவும் கொண்டு ஒவ்வொரு துறையும் வகை, விரி என்ற நிலையில் இந்நூல் விளக்குகிறது.

“இயற்கைப் புணர்ச்சி, வன்புறை (வற்புறுத்தல்), தெளிவு (தலைவி தலைவனை நம்புதல்), பிரிவுழி மகிழ்ச்சி, பிரிவுழிக் கலங்கல், இடந்தலைப்பாடு, பாங்கற்கூட்டம், பாங்கிமதி உடம்பாடு, பாங்கியற்கூட்டம்,

பகற்குறி, பகற்குறி இடையிடு, இரவுக்குறி, இரவுக்குறி இடையீடு, வரைவு வேட்கை, வரைவு கடாதல், ஒருவழித் தணத்தல், வரைவிடை வைத்துப் பொருள்வயிற் பிரிதல்” (Thamizhannal, 2005) என்பன 17 துறைகள் களவிற்குரிவையாகும்.

## களவுப் பிரிவு

“திருமணத்தில் பெண்ணுக்குப் பரிசம்போடக் காதலன் பிரிந்து பொருள் தேடி வரவேண்டும். இது சிறுபிரிவு. இதற்கு பருவம் வரையறை கிடையாது. வரைவிடைக்காகப் பொருள் தேடிவருவதற்கு பருவம் இரண்டு மாதத்தின் மேல் இருக்கக்கூடாது” என்கின்றார் (Thamizhannal, 2005).

## கற்பியல் துறைகள்

“கற்பியல், அகவாழ்க்கை முறையே இல்வாழ்க்கை, ஓதற்பிரிவு, காவற்பிரிவு, தூதிற்பிரிவு, துணைவயிற் பிரிவு, பொருள் வயிற்பிரிவு, பரத்தையிற் பிரிவு” என்பன ஏழு துறைகள் கற்பியலுக்குரியவையாகும் (Thamizhannal, 2005).

## கற்பியல் பிரிவு

“ஓதற், தூது, மன்னர்க்கு உற்றுழி உதவிசெய, பொருள்தேட, காவற்பிரிவு, பரத்தையிற் பிரிவு என ஆறு வகை. அவற்றுள் பரத்தையிற் பிரிவு அயல்மனை, அயற்சேரி, புறநகர்” என மூன்று பிரிவுகளாகும் (Thamizhannal, 2005).

## வரைவியல்

“வரைவு மலிதல், அறத்தொடு நிலை, உடன்போக்கு, கற்பொடு புணர்ந்தகவ்வை, மீட்சி, தன்மனை வரைதல், உடன்போக்கு இடையீடு வரைதல்” (Thamizhannal, 2005) போன்றன குறித்துள்ளார்.

அகவாழ்க்கை மரபுகளை வரன்முறைப்படுத்தித் துறைகளாக விளக்கப்பட்டிருக்கும் இலக்கண நூல்களில் நம்பியகப்பொருள் மட்டுமே ஆகும். தொல்காப்பியம் கூற்றுகளாக மட்டுமே நிகழ்ச்சிகளைக் கூறுகின்றது. நம்பியகப்பொருள் களவு, கற்பு வரை இயலாக வகைப்படுத்தி 32 துறைகளில் பல்வேறு கூற்றுகளாக விரித்துக் கூறியுள்ளது.

## மாந்தர்கள்

களவு கற்புக்குத் தொல்காப்பியரைப் போல் (தொல்.நூ.490-491) கூற்றிற்குரியோரைச் சுட்டுகின்றன. கற்பியல் நற்றாய் சேர்த்து பதின்மூன்றுபேர் (நம்பி.நூ.213-214) குறிப்பிடுவதோடு கூற்றுக்கு உரியமையற்றவர்களையும் தொல்காப்பியத்தை (தொல்.நூ.492) அடியொற்றி கூறுகின்றார்.

## கேட்போர்

தொல்காப்பியம் வழுவமைத்தது போல் (தொல்.நூ.501) தலைவி கூற்றிற்குப் புறநடையாக மக்கள் இன்றி திணைப்பொருள்கள் நம்பியகப்பொருள் கூறுகின்றன. அதாவது, தலைவி தன்னோடு பேசுவது போலக் கருதிப் பேசுவாள். “தன் நெஞ்சு, நாணம், அறிவு, ஞாயிறு, திங்கள், மாலைப்பொழுது, புள் (பறவை), மா (விலங்கு), புணரி (கடல்), கானல் (கடற்கரைச்சோலை) உள்ளிட்டனவும், இவை தவிர உப்பங்கழி, நெய்தற்பூ, புன்னை முதலான மரம், தழைபோல்வனவும் தன் பேச்சைக் கேட்பது போலவும், தனக்கு அவை இனிய ஆறுதல் பகர்வன போலவும் தான் ஏவியதை அவை செய்தமை போலவும் தம்மை அவை தேற்றுவது போலவும் தலைவி கூற்று அமையும்” (Thamizhannal, 2005). இஃது உளவியல் சார்ந்தது. இதைக் காமம் மிக்க கழிபடர்கிளவி எனவும் கூறுவர். இதனால் மனச்சுமை குறையும்; ஆறுதல் கிடைக்கும். “தலைவன், தலைவி, பார்ப்பான், பாங்கன், பாங்கி, செவிலி, கண்டோர் பாணன், கூத்தர், விறலி, பரத்தை, அறிவர், நற்றாய்” (தமிழண்ணல், 2005) முதலாகிய பதின்மூவரும் யாரொடும் பேசாது தம்மொடு தாமே கூறியும் அமைவர்.

## அகப்பொருள் விளக்கத்தில் காணலாகும் புதிய செய்திகள்

“உரைப்போர் கேட்போர் இல்லாமல் புலவன் கூறும் கவியே துறையாகும். அதாவது அகமரபுக்கும் கூற்றுக்கும் அல்லாத புதியதாக ஒருவர் கூறும் கூற்றாகும்” (தமிழண்ணல், 2005). இவர் காலத்தில் துறையின் பொருண்மையில் திரிபு ஏற்பட்டுள்ளதை அறியலாம். அதாவது துறை என்பது கூற்று நிகழிடத்தைக் குறிக்கவில்லை என்கிறார்; தி.வசந்தாள். எனவே, தொல்காப்பியர் கூற்றுமுறையில் அக இலக்கணங்களைக் கூறவும், இவர் அக்கூற்றுக்களைத் தொகுத்துக் கதை நிகழ்ச்சிபோல அமைத்து, கிளவித்தொகை, வகை, விரி என முப்பிரிவாக வகுத்துரைத்திருப்பது புதியதாகும்.

“ஊடலைப் போக்குகின்ற வாயில்களாகப் பார்ப்பனர், பாங்கர், சூத்திரர், பாங்கர் என இருவகைப் பாங்கர், காமக்கிழத்தி, காதற்புதல்வன் ஆற்றாமை” ஆகியோர் தொல்காப்பியர் குறிப்பிடாத வாயில்கள், தொல்காப்பியர் தாயை வாயில்களில் வைத்துக்காட்டுவர் (தொல்.நூ.197) நாற்கவிராச நம்பி தாயைப் பற்றி கூறவில்லை. அக இலக்கணத்தில் நுட்பமான துறைகளில் ஒன்று அறத்தொடு நின்றல் என்கிற துறை. களவைக் கற்பாக மாற்றுவதற்கான முயற்சியாகும். தொல்காப்பியம் அறத்தொடு நின்றல் பற்றி விளக்கமாகக் கூறவில்லை. இரத்தினச் சூருக்கமாக ‘புரையீர் கிளவி’ என்கிறது. அறத்தொடு நிற்கும் மரபு ஏழு வகைப்படும் என்பதனை (தொல்.பொரு.நூ.203) கூறுகின்றார். இவ்வேழு வகைகளையும் தொகுத்து இருவகையுள் அடக்குவர். அகத்திணை இயல் (நம்பி.நூ.47-54) வரைவியலில் (நம்பி.நூ.175-179) ஆகிய 13 நூற்பாக்களில் விரிவான தகவல்களைத் தருகின்றார் நாற்கவிராசநம்பி.

அறத்தொடு நின்றல், நிகழுமிடம், நின்றற்குரியார், நிற்கும்நெறி, தலைவி, பாங்கி, செவிலி, நற்றாய் ஆகியோர் அறத்தொடு நின்றல் திறம் உடன்போக்கில் அறத்தொடு நின்றற்குரியார் யார் யார்? அறத்தொடு நின்றலின் வகை, அதன் விரி ஆகியவை விரிவாகக் கூறுவதினால் அகப்பொருள் வளர்ச்சிக்குத் தக்கதொரு சான்றாகும்.

தொல்காப்பியர் கற்புக்கும் களவிற்கும் பிரிவுகள் குறிப்பிட்டாரேயன்றி அவற்றை வகைப்படுத்திக் கூறவில்லை. ஆனால் பல நூற்பாவில் அவை பற்றிய செய்திகள் (நம்பி.நூ.62) நூற்பாவில் களவுக்குரிய பிரிவுகளை வகைப்படுத்திக் கூறியிருக்கின்றார்.

## முடிவுரை

நம்பியகப்பொருளுக்கு இலக்கிய நூலாகத் தோன்றியது தஞ்சை வாணன் கோவை என்பது அறியலாயிற்று. தொல்காப்பியர் செய்யுள் உறுப்புகளைப் பொதுவாகக் கூறியுள்ளார். நாற்கவிராச நம்பி அகப்பாட்டு உறுப்புகளாக ஒழிபியலில் வைத்துள்ளதை அறியமுடிந்தது. அகப்புறக் கைக்கிளைக்கு விளக்கம் முதன் முதலாக இந்நூலின்தான் காணமுடிந்தது. பெருந்திணைப் பாகுப்பாடுகள் தெளிவாக இல்லை என்பதனை உணரமுடிந்தன.

கற்பிற்புணர்ச்சியில் தொல்காப்பியர் மறைவெளிப்படுத்தல், தமரிற்பெறுதல் என்பர். நம்பியார் குரவரிற்புணர்ச்சி, வாயிற் கூட்டம் என்பர். ஆனால் பொருள் அடிப்படையில் மாற்றம் இல்லை பரத்தையிற் பிரிவு மூன்றாகப் பிரித்துள்ளார். கைக்கோள் கூற்றுக்குரியோர் பதின்பேர் என்பர். கற்பில் நற்றாய் சேர்த்து பதின்புன்று பேர் என்று குறிப்பிட்டுள்ளார். அகக்கூற்றுக்களைத் தொகுத்துக் கதை நிகழ்ச்சிபோல் அமைத்து, கிளவித்தொகை, வகை, விரி, என மூன்று பிரிவாக வகுத்து உரைத்திருப்பது புதியதாகும்.

தொல்காப்பியர் தாயை வாயில்களில் வைப்பார். இவர் தாயைப் பற்றிக் கூறவில்லை. ஊடலைப் போக்குகின்ற வாயில்களாகப் பார்ப்பன், பாங்கர், சூத்திரர் இருவகை பாங்கர், காமக்கிழத்தி, காதற்புதல்வன் ஆகியோர் ஊடலைப் போக்குகின்ற வாயில்கள் ஆவார். அறத்தொடு நின்றலை ஏழு வகைகளையும் தொகுத்து அகத்திணை, வரைவியல் என்ற பகுதியில் விரிவாகப் பேசியுள்ளார்.

களவு, கற்புக்குரிய பிரிவுகளை வகைப்படுத்தி விரிவாகக் கூறியுள்ளதையும் அறியமுடிந்தன. தொல்காப்பியம் போன்று இயல் பாகுப்பாடுகள் உடையது. பழைய, புதிய மரபு கொண்டு எழுந்த ஒரு நாடகப்பாங்கோடும், இலக்கிய நயத்தோடும் விளங்கும் சிறப்புக்குரிய நம்பியகப்பொருள் இலக்கண மரபு வளர்ச்சியில் நிகழ்ந்துள்ள அக மரபு மாற்றங்கள் குறித்துத் தெளிவாக ஆராயப்பட்டுள்ளன. எனவே, இந்நூல்

மேற்குறிப்பிட்ட அகவாழ்க்கை மரபு வளர்ச்சியடையப் பல காலங்கள் தேவைப்பட்டினும், இத்தகையதொரு முழுமையான வளர்ச்சியை அடையப் பிறிதொரு இலக்கண நூல் இருந்திருக்கலாம். அது மறைந்துபோனதால் அந்த இலக்கண நூலுக்கு இலக்கியமாக அமைந்த திருக்கோவையாரை வழி நூலாகக் கொண்டு நாற்கவிராசநம்பி இத்தகைய அக இலக்கண நூலை வரையறுத்திருக்கலாம் என்கிற கருத்தும் நிலவுகிறது.

பண்படுத்தப்பட்ட சமூகத்தின் ஒழுக்கநெறி சார்ந்த விளைச்சலே இலக்கணம். அது இலக்கணம் நூல் இயற்றியோரின் அறிவுத்திறத்தை மட்டும் வெளிப்படுத்துவன அல்ல. பல சமூக மாற்றங்களையும், அச்சூழலில் வாழும் மக்களின் வாழ்வாதாரங்களையும், பழக்க வழக்கங்களையும், நாகரிகப் பண்பாட்டையும், வரலாற்றுத் தரவுகளையும் எடுத்து இயம்பக் கூடியதாக அமைகின்றன.

திணை மரபை அடியொற்றி எழுதப்பட்டுள்ள பொருளிலக்கண நூல்கள் பெரும்பாலும் வேறுபாடின்றி ஒரு நூல் ஒரு பகுப்பின்கீழ்க் கூறிய அகம், புறம் சார்ந்த சில கருத்துக்களை மற்ற இலக்கண நூல்களில் கால மாற்றத்திற்கேற்ப மாற்றங்கள் நிகழ்ந்துள்ளதையும் அறிய முடிந்தன.

## References

- Ilavarasu, S., (2010) Ilakkana Varalaru, Meyyappan Pathippakam, 2<sup>nd</sup> Edition, Chennai, India.
- Kumarakuruparan, (2015) Tamilarin Kalavu - Marapum Pathivum, Madurai Kamaraj University, India.
- Manickam, Va Suba., (2009) Tamilkadhal, Sree Indhu Publications, Chennai, India.
- Selvarasu, S.N., (1998) Sanga Ilakkiyam Maruvaasippu Samuga Manudaviyal Aayvukal, kavya pathippakam, Chennai, India.
- Thamizhannal, (2005) Nambiyaga Porul, 1st edition Meenakshi Puthaka Nilayam, Madurai, India.
- Velupillai, A., (2002) Tamil Varalatu Ilakkanam, Kumaran Book House, Chennai, India.

**Funding:** NIL

**Acknowledgement:** NIL

**Conflict of Interest:** NIL

**About the License:**



© The author 2021. The text of this article is licensed under a Creative Commons Attribution 4.0 International License

சிறப்பிதழ்  
Special Issue

13-15 பங்குனி 2022  
26<sup>th</sup> - 28<sup>th</sup> March 2021

ISSN : 2321 - 984X

# நவீனத் தமிழாய்வு

(பன்னாட்டுப் பன்முகத் தமிழ் ஆய்விதழ்)

Journal of

## Modern Thamizh Research

(A Quarterly International Multilateral Thamizh Journal)  
Arts and Humanities (all), Language  
Literature and Literary Theory, Tamil  
UGC Care Listed (Group-I) Journal

சிறப்பிதழ் :  
இணையவழிப் பன்னாட்டுக் கருத்தரங்கம் - 2021  
தமிழ்த்துறை,  
கேரளப் பல்கலைக்கழகம்  
காரியவட்டம், திருவனந்தபுரம், கேரளா

## பெண் தெய்வங்கள்

சிறப்பிதழ் ஆசிரியர்  
Special Issue Editor

முனைவர் ஹெப்சி ரோஸ் மேரி. அ  
தமிழ்த்துறைத் தலைவர்



Published by

**RAJA PUBLICATIONS**  
10, (Upstair), Ibrahim Nagar, Khajamalai,  
Tiruchirappalli - 620 023, Thamizh Nadu, India.  
Mobile : +91-9600535241  
website : rajapublications.com

17 பகுதி-1  
Part -1

Chief Editor

Dr. M. Sadik Batcha

Advisory Editor

Dr. N. Chandra Segaran

Editorial Board

Dr. MAM. Rameez

Dr. Jeyaraman

Dr. A. Ekambaram

Dr. G. Stephen

Dr. S. Chitra

Dr. S. Senthamizh Pavai

Dr. A. Shunmughom Pillai

Dr. P. Jeyakrishnan

Dr. Seetha Lakshmi

Dr. S. Easwaran

Dr. Kumara Selva

Dr. Ganesan Ambedkar

Dr. Krishanan

Dr. Kumar

Dr. S. Kalpana

Dr. T. Vishnukumaran

Dr. M. N. Rajesh

Dr. Govindaraj

Dr. Uma Devi

Dr. Senthil Prakash

Dr. Pon. Kathiresan

Dr. S. Vignesh Ananth

Dr. M. Arunachalam

Dr. S. Bharathi Prakash



மற்றொன்று:

## செம்மொழித் தமிழ்

(பன்னாட்டுப் பன்முகத் தமிழ் காலாண்டு ஆய்விதழ்)

ஜனவரி - மார்ச்

ஏப்ரல் - ஜூன்

ஜூலை - செப்டம்பர்

அக்டோபர் - டிசம்பர்

Journal of

## Classical Thamizh

(A Quarterly International Multi lateral Thamizh Journal)

January - March

April - June

July - September

October - December

ISSN:2321-0737

1. அ. ஹெப்சி ரோஸ் மேரி	நாட்டார் பெண்தெய்வ வழிபாட்டில் தோற்றக்கதைக்கூறுகள்	1-7
2. த. விஜயலட்சுமி	கேரளத்தில் கண்ணகி வழிபாடு	8-13
3. அ. பிரசில்லா	புலம் பெயர்ந்தோர் வழிபாடும் சாதியக் கட்டமைப்பும்	14-21
4. லீமா மெட்டில்லா. அ	நாட்டார் நிகழ்த்து கலைகளில் பெண் தெய்வங்கள் (பாலக்காடு மாவட்டம், கேரளம்)	22-28
5. முத்துலெட்சுமி. ச	நாட்டுப்புற தெய்வ வழிப்பாட்டில் செந்திட்டை தேவி	29-33
6. அ. ஏஞ்சல் ராணி	கத்தோலிக்கத் திருச்சபையும் மரியாளும்	34-40
7. த. அஜி	தமிழ்ச் சமூக மரபில் மணிமேகலா தெய்வம்	41-46
8. தி. அல்பா கிரேஸ்	நாட்டுப்புற பெண் தெய்வம் மண்டைக்காடு பகவதி அம்மன்	47-50
9. இ. அல்போன்சாள்	வீரமாமுனிவரின் படைப்புகளில் மரியன்னை	51-56
10. க. அமரேசன்	மக்கள் மரபில் பிடாரி அம்மன் வழிபாடு	57-61
11. தே. அம்சவள்ளி	ஆற்றுப்படையில் பெண் தெய்வங்கள்	62-65
12. மு. அமுதா	பெண் தெய்வங்கள் காட்டும் பக்திநெறி	66-70
13. ற. ஆனந்த மல்லிகா	மாசற்ற மாசாணியம்மன்	71-75
14. க. ஆனந்தராஜன்	பெண்தெய்வ வழிபாட்டில் மதுரை இராக்காயி அம்மன் பெறுமிடம்	76-82
15. செ. ஆனந்தி	தீ பாய்ந்த அம்மன்	83-87
16. க. அன்பழகன்	அம்மன் தோற்றமும் வரலாறும்	88-93
17. செ. அன்பு	"நல்லதங்காள்" என்னும் வாழும் தெய்வம்	94-97
18. கே. எஸ். அன்புகலா	நாவல்களில் பெண்தெய்வச் சித்தரிப்புகள்	98-102
19. யா. ஆரோக்கிய நாயகம்மாள்	கிறித்தவச் சிற்றிலக்கியங்களில் மரியாள்	103-107
20. ப. அருணாதேவி	இலக்கியங்களில் மீவியலாற்றலான அணங்கு வழிபாடு	108-114
21. ஜா. அருள் கனிலா	கிறித்தவர்களின் தாய் அன்னை மரியாள்	115-121
22. இரா. அருள்மொழி	பெண் தெய்வ வழிபாடு	122-126
23. து. அருண்பாண்டியன்	காட்டேரி சிறுதெய்வ வழிபாடும் இறை தத்துவமும்	127-131
24. வே. அருட்பாமணி	சகலமும் நல்கும் ஸம்பக்கர்தேவி அல்லது அரசு காத்த அம்மன் (வழிபாட்டு மரபுகள்)	132-134
25. நீ. பகவதியம்மாள்	வலிகளின் பின்னணியில் வாழ்ந்து சிலையான கருவறைத் தெய்வங்கள்	135-141
26. பி. பாலச்சந்திரன்	சக்தி வடிவத்தின் தத்துவக் கோட்பாடுகள்	142-147
27. அ. பெனிலா ஜாய்	கண்ணகி வழிபாட்டு தொன்மை	148-153
28. பாரதி ராஜா. வே	ஜெயமோகனின் காமரூபினி கதையில் யட்சிகளும், இசக்கிகளும்	154-160
29. மு. பிருந்தாவனம்	தமிழ் இலக்கியங்களில் தாய்த்தெய்வ வழிபாடு	161-165
30. சீ செஞ்சுலட்சுமி	செல்லியம்மன் வழிபாட்டு மரபுகள்	166-171
31. மு. சென்னப்பன்	தமிழரின் களவொழுக்கத்தில் வெறியாட்டு	172-175
32. அ. டெய்சி	நாட்டார் இலக்கியங்களில் பெண் தெய்வமும் வழிபாடும்	176-180
33. க. தேவி	நாட்டார் வழிமரபில் சுயம்புவாகத் தோன்றிய பெண் தெய்வங்கள்	181-185
34. வி. தேவி	சரபேந்திரர் பூபாலக் குறவஞ்சியில் - பெண் தெய்வங்கள்	186-189
35. ந. தனசேகர்	கொல்லிப்பாவை	190-194
36. அ. திவ்யா	பெண் தெய்வ தோற்றக் கதைகள் - பேச்சிப்பாறை பேச்சியம்மன்	195-200
37. கோ. சாந்தமூர்த்தி	தமிழ் இலக்கியங்களில் பெண் தெய்வ வழிபாடு	201-205
38. க.நீ. இளங்கோவன்	செல்லாண்டியம்மன், மதுரகாளியம்மன் வரலாறும் வழிபாடும்	206-210
39. சு. பாத்திமா	தமிழ் - மலையாளப் புதினங்களில் பெண் தெய்வ வழிபாடுகள்	211-217
40. ச. காயத்ரி	திரௌபதியம்மன் பெண் தெய்வ தோற்ற மரபுகள்	218-222
41. ச. கீதா	பெண் தெய்வங்களில் காத்தாயி அம்மன் வழிபாடு	223-228
42. கீதா இராமலிங்கம்	இசக்கியம்மன் வழிபாடு	229-235
43. க. கிரிவாசன்	மதுரகாளியம்மன் வழிபாட்டில் மரபும் புதுமையும்	236-240
44. மா. கோமதி	சித்தர் இலக்கியங்களில் பெண் தெய்வங்கள்	241-245
45. சு. கோமதி அழகு	எண்ணெய்க்காரச்சி அம்மன் வரலாறும் வழிபாடும்	246-252
46. ச. குருஞானாம்பிகா	இருக்கன்குடி மாரியம்மன் ஆலய வழிபாட்டு முறைகள்	253-261
47. செ. லீ. ஹெலன்	தத்துவ நோக்கில் பெண் தெய்வ வழிபாடு	262-266
48. பீ. இலக்கியா	முப்பந்தல் இசக்கியம்மன் தோற்றக் கதையும் தற்போதைய நிலையும்	267-273
49. வி. இளமதி கனகசுந்தரம்	பெண் தெய்வ வழிபாடு மலர்ந்து வந்த பாதை	274-281
50. கு. ஜெயந்தி	அகநூல்களில் முல்லைத்திணையில் பெண்கள்	282-285
51. வெ. ஜெயந்தி & என். விஜயலட்சுமி	இறையருள் நாட்டிய பெண் தெய்வங்கள்	286-290
52. ஜென்ஸிஸ் குமார். பி.	தாய்த்தெய்வ வழிபாட்டில் வளமைசார் கருத்தாக்கங்கள்	291-295
53. ஜென்சி வை.கி	நாட்டார் பெண் தெய்வங்களில் இசக்கியம்மன் வழிபாடு	296-303
54. தா. ஜெயலக்ஷ்மி	சு. தமிழ்ச்செல்வியின் நாவல்களில் பெண் தெய்வ வழிபாட்டு முறைகள்	304-308
55. ஜெ.சா. ஜிஜி கிறிஸ்டோபெல்	நாட்டுப்புற வழிபாட்டில் சப்த கன்னிமார்கள் குறித்தான வழிபாடு	309-314
56. லூ. ஜோன் சில்வியா பிரேமா	பெண் தெய்வ வழிபாட்டு முறைகளும் மரபுகளும்	315-319
57. அ. ஜோதிரவிந்திரன்	பாரதியார் கவிதைகளில் பெண்தெய்வ வழிபாடு	320-324
58. அ. கலைச்செல்வி	கதைப் பாடல்கள் காட்டும் கொலையில் உதித்தப் பெண் தெய்வங்கள்	325-329
59. இரா. கலைச்செல்வி	அழியாப் பெண்ணினத்தின் மீட்சி (அழியா இலங்கை அம்மன்)	330-334
60. கல்பனா. ச & க. கலாவதி	மலசர் பழங்குடியின் மாகாளியம்மன் வழிபாடும் தாய்வழி பண்பாட்டியங்கியலும்	335-340

## தமிழரின் களவொழுக்கத்தில் வெறியாட்டு

மு. சென்னப்பன்

முனைவர் பட்ட ஆய்வாளர் (முழுநேரம்), தமிழ்த்துறை,  
அரசு கலைக்கல்லூரி, தருமபுரி - 636 705. தமிழ்நாடு, இந்தியா.

### ஆய்வுச் சுருக்கம்

பழந்தமிழர் திருமணமாகாத கன்னிப் பெண்களை சூர், அணங்கு மற்றும் முருகப்பெருமானும் துன்புறுத்துவதாக நம்பினர். அதை மெய்பிக்கும்வகையில் பெண் ஒருத்தி களவொழுக்கத்தினால் அவளுடைய உடலில் சில மாற்றங்கள் உண்டாகின்றன. அதற்கான காரணத்தை அறியாமல் அப்பெண்ணின் தாயும் செவிலியும் இந்த நோய் முருகப்பெருமானால் வந்தது என்று எண்ணி முருகனுக்கு தொண்டு செய்யும் வேலனை அழைத்து வெறியாட்டு எடுத்து வழிபாட்டு சடங்குகளைச் செய்து இது தெய்வக் குற்றமெனக் கூறி அதற்கான பரிகாரங்களைச் சொல்லி அதைச் செய்துள்ளதையும், நற்றிணை, குறுந்தொகை, அகநானூறு, கலித்தொகை வெறியாடல் பொருள் பற்றியே ஐங்குறுநூற்றில் வெறிபத்து என ஒரு பத்து அமைந்துள்ளன. இவ்வகையில் சிலப் பாடல்களைக் கொண்டு சங்ககால மக்கள் வாழ்வில் வெறியாட்டு நிகழ்வுகளையும் அதற்கான காரணத்தையும் இக்கட்டுரையில் தெளிவாக ஆராயப்பட்டுள்ளன.

கலைச்சொற்கள்: முருகன், வேலன், பூசாரி, கட்டுவிச்சி, வெறியாட்டு, அணங்கு, செவிலி, நற்றாய், தோழி, தலைவி, களவு, காதல்

### முகப்புரை

சங்க காலச் சமுதாயம் பெரிதும் இம்மை வாழ்வின் செம்மையிலும் இன்பத்திலும் நாட்டமுடையதாக இருந்தது. எனினும் மக்கள் தங்கள் வாழ்வும் வளமும் சிறக்கவும் தாங்கள் எண்ணிய வினைகள் இனிதே நிறைவேறவும், மனித சக்திக்கு அப்பாற்பட்ட மற்றொரு சக்தியான தெய்வ சக்தியைப் பண்டைய காலம்

முதல் இன்று வரை இந்த மானிடச் சமூகம் நம்பிக்கையோடு வழிபட்டு வருகின்றன. இந்த தெய்வ வழிபாடு என்பது இறைவனை மனதால் நினைத்து இரு கரங்களால் கூப்பித் தொழுதலே ஆகும். 'வழிபாடு' எனும் சொல் 'தொழுதல்' என்ற பொருளிலேயே பெரும்பாலும் வழங்கப்படுகின்றன.

சங்க கால மக்களின் கடவுள் வழிபாடு என்பது நிலத்தின் தன்மைக்கேற்ப வழிபாட்டு முறைகள் அமைகின்றன. முருகன் வழிபாடு அதன் தொன்மை தொல்காப்பியர் காலம் முதல் 'சேயோன் மேய மைவரை உலகமும்' என்ற தொடர் மூலம் அறிந்துகொள்வதோடு குறிஞ்சி நிலத்துக் கடவுளாகவும் விளங்குகின்றன. புறப்பொருள் நூல்கள் முருகனைப் போர் கடவுளாகக் குறிப்பிடுகின்றன. அகப்பொருள் நூல்கள் முருகனை காதற் கடவுளாகப் பேசப்படுகின்றன. தமிழரின் களவொழுக்கம் பற்றிப் பேசப்படும் இடங்களில் எல்லாம் வேறு கடவுளுக்கு இடமில்லை. முருகனே முதன்மை பெறுகின்றான். பண்டைத் தமிழ் மக்களின் அகவாழ்வு முருகனோடு பின்னிப்பிணைந்துள்ளதையும் வெறியாட்டு நிகழ்வுகளையும் பற்றி ஆராய் வதே இக்கட்டுரையின் நோக்கமாகும்.

### மலைக் கடவுள்

சங்க இலக்கியங்கள் முருகனை மலைநிலக் கடவுளாகவே வருணிக்கப்பட்டுள்ளன.

“வான் கோட்டுக் கடவுள்”<sup>1</sup>

“பிறங்கு மலை மீமிசைக் கடவுள்”<sup>2</sup>

இந்த வரிகள் மூலம் முருகன் குன்று, மலைகளில் வாழும் குறிஞ்சிநிலக் கடவுளாக இலக்கண இலக்கியங்கள் வழி உணரமுடிகின்றன.

முருகன் தலங்கள்

திருச்சீரலைவாய், திருவாவிநன் குடி திருப்பரங்குன்றம் ஆகிய மூன்று தலங்கள் பற்றி அகநானூற்றின் வாயிலாக,

“முருகன் நற்போர் நெடுவேள் ஆவி அறுகோட் டியானைப் பொதினி”<sup>3</sup>

“பல்பொறி மஞ்சை வெல்கோடி உயரிய ஓடியா விழவின் நெடியோன் குன்றம்”<sup>4</sup>

“திருமணி விளக்கின் அலைவாய் செருமுகு சேஎம்”<sup>5</sup>

என்பது அறியமுடிகின்றது.

போர் கடவுள்

குறிஞ்சிலக் கடவுளான முருகனை வீரத்தின் வடிவமாகவும், போர்க்கடவுளாகவும் மக்கள் வழிபடுகின்றனர் என்பதை,

“முருகன் நற்போர்”<sup>6</sup>

“செங்களம் படக்கொன்றவுணர் தேய்த்த”<sup>7</sup>

“போர்வெல் வல்லான்”<sup>8</sup>

இப்பாடல்களின் மூலம் உணரலாம். முருகனைப் பெண் தெய்வங்களோடு தொடர்புபடுத்தி பெரும்பாணாற்றுப்படையில் முருகனைப் ‘பேய் கூத்தாடும் துணங்கையெம் செல்வியின் குழவியெனக்’ கூறுகின்றது. நக்கீரர் திருமுருகாற்றுப்படையில் கொற்றவை சிறுவனாகவும், பழையோள் குழவியாகவும், மலைமகள் மகனாகவும் குறித்துள்ளார்.

வெறியாடல்

களவொழுக்கத்தில் தலைவியின் உடல் மற்றும் நடத்தையில் மாற்றம் ஏற்படுகின்றன. இதனைக் கண்ட செவிலி, நற்றாய் இதற்குக் காரணம் முருகனே என்று முதுபெண்டிர் சொல்படி வெறியாட்டை நிகழ்த்துகின்றனர். வெறியாட்டை நிகழ்த்துபவன் வேலன் என்னும் பூசாரி. வேலன் ஆடுகளம் அமைத்து ஆடுபலி கொடுத்து நெற்பொரி, தினை தூவி முருகனை வழிபட்டு ஆவேசமாக ஆடித் தலைவிக்கு வந்த

மாற்றத்திற்கு முருகன்தான் காரணம் என்று கூறுகின்றான்.

“களவு அலர் ஆயினும் காமம் மெய்ப்படுப்பினும் அளவுமிகத் தோன்றினும் தலைப்பெய்து காணினும்”<sup>9</sup>

என்கிற தொல்காப்பிய நூற்பாவின் மூலம் வெறியாட்டு நிகழ்ச்சியின் தன்மையை அறியமுடிகின்றது.

செவிலித்தாய், தலைவியின் தாய் தலைவியின் மாற்றத்தைக் கண்டு வேலனை அழைத்து வெறியாட்டு மற்றும் குறி சொல்பவளை அழைத்து மக்களின் நோய்க்கான காரணம் கேட்கிறாள். இத்தருணத்தில் தோழி குறிக்கிட்டு மலைத் தலைவனைப் பற்றி கூறுமாறும் கேட்கிறாள்.

“அகவன் மகளே அகவன் மகளே!

மனவுக்கோப் பன்ன நன்னெடுங் கூந்தல்”<sup>10</sup>

ஆக, தலைவன் தலைவியின் களவொழுக்கம் வெறியாடல் மூலம் தோழி வெளிப்படுத்துகின்றான்.

தலைவியின் களவு பலரால் அறியப்பட்டு அலர் ஏற்படுகின்றன. காமத்தினால் தலைவியின் உடலில் மாற்றம் நிகழ்கின்றன. இவை முருகனால் வந்தது என்று கட்டுவிச்சி மற்றும் வேலன் மூலமும் குறி பார்த்து வெறியாடல் நிகழ்த்துகின்றனர்.

“கறிவளர் சிலம்பின் கடவுட் பேணி அறியா வேலன்வெறியனெக் கூறும்”<sup>11</sup>

“பொய்யா மரபின் ஊர்முது வேலன் கழங்குமெய்ப் படுத்துக் கன்னம்தூக்கி”<sup>12</sup>

“மென்தோள் நெகிழ்த்த செல்லல் வேலன் வென்றி நெடுவேள் என்னும் அன்னையும்”<sup>13</sup>

என்ற பாடல்கள் வழியே முருகனால் மகளிர் அணங்குப் பெற்றுள்ளதையும் அறியமுடிகின்றன.

களவொழுக்கத்தில் முருகனைப் பற்றி வரும் இடங்களில் எல்லாம் ‘வெறியாடல்’ என்னும் வழிபாட்டுமுறையே முதன்மை பெறுகின்றன. களவில் ஈடுபட்டிருந்த தலைவி தலைவனைச்

மு. சென்னப்பன்

சந்திக்க முடியாமையால் அவளது உடல் மெலிந்து வாடினாள். இதனை அறியாத தாய் வெறியாடல் என்னும் வழிபாடு செய்ய 'வேலன்' என்னும் முருகப் பூசாரியை வரவழைத்துவிட்டாள். வேலனும் கட்டும் கழங்கம் பார்த்து 'இந்நோய் முருகனால் வந்தது' எனக் கூறி வெறியாடலைத் தொடங்கினான். முருகா! தலைவிக்கு ஏற்பட்டுள்ள நோய் தலைவனால் வந்தது என்று நீ அறிந்திருப்பதால் வேலன் வேண்டினான் என்பதற்காக நீ வருதல் உன் பெருமைக்கு ஏற்றதல்ல. நீ கடவுள் ஆயினும் மடவை' என்று கடிந்துரைக்கின்றான். தோழி,

“கார் நறுங் கடம்பின் கண்ணிகுடி  
வேலன் வேண்ட வெறிமனை வந்தோய்  
கடவுள் ஆயினும் ஆக  
மடவைமன்ற வாழிய முருகே”<sup>14</sup>

என்று தலைவியின் காதல் ஒழுக்கத்தை தெரிந்துக் கொள்ளாமல் அவளது தாய் வேலனைக் கொண்டு வெறியாட்டை நிகழ்த்துகின்றான். 'காதல் வாழ்வினை முருகனது விளையாட்டுகளுடன் இயைபுபடுத்துதல் முற்றிலும் ஒரு தமிழ் மரபு' என்கிற கருத்தும் உள்ளம் கொள்ளத்தக்கதாகும் (Dr. N. Subramanian, Sangam Policy, P.36).

வெறியாடல் நிகழ்ச்சி நடத்தப்பட்ட முறைமைக் குறித்து அகநானூறு 22,29-ஆம் பாடல்கள் கூறுகின்றன.

வெறியாடல் நடந்த முறை

வேலன் வெறியாட்டுக் களத்தை அமைத்து வேலுக்கு மாலை அணிவித்து ஆட்டுக்குட்டியைப் பலி கொடுத்துச் சிவந்த திணையை அதன் இரத்தத்துடன் சேர்த்துக் கலந்து தூவி ஒலி எழுப்பி நடு இரவில் முருகனை அழைக்கின்றான். அதன் பின் வெறியாடுகிறான். கழற்காயைத் தன் உடலில் அணிந்து படிமக்கலத்தைத் தூக்கிக் கொண்டு தலைவிக் க வந்திருப்பது முருகணங்கின் குறையே என்று வேலன் கட்டுவதாக.

“நெடுவேட் பேணத் தணிகுவள் இவள்  
முதுவாய்ப் பெண்டிர் அதுவாய் கூற”<sup>15</sup>

இப்பாடல் மூலம் நாம் உணரமுடிகின்றது. வேலனைப் போன்று வெறியாடலைப் பெண்களும் நடத்தியுள்ளனர். பெண்டிர் தெய்வமுற்று வெறிகொண்டு ஆடியுள்ளதாக,

“வெறிகொள் பாவையிற் பொலிந்தஎன்  
அணிதுறந்து  
ஆடுமகள் போலப் பெயர்தல்”<sup>16</sup>

இப்பாடல் மூலம் உணரமுடிகின்றன.

வெறியாடலில் பெண்கள் நிலை

தலைவியின் காதலை அறியாதத் தாய் வெறியாட்டு நிகழ்த்துவதாகப் பல பாடல்கள் உள்ளன. வெறி, அணங்கு, நோய் என மாறுபட உணர்ந்த பெண்களாக இருந்துள்ளதை,

“அறியாமையின் வெறியென மயங்கி  
அன்னையும் அருந்துயர் உழந்தஎன்”<sup>17</sup>

இப்பாடல் தாயின் அறியாமை உண்மையாகின்றன. ஐங்குறுநூறு 241:1-2, அகநானூறு 272:13-15. இப்பாடல்கள் தலைவியின் தாயின் அறியாமை பற்றிக் குறிப்பிடுகின்றது.

வெறியாட்டு நிகழ்ந்த நாளன்று இரவில் தலைவன் வந்ததால் தலைவியின் நோய் தீர்ந்ததாக,

“வெறியென உணர்ந்த வேலனோய் மருந்  
தறியா னாகுதல் அன்னை காணிய”<sup>18</sup>

என்கிற இப்பாடல் உணர்த்துகிறது. ஆனால் வேலனின் வெறியாட்டலால் இந்நோய் தீர்ந்ததாக தலைவியின் தாய் எண்ணுகிறாள். இது தாயின் அறியாமைத் தனத்தைக் காட்டுவதாக அமைந்துள்ளன.

வேலன் வெறியாட்டு செயல்களைக் கண்டு தலைவி, தோழி போன்ற பெண்கள் எள்ளல் நகைப்பதாக உள்ளன.

“வேலன் வேண்ட வெறிமனை வந்தோய்  
கடவுள் ஆயினும் ஆக”<sup>19</sup>

இதன் மூலம் கடவுளும் அறியாமை உடையவராக உள்ளனர். தலைவியின் காதலை தெரியாதவன் வேலன் என்று இகழப்பட்டதை அறியலாம்.

வெறியாடலில் தாயின் நிலை வேறாகவும், தலைவி, தோழி இவர்களது நிலை வேறாகவும் இருப்பதை அறியமுடிந்தது. ஆம்! தலைவியின் உடல் வேறுபாடு முருகனால் ஏற்பட்டது என்று தாய் எண்ணி வருந்துகின்றாள். ஆனால் தலைவிக்கும் தோழிக்கும் இந்த வேறுபாடு தலைவனால் ஏற்பட்டது என்பதனை வெறியாடல் பாடல்கள் மூலம் அறியமுடிந்தன.

### தொகுப்புரை

முருகன் குன்று மலைகளில் வாழும் குறிஞ்சிநிலக் கடவுளாகும். வீரத்தின் வடிவமாகவும் போர்க் கடவுளாகவும் வழிபட்டுள்ளனர். களவொழுக்கத்தில் தலைவிக்கு ஏற்பட்டது காதல் நோய். ஆனால், அதை அறியாமல் தாய், செவிலி ஆகிய இருவரும் இந்த நோய் முருகனால் வந்தது என்று எண்ணி வேலனை அழைத்து வெறியாட்டு நிகழ்த்தியுள்ளனர். அதற்கான வழிபாட்டு சடங்குகளும் பரிகாரங்களும் செய்துள்ளனர். இதைக் கண்ட தலைவியும் தோழியும் இந்த நோய் தலைவன்பால் வந்தது. ஆனால், இவர்கள் செய்யும் நிகழ்வுகளைப் பார்த்து நகைக்கின்றனர். எனவே, இது தாயின் அறியாமையும், தலையின் மீது கொண்ட பற்றுப்பாசத்தையும் காட்டுவதோடு தெய்வக்குற்றம் ஏதாவது நிகழ்ந்துவிடுமோ என்ற அச்ச உணர்வினால் வெறியாட்டு நிகழ்த்தியதின் மூலம் இறை நம்பிக்கையும் உணரமுடிகின்றன.

### முடிவுரை

தமிழகத்தில் முருக வழிபாடு என்பது தொன்றுதொட்டு உருவான குலவழிபாடே என்பதற்கு வேலன் வெறியாடலே இதற்குச் சான்றாகும். உயிர்பலியிடல் முருக வழிபாட்டில் இருந்துள்ளது. தலைவி களவு வாழ்க்கையில் இருக்கும்பொழுது இக்களவு தாய்க்கு தெரியாமல் இருந்துள்ளதையும் அறியமுடிகின்றன.

தலைவியின் உடல் வேறுபாடு முருகனால் வந்தது என்று எண்ணி அதைத் தீர்ப்பதற்கு முதுபெண்டிர்கள் வெறியாடல் நிகழ்த்தியதையும் அறிந்துகொள்ளமுடிந்தது. தலைவியின் தாய்க்கு தலைவியின் களவொழுக்கத்தை தோழி அறத்தொடு நின்று வெறியாட்டின் மூலம் தெளிவுப்படுத்தியதும் அறியமுடிந்தன. தெய்வ வழிபாடு என்பது மானிடச் சமூகம் உள்ள வரை பரிணமித்துக் கொண்டுதான் இருக்கும் என்பதுதான் நிதர்சனமான உண்மை.

### அடிக்குறிப்புகள்

1. அகநானூறு, பா.348, வரி.7:8.
2. குறிஞ்சிப்பாட்டு, பா.208, வரி.9.
3. அகநானூறு, பா.1.
4. மேலது, பா.149.
5. மேலது, பா.266.
6. மேலது, பா.1:3.
7. குறுந்தொகை, பா.1, வரி.1.
8. கலித்தொகை முல்லை, பா.4, வரி.13-14.
9. தொல்காப்பியம் பொருள் களவு, 1061.
10. குறுந்தொகை, பா.23.
11. ஐங்குறுநூறு, பா.243, வரி.1-2.
12. மேலது, பா.245, வரி.1-3.
13. குறுந்தொகை, பா.111, வரி.1-3.
14. நற்றிணை, பா.14, வரி.34.
15. அகநானூறு, பா.22, வரி.6-10.
16. மேலது, பா.370, வரி.14-16.
17. ஐங்குறுநூறு, பா.242, வரி.1-2.
18. குறுந்தொகை, பா.360.
19. நற்றிணை, பா.34, வரி.9-010.

ஓ



## Analysis of groundwater quality for irrigation purpose in Pennagaram block of Dharmapuri District, Tamilnadu, India

K. Vijai\*, S.M. Mazhar Nazeeb Khan

PG & Research Department of Chemistry, Jamal Mohamed College (Autonomous), (Affiliated to Bharathidasan University – Tiruchirappalli), Tiruchirappalli 620020, Tamilnadu, India

### ARTICLE INFO

#### Article history:

Received 18 March 2021

Received in revised form 14 July 2021

Accepted 15 July 2021

Available online 8 August 2021

#### Keywords:

Groundwater irrigation quality

Physico-chemical parameters

Parameters to examine irrigation quality

Dharmapuri district

Tamil Nadu

### ABSTRACT

Groundwater is an indispensable source of water due to its substantial use for domestic, irrigation, and industrial purpose. This study is determined to examine the irrigation quality of groundwater in the seasons of pre-monsoon (PRM) and post-monsoon (POM) in the year 2013 at Pennagaram block of Dharmapuri district, Tamilnadu. A few samples of groundwater from the study area are analyzed for their physicochemical parameters (APHA, 1998). The parameters to examine irrigation quality of the samples taken in this study are  $\text{Cl}^-/\text{HCO}_3^-$  ratio, percent sodium (%Na), Index of Base Exchange (IBE), Residual Sodium Carbonate (RSC), Kelly's ratio (KR), Permeability Index (PI), Sodium Adsorption Ratio (SAR), Potential Salinity (PS), Magnesium Ratio (MR), Salinity Index and Sodicity Index. The classification of groundwater samples for irrigation was identified using the USSL Diagram, Doneen's plot, and Wilcox diagram. The spatial distribution map gives a clear depiction of the groundwater quality for irrigation purposes, in both seasons. The plot of  $\text{Cl}^-/\text{HCO}_3^-$  versus  $\text{Cl}^-$  indicates that the groundwater samples are strongly affected by salinity. It illustrates the exchangeable mechanism which has one of the responses for the chemical composition of groundwater in the study area. According to %Na, RSC, KR, SAR, PI, MR, Salinity index, and Sodicity index makes the groundwater of the study area was safe for irrigation. According to the results of PS and Sodicity index the groundwater of marginal quality i.e., closely unfit for irrigational purpose.

© 2019 Elsevier Ltd. All rights reserved.

Selection and peer-review under responsibility of the scientific committee of the International Conference On Impact Of Innovations In Science And Technology For Societal Development: Materials Science.

### 1. Introduction

Phansalkar et al. [7] Water is the main constituent of Earth's hydrosphere and a transparent and tasteless fluid which is considered the most important one for living organisms. It plays a vital role for all organisms in their day-to-day life. Groundwater is the water that is resented under the earth's surface where it occupies all or a small part of void spaces in between soils. In the case of the environment, groundwater plays a significant role by keeping the water level and also responsible for the flow of rivers, wetlands, and lakes (Tables 1–4).

Water for drinking is the basic need for an organism living on the Earth. In recent times due to pollution in water and over-extraction of water, it has become an unavailable one for mankind. Groundwater is an important natural resource for mankind and it

also plays a significant role in the economy of many nations. Water is the basic need for irrigation and the food industry. From a study, it was found that nearly 320 Billion Gallon was consumed by mankind on a daily basis from which almost 77 billion gallons of water are consumed from Groundwater by mankind for a day. So the extraction of groundwater is the mandatory one for mankind.

In India, around 90 percent of water is extracted from the ground and used for irrigation. Around 60 percent of irrigation is supported by groundwater supply and almost 90% rural households directly or indirectly dependent on groundwater for irrigation. The water quality can be identified by its chemical, physical, and biological parameters. In a study, it was found that nearly 80 percent of disease worldwide is caused because of poor drinking water.

Federation et al. [2], (Doneen et al., 1964) Contamination of Fluoride in Groundwater is considered a serious issue in many parts of the world. The reason for fluoride contamination in groundwater is due to dissolving materials containing fluoride such as cryolite,

\* Corresponding author.

E-mail address: [kvijay21@gmail.com](mailto:kvijay21@gmail.com) (K. Vijai).

**Table 1**  
Seasonal variations of Cl<sup>-</sup>/HCO<sub>3</sub><sup>-</sup> ratio.

Cl <sup>-</sup> /HCO <sub>3</sub> <sup>-</sup> ratio	Not affected (<0.5)	Slightly to moderately affected (0.5–6.6)	Severely affected (>6.6)
<b>PRM</b>	–	100%	–
<b>POM</b>	–	93.75%	6.25%

**Table 2**  
Seasonal Variations of Sodium Percentage.

Sodium percent	Water type	Clarifying samples	
		PRM	POM
<20	Excellent	–	–
20–40	Good	77(46.25%)	79(98.75%)
40–60	Permissible	3(3.75%)	1(1.25%)
60–80	Doubtful	–	–
>80	Unsuitable	–	–

hydroxyapatite, fluorspar, etc. [4]. Some others reason for fluoride contamination in groundwater was found to be due to fertilizers used for agricultural purpose, pesticide, and sewage discharge also considered as the reason for increased fluoride substance in groundwater [3]. Fluoride is found in all regions of the earth's surface, due to its occurrence as compounds and complexes. Fluoride enters groundwater due to weathering of minerals which contains fluoride substance and by which it enters into the surface of the water and sometimes through direct contact.

Szabolcs [12] Contamination of fluoride in groundwater can be identified by a human being when they under certain symptom for fluorosis and it is one of the endemic diseases which may occur due to high intake of fluoride by water, and by food with a level of 1.5 mg per liter or above [5]. Fluorosis in teeth may affect the enamel and fluoride substances above 10 mg per liter may cause a pathological change in the bones of human beings which leads to skeletal fluorosis.

Staff [13] In India almost 61.5 M people at high risk of fluorosis. 17 states across India were listed as states with endemic for Fluorosis. Even states in the southern part of India Tamil Nadu were also one among the state on the list. In Tamil Nadu, High Fluoride Contamination in Groundwater was found in the districts of Salem and Dharmapuri. Pennagaram block of Dharmapuri district was taken for our study [1]. Pollution level in groundwater must be addressed immediately. Globally many are trying to provide a healthy and safe water supply for household purposes. The water quality is detected through chemical, physical, and biological variables. Groundwater pollution will be assessed with several types of parameters. The quality of water data made by many indices was found to be simplistic and easier to understand.

The usage of groundwater for household purposes as a surface water resource is limited. The demand for groundwater for domestic purposes has increased due to the growing population. Groundwater is highly contaminated with organic and inorganic pollutants in rural regions by agriculture and by agrochemicals. Hence, it is necessary to determine the suitability of groundwater for drinking and irrigation purposes based on the presence of major ions in the groundwater. The important chemical param-

**Table 3**  
Seasonal variations of CAI-1, CAI-2 and RSC.

Parameter	CAI-I		CAI-II		RSC	
	MIN	MAX	MIN	MAX	MIN	MAX
<b>PRM</b>	0.33386	0.68016	0.83374	2.47471	-16.159	-8.1204
<b>POM</b>	0.28237	0.67352	0.68684	2.26974	-16.39	-7.1475

**Table 4**  
Seasonal variations of Kelley's Ratio (KR).

Kelley's Ratio	PRM	POM
<b>Min</b>	0.28145	0.31181
<b>Max</b>	0.67846	0.67527

ters for judging the degree of suitability of water for irrigation purpose has been selected. In this regard, the computations were carried out for the pre and post-monsoon seasons of 2013.

**2. Study area**

**2.1. Profile of the study area**

The area of study for this proposed research lies between the longitude of 77° 46' to 78° 4' and the Northern latitude of 11° 53' to 12° 19'. Fig. 1 represents the plain area covering about 604.48 km square. The specific area selected for this study includes the Pennagaram Block which belongs to the District of Tamil Nadu known as Dharmapuri. The main source of water in this area is due to seasonal rainfall from the monsoon. The average yearly rainfall for this area is about 902 mm. But during the period of 2013 to 2014, the rainfall in this region was found to be 757 mm only. This area of study for this research lies within the region of Archean Crystalline Rock, the groundwater in this region is due to fractured rocks. The temperature in this area lies up to 36°Celsius and during the winter season, the temperature was found to be between 12 and 16°Celsius (Figs. 2–9).

**2.2. Geomorphology**

Dharmapuri district lies on 455 m above sea level and the climate in this region is termed as tropical climate. The western part of Dharmapuri district which connects to Pennagaram has a hill range of Mysore plateau connecting the hill. The southern region of the district is bordered by Shervaroy Hill.

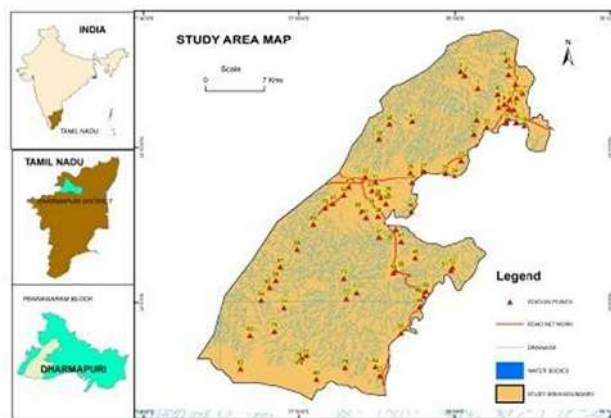


**Fig. 1.** Study area Location map.



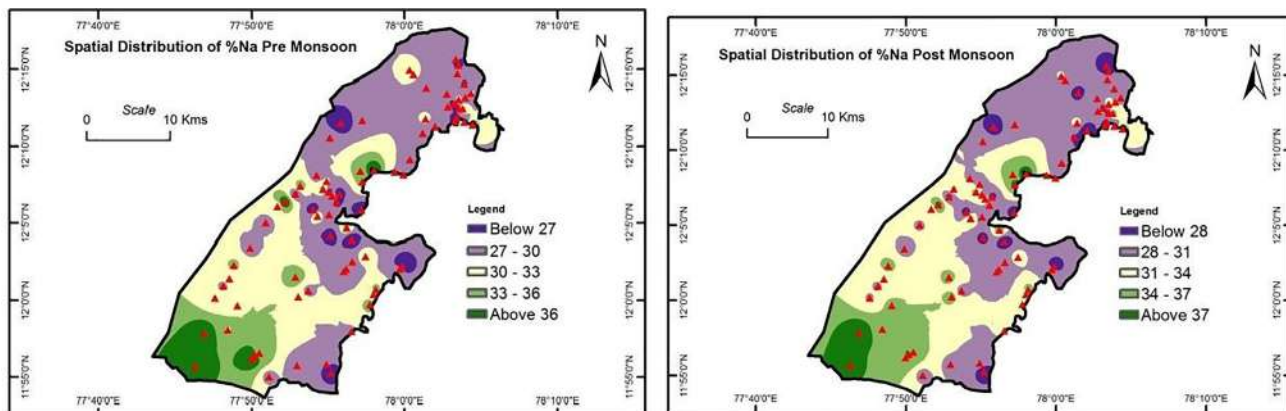


Fig. 2. Seasonal Variations of Sodium Percentage.

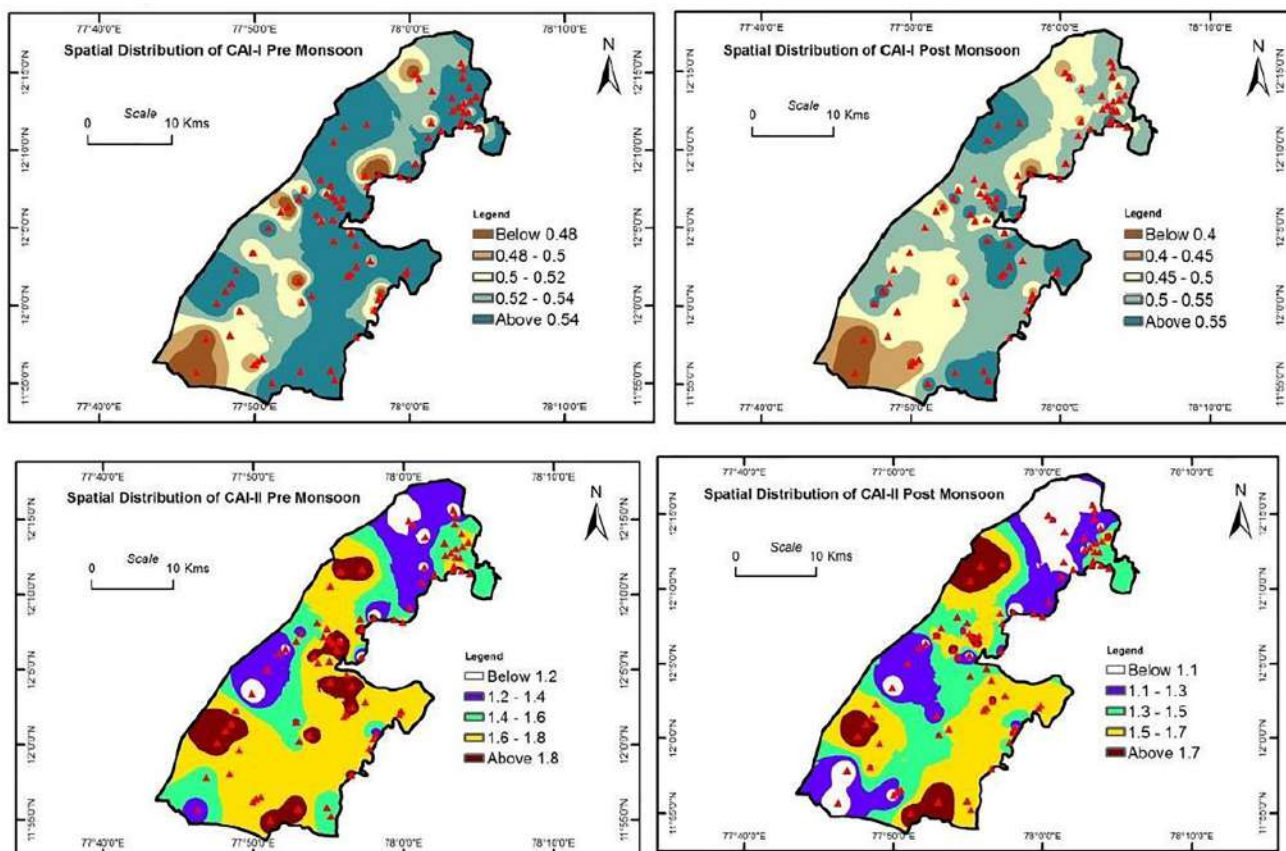


Fig. 3. Seasonal Variations of CAI-1 and CAI-2.

2.3. Hydrogeology

The Dharmapuri District is beneath Archean Crystalline metamorphic rock formed with alluvial deposits of limited vertical and areal extents alongside to main rivers. The major Aquifer setup in the Dharmapuri District is due to

- Semi and Un- Consolidated Formation of sediments
- Broken and weather rocks of Crystalline.

The areas beneath crystalline rock would have a limited source for underground water due to fracturing and weathering which occur in this zone. The Hard Rock Aquifers are heterogeneous in

nature, which can be identified through their composition, texture, and lithology, etc. The presence of groundwater beneath the phreatic surrounding in weathered rocks. The Weathered material thickness varies between lesser to 1 m below ground level (bgl) or >20 m below ground level.

3. Materials and methods

3.1. Sample collection

For this research, a total of 80 underground water as being taken as samples through bore wells and hand pumps across several locations of Pennagaram block during the pre-monsoon season

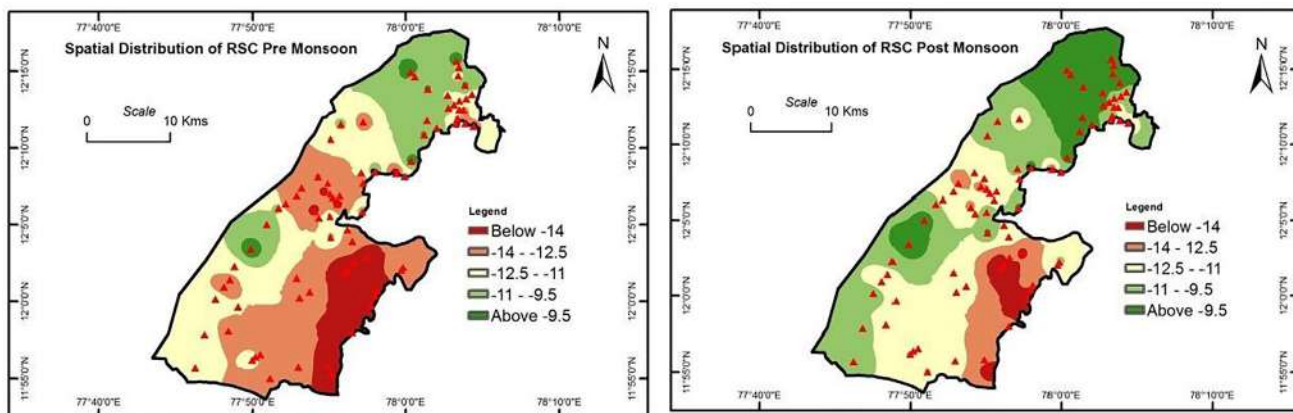


Fig. 4. Seasonal Variations of RSC.

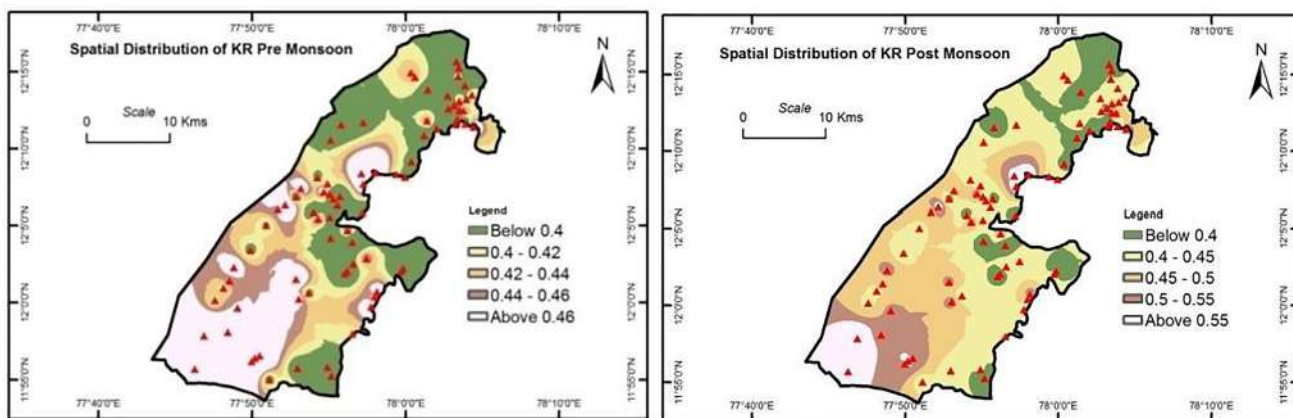


Fig. 5. Seasonal Variations of KR.

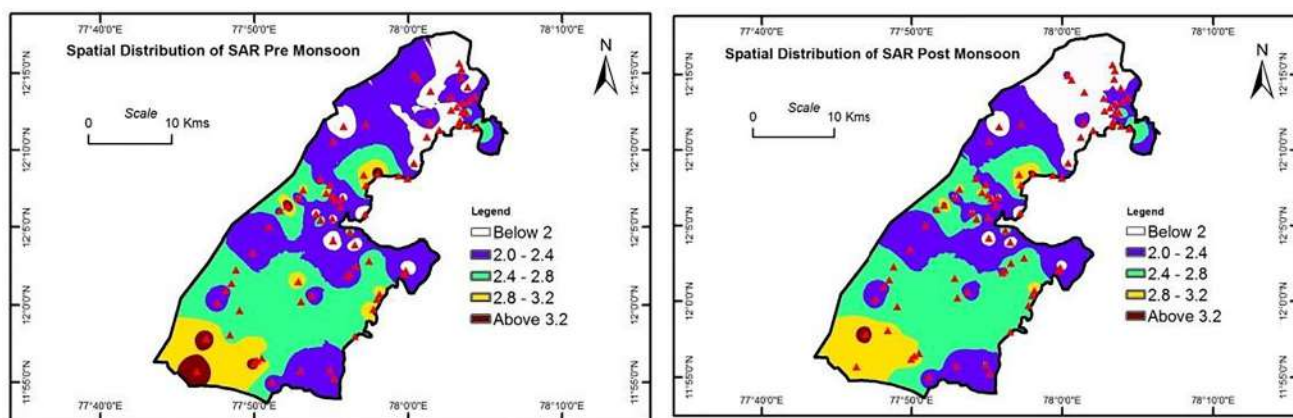


Fig. 6. Seasonal Variations of SAR.

in May 2013. The collected samples of water were cleaned and taken in sterilized bottles having the capacity of containing 2 Liter water in it without any air bubbles.

### 3.2. Methodology

The collected samples were first examined in order to assess it through the Physico-chemical process as per the standard procedure recommended by the APHA method. The spatial distribution

map was drawn GIS (ArcGIS 9.3) software. For this research, the groundwater quality from the selected samples for the process of irrigation is analyzed through calculating the  $Cl^-/HCO_3^-$  ratio, percent sodium (%Na), Index of Base Exchange (IBE), Sodium Adsorption Ratio (SAR), Kelly's ratio (KR), Permeability Index (PI), Magnesium Ratio (MR), Residual Sodium Carbonate (RSC), Potential Salinity (PS), Salinity Index and Sodicity Index. The classification of groundwater samples for irrigation was identified using the USSL Diagram, Doneen's plot, and Wilcox diagram.

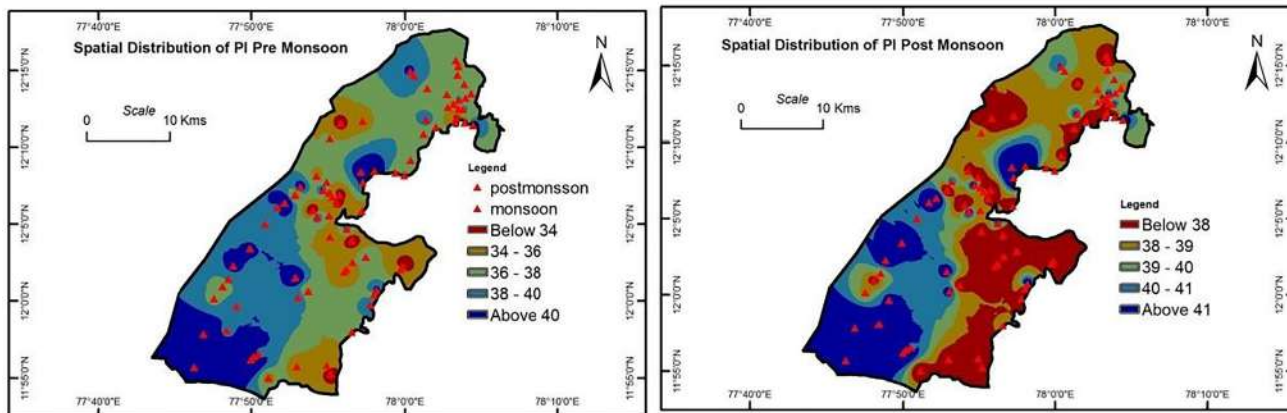


Fig. 7. Seasonal Variations of PI.

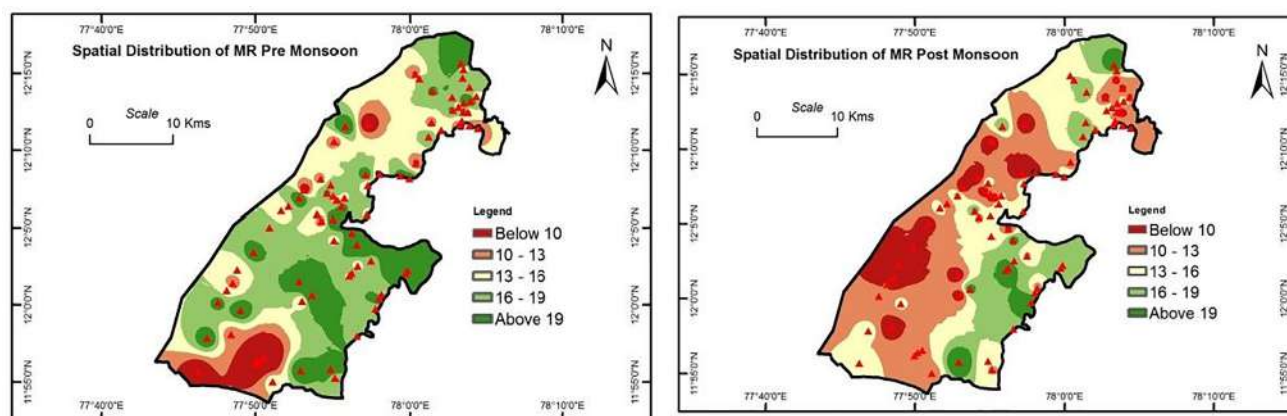


Fig. 8. Seasonal Variations of MR.

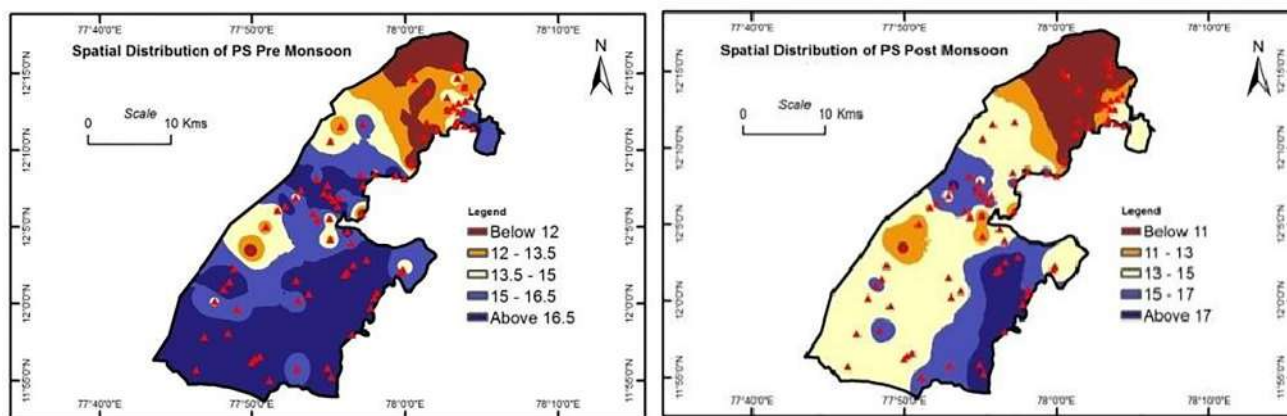


Fig. 9. Seasonal Variations of PS.

## 4. Results and discussion

### 4.1. Irrigation standard

#### 4.1.1. $Cl^-/HCO_3^-$ ratio

The  $Cl^-/HCO_3^-$  ratio is used for classifying the amount of salinization present in groundwater.  $Cl^-/HCO_3^-$  ratio was classified based on the numerical values as 'not affected' (ratio < 0.5), 'slightly to moderately affected' (ratio between 0.5 and 6.6), and

'severely affected' (ratio > 6.6) [9]. This indicates the difference in composition of dissolved salts that's normally found in groundwater and it can be used as a useful principle. The  $Cl^-/HCO_3^-$  ratios of all the groundwater samples have been computed for all the seasons in 2013. None of the samples from the study region has <0.5 and >6.6  $Cl^-/HCO_3^-$  ratios in PRM. During post-monsoon season, 93.75% of the samples were under the 'slightly to moderately' affected category and 6.25% of the samples were severely affected category. Therefore, the majority of the groundwater samples of

the studied area fall within the range of slight to moderate salinity affected condition. It may be some anthropogenic activities like domestic sewage disposal and possible uncontrolled agricultural practices.

4.1.2. Sodium percent

The amount of sodium present in groundwater is one of the important parameters to be known for using water for irrigation purposes. The presence of sodium % in groundwater is calculated using this formula as follows:

$$\% \text{Sodium} = \frac{\text{Na}^+ + \text{K}^+}{\text{Ca}^{2+} + \text{Mg}^{2+} + \text{Na}^+ + \text{K}^+} \times 100$$

The sodium concentration is expressed using Milliequivalents per liter (meq/l) [8]. The sodium percentage is exactly 60% and is the maximum acceptable limit for groundwater. The outcomes from the tested samples show that certain samples are considered as good water and the other few samples are within the range of permitted limit of pre-monsoon and post-monsoon season. The seasonal variations of Na % are tabulated in 2 [3]. A higher % of Sodium may lead to impairment and deflocculation of tilth and soil permeability.

4.1.3. Index of Base Exchange (IBE)

Schoeller [11] IDE helps in identifying metasomatism in groundwater. The Chloro Alkaline indices are calculated for groundwater samples the results from the tested samples may be positive or either negative based on the interchange of Na<sup>+</sup> and K<sup>+</sup> occurrence in groundwater along with Ca and Mg presence in rocks. The recharge area will have a positive ratio and the discharge area will have a negative ratio [11] gave a suggestion for 2 Chloro Alkaline Indices as CAI-1 and CAI-2 for specifying the exchange of ions in the environment and groundwater. The CAI-1 and CAI-2 can be calculated using these formulas:

$$\text{CAI1} = \frac{\text{Cl}^- - (\text{Na}^+ + \text{K}^+)}{\text{Cl}^-}$$

$$\text{CAI2} = \frac{\text{Cl}^- - (\text{Na}^+ + \text{K}^+)}{(\text{SO}_4^{2-} + \text{HCO}_3^- + \text{CO}_3^{2-} + \text{NO}_3^-)}$$

The value of CAI-1 ranges between 0.33386 and 0.68016, the CAI-2 value ranges between 0.83374 and 2.4747. The mentioned values are tabulated in 3 as follows. From the results from, the tested samples it was found that almost 95 percent of the selected sample lies under the negative zone. The remaining values lie under the positive zone which is evident that the interchange reaction took place in chloro-alkaline equilibrium. The cation interchange is the reason for the chemical composition of groundwater in the selected sample region.

4.1.4. Residual sodium chloride (RSC)

The residual alkalinity of water used for irrigation can be calculated using the RSC formula as follows:

$$\text{RSC} = (\text{HCO}_3^- + \text{CO}_3^{2-}) - (\text{Ca}^{2+} + \text{Mg}^{2+})$$

[13] the value of RSC <1.25 meq per liter is safer for using groundwater for irrigation and the value ranging between 1.25 and 2.5 meq per liter is known as the minimal quality and the value ranging >2.5 meq per liter is considered as unsuitable one for irrigation. The Residual Sodium Chloride value of the selected sample ranges between -16.39 and -7.1475 meq per liter tabulated in 3 as follows. The groundwater from the selected sample area for this research is safe and secured for irrigation.

4.1.5. Kelley's ratio (KR)

Kelley [6] Kelley's ratio is the ratio of Na<sup>+</sup> ion to Ca<sup>2+</sup> and Mg ion. Kelley's ratio is calculated using the following formula:

$$\text{Kelley's ratio} = \frac{\text{Na}^+}{\text{Ca}^{2+} + \text{Mg}^{2+}}$$

A complete balance in the water among Na<sup>+</sup>, Ca<sup>2+</sup>, and Mg<sup>2+</sup> ions is displayed using Kelley's ratio. The Kelley's ratio with a value higher than 1 is known as the extended level of Na<sup>+</sup> ions in water and the value more one does not for irrigation purposes. The KR value lesser than one is water perfectly suits for the irrigation process. The KR value is tabulated in 4 as follows, the value ranges between 0.28 and 0.67. The value of KR in the selected sample area perfectly suits for irrigation because of the value area lesser than one.

4.1.6. Sodium Adsorption ratio (SAR)

The SAR is used for assisting the alkalinity hazard for the process of irrigation water [13] the SAR can be determined using:

$$\text{SAR} = \frac{\text{Na}^+}{\sqrt{(\text{Ca}^{2+} + \text{Mg}^{2+})/2}}$$

Raihan & Alam [3] The SAR value is the best evaluation process for water which is used for irrigation purposes. The relationship between SAR used for irrigation and the degree of Na<sup>+</sup> level absorbed by the soil [13]. If water meant for irrigational use is high in Na<sup>+</sup> and low in Ca<sup>2+</sup>, the cation change complex can become saturated with Na<sup>+</sup>. The presence of Na<sup>+</sup> in water leads to reduced permeability and its recurrent use makes the soil impermeable, whereas elevated Na<sup>+</sup> increases the alkalinity of the soil. On the other hand, the presence of alkali earth salts (Ca<sup>2+</sup> and Mg<sup>2+</sup>) in irrigation water hinders the harmful effect of sodium by increasing soil permeability. According to the classification of Ayers and Tanji [4], the majority of the samples of the study area are safe for irrigation (Table 5).

4.1.7. Permeability index (PI)

Irrigation water used for a long period can affect the soil permeability of water due to the influence of Na, Mg, HCO<sub>3</sub><sup>-</sup>, and Ca content in the soil. [2] proposed a proper PI index for groundwater for utilizing it for irrigation purpose and the concentration values are given in milliequivalents per liter and the Permeability index is expressed using the formula:

$$\text{Permeability Index} = \frac{\text{Na}^+ + \sqrt{\text{HCO}_3^-}}{\text{Ca}^{2+} + \text{Mg}^{2+} + \text{Na}^+} \times 100$$

PI index in the selected sample area was found to be ranging between 29.59 and 48.51 given in table 6 as follows. All the samples are categorized as suitable for irrigation (PI < 60) Table 7.

4.1.8. Magnesium ratio (MR)

The Ca and Mg maintain a state of equilibrium level in groundwater. [12] A higher concentration of Mg in water will disturb the quality of soil making it alkaline which is capable of decreasing the yield of the crop. The MR ratio for irrigation of water is given as:

$$\text{Magnesium ratio} = \frac{\text{Mg}^{2+}}{\text{Ca}^{2+} + \text{Mg}^{2+}} \times 100$$

Table 5 SAR classification and its variations.

SAR [4]	Safe for irrigation (<3)	Increasing Problem for irrigation (3–9)	Severe problem for irrigation (>9)
PRM	85%	15%	–
POM	87.50%	12.50%	–

**Table 6**  
Seasonal variations of PI, MR and PS.

Parameter		Permeability Index (PI)	Magnesium Ratio (MR)	Potential Salinity (PS)
PRM	MIN	29.5995	4.28135	9.48421
	MAX	49.2334	32.8976	20.271
POM	MIN	32.6889	3.075061	8.35798
	MAX	48.5181	51.23547	19.6988

**Table 7**  
Classification of salinity index using EC values.

Water class	Electrical Conductivity (EC) $\mu\text{S/cm}$	Type of water
<b>I (Non-Saline)</b>	<700	Drinking and irrigation water
<b>II (Slightly Saline)</b>	700–2000	Irrigation water
<b>III (Moderately Saline)</b>	2000–10000	Primary drainage water and groundwater
<b>IV (Highly Saline)</b>	10000–25000	Secondary drainage water and groundwater
<b>V (Very High Saline)</b>	25000–45000	Very highly saline
<b>VI (Brine)</b>	>45000	Sea water.

An  $\text{Mg}^{2+}$  ratio >50 percent is termed as unfit and harmful one for irrigation. The selected sample area has a lesser value of 3.07 percent and a maximum value of 51.23 percent. From the result, it was found that the selected sample area has a value of <50 percent which is the best fit for irrigation.

**4.1.9. Potential salinity (PS)**

Eassa & Mahmood [1] the PS value of irrigation shows that the suitability of water for the irrigation process is not only dependent on salt concentration alone. The PS value can be determined using

$$\text{Potential Salinity (PS)} = \text{CI}^- + \frac{\text{SO}_4^{2-}}{2}$$

Lower soluble salt content in soil is best suited for irrigation but the one with a higher concentration of soluble salt may be the reason for increasing salinity in the soil. The PS values range from 4.72 meq/l to 21.47 meq/l. the salinity in the soil is due to chloride content present in the selected sample area. It makes the groundwater closely unsuitable for irrigation purposes.

**4.1.10. Salinity index**

The eligibility of saline content in water used for irrigation purpose are based on a certain condition which includes soil, crop, climate and adopted method for irrigation, etc. [10] the SI is used for knowing the water eligibility for water for irrigation. But, to determine the water salinity levels for which these guidelines are intended, it is helpful to give a classification scheme.

Fig. 10, shows the salinity classification of groundwater from the selected sample area. The majority of the groundwater samples from the selected area are classified as class II (slightly saline) and class III (moderately saline). However, in the PRM and POM seasons, many samples were not suitable for irrigation from the selected sample area.

**4.1.11. Sodidity index**

Sodicity index is a crucial parameter to determine the suitability of irrigation water and it is calculated by using SAR. Water with SAR ranging from 0 to 3 is considered to be good; 3 to 9 causes a problem for irrigation and is considered not the best water for irrigation whereas, SAR that exceeds 9 is considered unsuitable for irrigation purposes as it causes severe problems. From Fig. 11, in PRM, MON, and POM seasons water samples containing SAR of 85%, 80%, and 87.5%, respectively, are safe for irrigational use. But SAR of 15%, 20%, and 12.5% increases the problem for irrigation in PRM, MON, and POM seasons, respectively. However, none of the samples were severely problematic for irrigation in the area under study.

**5. Conclusion**

The results of the hydrochemical analysis showed that most of the groundwater samples in the study area were suitable for irrigational purposes. The plot of  $\text{Cl}^-/\text{HCO}_3^-$  versus  $\text{Cl}^-$  showed that the studied groundwater is affected by salinity. The chloro alkaline

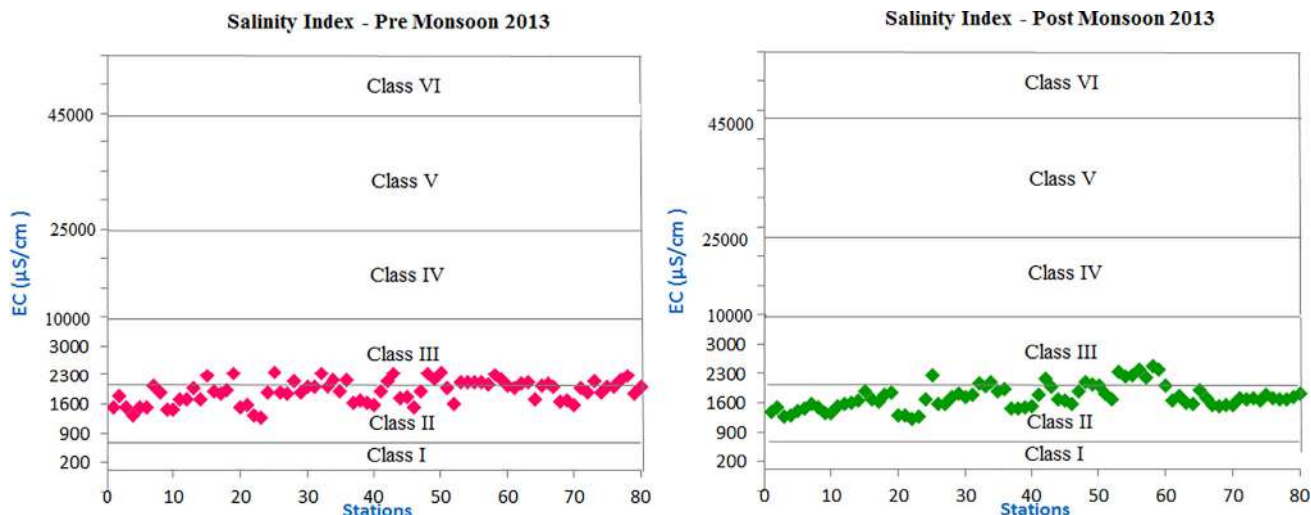


Fig. 10. Salinity Index for the groundwater samples of the study region.

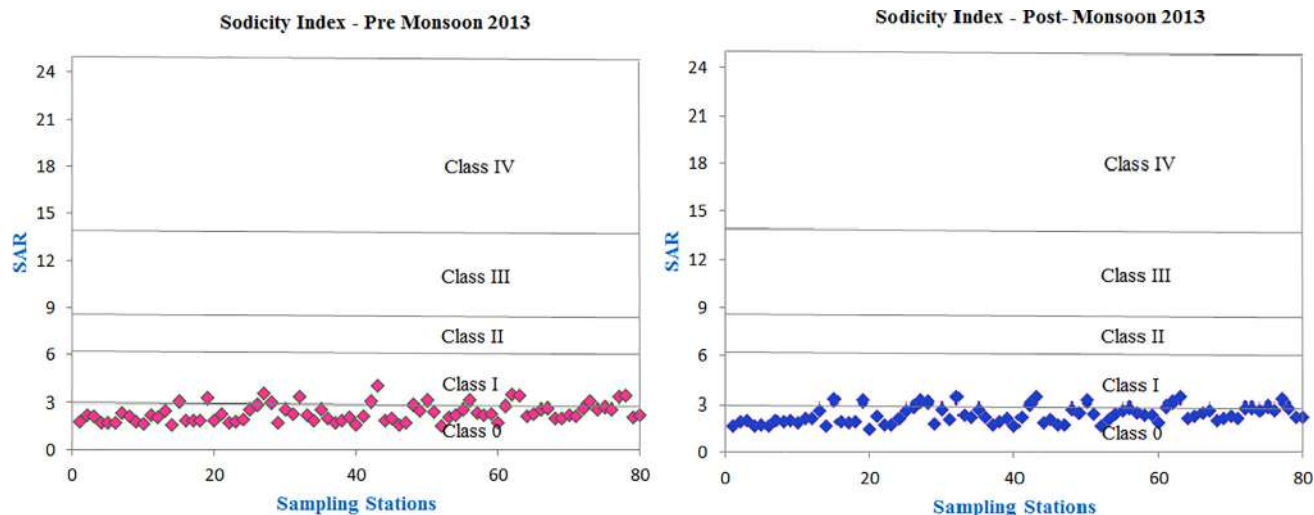


Fig. 11. Sodicity index for the groundwater samples in the study area.

indices results illustrate the exchangeable mechanism that has one of the responses for the chemical composition of groundwater in the studied area. According to the results of %Na, RSC, KR, SAR, PI, MR, Salinity index, and Sodidity index, groundwater of the study area is safe and fit for irrigation. However, the results of PS and Sodidity index indicate that the groundwater was of marginal quality for irrigation purposes. The outcome of this study will be very useful in the sustainable development of groundwater resources and also will help planners and policymakers in developing schemes to solve similar problems elsewhere.

#### CRediT authorship contribution statement

**K. Vijai:** Conceptualization, Methodology, Data curation, Writing - original draft. **S.M. Mazhar Nazeeb Khan:** Supervision.

#### Declaration of Competing Interest

The authors declare that they have no known competing financial interests or personal relationships that could have appeared to influence the work reported in this paper.

#### Acknowledgement

We thankfully acknowledge the principal and the management committee of Jamal Mohamed College, Trichy, Tamilnadu, India for their support amid the research work. We are truly appreciated to principal and the management committee of Don Bosco College, Dharmapuri for his help during research work.

#### References

- [1] A.M. Eassa, A.A. Mahmood, An assessment of the treated water quality for some drinking water supplies at Basrah, *J. Basrah Res. (Sciences)* 38 (3A) (2012) 95–105.
- [2] Federation, Water Environmental, and American Public Health Association. "Standard methods for the examination of water and wastewater." American Public Health Association (APHA): Washington, DC, USA (2005).
- [3] F. Raihan, J. B. Alam. "Assessment of groundwater quality in Sunamganj of Bangladesh." (2008): 155-166.
- [4] Robert S. Ayers, Kenneth K. Tanji. "Agronomic aspects of crop irrigation with wastewater." (1981).
- [5] D.C. Kantharaja, T.K. Lakkundi, M. Basavanna, S. Manjappa, Spatial analysis of fluoride concentration in groundwaters of Shivani watershed area, Karnataka

state, South India, through geospatial information system, *Environ. Earth Sci.* 65 (1) (2012) 67–76.

- [6] Kelley, Walter Pearson. Alkali soils; their formation, properties, and reclamation. No. 04; RMD, S595 K4.. 1951.
- [7] S.J. Phansalkar, V. Kher, P. Deshpande, Expanding rings of dryness: water imports from hinterlands to cities and the rising demands of mega-cities, *IWMI-Tata annual partner's meet*, Anand, 2005.
- [8] M. Ramachandran, C. Sabarathinam, K. Ulaganthan, A. Paluchamy, M. Sivaji, S. Hameed, Mapping of fluoride ions in groundwater of Dindigul district, Tamilnadu, India—using GIS technique, *Arabian J. Geosci.* 5 (3) (2012) 433–439.
- [9] R. Revelle, Criteria for recognition of the sea water in ground-waters, *Eos, Trans. American Geophys. Union* 22 (3) (1941) 593–597.
- [10] J.D. Rhoades, A. Kandiah, and A. M. Mashali. "The use of saline waters for crop production-FAO irrigation and drainage paper 48." FAO, Rome 133 (1992).
- [11] H. Schoeller, "Geochemistry of groundwater." *Groundwater studies—an international guide for research and practice* 15 (1977): 1–18.
- [12] I. Szabolcs, The influence of irrigation water of high sodium carbonate content on soils, *Agrokémia és talajtan* (13.sup) (1964) 237–246.
- [13] Staff, US Salinity Laboratory. "Diagnosis and improvement of saline and alkali soils." *Agriculture Handbook* 60 (1954): 83–100.

#### Further Reading

- [1] A. Balachandran, District groundwater brochure Thoothukudi District. Tamil Nadu, Technical Report Series, Central Ground water board, South Eastern Coastal Region, Chennai, 1-19, 2009.
- [2] S.K. Sundarar, B.B. Nayak, D. Bhatta, Environmental studies on river water quality with reference to suitability for agricultural purposes: Mahanadi river estuarine system, India—a case study, *Environ. Monit. Assess.* 155 (1-4) (2009) 227–243.
- [3] K.P. Cantor, Drinking water and cancer, *Cancer Causes Control* 8 (3) (1997) 292–308.
- [4] A. Farooqi, H. Masuda, N. Firdous, Toxic fluoride and arsenic contaminated groundwater in the Lahore and Kasur districts, Punjab, Pakistan and possible contaminant sources, *Environ. Pollut.* 145 (3) (2007) 839–849.
- [5] J. Hussain, I. Hussain, K.C. Sharma, Fluoride and health hazards: community perception in a fluorotic area of central Rajasthan (India): an arid environment, *Environ. Monit. Assess.* 162 (1-4) (2010) 1–14.
- [6] T. Subramani, L. Elango, S.R. Damodarasamy, Groundwater quality and its suitability for drinking and agricultural use in Chithar River Basin, Tamil Nadu, India, *Environ. Geol.* 47 (8) (2005) 1099–1110.
- [7] C. Thivya, S. Chidambaram, C. Singaraja, R. Thilagavathi, M.V. Prasanna, P. Anandhan, I. Jainab, A study on the significance of lithology in groundwater quality of Madurai district, Tamil Nadu (India), *Environ. Dev. Sustain.* 15 (5) (2013) 1365–1387.
- [8] United Nations. Economic Commission for Asia, and the Far East. Division of Water Resources Development. Methods and Techniques of Ground-water Investigation and Development. No. 33. New York: United Nations, 1967.
- [9] World Health Organization. Guidelines for drinking-water quality. World Health Organization, 1993.



## Groundwater quality for drinking purpose in Pennagaram block, Dharmapuri district, Tamilnadu, India

K. Vijai\*, S.M. Mazhar Nazeeb Khan

Department of Chemistry, Jamal Mohamed College (Autonomous), (Affiliated to Bharathidasan University – Tiruchirappalli), Tiruchirappalli 620020, Tamil Nadu, India

### ARTICLE INFO

#### Article history:

Received 14 March 2021

Received in revised form 25 July 2021

Accepted 29 July 2021

Available online 16 August 2021

#### Keywords:

Physico-chemical parameters

Salinity

Fluoride

Groundwater

Pennagaram

### ABSTRACT

Groundwater is an essential source of water due to its substantial use of domestic, irrigation and industrial purpose. The present study was pointed to examine the groundwater quality of groundwater in pre-monsoon and post-monsoon seasons on the year of 2013 at Pennagaram block of Dharmapuri district, Tamilnadu. A few groundwater samples of the study area were analyzed for their physico-chemical parameters (APHA, 1998). The spatial distribution map provides a clear explanation for hydrochemical characteristics of groundwater quality for domestic and irrigational purpose in both the seasons. The results of showed the most of the groundwater samples in the study area showed that the pH is slightly acidic to alkaline in nature. The TDS and EC content of the samples in PRM and POM were measured and found 80% of the samples within the WHO limit (1500 mg/L). The water constituents are highly adjustable with respect to cationic and anionic constituents. However, to summarize the average of cations is  $Ca^{2+} > Na^{+} > Mg^{2+} > K^{+}$  and anions are  $Cl^{-} > HCO_3^{-} > SO_4^{-} > NO_3^{-} > F^{-}$ . The spatial analysis output indicates that in some stations there is need for some degree of treatment for groundwater in the study area before consumption.

© 2019 Elsevier Ltd. All rights reserved.

Selection and peer-review under responsibility of the scientific committee of the International Conference On Impact Of Innovations In Science And Technology For Societal Development: Materials Science.

### 1. Introduction

[11] Water is the main constituent of Earth's hydrosphere and a transparent and tasteless fluid which is considered the most important one for living organisms. It plays a vital role for all organisms in their day-to-day life. Groundwater is the water that is resented under the earth's surface where it occupies all or a small part of void spaces in between soils. In the case of the environment, groundwater plays a significant role by keeping the water level and also responsible for the flow of rivers, wetlands, and lakes.

Water for drinking is the basic need for an organism living on the Earth. In recent times due to pollution in water and over-extraction of water, it has become an unavailable one for mankind. Groundwater is an important natural resource for mankind and it also plays a significant role in the economy of many nations. Water is the basic need for irrigation and the food industry. From a study, it was found that nearly 320 Billion Gallon was consumed by mankind on a daily basis from which almost 77 billion gallons of water

are consumed from Groundwater by mankind for a day. So the extraction of groundwater is the mandatory one for mankind.

[25] in India, around 90 percent of water is extracted from the ground and used for irrigation. Around 60 percent of irrigation is supported by groundwater supply and almost 90 M rural households directly or indirectly dependent on groundwater for irrigation. The water quality can be identified by its chemical, physical, and biological parameters. In a study, it was found that nearly 80 percent of disease worldwide is caused because of poor drinking water.

Federation, Water Environmental, and American Public Health Association. "Standard methods for the examination of water and wastewater." American Public Health Association [7], Contamination of Fluoride in Groundwater is considered a serious issue in many parts of the world. The reason for fluoride contamination in groundwater is due to dissolving materials containing fluoride such as cryolite, hydroxyapatite, fluorspar, etc.

[9] Some others reason for fluoride contamination in groundwater was found to be due to fertilizers used for agricultural purpose, pesticide, and sewage discharge also considered as the reason for increased fluoride substance in groundwater.

\* Corresponding author.

E-mail address: [kvijjay21@gmail.com](mailto:kvijjay21@gmail.com) (K. Vijai).

[8] Fluoride is found in all regions of the earth's surface, due to its occurrence as compounds and complexes. Fluoride enters groundwater due to weathering of minerals which contains fluoride substance and by which it enters into the surface of the water and sometimes through direct contact.

Contamination of fluoride in groundwater can be identified by a human being when they under certain symptom for fluorosis and it is one of the endemic diseases which may occur due to high intake of fluoride by water, and by food with a level of 1.5 mg per liter or above.

Fluorosis in teeth may affect the enamel and fluoride substances above 10 mg per liter may cause a pathological change in the bones of human beings which leads to skeletal fluorosis.

In India almost 61.5 M people at high risk of fluorosis. 17 states across India was listed as states with endemic for Fluorosis. Even states in the southern part of India Tamil Nadu was also one among the state on the list. In Tamil Nadu, High Fluoride Contamination in Groundwater was found in the districts of Salem and Dharmapuri. Pennagaram block of Dharmapuri district was taken for our study.

## 2. Study area

### 2.1. Profile of the study area

The area of study for this proposed research lies between the longitude of 77°46' to 78°4' and the Northern latitude of 11°53' to 12°19'. Fig. 1 represents the plain area covering about 604.48 km square. The specific area selected for this study includes the Pennagaram Block that belongs to the District of Tamil Nadu named 'Dharmapuri'. The main source of water in this area is the seasonal rainfall in the monsoons. The average yearly rainfall for this area is about 902 mm. But during the period of 2013 to 2014, the rainfall in this region was recorded for 757 mm only. This area of study lies within the region of Archean Crystalline Rock and

the groundwater in this region is affected due to fractured rocks. The temperature in this area is up to 36 °C and during the winter season, the temperature is found to be between 12 and 16 °C.

### 2.2. Geomorphology

Dharmapuri district lies 455 m above sea level and the climate in this region is termed as Tropical climate. The western part of Dharmapuri district which connects to Pennagaram, has a hill range of Mysore plateau. The southern region of the district is bordered by Shervaroy Hill.

### 2.3. Hydrogeology

The Dharmapuri District is beneath Archean Crystalline metamorphic rock formed with alluvial deposits of limited vertical and areal extents alongside to main rivers. The major Aquifer setup in the Dharmapuri District is comprised of;

- Semi and un- consolidated formation of sediments
- Broken and weather rocks of crystalline

The areas beneath crystalline rock would have a limited source for underground water due to fracturing and weathering of rocks which occur in the zone. The Hard Rock Aquifers are heterogeneous in nature, which can be identified by their composition, texture and lithology. The presence of groundwater beneath the phreatic surrounding in weathered and through semi to confined state and by fissured and fractured regions of the rocks. The Weathered material thickness will either be lesser to 1 m below ground level (bgl) or more than 20 m below ground level.

The locations for the study were selected randomly, so that the sample locations are spread all over the Pennagaram block. Groundwater samples were collected, and their respective latitude

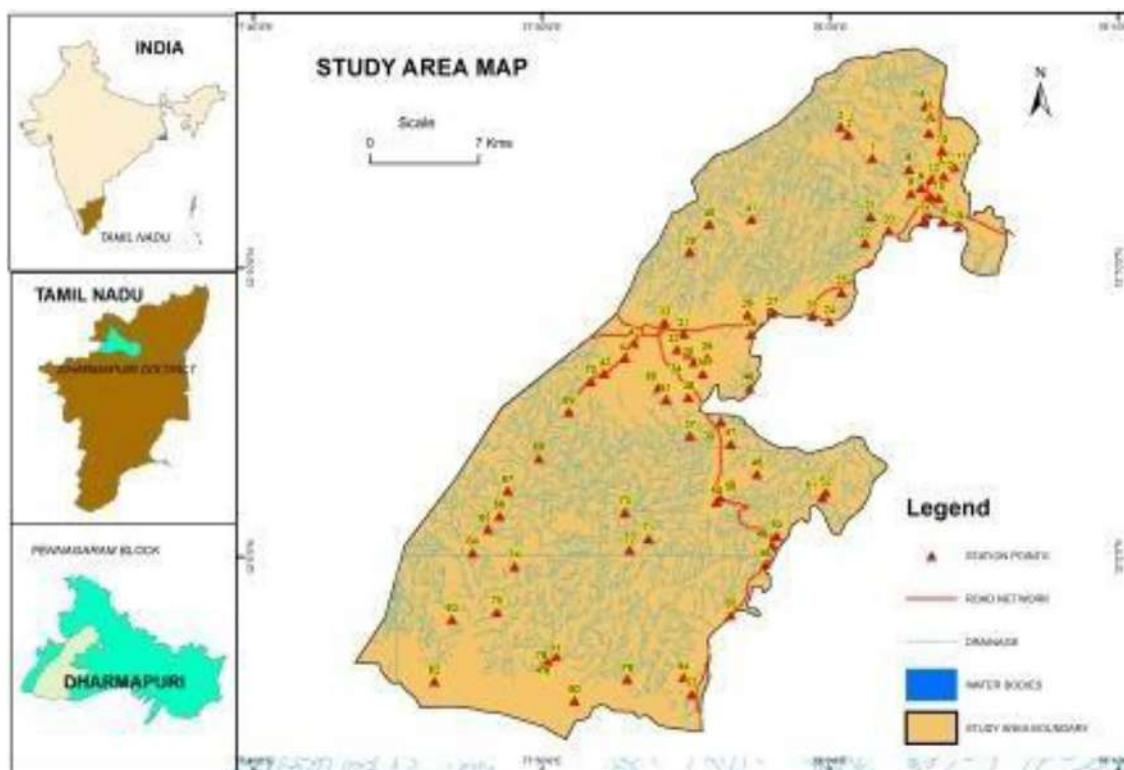


Fig. 1. Study area Location map.



and longitude were noted using GPS Essentials App in android Smartphone Redmi 2. Then, each sample location was marked out on the digitized base map using the software ArcGIS 9.3.

### 3. Materials and Methods

For this research, a total of 80 underground water samples were collected from bore wells and hand pumps across several locations of Pennagaram block, during the pre-monsoon season in May 2013 and the post-monsoon season in May month of 2013. The collected samples of water were taken in sterilized bottles having the capacity of containing 2 Liters, without any air bubbles. The collected samples were first examined in order to assess it for the physico-chemical process as per the standard procedure recommended by the APHA method. The spatial distribution map was drawn using GIS (ArcGIS 9.3) software. See (Table 1).

### 4. Results and discussion

#### 4.1. pH

pH shows the negative logarithm of hydrogen ion concentration in water and it is considered as the degree for hydrogen ion concentration. The pH of an aqueous solution with a value below 7 is termed as acidic and the pH value above 7 is termed as alkaline or a basic solution. The one with an exact pH value of 7 is termed as a neutral solution. The pH value of the selected sample of groundwater contains the value ranging between 6.95–8.14 & 6.92–8.21 during both pre and post-monsoon seasons, respectively. The pH value of groundwater of the selected sample is within permitted range of 6.4–8.4. The pH values of selected groundwater samples are illustrated in Fig. 2 and in Table 2, for all seasons.

#### 4.2. Electrical conductivity (EC)

The conductivity of water refers to the ability of water to conduct electric current. Pure water is not considered a good conductor of electricity. Electric current is transported to water by ions present in the solution.

[6] The Electrical Conductivity and Total Dissolved Solid (TDS) values are contributed for geochemical activity which includes the exchange of ions, weathering of silicate rocks, interaction with water, and also for anthropogenic activity.

The Electrical Conductivity value ranges between 1264 and 2381 micro siemens per centimeter ( $\mu\text{S}/\text{cm}$ ) and 1222–2490  $\mu\text{S}/\text{cm}$ , during both pre and post monsoon seasons. The results are given in Table 2 and the graphical representation is given in Fig. 3. According to the World Health Organization (WHO report) the Mean value in the selected area was above the permitted value. The value during the post-monsoon season was found to be 18.75% and during pre-monsoon, it was 6.25%. The Electrical Conductivity in the selected study area of this research was above the permitted limit.

#### 4.3. Total dissolved solids (TDS)

TDS is measured as volume of water with the unit milligram per liter. This may also be the reason for reducing the taste of water. The presence of TDS is due to sewage, agricultural run-off and wastewater from industries. The presence of Total Dissolved Solids in water may not affect a healthy human being, but a higher concentration of TDS will affect people those who are suffering from heart disease and kidney disorders. The Total Dissolved Solids values are shown in Table 2 and the variation of TDS is illustrated in Fig. 4. The Total Dissolved Solids mean value is 1322 mg per liter

during pre-monsoon and during post-monsoon the value raised to 1204 mg per liter. The TDS content of 80.25% of the samples in PRM and 88.75% of the samples in POM, were found to be within the WHO limit of 1500 mg/L.

#### 4.4. Total alkalinity

Alkalinity is an extent of neutralizing the acidic capacity of water. The Compounds of Alkaline in water include carbonates, bicarbonates and hydroxide without  $\text{H}^+$  ions which reduces the acidity level in the water.

[3] Measuring the Alkalinity level in water is very important. The polyatomic anion ( $\text{HCO}_3^-$ ) will not cause any ill effect yet the level in water should not rise above 300 mg per liter. The seasonal variation of Total Alkalinity has shown in Table 2 and is also illustrated in Fig. 5.

#### 4.5. Total hardness

Calcium and Magnesium origins are the major reasons for the hardness of the water. The total hardness of water consists of carbonate hardness and non-carbonate hardness. Carbonate hardness contains the portion of the calcium and magnesium ions that would combine with bicarbonate and carbonate ions present. This is known as temporary hardness and this could be removed by boiling the water. The non-carbonate hardness, which is also known as permanent hardness, is the difference between the total hardness and the carbonate hardness. This is caused by the amount of calcium and magnesium ions that would normally combine with the sulfate, chloride, and nitrate ions, and the slight hardness effect of other minor constituents. This type of hardness cannot be removed by boiling of the water [5]. The seasonal variation of total hardness is shown in Table 2. The total hardness (TH) values of 7.5% of the samples (560 to 1022 mg/L) in pre-monsoon season and 12.5% of the samples (510 to 1022 mg/L) in post-monsoon season were within the allowable limit of 300 to 600 mg/L. This is due to the presence of alkaline earth metals such as calcium and magnesium.

#### 4.6. Calcium

In hydrochemistry, increased  $\text{Ca}^{2+}$  ion concentration with increased total dissolved solids is due to the gradual dissolution of carbonate minerals or  $\text{Ca}^{2+}$  bearing minerals in aquifer (Kim, et al. 2001 and Sujatha, 2003). During post-monsoon season, the  $\text{Ca}^{2+}$  concentration varies from 156 to 333.2 mg/L with the mean of 241.4 mg/L and pre-monsoon  $\text{Ca}^{2+}$  varies from 154 to 353 mg/L and the mean of 254 mg/L (Table 2). The seasonal variation of  $\text{Ca}^{2+}$  ions can be drawn from Fig. 6.

#### 4.7. Magnesium (Mg)

Magnesium (Mg) is calculated from Total hardness and calcium ion concentration. [10] Clay Stone is the reason for the presence of Mg ion in groundwater in the selected area of research. In the selected area, the Mg value in groundwater was ranging from 8.40 mg per liter to 63.85 mg per liter in pre-monsoon and from 5.144 mg per liter to 71.11 mg per liter in the post-monsoon season (Table 2). The variation of Mg ion concentration in the selected samples during the studied seasons can also be illustrated graphically, from Fig. 7. According to the WHO report in this selected area, the Mg value during winter was 6.25% and during the dry season, the Mg value extends the permitted limit up to 50 mg per liter.

**Table 1**  
Details of the sample locations.

Sample no	Station Name	Station ID	Latitude (N)	Longitude (E)
1	Pikkili	Malaiyur	12°13'49.76"N	78° 1'28.22"E
2	Pikkili	Pikkili	12°14'30.15"N	78° 0'37.11"E
3	Pikkili	PEariyur	12°14'55.62"N	78° 0'21.94"E
4	Panaikulam	Nagamarathupallam	12°15'38.50"N	78° 3'19.11"E
5	Panaikulam	Thirumalvadi	12°15'15.13"N	78° 3'29.24"E
6	Panaikulam	Panaikulam	12°13'48.30"	N 78° 3'9.79"E
7	Giddanahalli	Giddanahalli	12°14'41.94"N	78° 3'26.00"E
8	Veppilaihalli	Veppilaihalli	12°13'26.86"N	78° 2'44.40"E
9	Veppilaihalli	Valloor	12°12'36.48"N	78° 2'48.02"E
10	Acharahalli	Thotlampatti	12°14'5.36"N	78° 3'53.58"E
11	Acharahalli	Acharahalli	12°13'30.35"N	78° 4'19.81"E
12	Acharahalli	Ettiyampatti	12°13'12.09"N	78° 3'56.94"E
13	Acharahalli	Palayapauparappatti	12°13'4.84"N	78° 3'30.33"E
14	Madehalli	Matheyhalli	12°12'30.23"	N 78° 3'30.18"E
15	Madehalli	Pilapanaikanahalli	12°12'27.45"N	78° 3'46.61"E
16	Onnappagoundanahalli	Kochahalli	12°11'55.04"N	78° 3'22.76"E
17	Onnappagoundana	Sitlakarpatti	12°11'39.42"N	78° 3'16.13"E
18	Velampatti	Velampatti	12°11'36.29"N	78° 3'53.38"E
19	Pallipatti	Pallipatti	12°11'25.50"N	78° 4'26.28"E
20	Thithyoppanahalli	Manneri	12°11'19.19"N	78° 2'1.83"E
21	Thithyoppanahalli	Sanjeevapuram	12°11'48.12"N	78° 1'23.97"E
22	Thithyoppanahalli	Gandhipuram	12°10'52.52"N	78° 1'13.01"E
23	Billiyanoor	Pikkampatti	12° 9'10.22"N	78° 0'23.72"E
24	Billiyanoor	Thalappallam	12° 8'9.96"N	77°59'58.61"E
25	Billiyanoor	Nagathasampatti	12° 8'20.76"N	77°59'23.08"E
26	Anjehalli	Palinjacharahalli	12° 8'24.34"N	77°57'7.91"E
27	Anjehalli	Sinnaperamanur	12° 8'27.52"N	77°58'0.48"E
28	Mangarai	Nallampatti	12° 7'43.46"N	77°57'15.17"E
29	Mangarai	Mangarai	12° 6'54.48"N	77°55'43.85"E
30	Mangarai	Vannathippatti	12° 7'41.20"N	77°56'13.33"E
31	Paruvathanahalli	Paruvathanahalli	12° 7'44.06"N	77°54'55.08"E
32	Paruvathanahalli	Kodiyur	12° 7'12.15"N	77°54'41.61"E
33	Paruvathanahalli	Erankadu	12° 8'8.43"N	77°54'15.72"E
34	Sathiyathanapuram	Aanaikkallanoor	12° 7'2.44"N	77°55'4.28"E
35	Sathiyathanapuram	Mottuppatti	12° 6'45.54"N	77°55'16.94"E
36	Sathiyathanapuram	Kottavoor	12° 6'21.36"N	77°55'35.00"E
37	Kukuttamaruthahalli	Valakkamparai	12° 4'12.07"N	77°55'8.57"E
38	Kukuttamaruthahalli	Naikanoor	12° 5'32.96"N	77°55'4.89"E
39	Vattuvanahalli	Kadaikkarisikottai	12°10'34.72"N	77°55'8.53"E
40	Vattuvanahalli	Kottuppatti	12°11'32.57"N	77°55'48.89"E
41	Vattuvanahalli	Marukkampatti	12°11'43.10"N	77°57'16.21"E
42	Koothappadi	Madam	12° 7'25.11"N	77°53'11.80"E
43	Koothappadi	Puthur	12° 6'21.77"N	77°52'9.43"E
44	Koothappadi	Agraharam	12° 6'54.22"N	77°52'52.99"E
45	Koothappadi	Ootamalai	12° 7'40.78"N	77°46'12.17"E
46	Manjanaickanahalli	Manjanaickanahalli	12° 5'51.43"N	77°57'12.66"E
47	Manjanaickanahalli	Chinnakadamadai	12° 3'55.57"N	77°56'33.00"E
48	Manjanaickanahalli	Pudhuppatti	12° 2'52.86"N	77°57'27.38"E
49	Chinnapatti	Chinnamballi	12° 0'24.50"N	77°57'59.25"E
50	Chinnapatti	Tholur	12° 0'43.80"N	77°58'8.45"E
51	Arakasanahalli	Kannampalli	12° 2'4.37"N	77°59'43.85"E
52	Arakasanahalli	Arakasanahalli	12° 2'14.50"N	77°59'51.06"E
54	Gendenahalli	Kavakarankottai	11°55'49.57"N	77°54'54.96"E
55	Perumbalai	Perumbalai	11°57'58.83"N	77°56'32.97"E
56	Perumbalai	Boothanaickanahalli	11°59'45.11"N	77°57'45.51"E
57	Kalappambadi	Thalihalli	12° 2'32.39"N	77°56'35.73"E
58	Kalappambadi	Kalappambadi	12° 2'3.29"N	77°56'12.63"E
59	Kalappambadi	Koppalur	12° 1'54.37"N	77°56'3.14"E
60	Senganur	Senganur	12° 5'52.21"N	77°54'2.36"E
61	Senganur	Rajavur	12° 5'27.98"N	77°54'18.62"E
62	Nagamarai	Nagamarai	11°55'42.02"N	77°46'15.98"E
63	Nagamarai	Neruppur	11°57'50.89"N	77°46'52.84"E
64	Sunchalnatham	Dhinnaipellur	12° 0'10.00"N	77°47'35.62"E
65	Sunchalnatham	Eariyur	12° 0'57.95"N	77°48'8.30"E
66	Sunchalnatham	Pattukkaranakottai	12° 1'25.43"N	77°48'31.45"E
67	Ajjanahalli	Ajjanahalli	12° 2'18.16"N	77°48'48.73"E
68	Ajjanahalli	Vathalapuram	12° 3'25.83"N	77°49'53.78"E
69	Kodihalli	Manthamedu	12° 5'2.68"N	77°50'55.98"E
70	Kodihalli	Jakkampatti	12° 6'5.58"N	77°51'41.83"E
71	Donnakuttanahalli	Donnakuttanahalli	12° 0'38.03"N	77°53'41.98"E
72	Donnakuttanahalli	Aththimarathur	12° 0'14.75"N	77°53'2.75"E
73	Donnakuttanahalli	Begiumputhukadu	12° 1'32.62"N	77°52'52.99"E
74	Ramakondanahalli	Malaiyanoor	11°59'40.81"N	77°49'2.99"E
75	Ramakondanahalli	Ramakondanahalli	11°58'5.42"N	77°48'26.40"E

Table 1 (continued)

Sample no	Station Name	Station ID	Latitude (N)	Longitude (E)
76	Manjarahalli	Sithirappatti	11°56'34.59"N	77°50'29.80"E
77	Manjarahalli	Sellamudi	11°56'24.66"N	77°50'12.07"E
78	Manjarahalli	Narasimedu	11°56'12.12"N	77°49'58.60"E
79	Badrahalli	Oothupallathur	11°55'46.24"N	77°52'57.90"E
80	Badrahalli	Poochoor	11°56'2.07"N	77°51'7.68"E

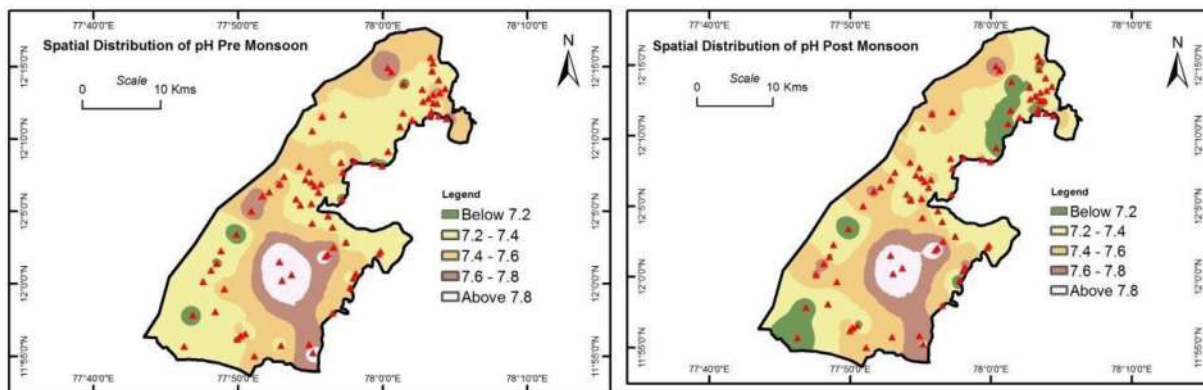


Fig. 2. Spatial distribution of pH values for the selected groundwater samples.

Table 2

Description of the analyzed chemical components from 80 sampling stations.

S.No	Parameters	Unit	Pre-Monsoon (PRM)				Post-Monsoon (POM)			
			Min	Max	Mean	Std	Min	Max	Mean	Std
1	Ph	-	6.95	8.14	7.43	0.27	6.92	8.21	7.386	0.288
2	EC	µs/cm	1264	2381	1905	277	1222	2490	1735	286.4
3	TDS	mg/L	877	1652	1322	192	847.8	1728	1204	198.7
4	TH	mg/L	560	1022	768	108	510	1022	696.9	111.6
5	TA	mg/L	125	319	191	35.8	120	296	179.2	36.44
6	Cl <sup>-</sup>	mg/L	318	686	526	100	276	659	466.2	97.25
7	so 2-4	mg/L	33	109	70.1	16.7	30	110	68.44	18.35
8	ca <sup>2+</sup>	mg/L	154	353	257	41.5	156	333.2	241.4	39.19
9	Mg <sup>2+</sup>	mg/L	8.403	63.85	31.28	12.52	5.144	71.11	22.96	10.98
10	NO <sup>-3</sup>	mg/L	14.2	49.3	33.4	6.98	13.4	45	29.95	6.559
11	po 3-4	mg/L	0.79	3.1	1.21	0.39	0.24	2.45	1.024	0.439
12	F <sup>-</sup>	mg/L	0.24	3.33	1.44	0.78	0.32	2.98	1.347	0.682
13	K <sup>+</sup>	mg/L	3	35	8.41	5.65	3	40	8.1	5.444
14	Na <sup>+</sup>	mg/L	91	271	150	39.9	80	222	142.2	35.85

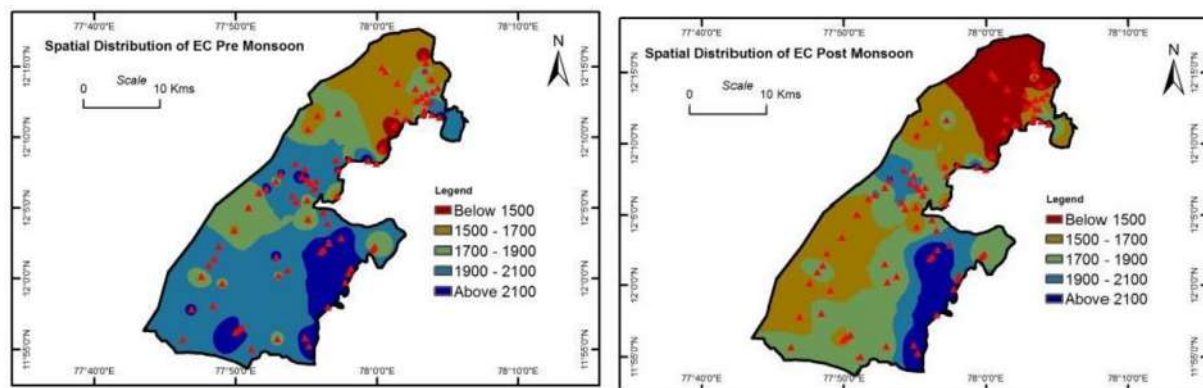


Fig. 3. Spatial distribution of EC values for pre and post-monsoon seasons.

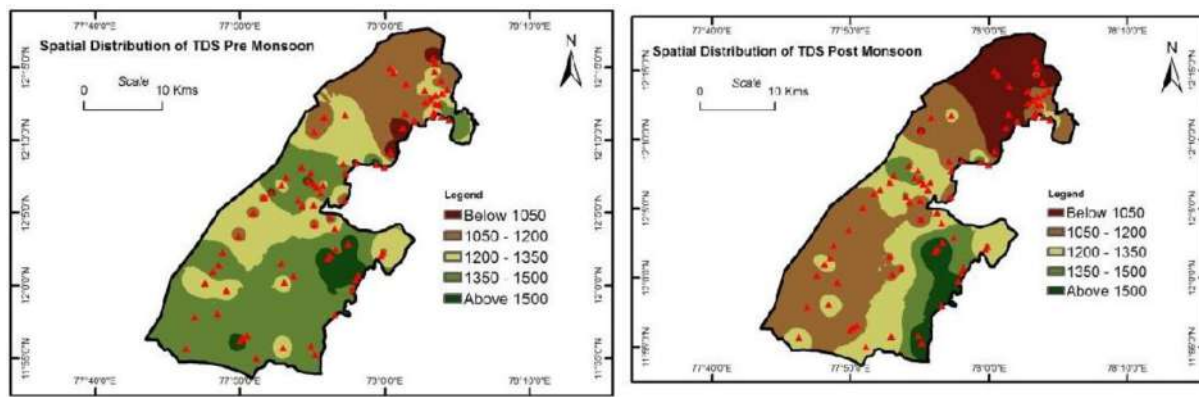


Fig. 4. Spatial distribution of TDS for pre and post-monsoon seasons.

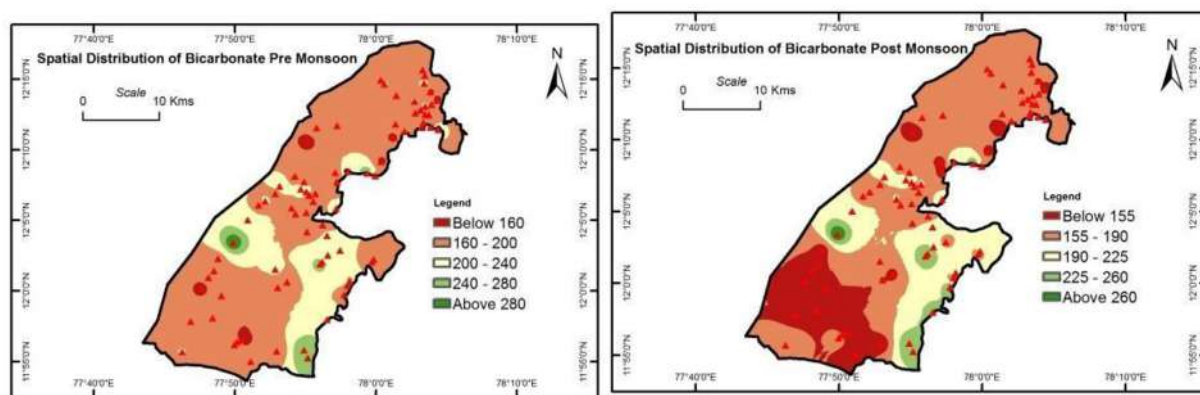


Fig. 5. Spatial distribution of Bicarbonate ions for pre and post-monsoon seasons.

#### 4.8. Sodium

Among the alkalis, Sodium is a predominant chemical constituent of natural water. The Sodium level in the earth's crust is 2.27% making it the 7th most abundant element on Earth. Sodium is one of the necessary elements for animals as well as plants. Generally, sodium is an important constituent in drinking water. The sodium ion concentration ranges from 73 to 283 mg/L in summer, from 80 to 222 mg/L in the rainy season, and from 91 to 271 mg/L in winter season (Table 2). The seasonal variation of sodium ion concentration can also be illustrated graphically, from Fig. 8. According to the World Health Organization report, the maximum

level of Sodium must be 200 mg per liter, but in the selected area during the summer season the sodium level raised more than the permitted level up to 16.25%, 10% during rainy season, and 8.75% during winter season. (Thiyya et al., 2013) Excess amount of sodium, potassium, and magnesium constituents shows evidence of granite-water interaction of them, i.e. the ions exchanging from granite to water.

#### 4.9. Potassium

About 2.4 % of the mass of earth's crust is filled with potassium and it is considered equal to sodium in earth's crust. When com-

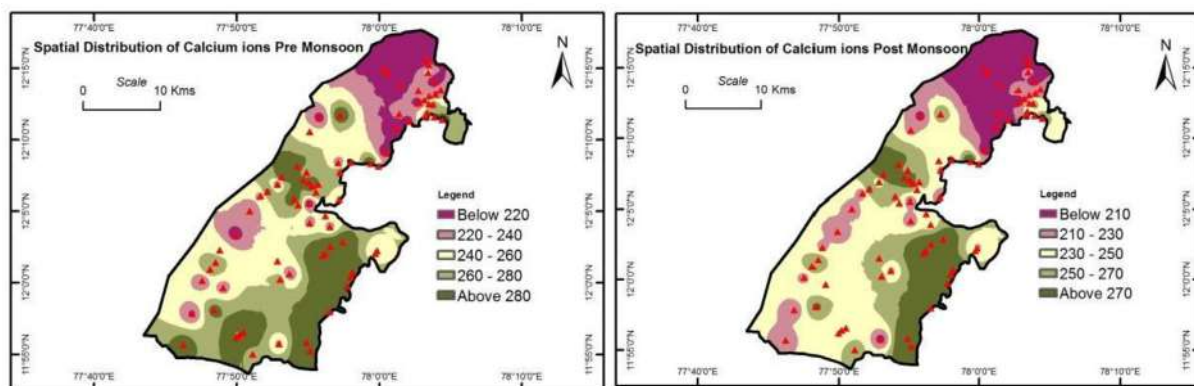


Fig. 6. Spatial distribution of Calcium ions for pre and post-monsoon seasons.

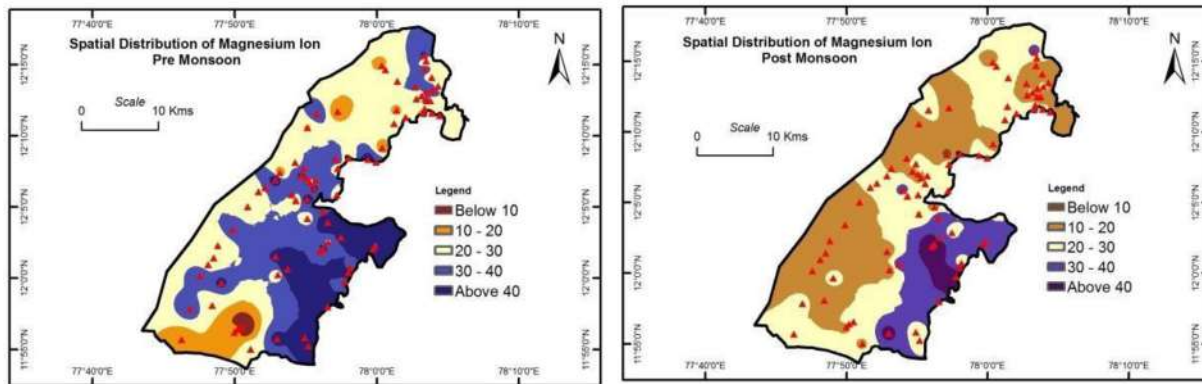


Fig. 7. Spatial distribution of Magnesium ions for pre and post-monsoon seasons.

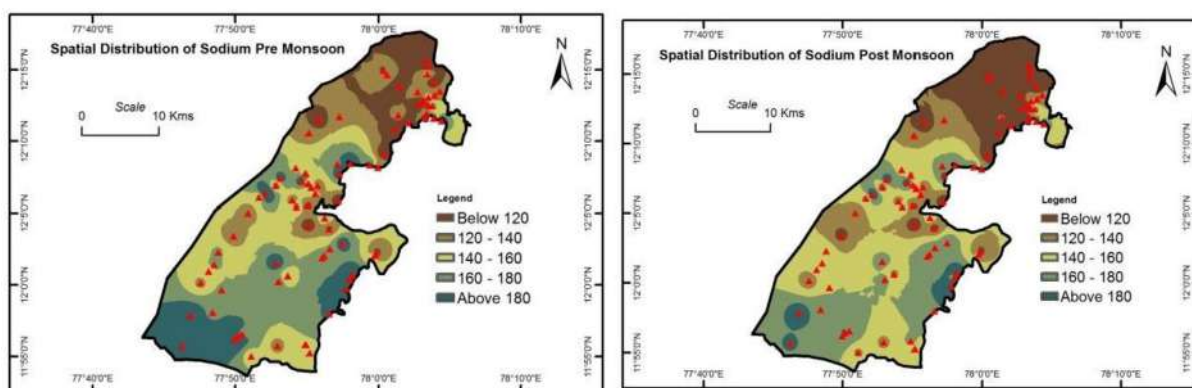


Fig. 8. Spatial distribution of Sodium ions for pre and post-monsoon seasons.

paring potassium with sodium, potassium is present in lesser concentrations in water and it is also a necessary element for animals and plants. The variation of potassium concentration during seasons is shown in Table 2 and shown graphically in Fig. 9. The value of potassium in the selected area ranges from 3 to 35 mg per liter and from 3 to 40 mg per liter in pre and post-monsoon seasons, respectively. According to the World Health Organization report, the permitted level of potassium in groundwater has to be 12 mg per liter, but in the selected sample it was found elevated up to 17.5% and 16.25% during pre and post-monsoon seasons, respectively. (WHO permit level given in mg/L but comparison of results done in %)

#### 4.10. Chloride

Chloride is a major anion in the study area. Most of the chlorides are salts that are either formed directly by the union of chlorine with a metal or formed by the reaction of hydrochloric acid with metals. Chloride salts include Sodium Chloride, calcium chloride, potassium and ammonium chloride. In the selected sample, sodium chloride is highly found. The chloride in groundwater is due to the deposit of halite. The taste of water becomes salty when the chloride level exceeds 100 parts per liter (ppm). [3] plants can grow with less amount of chloride element in it. Animals may consume water that has a chlorine level of 4000 parts per liter.

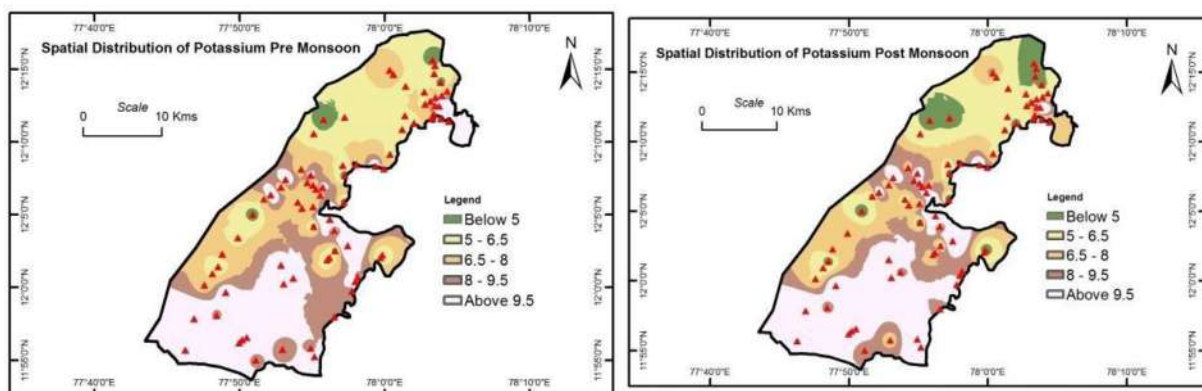


Fig. 9. Spatial distribution of Potassium ions for pre and post-monsoon seasons.

In the selected study area the chloride level present during monsoon, pre and post-monsoon seasons is illustrated in Table 2. According to World Health Organization Report, the Chloride value during pre and post-monsoon must be within the limit of 200–1000 mg per liter and in the study during monsoon, it was found to be 7.25% which is below the permitted level. The total hardness (TH) values of 7.5% of the samples (560 to 1022 mg/L) and 12.5% of the samples (510 to 1022 mg/L) in pre and post-monsoon seasons respectively, were within the allowable limit of 300 to 600 mg/L (Table 2). Fig. 10 shows the graphical representation of the variation of chloride ion concentration among samples during the studied seasons. This is due to the existence of alkaline metals like Magnesium and Calcium. (WHO permit level given in mg/L but comparison of results done in %).

4.11. Sulfate

The source of Sulfate is from Sulphide ores, anhydrite and gypsum. The higher presence of Sulfate through Na and Mg ions is the reason for the bitterness of water.

[11] found the presence of sulfate which was due to usage of agricultural fertilizers and due to the replacement of sulfate to Sulphur that takes place in groundwater. Sulphate is capable of reducing bacteria which further gives hydrogen sulphate that creates an unpleasant odor in the water while drinking and it also increases the corrosiveness of pipes and metals. The variation of sulphate during all the seasons in the study area has been shown in Table 2 and is graphically represented in Fig. 11. The sulphate ions range from 33 to 109 mg/L in summer (pre-monsoon) and 30 to 110 mg/L in the winter (post-monsoon) seasons. All the samples were analyzed for the presence of free sulphate ions and were found to be within the permitted limit suggested by the World health organization (WHO) and Bureau of Indian Standards (BIS).

4.12. Nitrate

(Kantharaja et al., 2012) Nitrogen is one of the most abundant elements in our earth’s crust, and it is crucial to life. Nitrogen can be found in soil, in plants, in the water we drink and also in the air we breathe. Excess nitrogen in drinking water may lead to several diseases like blue baby syndrome among children and gastric ailments. An excessive concentration of nitrate affects the health of both mankind and animals. Nitrate content varies from 14.2 to 49.3 mg/L and 13.4 to 45 mg/L in pre and post-monsoon seasons, respectively (Table 2). Fig. 12 shows a graphical illustration of the varied concentrations of nitrate ions in samples during the seasons of pre and post-monsoon. During the pre-monsoon season, only 5% of the samples and in the post- monsoon season

1.25% of the samples, had nitrate content above the maximum allowable limit of 45 mg/L as prescribed by WHO and BIS.

[4] The anthropogenic impact was found in the selected study area due to the presence of high contamination of nitrate in groundwater.

4.13. Phosphate

The dissolved forms of phosphate and phosphorus found in natural water and from wastewater is a significant parameter for analysis of water quality. The ground and surface water get contaminated by anthropogenic and natural means of phosphates. The natural form of phosphorus in groundwater helps in the natural decomposition of minerals and rocks. But, when there is exceeded amount of phosphate in water, it may cause eutrophication of rivers and lakes.

[1] Bacteria are the reason for the scarcity of dissolved oxygen in water bodies. All the phosphate values of groundwater samples in the study area are within the permissible limit (5 mg/L). Table 2 illustrates the seasonal variations of phosphate.

4.14. Fluoride

The Fluoride concentration in the selected area was not uniformly present in groundwater. The source of fluoride in the selected sample is the presence of fluoride containing rocks and minerals which include apatite, topaz, fluorite, tourmaline, etc.

[2] Due to chemical weathering, the above minerals serve as good sinks for fluoride ions in ground water.

Fluoride concentration ranges from 0.24 – 3.33 mg per litre and 0.32–2.98 mg/L in pre and post- monsoon seasons, respectively (Table 2). Besides, a graphical illustration of the concentration variation of fluoride ions can be drawn from Fig. 13. During pre-monsoon season 49.75% of the samples and in post- monsoon season 47.5% of the samples were above the maximum allowable limit of 1.5 mg/L. On the other hand, 7.5% of the samples in the pre-monsoon season and 10% of the samples in the post-monsoon season were below the required limit of 0.5 mg/L. Fluoride for both lower and higher concentrations in drinking water causes health impacts (dental and skeletal fluorosis). The study indicates that most villages of the study region need the awareness of fluorosis.

5. Conclusion

The foremost data for groundwater EC, TDS, pH, and cations and anions were given in Table 2. Groundwater pH is slightly acidic to alkaline in nature. It varies between 6.95 and 8.14 with a mean of 7.43 in PRM and 6.92 to 8.21 with a mean of 7.38 in POM seasons.

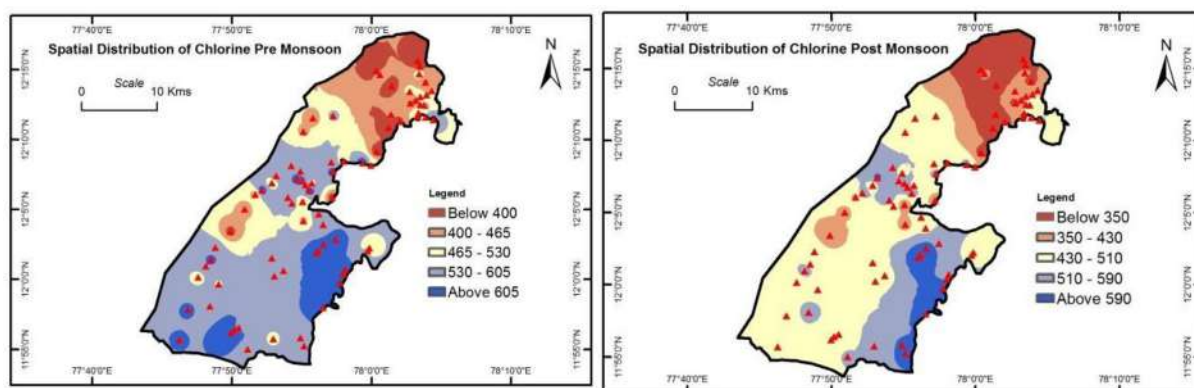


Fig. 10. Spatial distribution of Chloride ions for pre and post-monsoon seasons.

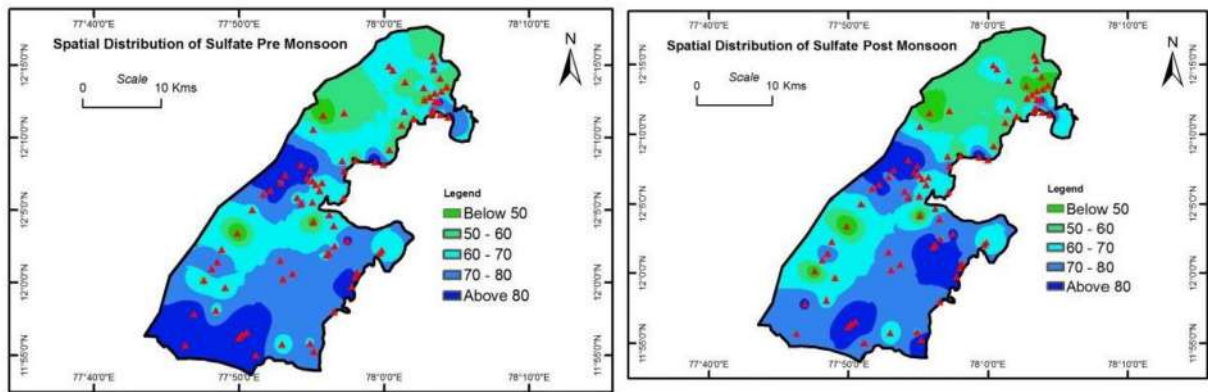


Fig. 11. Spatial distribution of sulfate ions for pre and post-monsoon seasons.

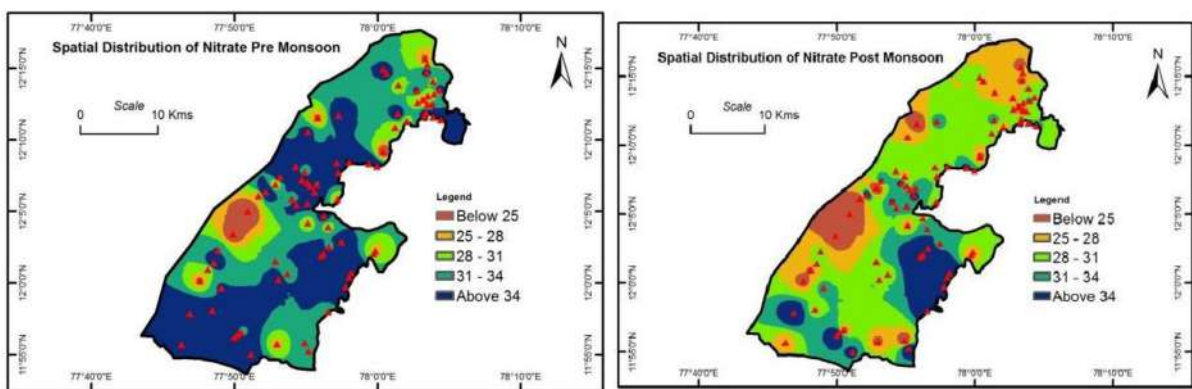


Fig. 12. Spatial distribution of Nitrate ions for pre and post-monsoon seasons.

The TDS average concentration of 1322 mg/L in pre-monsoon and 1204 mg/L in the post-monsoon season. The TDS content of 80.25% samples in PRM and 88.75% samples in POM were measured and found to be within the WHO limit (1500 mg/L). Water constituents are highly adjustable considering the cationic and anionic constituents. However, to summarize the average of cations is  $Ca^{2+} > Na^{+} > Mg^{2+} > K^{+}$  and anions is  $Cl^{-} > HCO_3^{-} > SO_4^{2-} > NO_3^{-} > F^{-}$ . However, this analysis may vary from one observation to another and it depends on the spatial location, where the sample was taken which in turn is a function of climate, anthropogenic activities, etc. The spatial analysis output indicates that in some stations of the

study area there is a need for treatment for groundwater to some extent, before consumption. The present study supports to understand the quality of groundwater as well as to progress with suitable controlling practices for protection and preservation of the groundwater sources.

**CRedit authorship contribution statement**

**K. Vijai:** Conceptualization, Methodology, Data curation, Writing - original draft. **S.M. Mazhar Nazeeb Khan:** Supervision, Writing - review & editing.

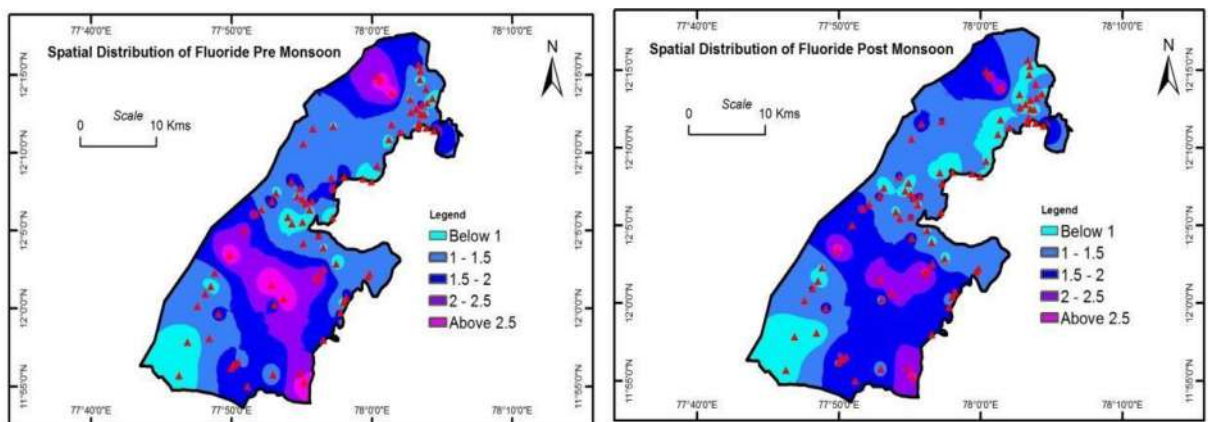


Fig. 13. Spatial distribution of Fluoride ions for pre and post-monsoon seasons.

## Declaration of Competing Interest

The authors declare that they have no known competing financial interests or personal relationships that could have appeared to influence the work reported in this paper.

## Acknowledgement

We thankfully acknowledge the Principal and the Management Committee of Jamal Mohamed College, Trichy, Tamilnadu, India for their support amid our research work. We are truly appreciated to Principal and the Management Committee of Don Bosco College, Dharmapuri for their help during the research work.

## References

- [1] A.O. Fadiran, S.C. Dlamini, A. Mavuso, A comparative study of the phosphate levels in some surface and ground water bodies of Swaziland, *Bull. Chem. Soc. Ethiop.* 22 (2008) 2.
- [2] G. Jacks, K. Rajagopalan, T. Alveteg, M. Jönsson, Genesis of high-F groundwaters, southern India, *Appl. Geochem.* 8 (1993) 241–244.
- [3] J.R. Mullaney, D.L. Lorenz, A.D. Arntson, Chloride in groundwater and surface water in areas underlain by the glacial aquifer system, northern United States, Vol. 5086. Reston, VA: US Geological Survey, 2009.
- [4] J.-Y. Kim, H.-T. Chon, Pollution of a water course impacted by acid mine drainage in the Imgok creek of the Gangreung coal field, Korea, *Appl. Geochem.* 16 (11–12) (2001) 1387–1396.
- [5] I.V. Mudryi, The effect of the mineral composition of drinking water on the health of the population (a review), *Gig. Sanit.* 1 (1999) 15–18.
- [6] A.M. Eassa, A.A. Mahmood, An Assessment of the treated water quality for some drinking water supplies at Basrah, *J. Basrah Res. (Sciences)* 38 (3A) (2012) 95–105.
- [7] Federation, Water Environmental, and American Public Health Association. "Standard methods for the examination of water and wastewater, American Public Health Association (APHA): Washington, DC, USA (2005).
- [8] F. Raihan, J.B. Alam, Assessment of groundwater quality in Sunamganj of Bangladesh, 2008, 155–166.

- [9] R.S. Ayers. K.K. Tanji, Agronomic aspects of crop irrigation with wastewater, 1981.
- [10] S.K. Sundaray, B.B. Nayak, D. Bhatta, Environmental studies on river water quality with reference to suitability for agricultural purposes: Mahanadi river estuarine system, India—a case study, *Environ. Monit. Assess.* 155 (1–4) (2009) 227–243.
- [11] S.J. Phansalkar, V. Kher, P. Deshpande, Expanding rings of dryness: water imports from hinterlands to cities and the rising demands of mega-cities, IWMI-Tata annual partner's meet, Anand, 2005.

## Further Reading

- [1] K. Arumugam, K. Elangovan, Hydrochemical characteristics and groundwater quality assessment in Tirupur region, Coimbatore district, Tamil Nadu, India, *Environ. Geol.* 58 (7) (2009) 1509.
- [2] H. John David, Study and interpretation of the chemical characteristics of natural water, Vol. 2254, Department of the Interior, US Geological Survey, 1985.
- [3] N. Arveti, M.R.S. Sarma, J.A. Aitkenhead-Peterson, K. Sunil, Fluoride incidence in groundwater: a case study from Talupula, Andhra Pradesh, India, *Environ. Monit. Assess.* 172 (1–4) (2011) 427–443.
- [4] J. Hussain, I. Hussain, K.C. Sharma, Fluoride and health hazards: community perception in a fluorotic area of central Rajasthan (India): an arid environment, *Environ. Monit. Assess.* 162 (1–4) (2010) 1–14.
- [5] S.K. Kumar, V. Rammohan, J.D. Sahayam, M. Jeevanandam, Assessment of groundwater quality and hydrogeochemistry of Manimuktha River basin, Tamil Nadu, India, *Environ. Monit. Assess.* 159 (1–4) (2009) 341–351.
- [6] N. Mohammed Muthanna, Quality assessment of Tigris river by using water quality index for irrigation purpose, *Euro. J. Sci. Res.* 57 (1) (2011) 15–28.
- [7] S. Naseem, T. Rafique, E. Bashir, M.I. Bhangar, A. Laghari, T.H. Usmani, Lithological influences on occurrence of high-fluoride groundwater in Nagar Parkar area, Thar Desert, Pakistan, *Chemosphere* 78 (11) (2010) 1313–1321.
- [8] World Health Organization, Guidelines for drinking-water quality, World Health Organization, 1993.
- [9] World Health Organization, Lead in drinking-water: background document for development of WHO guidelines for drinking-water quality, No. WHO/SDE/WSH/03.04/09, World Health Organization, 2003.
- [10] R. Manivannan, et al. Mapping of fluoride ions in groundwater of Dindigul district, Tamilnadu, India—using GIS technique, *Arabian Journal of Geosciences*, 5(3), 2012, 433–439.



# Synthesis And Docking Studies Of Innovative Pyrazole Hydrazides

S.Gunasekar\*, M.Saamanthi, S.Aruna and R.Girija

Department of chemistry, Queen Mary's college. Chennai 600004, Tamilnadu, India

Corresponding Authors : S. Gunasekar - [sgsjain@gmail.com](mailto:sgsjain@gmail.com)

S. Aruna- [arunaschemqmc@gmail.com](mailto:arunaschemqmc@gmail.com)

DOI: 10.47750/pnr.2023.14.S02.22

## Abstract

The heterocyclic chemistry is never ending and ever-growing subject. Pyrazole, a heterocyclic molecule, which leading the pharmaceutical business due to their immense therapeutic activities. Due to the potential biological activities of the pyrazole compounds, more research work is being conducted on these molecules and which further leads to the large investment on pyrazoles followed by invention of new potential drugs. An array of pyrazole benzamides (8a-8s) were prepared by reacting pyrazole hydrazides with different aldehydes and among the synthesized molecules 8g and 8i was the lead molecules. Structures of 8a-8s were confirmed by <sup>1</sup>H NMR, LC-MS and IR spectroscopy and its biological activities were studied by molecular docking study and study shows almost all molecules have the activity for rheumatoid arthritis disease.

## INTRODUCTION

The heterocyclic chemistry is greatest prime concern and interesting part of the organic chemistry, this is due to its theoretical insinuations and its wide business applications. Heterocyclic molecules are inherently having some therapeutic activities, which further increasing while fusing with other ring systems which results in the enhancement of biological activity. Among the heterocyclic molecules, pyrazole moiety is special scaffold which demonstrates the diversity biological activities like anti-arthritis, anti-tuberculosis, anaesthetic, hypnotic, anti-viral, anti-inflammatory and much more. As the result, research scientists and research investors like NCE and NDD organizations (New chemical entities and new drug discovery respectively) are being showing very special interest towards the synthesis of heterocyclic molecules especially compounds containing pyrazole heterocycles. The pyrazole molecules are generally being prepared by the reaction of unsaturated aldehyde with hydrazine.

Organic molecules are massive significant in our daily life and it is being primarily used in pharmaceutical, agrochemicals and veterinary products etc. In the field of organic chemistry, Heterocyclic compounds are being account for the largest family of organic molecules. Pyrazoles of heterocyclic family dominantly lead the pharmaceutical industry, the drugs made up of pyrazole rings are used to treat different diseases and examples for the few are Celebrex (arthritis and acute pain), Crizotinib (non-small cell lung cancer), Difenamizole (Anti-inflammatory), Epirizole (Anti-inflammatory), Lonazolac (Rheumatic pains), Ruxolitinib (Myelotibrosis) and Tosasertib (Aurora kinase inhibitor). Before moving to clinical trials, it will be easier and time saving and money saving process would be "in silico" method.

To evade the drug development cost and to speed the early phase of drug discovery works, virtual screening is the best and cost-effective method. Structure based drug design method is the best among the exiting other kind of drug design methods due to its highest reliability. While discussing about the structure based drug design, the main and important tool to study the orientation of molecules is molecular docking, also it is largely being the more used method in the area of structure-based drug design. The relation of molecule and ligand protein is the bottle neck in the area of molecular docking. The data base for the molecular docking is Protein Data Bank (PDB), which clearly demonstrates the three-dimensional structural data of large biological molecules, such as proteins and nucleic acids. Based on the literature review, the protein data bank RCSB (PDB) chooses the 6NIX protein since the protein- ligand interaction of 6NIX is good for the synthesized molecules. 8g and 8i compounds were bound strongly with hydrogen bonds present in GLU-128, ILE-127 and VAL-159, LAL129, LEU-147 and THR-157 amino acid residues. The compound 8g and 8i docking with protein 6NIX having more docking score

such as -5.315 Kcal/mol and -4.561 Kcal/mol hence 8g and 8i are claimed more active compounds. In this paper we present, synthesis and docking studies of innovative pyrazole hydrazides and their biological activity study using molecular docking method.

## EXPERIMENTAL

The prepared molecular were elucidated and confirmed by proton NMR, Infrared spectroscopy and by LC-MS and the analysis was done in private college. Melting points of synthesized molecules were measured in an uncorrected open capillary tubes and IUPAC nomenclature were followed for newly synthesized molecules. Molecular docking study for the synthesized molecules were screened using Schrodinger software at Queen Mary's college. As the preliminary assessment, progress of all below reactions were ascertained by TLC.

**Synthesis of 1,1,3-tricyano-2-amino-1-propene (1).** Dicyanomethane (50 g, 0.75 mmol) and ethyl alcohol (250 ml) was added to a clean RBF and it cooled to 5-10 °C and portion wise KOH (14.025, 0.25 mmol) was added and heated to 50-55 °C for 30 minutes, the mass was cooled to 25-30 °C and solid was filtered. The solid was dissolved in water (200 mL), hydrochloric acid was added and pH adjusted to 2-3, the obtained solid was filtered to give compound **1**. Color of the solid; Off white and % of yield 45; <sup>1</sup>H NMR (400MHz DMSO-d<sub>6</sub>, δppm): 9.08 (s, 1H), 8.99 (s, 1H), (3.85, 2H) m/z: 131.0 [M]-

**Synthesis of 5-Amino-3-(cyanomethyl)-1H-pyrazol-4-yl cyanide (2).** To a stirred solution of compound **1** (45g, 0.34 mmol) in 450 ml of water, added hydrazine hydrate ~50% (25g, 0.39 mmol) slowly, the reaction mass temperature was raised to 90°C and stirred for 3 h, after completion of the reaction, the solid was filtered at 25-30 °C and washed with water to give 38g of Compound **2**; Color of the solid: Brown and % of yield 78. <sup>1</sup>H NMR (300MHz DMSO-d<sub>6</sub>, δppm): 12.00 (s, 1H) 6.5 (s, 2H) 3.94 (s, 2H) m/z: 149 [M] +

**Synthesis of 3-amino-5-(carboxymethyl)-1H-pyrazole-4-carboxylic acid (3).** Aq. Sodium hydroxide solution (12M, 60 mL) was added to Compound **2** (35 g, 0.24 mmol) at ambient temperature. The reaction was refluxed for overnight. The pH of the reaction was adjusted to ~2-3 further the obtained solid was filtered and filtrate was concentrated under vacuum to get 35g of compound **3** as grey solid with 66% yield. <sup>1</sup>H NMR (300MHz DMSO-d<sub>6</sub>, δppm): 11.89 (m, 3H), 5.71 (m, 2H), 3.55 (m, 3H) m/z: 186 [M] +

**Synthesis of 5-Amino-1H-pyrazol-3-ylacetic acid (4).** Water (700 ml) was added to Compound **3** (28 g, 0.15 mmol) and the slurry was maintained under stirring condition at RT for 5 minutes, then reaction temperature raised to 60 °C for 5h. The reaction was evaporated till complete concentration dryness to yield compound **4** and color of the solid is brown solid. <sup>1</sup>H NMR (300MHz DMSO-d<sub>6</sub>, δppm): 7.30 (m, 1H), 5.25 (s, 1H), 3.30 (s, 2H) mass: 142.3 [M] +

**Synthesis the methyl ester of 5-Amino-1H-pyrazol-3-ylacetic acid hydrochloride (5).** Methanol was charged to RBF having compound **4** (20g, 0.14 mmol) and to this stirred solution added thionyl chloride slowly (54.72 g, 0.45 mmol) at 0-5 °C and stirred for 4 hours and filtered the material. <sup>1</sup>H NMR (300MHz DMSO-d<sub>6</sub>, δppm): 10.72 (m, 3H), 5.91 (s, 1H), 3.8 (s, 2H), 3.63 (s, 3H) m/z: 156.2 [M] +

**Synthesis of methyl 2-(3-(4-chlorobenzamido)-1H-pyrazol-5-yl)acetate (6).** DMF (110 mL), DIEA (22.04 g, 0.161 mmol) was stirred and to this clear solution added 2-fluoro-5-bromo benzoic acid (15.02g, 0.073 mmol) and the reaction mass was cooled to 0-5 °C, in portion wise EDC.HCl (20.09g, 0.11 mmol) was added followed by HOBt (13.58g, 0.109 mmol). To this slurry, further compound **5** (amine) 13.781g, 0.073 mmol) was added and maintained for 30 minutes. The reaction was quenched with water and the product was extracted with ethyl acetate and it evaporated to dryness and further n-heptane was added and the solid was filtered to get Compound **6**, 11.01g; brown solid and % yield is 69, <sup>1</sup>H NMR (400MHz DMSO-d<sub>6</sub>, δppm): 12.62 (s, 1H), 10.87 (s, 1H), 8.02-7.93 (m, 2H), 7.58-7.55 (m, 2H), 6.50 (s, 1H), 3.74 (s, 3H).

**Synthesis of 4-chloro-N-(5-(2-hydrazinyl-2-oxoethyl)-1H-pyrazol-3-yl)benzamide (7).** Hydrazine hydrate (20g, 0.62 mmol) was added Compound **6** (11g, 0.030 mmol) and the slurry was stirred for 30-45 minutes at 25±5 °C, the solid was filtered to get compound **7** with 90% yield. <sup>1</sup>H NMR (400MHz DMSO-d<sub>6</sub>, δppm): 12.27 (s, 1H) 10.82 (s, 1H), 9.22 (s, 1H), 8.01-7.99 (d, 2H), 7.57-7.55 (d, 2H), 6.50 (s, 1H), 4.26(s, 2H), 3.40(s, 2H); m/z: 293.0 [M] +

**General Preparation technique for (8a- s):** compound **7** (500mg, 1 eq) was added to ethanol followed by aromatic aldehydes (1.1 eq) were refluxed with small amount of CH<sub>3</sub>COOH and maintained for 3h at reflux. The precipitated solids were filtered.

**<sup>1</sup>H NMR and LC-MS of compound 8a-8s: (E)-3-chloro-N-(5-(2-(2-(2-hydroxybenzylidene)hydrazinyl)-2-oxoethyl)-1H-pyrazol-3-yl) benzamide (8a).** white solid. MP 166-173 °C. Yield: 77 %. IR (KBr, cm<sup>-1</sup>): 3305 (NH), 1672 (C=O); <sup>1</sup>H NMR (400MHz DMSO-d<sub>6</sub>, δppm): 12.41-12.34 (d, 1H), 11.88 (s, 1H) 11.46-11.06 (d, 1H), 10.93-10.89 (d, 1H), 10.07 (s, 1H) 8.43-8.32 (d, 1H), 7.96-7.94 (d, 1H), 7.74-7.72 (t, 1H), 7.55-7.50 (m, 3H), 7.31-7.22 (s, 1H) 6.92-6.85 (m, 1H) 6.60-6.54 (s, 1H), 4.02-3.64 (d, 2H), MS m/z: 474.10 [M] +

**(E)-3-chloro-N-(5-(2-(2-(3-hydroxybenzylidene)hydrazinyl)-2-oxoethyl)-1H-pyrazol-3-yl) benzamide (8b).** Pale brown solid. MP 177-172 °C. Yield: 77 %. IR (KBr, cm<sup>-1</sup>): 3259 (NH), 1655(C=O); <sup>1</sup>H NMR (400MHz DMSO-d<sub>6</sub>, δppm): 12.39-12.35 (d, 1H), 11.60-11.47 (d, 1H), 10.93-10.90 (d, 1H), 9.63-9.62 (s, 1H) 8.12-7.93 (t, 3H), 7.64-7.62 (d, 2H), 7.26-7.22 (t, 2H), 7.17-7.07 (m, 2H), 6.83-6.81 (q, 1H) 6.59-6.55 (d, 1H), 4.03-3.61 (d, 2H); MS m/z: 398.4 [M] +

**(E)-3-chloro-N-(5-(2-(2-(4-chlorobenzylidene)hydrazinyl)-2-oxoethyl)-1H-pyrazol-3-yl)benzamide (8c).** White solid. MP 197-199 °C. Yield: 75%. IR (KBr, cm<sup>-1</sup>): 3310 (NH), 1676(C=O); <sup>1</sup>H NMR (400MHz DMSO-d<sub>6</sub>, δppm): 12.40-12.35 (d, 1H), 11.72-11.59 (d, 1H),

10.92-10.89 (d, 1H), 8.21 (s, 2H) 8.02 (s, 1H), 7.95-7.92 (t, 2H), 7.76-7.72 (t, 1H), 7.654-7.50 (m, 3H), 6.59-6.55 (d, 1H), 4.04-3.62 (d, 2H); MS m/z: 416.5 [M] +

**(E)-3-chloro-N-(5-(2-(2-(4-methoxy-2,3-dimethylbenzylidene)hydrazinyl)-2-oxoethyl)-1H-pyrazol-3-yl) benzamide (8d).** Pale pink solid. MP 189-192 °C. Yield: 55%. <sup>1</sup>H NMR (400MHz DMSO-d<sub>6</sub>, δppm): 12.39-12.34 (d, 1H), 11.48-11.29 (d, 1H), 10.92-10.89 (d, 1H), 8.50 (s, 1H) 8.33 (s, 1H), 8.03 (s, 1H) 7.95-7.93 (d, 1H), 7.68-7.62 (m, 2H), 7.54-7.50 (m, 1H), 6.93-6.90 (m, 1H), 6.59-6.54 (s, 1H) 4.01-3.59 (d, 2H), 3.81 (s, 3H), 2.32-2.31 (d, 3H), 2.12 (s, 3H); m/z: 440.7 [M] +

**(E)-N-(5-(2-(2-(4-bromo-3,5-dimethoxybenzylidene) hydrazinyl)-2-oxoethyl)-1H-pyrazol-3-yl)-3-chlorobenzamide (8e).** Off white powder. MP 199-201 °C. Yield: 63%. <sup>1</sup>H NMR (400MHz DMSO-d<sub>6</sub>, δppm): 12.36 (s, 1H), 11.75-11.66 (d, 1H), 10.94-10.90 (d, 1H), 8.21-8.02 (m, 2H), 7.98-7.92 (m, 1H), 7.63-7.62 (d, 1H), 7.55-7.50 (m, 1H), 7.28-7.27 (s, 1H), 7.05 (s, 2H) 6.55 (s, 1H) 4.05-3.63 (m, 8H); MS m/z: 520.8 [M] +

**(E)-3-chloro-N-(5-(2-(2-(2,5-dichloro-4-methylbenzylidene)hydrazinyl)-2-oxoethyl)-1H-pyrazol-3-yl) benzamide 8(f).** Gray solid. MP 200-203 °C. percentage of Yield: 66%. <sup>1</sup>H NMR (400MHz DMSO-d<sub>6</sub>, δppm): 12.38-12.30 (d, 1H), 11.86-11.72 (d, 1H), 10.92-10.88 (d, 1H), 8.39-8.27 (d, 1H), 8.03-7.93 (t, 2H) 7.95-7.93 (d, 1H), 7.64-7.62 (d, 2H), 7.54-7.50 (m, 1H), 6.93-6.90 (m, 1H), 6.59-6.53 (s, 1H) 3.99-3.63 (d, 2H), 2.33 (s, 3H), MS m/z: 464.5 [M] +

**(E)-3-chloro-N-(5-(2-(2-(2,3-dihydroxybenzylidene)hydrazinyl)-2-oxoethyl)-1H-pyrazol-3-yl) benzamide 8(g).** Off white crystal. MP 211-213 °C. Yield: 58%. <sup>1</sup>H NMR (400MHz DMSO-d<sub>6</sub>, δppm): 12.33 (s, 1H), 11.87-11.45 (d, 1H), 10.93-10.88 (t, 1H), 9.53-9.21 (t, 3H), 8.37-8.32 (s, 1H) 8.03-7.92 (m, 1H), 7.64-7.62 (d, 1H), 7.55-7.50 (m, 1H), 7.17-7.15 (d, 1H) 6.97 (s, 1H), 6.97-6.95 (s, 1H), 6.85-6.80 (m, 1H), 6.68-6.66 (m, 1H), 6.56-6.50 (s, 1H) 3.99-3.63 (m, 8H), MS m/z: 414.7 [M] +

**(E)-3-chloro-N-(5-(2-(2-(3,5-dichlorobenzylidene)hydrazinyl)-2-oxoethyl)-1H-pyrazol-3-yl)benzamide (8h)** Brown solid. MP 203-204 °C. Yield: 61%. <sup>1</sup>H NMR (400MHz DMSO-d<sub>6</sub>, δppm): 12.19 (s, 1H), 11.90-11.72 (d, 1H), 10.93-10.89(d, 1H), 8.18-8.03 (d, 2H), 7.98-7.93 (t, 1H), 7.78-7.75 (d, 2H) 7.67-7.62(d, 2H), 7.55-7.50 (m, 1H) 6.55-6.51 (d, 1H), 4.06-3.33 (d, 2H); MS m/z: 450.8 [M] +

**(E)-3-chloro-N-(5-(2-(2-(4-hydroxy-3,5-dimethoxybenzylidene)hydrazinyl)-2-oxoethyl)-1H-pyrazol-3-yl) benzamide (8i)** Brown solid. MP 188-190 °C. Yield: 71%. <sup>1</sup>H NMR (400MHz DMSO-d<sub>6</sub>, δppm): 12.17 (s, 1H), 11.49-11.39 (d, 1H), 10.92-10.88(d, 1H), 8.89-8.84 (d, 1H) 8.03-8.02 (d, 1H), 7.95-7.92 (t, 1H), 7.63-7.61 (m, 2H), 7.54-7.50 (m, 1H) 6.96 (s, 2H), 6.54 (s, 1H), 4.02-3.59 (d, 2H), 3.81-3.80 (d, 6H); MS m/z: 458.6 [M] +

**(E)-3-chloro-N-(5-(2-(2-(2,3-dichlorobenzylidene) hydrazinyl)-2-oxoethyl)-1H-pyrazol-3-yl) benzamide (8j)** Brown solid. MP 200-201 °C. Yield: 62%. <sup>1</sup>H NMR (400MHz DMSO-d<sub>6</sub>, δppm): 12.40-12.20 (d, 1H), 12.05-11.65 (d, 1H), 10.93-10.89 (d, 1H), 9.10-8.71(t, 1H) 8.58-8.53 (m, 1H), 8.34-8.26 (m, 1H), 8.18-8.14 (t, 1H), 8.04-8.03 (t, 1H), 7.96-7.93 (t, 1H), 7.55-7.50 (m, 2H), 7.18-7.08 (m, 1H) 6.5-6.54 (d, 1H), 4.07-3.65 (d, 2H); MS m/z: 450.8 [M] +

**(E)-3-chloro-N-(5-(2-(2-(2-hydroxy-5-nitrobenzylidene)hydrazinyl)-2-oxoethyl)-1H-pyrazol-3-yl) benzamide (8k)** off white solid. MP 187-190 °C. Yield: 67%. <sup>1</sup>H NMR (400MHz DMSO-d<sub>6</sub>, δppm): 12.39-12.35 (d, 1H), 11.98-11.78 (d, 1H), 10.92-10.89 (d, 1H), 8.64-8.43 (d, 1H) 8.02-8.00 (d, 3H), 7.95-7.91 (m, 1H), 7.73-7.69 (m, 2H), 7.54-7.42 (m, 1H) 6.59-6.54 (d, 1H), 4.06-3.64 (d, 2H); MS m/z: 443.7 [M] +

**(E)-3-chloro-N-(5-(2-(2-(2,4-dichlorobenzylidene) hydrazinyl)-2-oxoethyl)-1H-pyrazol-3-yl) benzamide (8l)** Brown solid. MP 198-199 °C. Yield: 65%. <sup>1</sup>H NMR (400MHz DMSO-d<sub>6</sub>, δppm): 12.17 (s, 1H), 11.92-11.73 (d, 1H), 10.92-10.88 (d, 1H), 8.55-8.36 (d, 1H), 8.05-7.92 (m, 3H), 7.70-48 (m, 4H) 6.54-6.50 (d, 1H), 4.05-3.34 (d, 2H); MS m/z: 450.7 [M] +

**(E)-3-chloro-N-(5-(2-(2-(4-hydroxybenzylidene) hydrazinyl)-2-oxoethyl)-1H-pyrazol-3-yl) benzamide (8m).** Pale brown solid. MP 180-182 °C. Yield: 74 %. <sup>1</sup>H NMR (400MHz DMSO-d<sub>6</sub>, δppm): 12.14 (s, 1H), 11.44-11.30 (d, 1H), 10.93-10.89 (d, 1H), 9.92-9.89 (s, 1H) 8.10-7.92 (q, 3H), 7.64-7.62 (d, 1H), 7.54-7.50 (m, 3H), 6.80-6.81 (d, 2H), 6.53-6.51 (d, 1H), 4.00-3.57 (d, 2H); MS m/z: 398.5 [M] +

**(E)-N-(5-(2-(2-((2-bromopyridin-4-yl)methylene)hydrazinyl)-2-oxoethyl)-1H-pyrazol-3-yl)-3-chlorobenzamide (8n).** Pale pink solid. MP 177-183 °C. Yield: 66 %. <sup>1</sup>H NMR (400MHz DMSO-d<sub>6</sub>, δppm): 12.20 (s, 1H), 12.05-11.90 (d, 1H), 10.94-10.91 (d, 1H), 8.44-8.43 (d, 1H) 8.18-8.03 (d, 1H), 7.97-7.72 (m, 3H), 7.64-7.62 (d, 1H), 7.55-7.50 (m, 2H), 6.54-6.52 (d, 1H), 4.08-3.66 (d, 2H); MS m/z: 462.1 [M] +

**(E)-3-chloro-N-(5-(2-(2-(5-chloro-2-methoxybenzylidene) hydrazinyl)-2-oxoethyl)-1H-pyrazol-3-yl) benzamide 8(o).** pink solid. MP 182-185 °C. Yield: 57%. <sup>1</sup>H NMR (400MHz DMSO-d<sub>6</sub>, δppm): 12.18 (s, 1H), 11.77-11.56 (d, 1H), 10.94-10.90 (d, 1H), 8.87-8.03 (t, 2H), 7.95-7.73 (m, 3H), 7.64-7.62 (d, 1H), 7.56-7.50 (m, 2H), 6.54-6.51 (d, 1H), 4.05-3.59 (d, 2H), 3.90-3.86 (t, 3H); MS m/z: 446.5 [M] +

**(E)-N-(5-(2-(2-(4-(benzyloxy)benzylidene)hydrazinyl)-2-oxoethyl)-1H-pyrazol-3-yl)-3-chlorobenzamide 8(p).** Off white solid. MP 169-173 °C. Yield: 68%. <sup>1</sup>H NMR (400MHz DMSO-d<sub>6</sub>, δppm): 12.34 (s, 1H), 11.52-11.39 (d, 1H), 10.92-10.89 (d, 1H), 8.16-8.03 (d, 1H), 7.97-7.93 (t, 2H), 7.67-7.62 (t, 3H), 7.54-7.32 (m, 6H), 7.15-7.07 (m, 2H) 6.54 (s, 1H), 5.19-5.16 (d, 2H) 4.02-3.59 (d, 2H); MS m/z: 488.5 [M+] +

**(E)-3-chloro-N-(5-(2-(2-(3,4-dimethoxybenzylidene)hydrazinyl)-2-oxoethyl)-1H-pyrazol-3-yl) benzamide 8(q).** Grey solid. MP 188-192 °C. Yield: 67%. <sup>1</sup>H NMR (400MHz DMSO-d<sub>6</sub>, δppm): 12.40 (s, 1H), 11.52-11.40 (d, 1H), 10.89 (s, 1H), 8.64-8.14 (m, 2H), 7.94-

7.92 (d, 1H), 7.63-7.62 (d, 1H), 7.55-7.49 (m, 1H), 7.39-7.30 (s, 1H), 7.17-6.99 (m, 2H), 6.5 (s, 1H), 4.05-3.59 (m, 8H); MS m/z: 442.5 [M] +

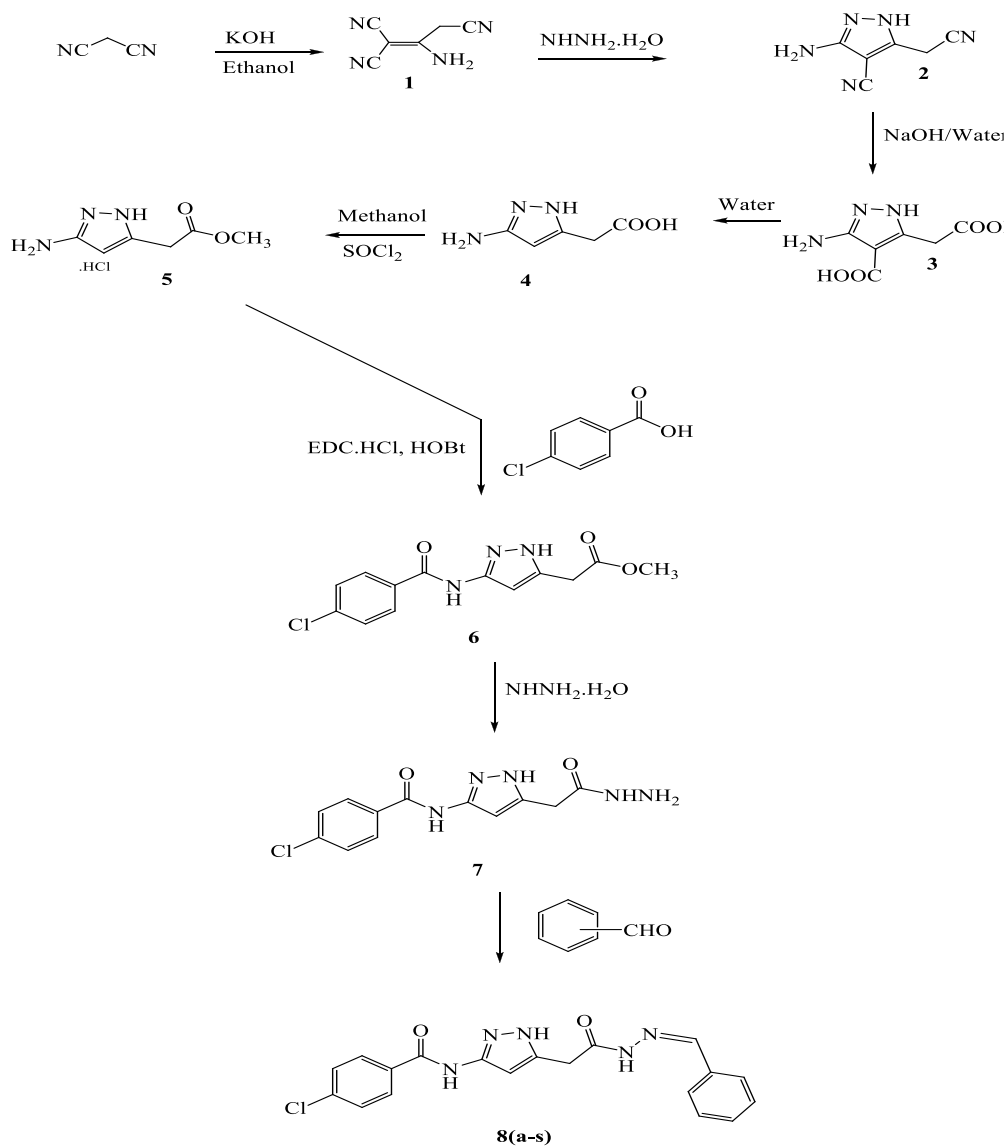
**(E)-3-chloro-N-(5-(2-(2-(3-nitrobenzylidene)hydrazinyl)-2-oxoethyl)-1H-pyrazol-3-yl)benzamide (8r)**. Off white solid. MP 193-195 °C. Yield: 75%. <sup>1</sup>H NMR (400MHz DMSO-d<sub>6</sub>, δppm): 12.39-12.22 (d, 1H), 11.90-11.75 (d, 1H), 10.93-10.89 (d, 1H), 8.94-8.73 (m, 2H) 8.57-8.51 (t, 1H), 8.40-8.30 (m, 2H), 8.26-8.14 (m, 2H), 8.03-7.50 (m, 3H), 6.54 (s, 1H), 4.08-3.65 (d, 2H); MS m/z: 427.5 [M] +

**(E)-N-(5-(2-(2-(5-bromo-2-nitrobenzylidene)hydrazinyl)-2-oxoethyl)-1H-pyrazol-3-yl)-3-chlorobenzamide (8s)**. White solid. MP 166-170 °C. Yield: 69%. <sup>1</sup>H NMR (400MHz DMSO-d<sub>6</sub>, δppm): 12.37 (s, 1H), 12.05-11.85 (d, 1H), 10.91 (s, 1H), 8.90-8.29 (m, 2H), 8.08-7.93 (m, 4H), 7.64-7.62 (d, 2H), 7.54-7.53 (m, 1H), 6.53 (s, 1H), 4.04-3.65 (d, 2H); MS m/z: 506.0 [M] +

## RESULTS AND DISCUSSION

**3.1 Chemistry:** Dicyanomethane was dissolved with ethanol and to it added potassium hydroxide at ambient temperature to give Compound **1**, it was reacted with 80% solution of hydrazine hydrate at 25± 5° C for 60-120 minutes to get compound **2** and it reacted with aq. NaOH at 100° C for overnight to have compound **3** and to it charged H<sub>2</sub>O and maintained for 4-6 hrs. at 50-55° C and it was evaporated to have compound **4**. To a slurry of Compound **4** and methyl alcohol, added SOCl<sub>2</sub> slowly to have **6**. To a DMF solvent, added Carboxylic acid, DIEA, N-(3-Dimethylaminopropyl)-N'-ethyl carbodiimide hydrochloride & Hydroxy benzotriazole and compound **5** and stirred for 4h at ambient temperature, to yield Compound **6**. Compound **6** was reacted with hydrazine hydrate in the ethanol solvent, post addition of hydrazine hydrate, The reaction mixture was maintained for 0.5h, to have Compound 7. Different aldehydes were refluxed with compound 7 in ethanol solvent media to have title molecules (pyrazole hydrazides). Synthetic scheme of 8 (a-s) is demonstrated below in **Synthetic scheme**.

### Synthetic scheme



## DOCKING SCREENING

**Preparation of Ligands:** Structures of ligands sketched and saved in SDF format were imported via selecting files. The imported ligands 8 a-s was set to minimize under force field OPLS3e. Minimization calculations can be performed on all structures of pyrazole derivatives.

**Preparation of Protein:** X-ray crystalline Structure of protein 6NIX was imported from Protein Data Bank (PDB) to workspace, which further set to preprocess followed by review and modification to remove unwanted chains and residues, further refined under force field of OPLS3e. The results were monitored in the job monitor.

**Molecular Docking:** The pyrazole compounds are selected for molecular docking. All the lead compounds showed good binding energy and exhibited interactions and better lower free energy values, indicating more thermodynamically favored interaction. As for Glide docking, crystal structures of 6NIX have been prepared by the protein preparation wizard in Schrodinger suite. Afterwards, the required receptor grids were made just before docking with the active site determined by the position of co crystal ligand. Crystal structures of 6NIX were imported into Glide, defined as the receptor structure and the location of active sites with a box. The PLS3e force field was used for grid generation. The standard precision (SP) and the extra precision (XP) protocols were set for docking studies with crucial residues, in constrained binding to get accurate results. Binding affinity was retrieved running Prime MM-GBSA. All other parameters were maintained as default

The research aims to find more prospective lead compounds with a drug discovery system, in which molecular docking studies achieve the logical drug design. Molecular docking is great tool and much being used technique in structure drug design due to its ability to predict the binding conformation of small mole molecule ligands to the appropriate target binding site. Docking scores, glide scores and glide energy of synthesized pyrazole cules are shown in the below **table 1** and 2D and 3D interactions of synthesized compounds are shown in **fig 1-18**.

**Table 1: Glide Docking and binding energy scores**

Title	Docking Score	Glide g score	Glide energy	Glide model
6NIX	- 5.505	-5.505	-48.561	-58.988
8g	- 5.315	-5.315	-44.561	-57.788
8i	- 4.561	-4.561	-41.442	-56.298
8k	-3.987	-3.987	-40.481	-54.867
8r	-3.923	-3.923	-41.344	-47.589
8b	-3.866	-3.866	-41.196	-54.896
8m	-3.571	-3.571	-36.51	-47.547
8a	-3.327	-3.327	-42.277	-57.014
8f	-3.151	-3.151	-43.084	-51.698
8e	-3.083	-3.083	-44.72	-51.411
8h	-3.024	-3.024	-42.615	-56.787
8c	-2.985	-2.985	-38.789	-48.78
8o	-2.915	-2.915	-42.48	-51.5
8l	-2.774	-2.774	-38.234	-55.803
8s	-2.655	-2.655	-41.704	-56.654
8j	-2.651	-2.651	-41.978	-55.02
8q	-2.633	-2.633	-35.397	-46.445

8n	-2.543	-2.543	-41.92	-59.364
8d	-2.414	-2.414	-37.257	-44.56
8p	-1.389	-1.389	-39.641	-56.392

**Note:** In the following figures 1 to 18, A and B with 2D and 3D interactions between ligands and receptor (hydrogen bonds are illustrated as arrows; C atoms are colored gray, N blue, and O red) and compound binding mode at the 6NIX active site. **Note:** In the following figures 1 A and B with 2D and 3D interactions between ligands and receptor (hydrogen bonds are illustrated as arrows; C atoms are colored gray, N blue, and O red) and compound binding mode at the 6NIX active site.

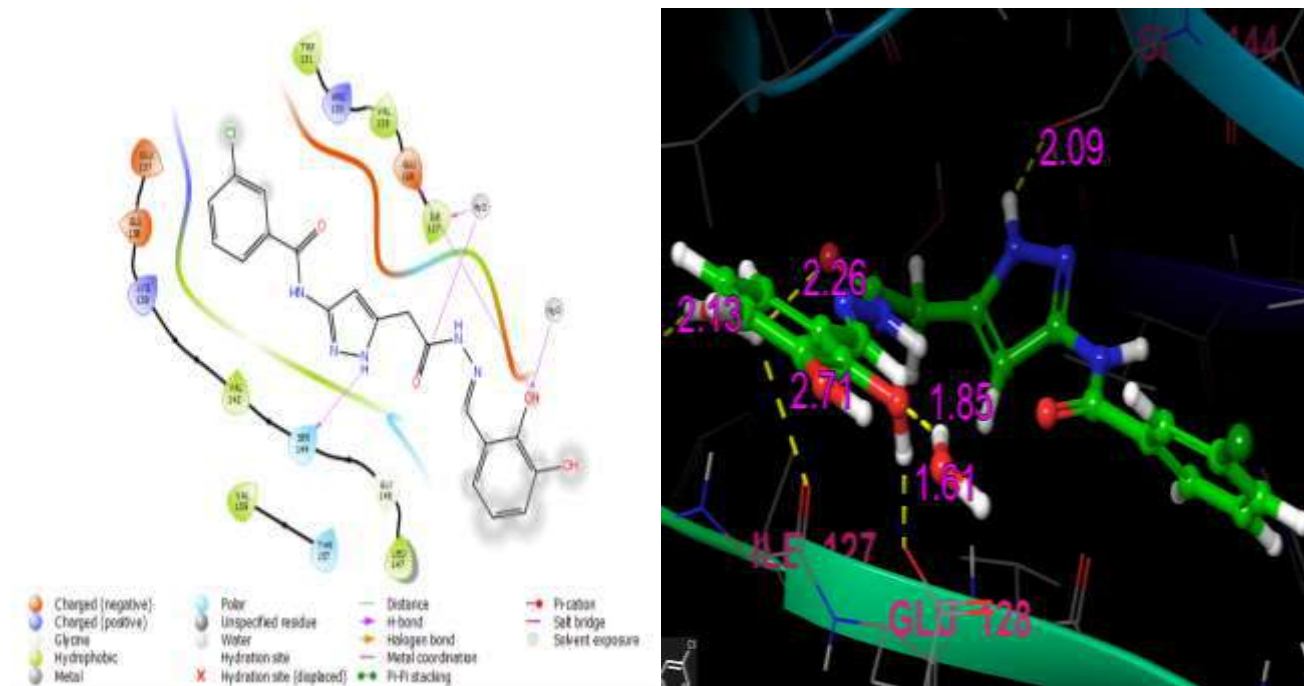


Figure 1: Compound 8g

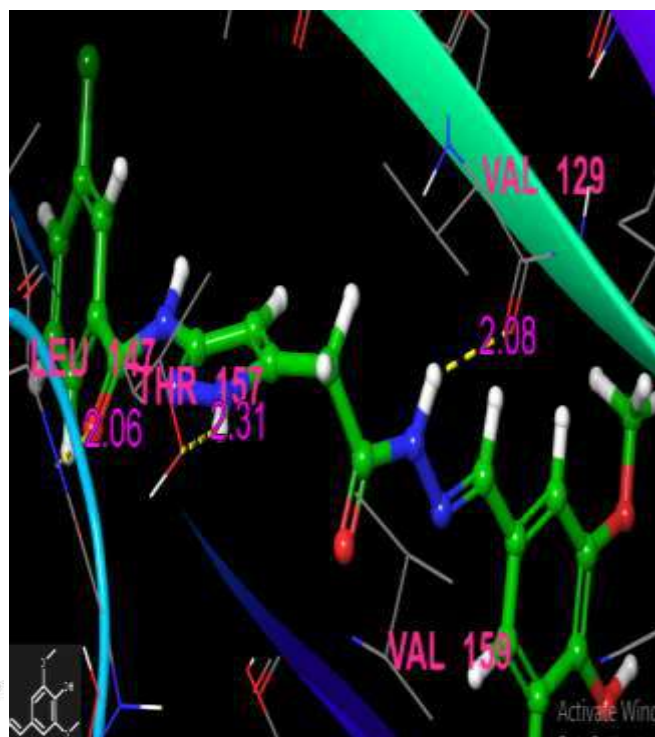
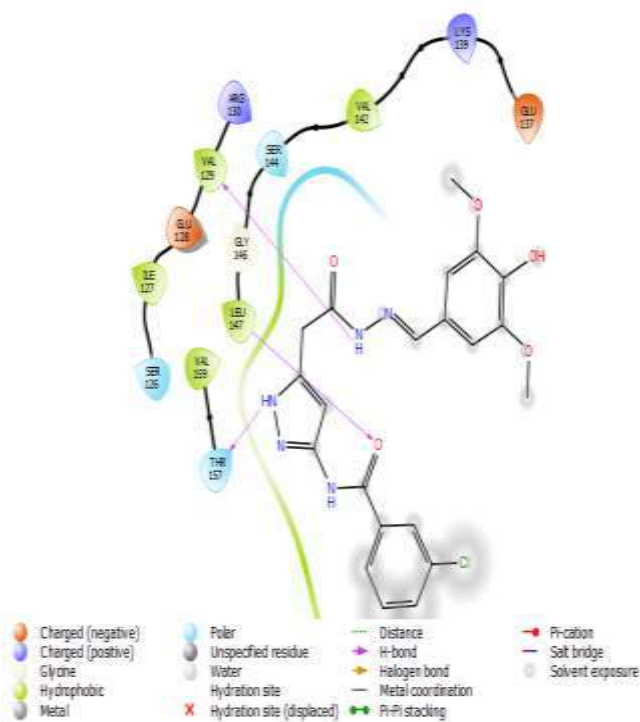


Figure 2: Compound 8i

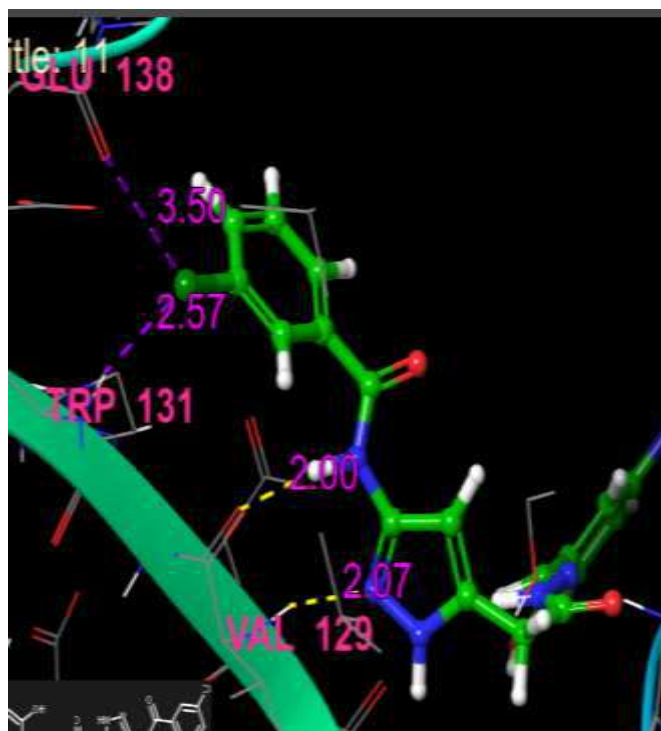
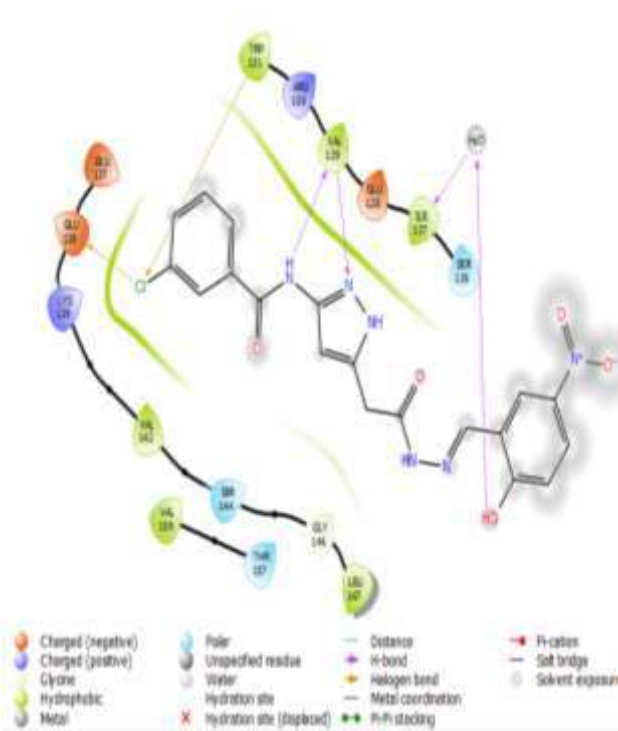


Figure 3: Compound 8k



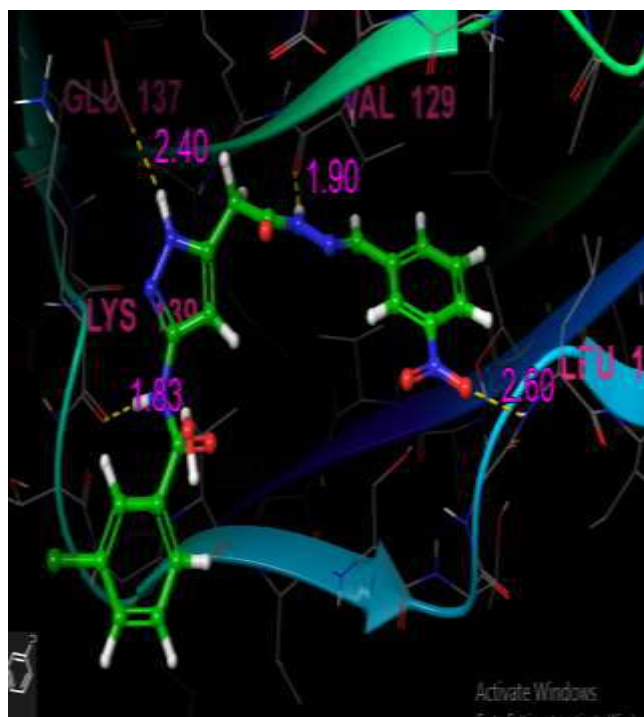
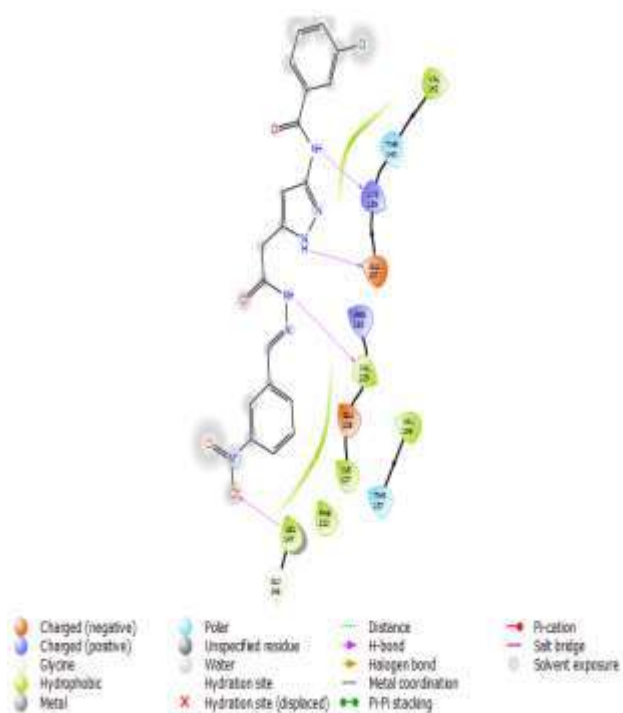


Figure 4: Compound 8r

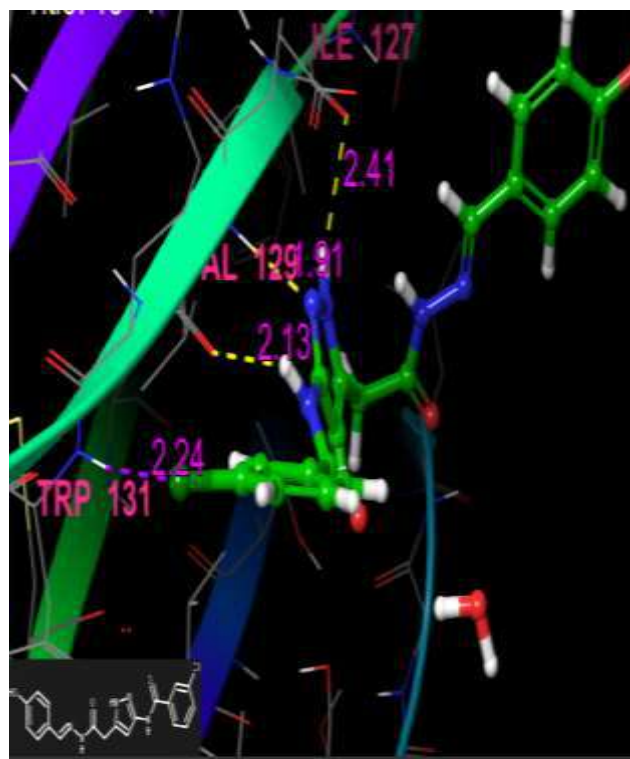
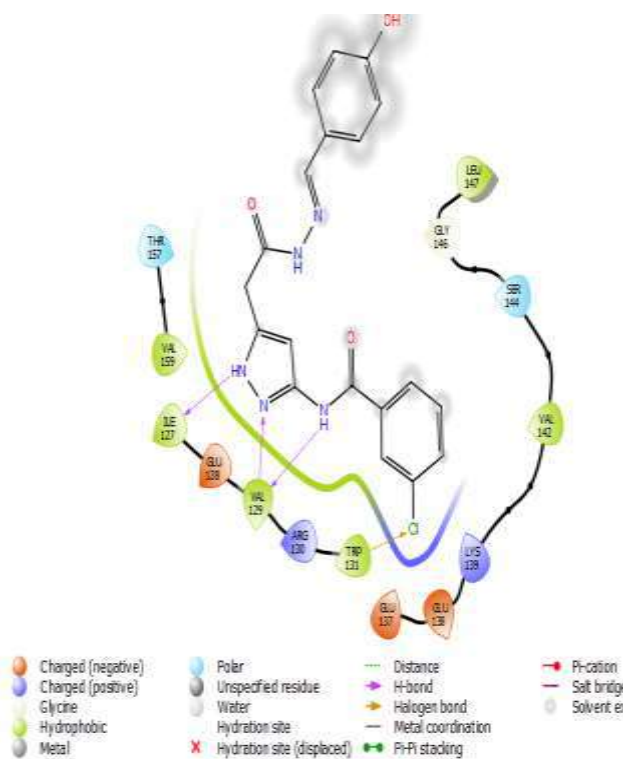


Figure 5: Compound 8m

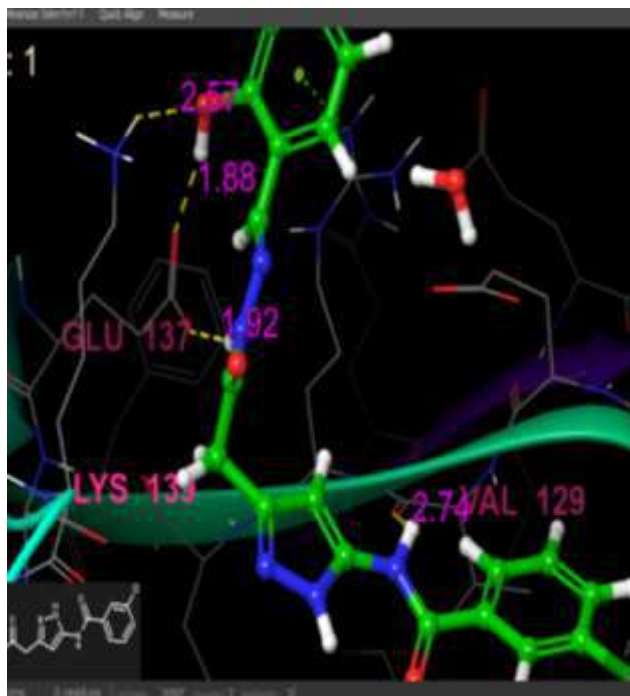
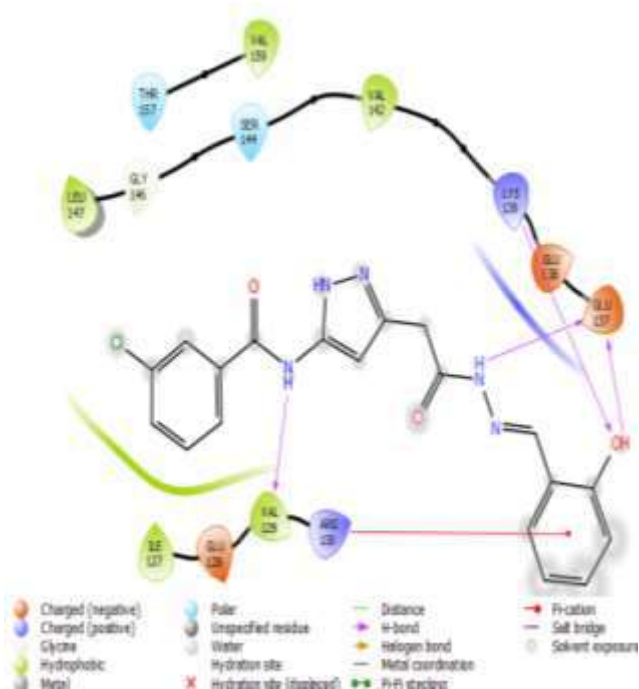


Figure 6: Compound 8a

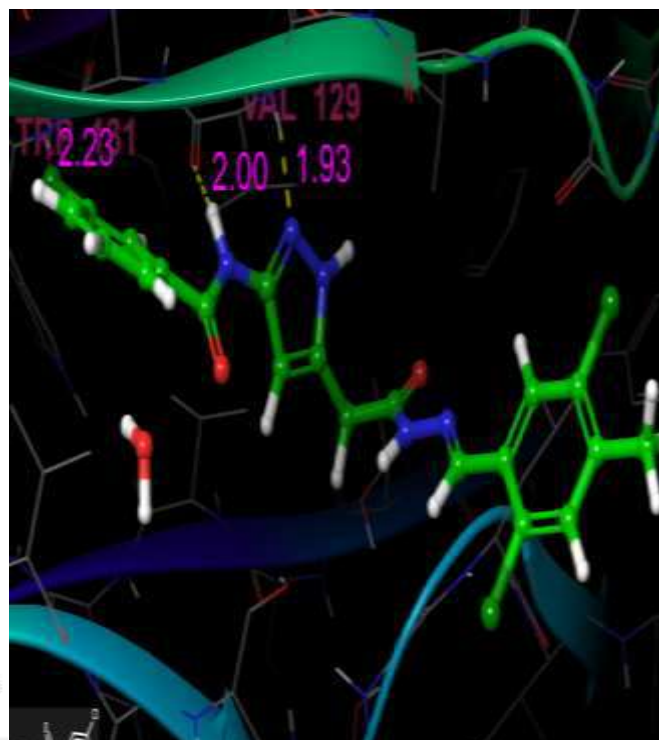
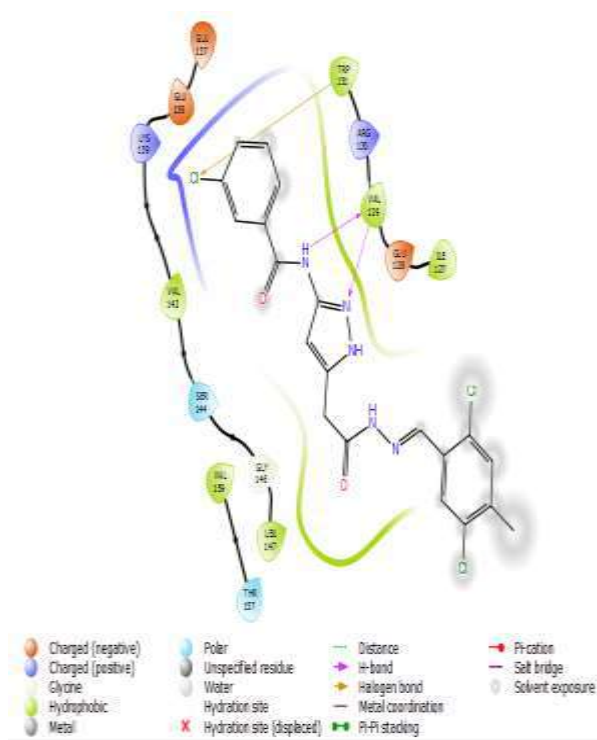


Figure 7: Compound 8f

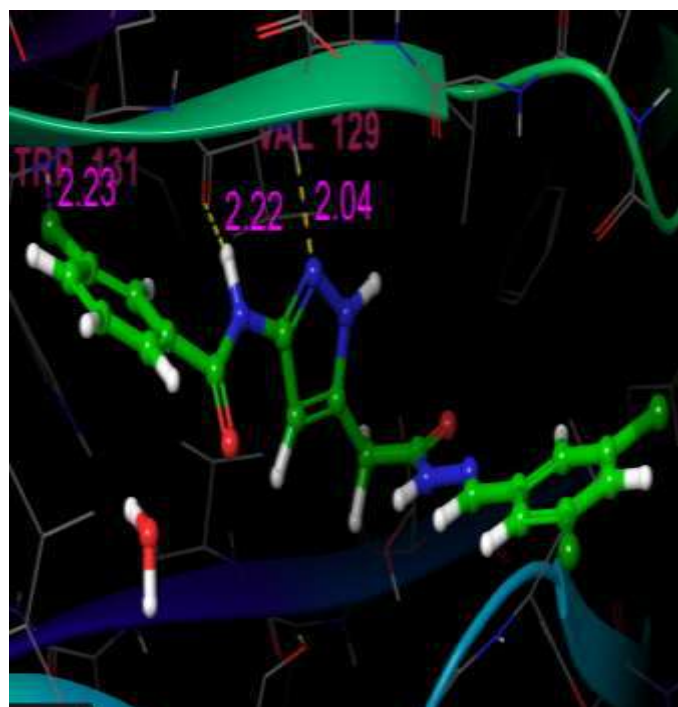
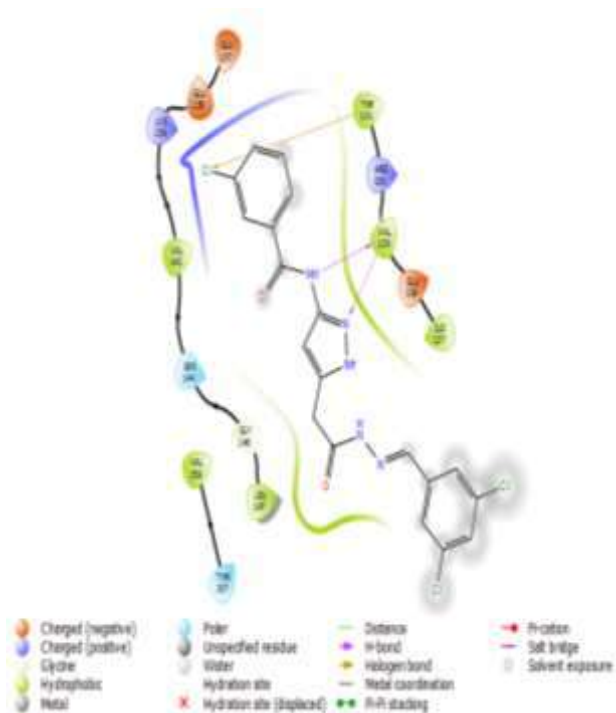


Figure 8: Compound 8h

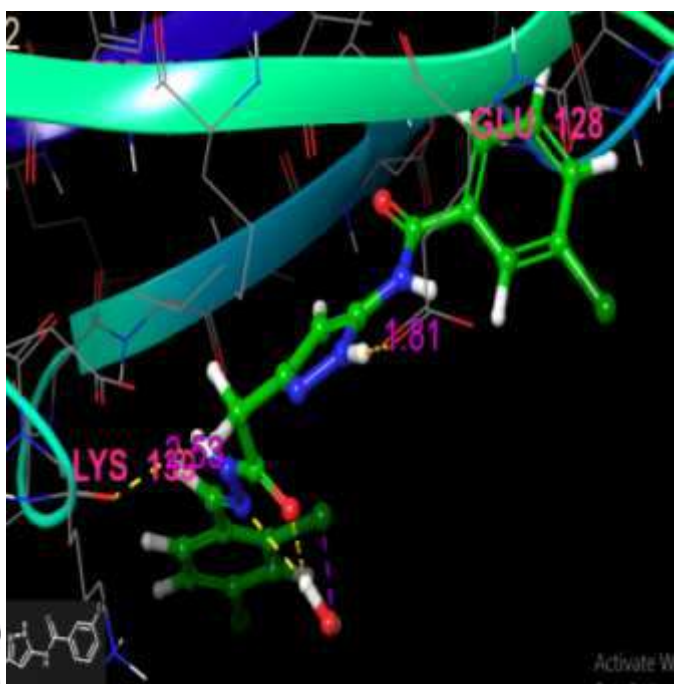
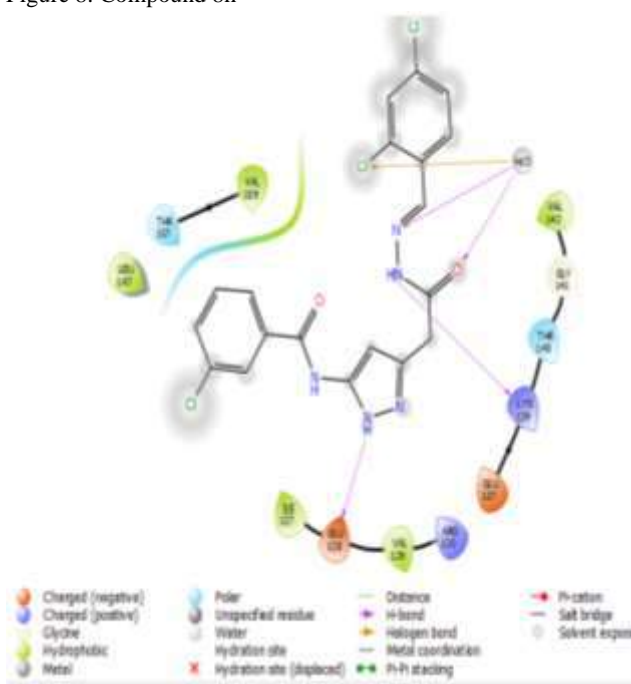


Figure 9: Compound 8l.

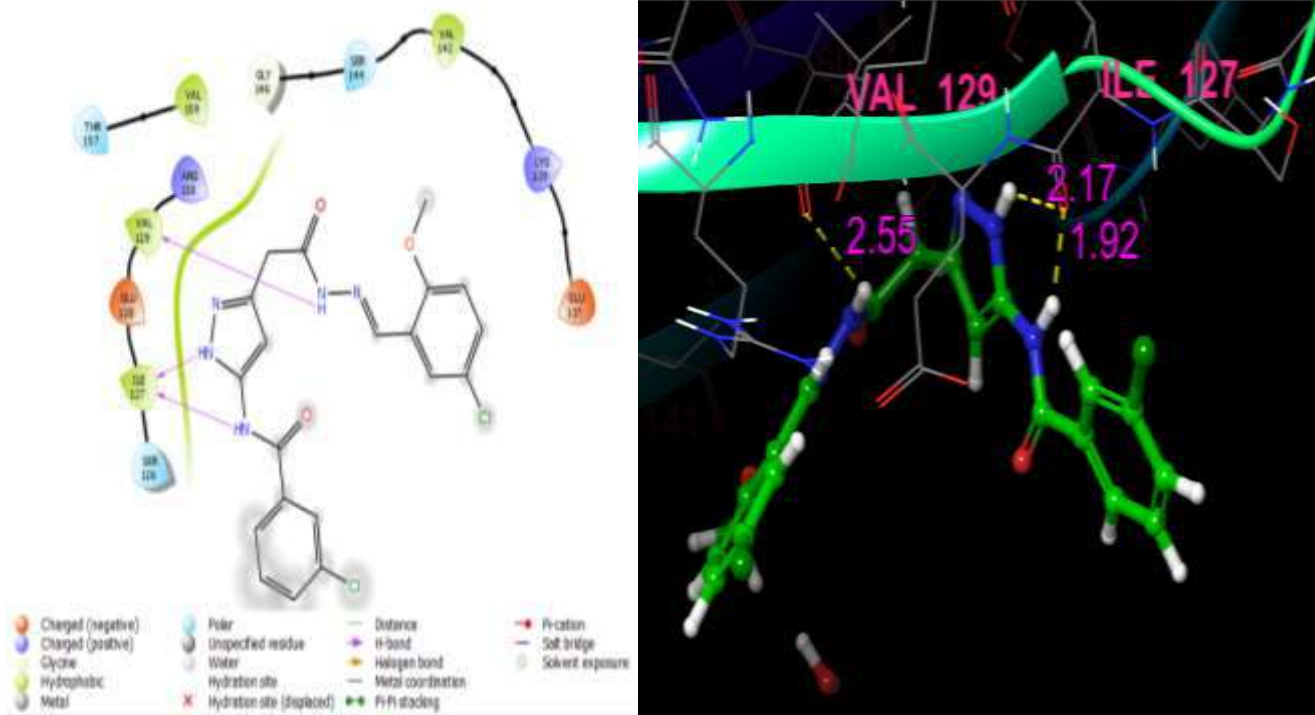


Figure 10: Compound 8o.

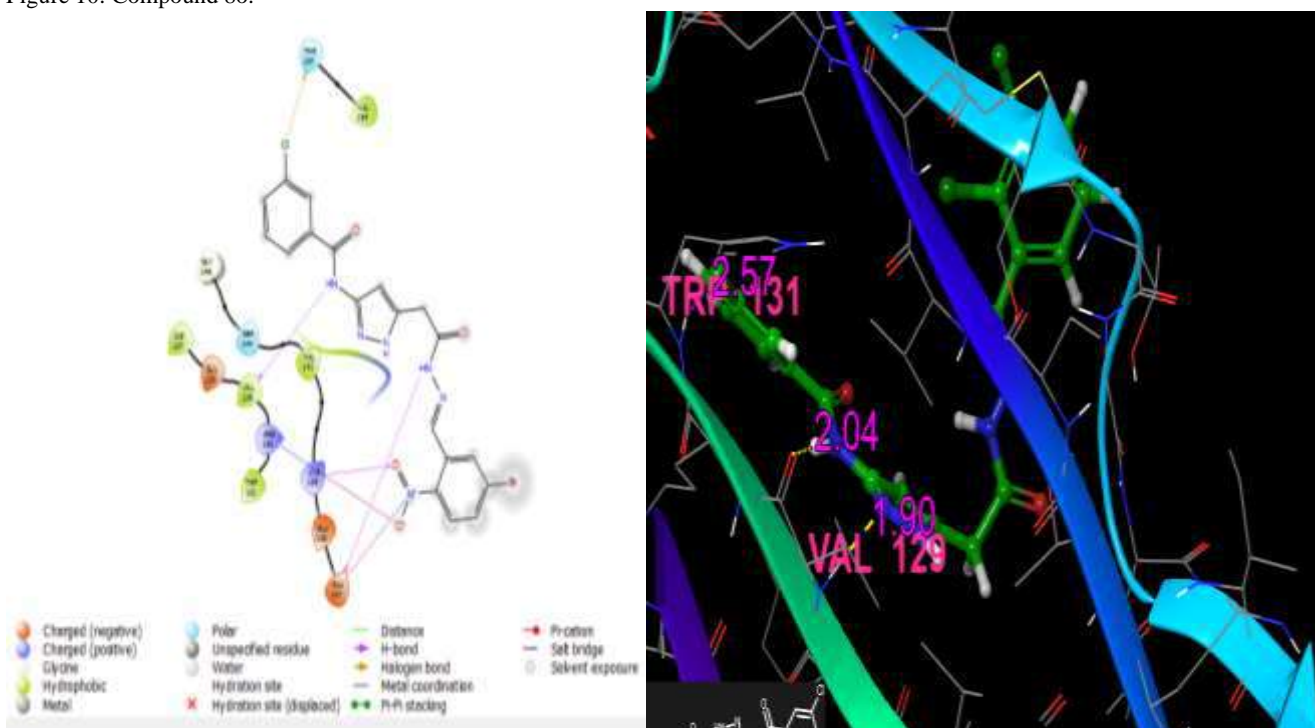


Figure 11: Compound 8s

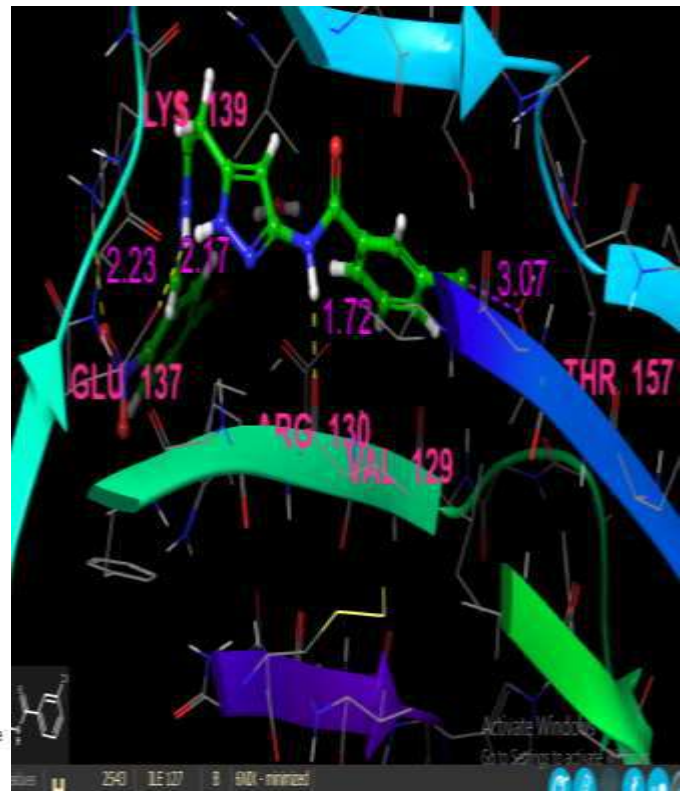
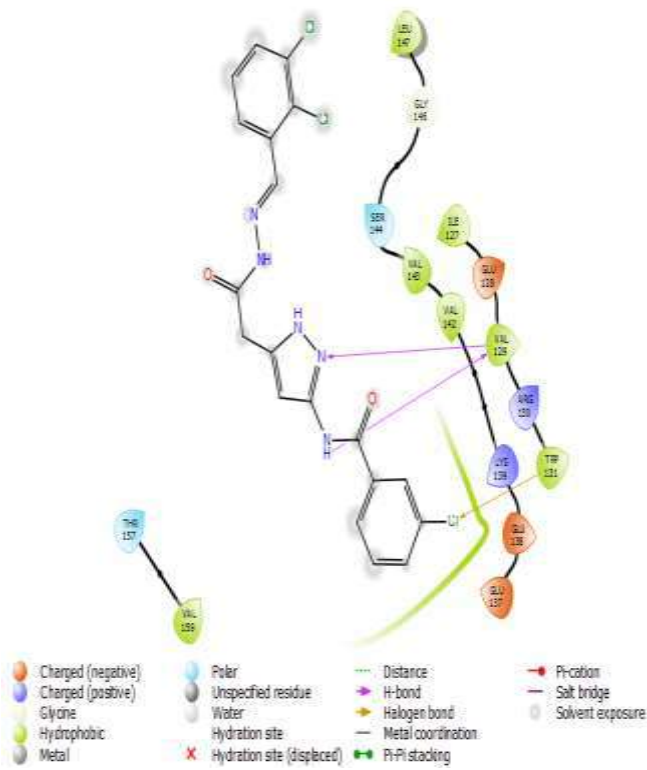


Figure12: Compound 8j

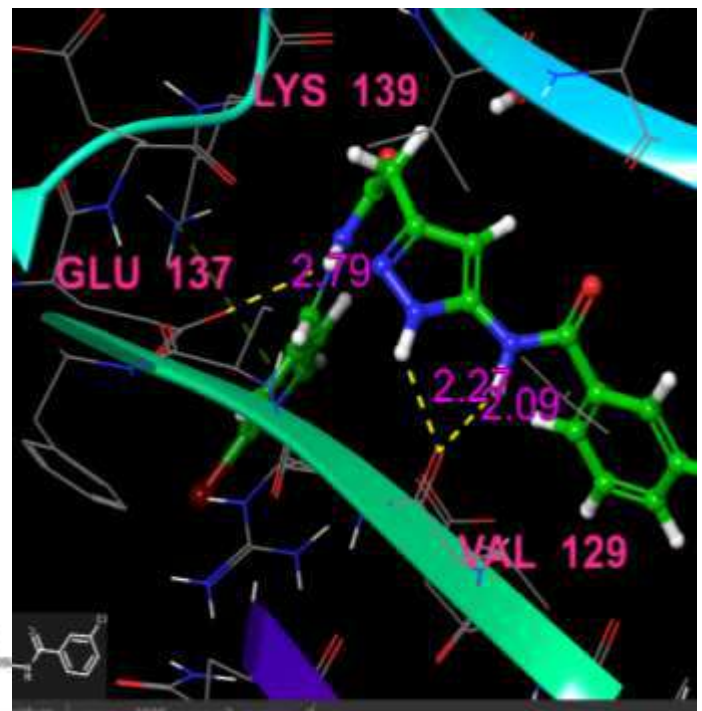
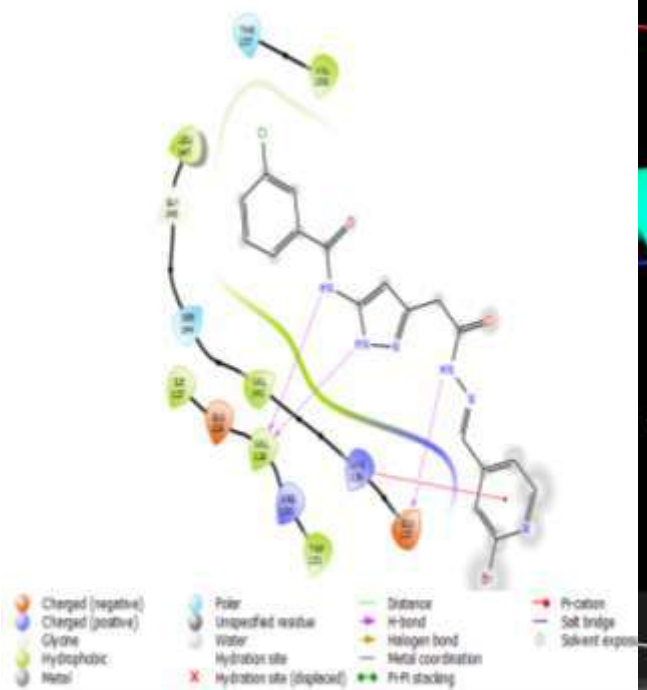


Figure 13: Compound 8n

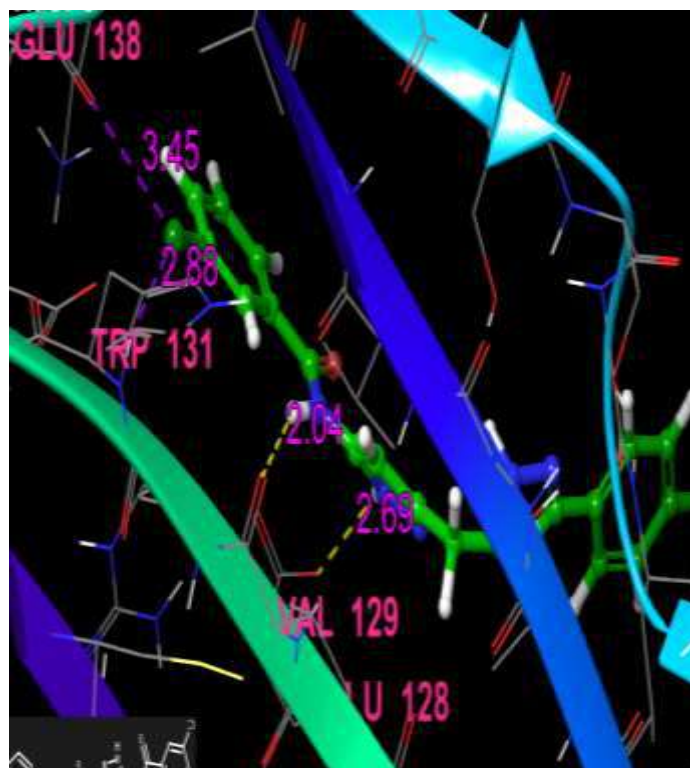
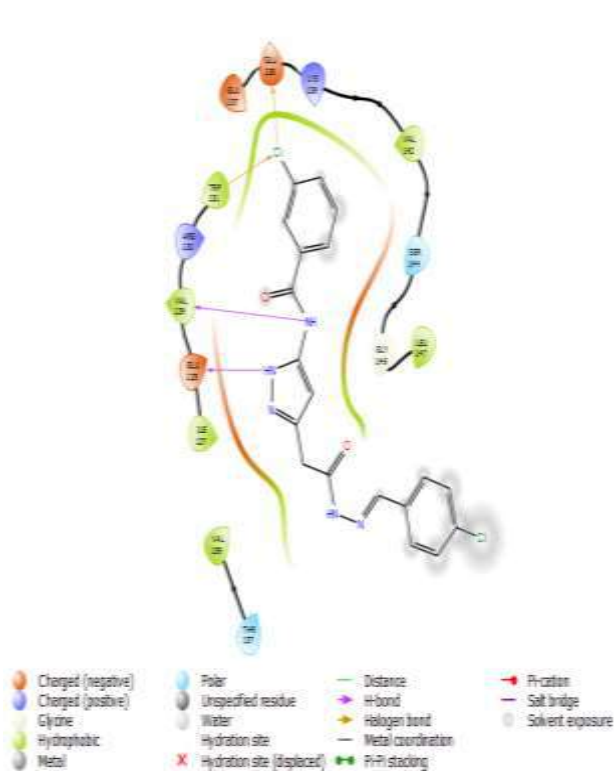


Figure 14: Compound 8c.

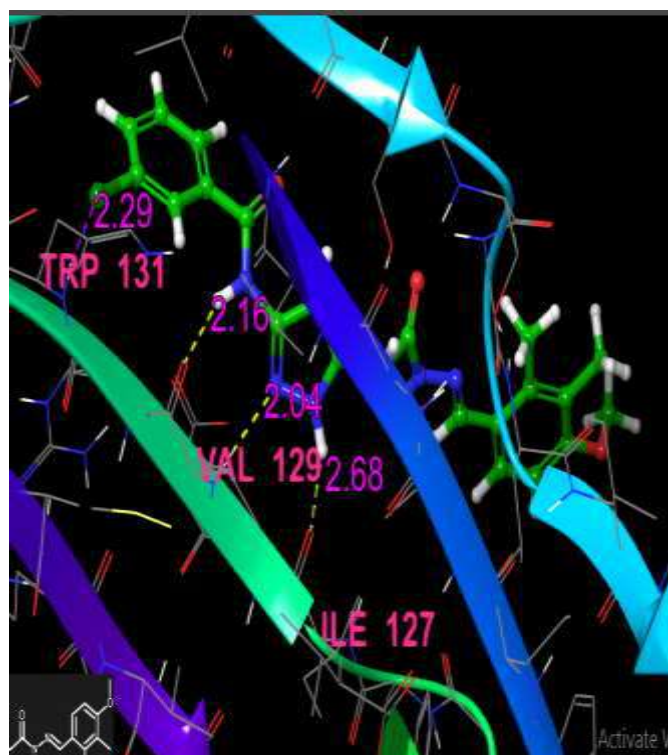
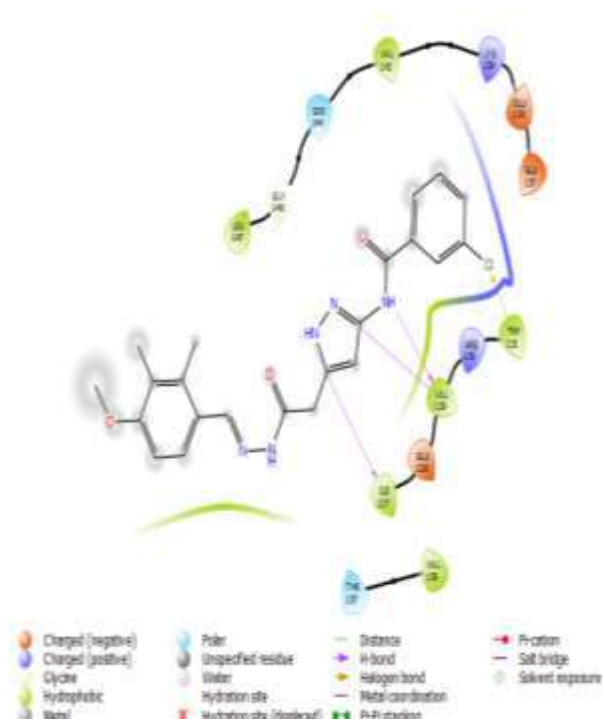


Figure 15: Compound 8d

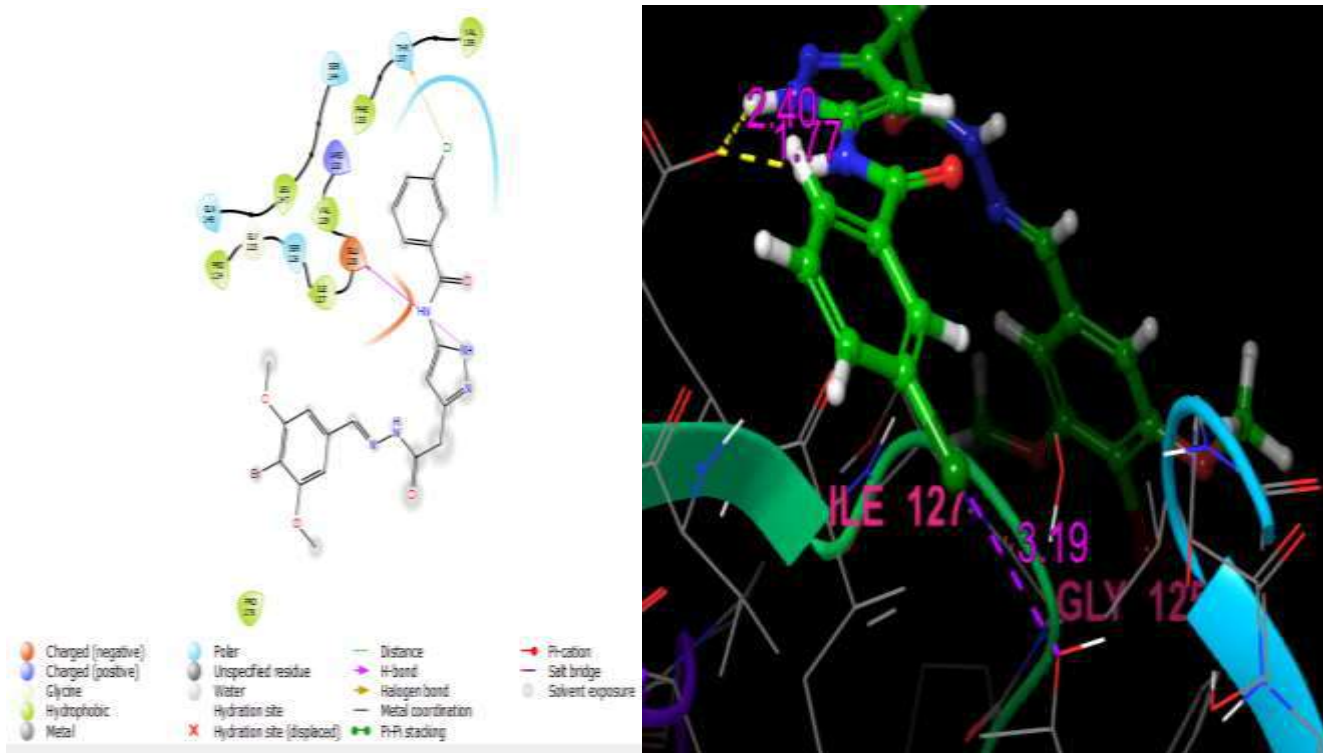


Figure 16: Compound 8e

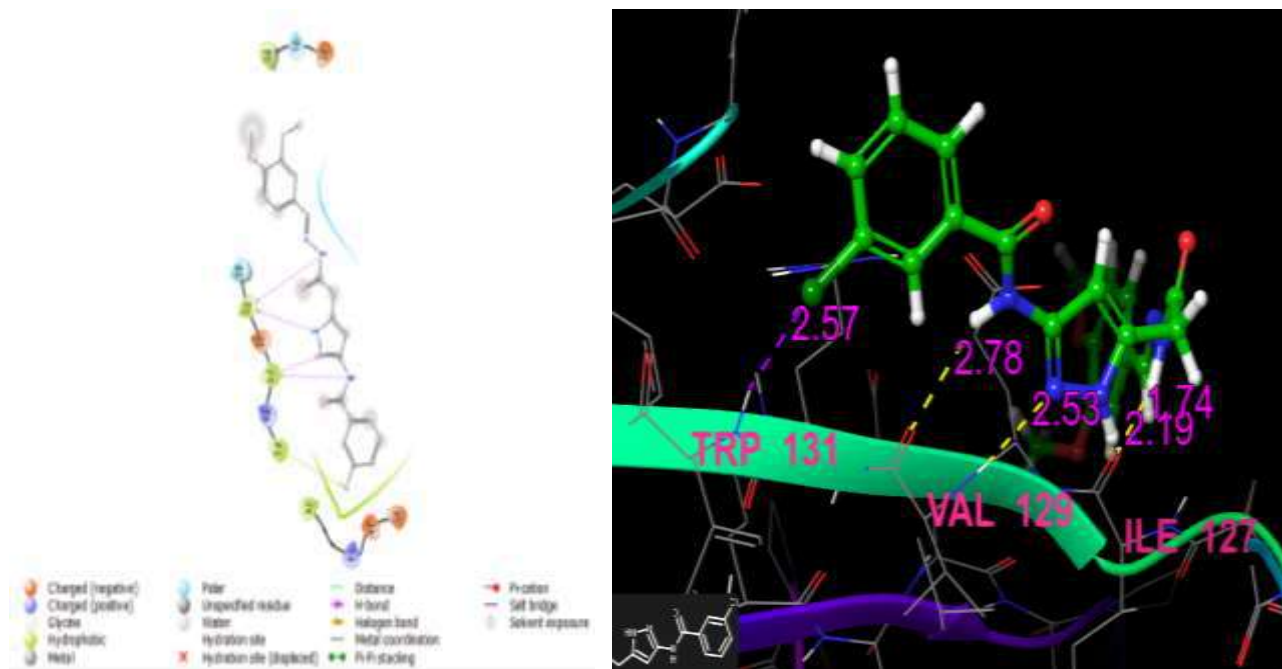


Figure 17: Compound 8q

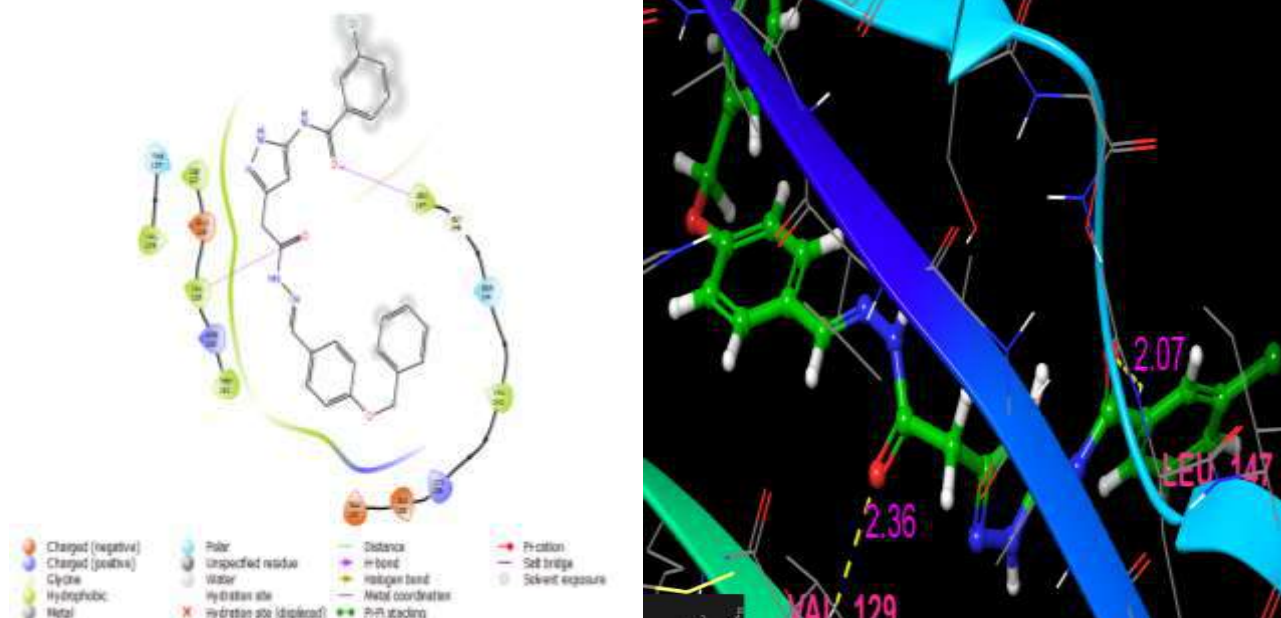


Figure 18: Compound 8p

## CONCLUSION

A sequence of novel pyrazole compound was prepared by a general synthetic method and molecular docking for the synthesized molecules was performed and found that **8g** and **8i** compounds are binds strongly with hydrogen bonds present in **GLU-128**, **ILE-127** and **VAL-129**, **THR-157**, **LEU-147** amino acid residues (**Figure 1-18**). The in silico molecular docking studies of synthesized pyrazole hydrazides shows that, almost all the synthesized compounds having therapeutic activities and among which, **8g** and **8i** having more ligand interactions when comparing with standard protein **8NIX**. With the help of Schrodinger software, an in vitro study of their **HLA class-II** inhibition for rheumatoid arthritis activity was performed and the research aim is to find more prospective lead compounds with a drug discovery system, in which molecular docking studies achieved the logical drug design.

## ACKNOWLEDGMENTS

Authors are thankful to Bioinformatics Infrastructure Facility Centre (BIFC), Queen Mary's College, Chennai. I am also thankful to Dr.R.Girija Co-Ordinator BIFC for their guidance and support. As a main author, it is my pleasure and covet to thank Dr.S.Aruna (My guide) for given me the opportunity to do Ph.D. under her supervising and further her help till completion of my Ph.D. Work.

## REFERENCES

- [1] Devendra Kumar, Vikramjeet judge, Rakesh Narang, Sonia Sangwan, Erik De clerq, Jan Balzarini, Balasubramanian Narasimhan, European journal of medicinal chemistry 2010, 45,2806-2816
- [2] Vikas Kumar, Ashok Kumar, Shalabh Sharma & Netra pal Singh, Indian journal of chemistry, 2011, 50B, 1496-1503
- [3] Kiran Bajaj, V K Srivastava and Ashok Kumar I, Indian journal of chemistry, 2003, 42, 1149-1155
- [4] Mittel Bach, Martin; Monat Shefte fur chemie, 1985, 116, 689-692
- [5] Brain E.Love and Jianhua Ren, Organic preparations and procedures international, 1999, 31, 399-405
- [6] V.Koteswara Rao, S.Subbha Reddy, B.Sathesh Krishna, Green chemistry letters and reviews, 2010, 3, 217-223
- [7] Swayansiddha Tripathy, Viswajanani j Sattigeri, S.K.Sahu, International journal of chemical and pharmaceutical review and research, 2015,1,6-9
- [8] Manisha R.Bhosle, Dayanand Kawale, D.Khillare, Amarsinh R.Deshmukh, Chemistry & Biology interface, 2017,7, 245-254
- [9] JC Sheehan, PA Cruickshank, GL Boshart, J.Org.Chem. 1961, 26, 2525
- [10] Shiori Tet.Lett, 1996, 37, 2261



- [11] C.A.G.N.Montalbetti and V.Falque, *Tetrahedron*, 2005, 61, 10827-10852
- [12] Paul J.Erdman, Jimmy L.Gosse, Jamey A.Jacobson & David E.Lewis, *synthetic communications*, 2004, 34, 1163-1171
- [13] S.Tumkevičius, V.Yakubkene, P.Vainilavicius, *Chemistry of heterocyclic compounds*, 1999, 35, 1334-1336
- [14] Ahmad Shaabani, Sayyed Emad Hoosahmand *Molecular diversity*, 2018, 22, 207-224
- [15] R.A. Carboni, D.D.Coffman and E.G. Howard, *J.Am.Chem.Soc*, 1958, 80, 2838-2840
- [16] M.Green and D.M.Throp, *J.chem.Soc.B.Phys.Org.*, 1967, 1067
- [17] Maria E.Due-Hansen, Sunil K.Pandey, Elisabeth Christiansen, Rikke Andersen, Steffen V.F.Hansen, Trond Ulvan, *Org.Bio-mol.Chem*, 2016, 14, 430-433
- [18] Vimal Bhat, S.D.Samant, Suhas Pednekar, *Letters in organic chemistry*, 2017, 14, 764-768
- [19] Eric Valeur, Mark Bradle, *chemical society reviews*, 2009, 38, 606-631
- [20] Moustafa A.Gouda, Maged A.Berghot, Ghada E.Abd El-Ghani, and Abd El-Galil M.khalil, *Journal of heterocyclic chemistry*, 2018, 55,1935-1941
- [21] Sabah Perveen, Hotam Singh Chaudhary, *Pharmacogn Mag*, 2015, 11 (Suppl 4): S550-S555
- [22] S Ekins, J Mestres and B Testa, *British journal of pharmacology*, 2007, 152 (1), 9-20
- [23] Bashir Lawal, Yen-Lin Liu, Ntlotlang Mokgautsi, Harshita Khedkar, Maryam Rachmawati Sumitra, Alexander T. H. Wu, Hsu-Shan Huang *Biomedicines*. 2021 Jan; 9(1): 92
- [24] Ah-Young Kim, Yi Na Yoon, Jiyeon Leem, Jee-Young Lee, Kwan-Young Jung, Minsung Kang, Jiyeon Ahn, Sang-Gu Hwang, Jeong Su Oh, Jae-Sung Kim  
*Front Oncol*. 2020; 10: 571601.
- [25]Anael Viana Pinto Alberto, Natiele Carla da Silva Ferreira, Rafael Ferreira Soares, Luiz Anastacio Alves, *Front Pharmacol*. 2020; 11: 01221.
- [26] Md. Sorwer Alam Parvez, Md. Adnan Karim, Mahmudul Hasan, Jomana Jaman, Ziaul Karim, Tohura Tahsin, Md. Nazmul Hasan, Mohammad Jakir Hosen, *Int J Biol Macromol*. 2020 Nov 15; 163: 1787–1797.
- [27] Zainab Ayaz, Bibi Zainab, Sajid Khan, Arshad Mehmood Abbasi, Mohamed S. Elshikh, Anum Munir, Abdullah Ahmed Al-Ghamdi, Amal H. Alajmi, Qasi D. Alsubaie, Abd El-Zaher M.A. Mustafa  
*Saudi J Biol Sci*. 2020 Sep; 27(9): 2444–2451
- [28] Kelton L. B. dos Santos, Jorddy N. Cruz, Luciane B. Silva, Ryan S. Ramos, Moysés F. A. Neto, Cleison C. Lobato, Sirlene S. B. Ota, Franco H. A. Leite, Rosivaldo S. Borges, Carlos H. T. P. da Silva, Joaquín M. Campos, Cleydson B. R. Santos, *Molecules*. 2020 Mar; 25(5): 1245
- [29] Mohd Javed Naim, Ozair Alam, Farah Nawaz, Md. Jahangir Alam, and Perwaiz Alam<sup>1</sup>*J Pharm Bioallied Sci*. 2016 Jan-Mar; 8(1): 2–17.
- [30] Khalid Karrouchi,<sup>1,2,3</sup> Smaail Radi,<sup>2,\*</sup> Youssef Ramli,<sup>1</sup> Jamal Taoufik,<sup>1</sup> Yahia N. Mabkhot,<sup>4,\*</sup> Faiz A. Al-aizari,<sup>4</sup> and Mohamed Ansari<sup>1</sup>*Molecules*. 2018 Jan; 23(1): 134.
- [31] "Front Matter". *Nomenclature of Organic Chemistry : IUPAC Recommendations and Preferred Names 2013 (Blue Book)*. Cambridge: The Royal Society of Chemistry. 2014. p. 141.
- [32] Schmidt, Andreas; Dreger, Andrij (2011). "Recent Advances in the Chemistry of Pyrazoles. Properties, Biological Activities, and Syntheses". *Curr. Org. Chem*. 15 (9): 1423–1463
- [33] A.M.VijeshArun M.IsloorbSandeepTelkarcT., ArulmolidHoong-KunFune, *Arabian Journal of Chemistry* Volume 6, Issue 2, April 2013, Pages 197-204
- [34] Arthington-Skaggs et al., 2000B.A. Arthington-Skaggs, M. Motley, D.W. Warnock, C.J. Morrison, Comparative evaluation of PASCO and National Committee for Clinical Laboratory Standards M27-A Broth Microdilution Method for Antifungal Drug Susceptibility Testing of Yeasts  
*J. Clin. Microbial.*, 38 (2000), pp. 2254-2260
- [35] Bekhita and Abdel-Aziem, 2004, A.A. Bekhita, T. Abdel-Aziem, Design, synthesis and biological evaluation of some pyrazole derivatives as anti-inflammatory-antimicrobial agents, *Bio-org. Med. Chem.*, 12 (2004), pp. 1935-1945

- [36] Moristal.,1998G.M. Moris, D.S. Goosell, R.S. Hallday, R. Huey, W.E. Hart, R.K. Blew, A.J. Olson, Automated docking using a Lamarckian genetic algorithm and an empirical binding free energy function, *J. Comput. Chem.*, 19 (1998), pp. 1639-1662
- [37] Sharma et al., 2010N.K. Sharma, K.K. Jha, Priyanka Molecular docking: an overview. *Adv. Sci. Res.*, 1 (2010), pp. 67-72
- [38] Yadav S, Pandey SK, Singh VK, Goel Y, Kumar A, Singh SM (2017) Molecular docking studies of 3-bromopyruvate and its derivatives to metabolic regulatory enzymes: Implication in designing of novel anticancer therapeutic strategies. *PLOS ONE* 12(5)
- [39] H. R. Umesh., K. V. Ramesh & K. S. Devaraju Beni-Suef University Journal of Basic and Applied Sciences volume 9, Article number: 5 (2020)
- [40] Gunasekar S., Saamanthi M., Aruna S. M; Synthesis and biological evaluations of new pyrazole hydrazides as potent anti-microbial agent; *Material today: Proceedings*. 45 (2021) 7132–7137

# Highly Efficient Base-Catalyzed Synthesis of Piperidine-4-Imine Lead Molecules For SARS-CoV-2 Mutant Spike Protease via In Silico Method

K.Sadhana<sup>1</sup>, M.Premalatha<sup>2</sup>, Dr. S. Aruna<sup>3\*</sup>, Sathiskumar Udayasan<sup>4</sup>, Dr. M.Saamanthi<sup>5</sup>

<sup>1</sup>Tamil Nadu Pollution Control Board, Maraimalainagar, Chengalpet.

<sup>4</sup>Adhi College of Engineering & Technology

<sup>2,3</sup> PG & Research Department of chemistry, Queen Mary's College, Chennai- 600004, India

Department of chemistry, Don Bosco College, Dharmapuri

DOI: 10.47750/pnr.2022.13.S09.448

## Abstract

For the discovery of drugs to SARS-CoV-2 pandemics, we have developed a new series of piperidine-4-imines as the central core owing to significant pharmaceutical demands on it. The synthesis of piperidine-4-imines involves a two-step base-catalyzed reaction, namely (i) condensations followed by cyclization with aromatic aldehyde, aliphatic ketone, and ammonia to yield piperidine-4-ketone core, and (ii) a simple Schiff base/piperidine-4-imines formation between piperidine-4-ketone and various aromatic primary amines. All the synthesized intermediate and target piperidine-4-imines molecular structures were well characterized by NMR, FT-IR, and mass spectral studies.

Further, the ground state geometry of synthesized molecules was optimized using density function theory (DFT) with basis set of b3lyp 6-31g (d,p) in Gaussian 09 program. Using this molecular geometry, we docked against SARS-CoV-2 mutant spike protease of delta, delta plus, and omicron, which shows an effective binding ability. In addition, Lipinski's rule, pre ADME and toxicity studies also reveal drug-likeness properties.

**Keywords:** Piperidine-4-imine, Base-catalyzed, SARS-Cov-2, Density functional theory, and Docking.

## 1. Introduction:

In 2019 onwards, the so-called term 'coronavirus' has transmitted very fast from human-to-human via aerosols and led to many sudden deaths from China, a city in Wuhan.<sup>[1,2]</sup> Later, this life-threatening corona viral disease gradually spread throughout the world. Therefore, global emergency was made on 11 Feb 2020 through the International Virus Classification Commission (ICTV) to categorize this new coronavirus as '2019-nCoV'. Meanwhile, the World Health Organization (WHO) also named the 2019-nCoV as 'COVID-19'.<sup>3</sup> The pandemic waves led to severe acute respiratory syndrome and other chronic illnesses to the affected human regardless of age. Later, the COVID-19 was resolved as 'severe acute respiratory syndrome coronavirus-2' (SARS-CoV-2).<sup>4</sup> An outbreak of the SARS-CoV-2 seems completely unable to stop or control because of the improper social distance all over the affected countries. Therefore, the pandemic distribution rate drastically increased by infected or asymptomatic patients via aerosols. Typically, symptoms of the SARS-CoV-2 include cough, fever, breathing difficulty, sore throat, diarrhea, headache, nausea, congestion, and loss of taste, leading to severe respiratory problems and finally to death.<sup>5,6</sup> Hence, the SARS-CoV-2 is now called a 'novel coronavirus'.<sup>7</sup> In SARS-CoV-2, the spike receptor protease plays a critical role, which facilitates the virus invasion on the human cell receptor (angiotensin converting enzyme-2, ACE2) and the host cell

receptor (transmembrane protease serine-2, TMPRSS2)<sup>8</sup>. Furthermore, the pandemic is quickly shifted to second waves of delta (variant B.1.617) and delta plus (variant 1.617.2), and then third waves of omicron (variant B.1.1.529)<sup>9,10,11</sup>. The WHO statistically reports that the global pandemic distribution rate is 53,75,91,764 confirmed cases as of 21 June 2022. Amongst them, 63,19,395 people have died in overall 223 countries. To overcome this situation, several researchers have suggested some of the repurposing small-molecule based antiviral drugs such as Remdesivir<sup>12</sup>, hydroxychloroquine<sup>13</sup>, favipiravir<sup>14</sup>, pirfenidone<sup>15</sup>, and lopinavir/ritonavir<sup>16</sup> for the effective treatment of SARS CoV-2 and its mutations. Unexpectedly, none of these drugs could effectively cure the completely. Also, they cause several side effects on post-COVID-19 treatment. Hence, the development of potential drugs is highly warranted.

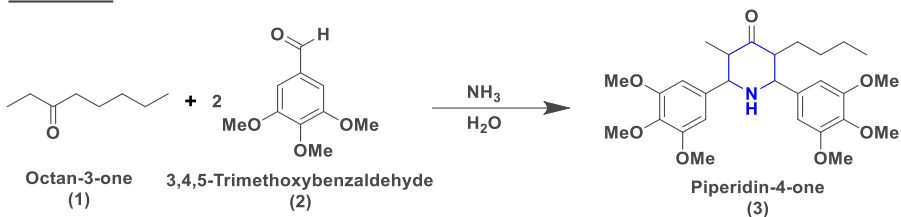
In our drug discovery program, we focused on piperidine-4-imines, which are naturally occurring bioactive compounds and having two nitrogen atoms including exocyclic imines. They possess significant biological properties for acting as anti-viral,<sup>17</sup> anti-microbial,<sup>18</sup> anti-inflammatory,<sup>19</sup> anti-cancer,<sup>20</sup> and anti-anxiety<sup>21</sup> agents. Among the piperidine-4-imines, N-benzhydrylpiperidine-4-amine derivatives exhibit a promising class of interest to anti-microbial (*Bacillus subtilis*, *Escherichia coli*, *Klebsiella pneumonia*, and *Streptococcus aureus*)<sup>21</sup> and anti-fungal activities (*Aspergillus niger*, *Aspergillus flavus*, and fungi).<sup>22</sup> A series of novel piperidine-4-imine derivatives show anti-tubercular agents against *Mycobacterium tuberculosis* H37Rv.<sup>23</sup> Similarly, Ghosh et al. developed a nitrogen-containing five-membered ring with chloropyridinyl derivatives for SARS-CoV-2.<sup>24</sup> Very recently, Pfizer have developed a nitrogen heterocyclic drug to inhibit the coronavirus 3CL protease for the potential treatment of COVID-19.<sup>25</sup>

Indeed, there is no selective anti-viral drug discovered against SARS-CoV-2 and its various mutations so far. This accelerates us to develop a novel and potential piperidine-4-imine-based anti-viral compounds for SARS CoV-2, delta, delta plus, and omicron. The synthesized lead molecules undergone complete experimental spectroscopic investigations such as FT-IR, NMR, and mass spectral analyses. Also, theoretical computations DFT/B3LYP method and 6-31g (d, p) basis set were used to optimize the ground state structures. Finally, the binding ability of the lead molecules was determined using Autodock Vina. In addition, the drug-likeness properties were calculated by online preADME software.

## 2. Results and discussion:

Here, we have synthesized a series of novel piperidine-4-imines via two-step reactions as shown in **Fig. 1**. Initially, a classical multi-component reaction of Petrenko-Kritschenko piperidin-4-one synthesis involved a ring-condensation of octan-3-one (**1**), 3,4,5-trimethoxy benzaldehyde (**2**) and ammonia in water medium to yield 88% as solid. Later, the synthesized piperidin-4-one precursor reacts with substituted aromatic primary amines offering a novel piperidin-4-ones as solid with 78% yield. The overall products were obtained in the range of 65 to 75% yields.

### Scheme-1



### Scheme-2

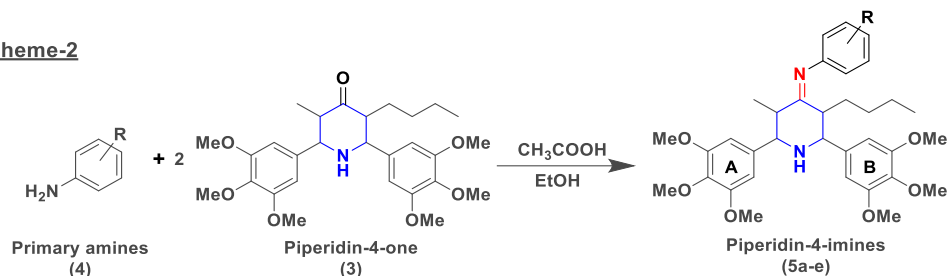


**Fig. 1. Synthesis of piperidin-4-imines**

Using piperidin-4-one, five piperidin-4-imines (**5a-e**) have been synthesized as shown in **Chart 1**. All the synthesized compounds and precursor molecular structures were well characterized by HR-MS, NMR, and FT-IR spectroscopic data.

### 3. Density Functional Theory

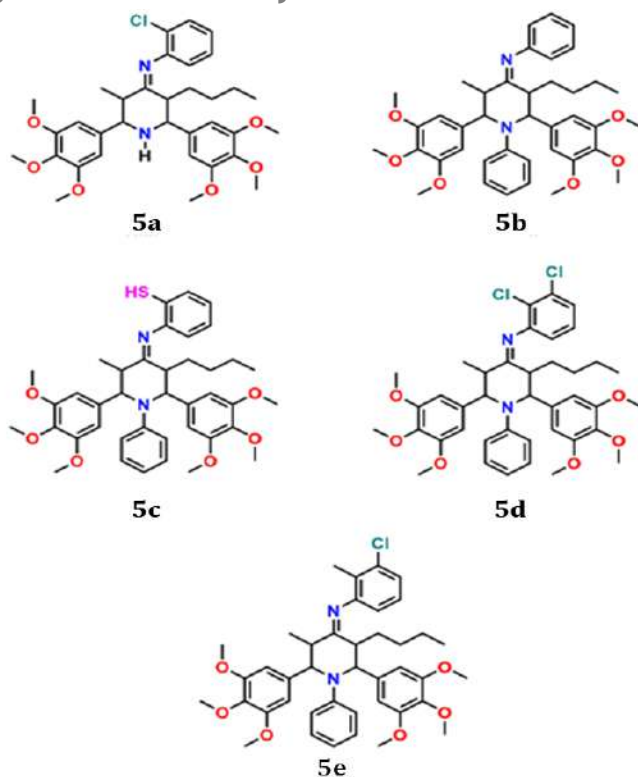


**Chart 1. Molecular structure of Piperidin-4-imines (5a-e).**

For the synthesized molecules, the ground state structures were optimized by density functional theory with basis set of b3lyp 6-31g (d,p) in Gaussian 09 program.<sup>26,27</sup> Using this theory, electronic transitions, and the charge transfers in molecular systems, frontier molecule orbitals (FMOs) are calculated as shown in Fig.2.

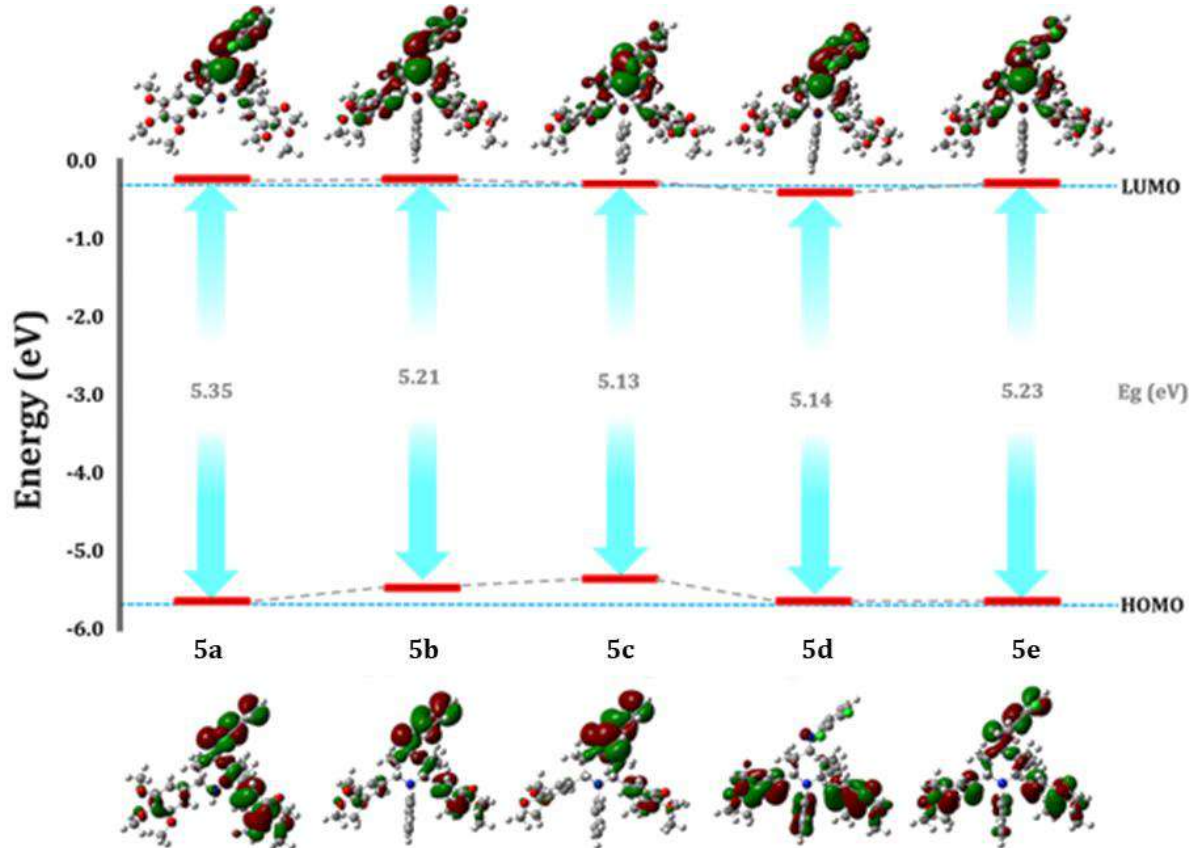


Fig. 2. DFT-optimized Frontier molecular orbitals and HOMO-LUMO energy gaps for Piperidine-4-imines (5a-e).

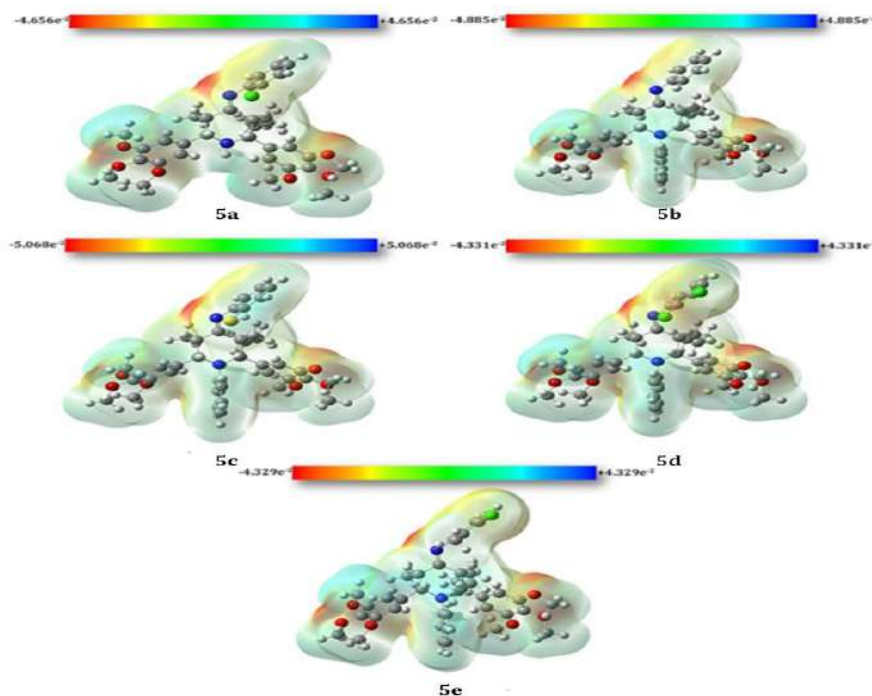
Based on the highest occupied molecular orbital (HOMO) and the lowest unoccupied molecular orbital (LUMO) energy values, some quantum mechanical descriptors such as energy band gap energy ( $E_{\text{HOMO}}-E_{\text{LUMO}}$ ), ionization potential ( $I=-E_{\text{HOMO}}$ ), electron affinity ( $A=-E_{\text{LUMO}}$ ), chemical hardness ( $\eta= (I-A)/2$ ), chemical softness ( $\zeta=1/2\eta$ ), electronegativity ( $\chi=(I+ A)/2$ ), chemical potential ( $\mu=- (I+A)/2$ ), electrophilicity index ( $\omega=\mu^2/2\eta$ ), and maximum charge transfer index ( $\Delta N_{\text{max.}}=-\mu/\eta$ ) for the compounds **5a-c** were calculated and summarized in Table 1.

Table 1. Energy band gap values and other quantum mechanical descriptors of the compounds 5a-e.

Quantum mechanical descriptors (eV)	5a	5b	5c	5d	5e
Band gap energy ( $E_{\text{HOMO}}-E_{\text{LUMO}}$ )	5.35	5.21	5.13	5.14	5.23
Ionization potential ( $I=-E_{\text{HOMO}}$ )	5.65	5.63	5.43	5.64	5.51
Electron affinity ( $A=-E_{\text{LUMO}}$ ),	0.39	0.45	0.40	0.58	0.30
Chemical hardness ( $\eta= (I-A)/2$ )	2.63	2.59	2.51	2.53	2.60
Chemical softness ( $\zeta=1/2\eta$ )	0.19	0.19	0.20	0.20	0.19

Electronegativity ( $\chi=(I+A)/2$ ),	3.02	3.04	2.91	3.11	2.90
Chemical potential ( $\mu=-(I+A)/2$ )	-3.02	-3.04	-2.91	-3.11	-2.90
Electrophilicity index ( $\omega=\mu^2/2\eta$ )	1.73	1.78	1.68	1.91	1.61
Maximum charge transfer index ( $\Delta N_{max.}=-\mu/\eta$ )	1.14	1.17	1.15	1.22	1.11

The molecular electrostatic potential (MEP) is a highly important descriptor to understand the electrophilic and nucleophilic sites in molecular structure. In MEP mapping system, six different colors are observed, such as red, orange, yellow, green, cyan, and blue. The red colour of map is the highly electron-rich region, while the blue colour is the extremely poor electron or electron-deficient region of the molecule. The decreasing order of electrostatic potential colour is blue > cyan > green > yellow > orange > red. The observed negative sites to positive electrostatic potential values are  $-4.656e^{-2}$  and  $+4.656e^{-2}$  for **5a**;  $-4.885e^{-2}$  and  $+4.885e^{-2}$  for **5b**;  $-5.068e^{-2}$  and  $+5.068e^{-2}$  for **5c**;  $-4.331e^{-2}$  and  $+4.331e^{-2}$  for **5d**; and  $-4.329e^{-2}$  and  $+4.329e^{-2}$  for **5e** compounds with B3LYP functional and 6-31g (d,p) basis set as illustrated in **Fig. 3**.



**Fig. 3.** The MEP surfaces of Piperidin-4-imines (**5a-e**).

In the present study, the negative regions are concentrated over the methoxy groups and imine moiety for all the compounds; on the other hand, the positive regions are located over hydrogen atoms in the alkyl chains and phenyl moieties. The obtained results clearly suggested that the high electronegativity of the methoxy moieties and imine units makes it the most reactive part of the all compounds for docking studies.

#### 4. Structure of the SARS-CoV-2

The SARS-CoV-2 belongs to a spherical  $\beta$ -coronavirus family and also pleomorphic in nature. The coronavirus structure<sup>28</sup> is composed of the following structural fragments, viz. (i) spike proteins (S), (ii) membrane proteins (M), (iii) envelope proteins (E), (iv) nucleocapsid (N), and (v) hemagglutinin-esterase dimer (HE) glycoproteins along with

RNA as genetic material. As shown in **Fig.4**. The ‘S’ protein peripheral surface sites resemble a crown shape in an electron microscope. The SARS-CoV-2 nucleotide is resembled as 80, 55, and 50% homolog to SARS-CoV-1, MERS, and common cold CoV, respectively.

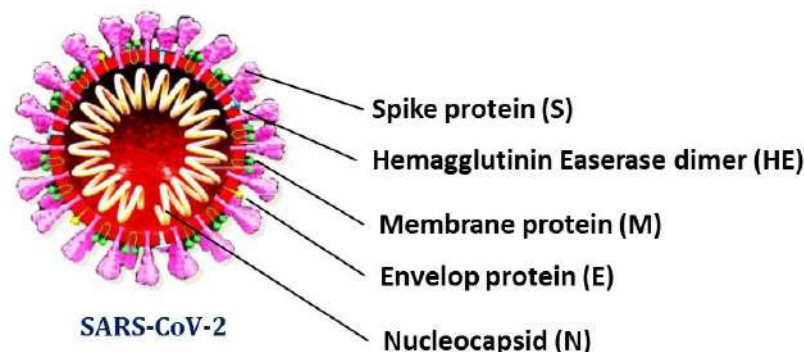


**Fig. 4. Structure of SARS-CoV-2.**

### The SARS-CoV-2 spike protease’s mechanistic action against the human cell

A brief mechanistic pathway of the SARS CoV-2 ‘S’ protein against humans is facilitated by the ACE2 biomolecule, which acts as a human entry receptor. Based on the sequence alignment results, the spike-receptor binding domain (RBD) sequences of the SARS-CoV-2 and the SARS-CoV are 76% analogous. Therefore, the SARS-CoV-2 easily binds to the ACE2 receptor. However, the pathogenic causing SARS-CoV-2 virus can be prevented by many pathways as follows: (i) the target viral enzyme proteins act as a blocker for virus RNA synthesis and replication, (ii) preventing viral entry to human cell ACE2 receptors; (iii) some of the virulence elements are generated to restore the innate host immunity, and (iv) specific receptors present in the host may prevent the virus entry into the host cells. The interactions between the virus and host cells that ACE2 binding site of antiviral drugs molecular design have to stop the ‘S’ protein physicochemical activities. Otherwise, TMPRSS2 protease, neuropilin-1, and interfaces of heptad repeat-1 and heptad repeat-2 domains might be in critical state. Thus, the molecular protein biology relationship is strongly limited in the beginning stage to prevent the novel coronavirus and its mutations.

### 5. Molecular docking study

In the modern drug discovery programs, molecular docking analysis of small molecules in the protein or receptor binding sites is carried out by computational technique. Herein, four different kinds of receptors of SARS CoV-2 (6lu7 protease) and its mutations (delta variant; 7w92 protease, delta plus variant; 7nx7 glycoprotease, and omicron; 7s0b protease) were used in molecular docking studies through AutoDock Vina software program<sup>29</sup> as shown in **Table 2**.

**Table 2. Molecular docking scores of piperidin-4-imines(5a-e) for SARS CoV-2 and its mutation proteases**

Compound	6lu7 protease		7w92 protease		7nx7glycoprotease		7s0b	
	Binding energy (kcal/mol)	Inhibition constant (μM)	Binding energy (kcal/mol)	Inhibition constant (μM)	Binding energy (kcal/mol)	Inhibition constant (μM)	Binding energy (kcal/mol)	Inhibition constant (μM)
<b>5a</b>	<b>-6.6</b>	<b>14.3482</b>	-6.2	28.2048	-5.9	46.8241	<b>-6.6</b>	<b>14.3482</b>
<b>5b</b>	-6.1	33.3969	-6.2	28.2048	-5.6	77.7347	-6.5	16.9894
<b>5c</b>	-5.8	55.4436	-6.0	39.5446	-6.2	28.2048	-5.9	46.8241
<b>5d</b>	-6.4	20.1168	<b>-6.3</b>	<b>23.8200</b>	-6.2	28.2048	-6.4	20.1168
<b>5e</b>	-6.2	28.2048	<b>-6.3</b>	<b>23.8200</b>	<b>-6.4</b>	<b>20.1168</b>	-6.5	16.9894



In molecular docking analysis, nine different poses were obtained for **5a-e** compounds. The obtained root mean square deviation lower bound and upper bound values are  $2 \text{ \AA}$  nearly; hence, the value is agreeable and reliable in molecular docking studies (SI). Furthermore, the inhibition constants were determined using  $K_i = \exp(\Delta G/RT)$  equation for **5a-e** compounds, where  $\Delta G$ ,  $R$ , and  $T$  are the docking binding energy, gas constant ( $1.9872036 \times 10^3 \text{ kcal/mol}$ ), and room temperature ( $298.15 \text{ K}$ ), respectively. All the covalent and non-covalent bonding interactions (SI, Table 1) for the protein 6lu7 protease, 7w92 protease, 7nx7 glucoprotease, and 7s0b protease were determined for Piperidin-4-imines (**5a-e**).

As can be seen in **Table 2**, the highest molecular docking score having SARS CoV-2 and its mutations of 2D and 3D protein-lead molecular interactions graphics are shown in **Fig. 4**.

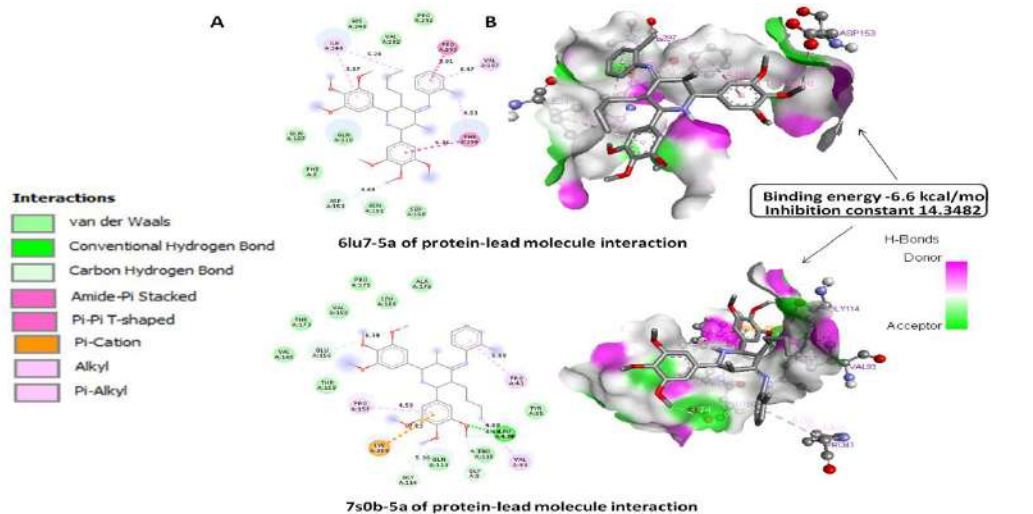


**Fig 4(i) 6lu7 & 7s0b protein-lead molecule interaction of 5a**

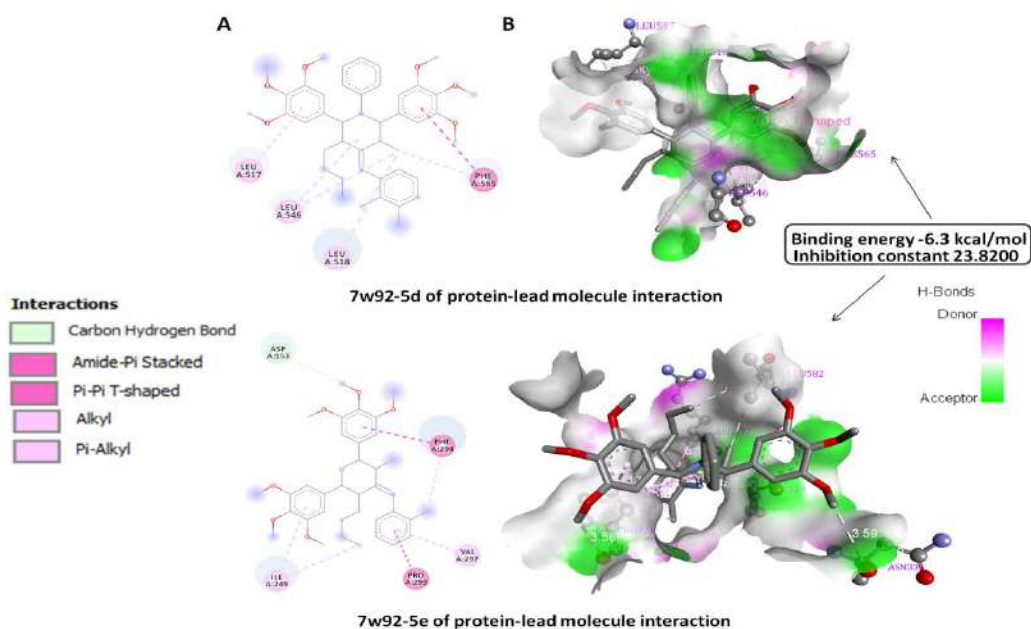


Fig 4(ii) 7w92 protein-lead molecule interactions of 5d and 5e

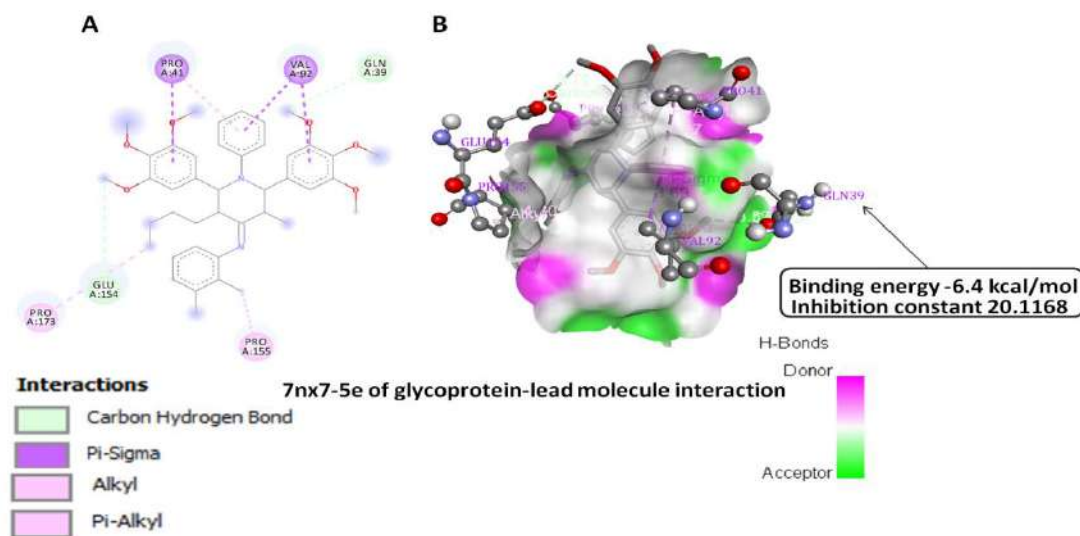


Fig 4(iii) 7nx7 protein-lead molecule interactions of 5e

The best affinity binding energy was calculated for **5a** [Fig-4(i)] compound against **6lu7 protease** as -6.6 kcal/mol with a corresponding inhibition constant of 14.3482  $\mu$ M. (i). One carbon hydrogen bond with a distance of 3.78 Å was observed between H-donor of -OCH<sub>3</sub> and H-acceptor of ASP153 amino acid residue. (ii). Two  $\pi$ -hydrophobic interactions, such as  $\pi$ - $\pi$  T-shaped and amide- $\pi$  stacked, were observed with distance of 4.99 (between  $\pi$ -orbital of trimethoxy substituted 'A' phenyl ring and of  $\pi$ -orbital of PHE294 amino acid) and 4.03 Å (between amide carbonyl carbon [PRO294:Carboxylic acid residue and PHE294:Amide amino acid residue]), respectively. (iii). One alkyhydrophobic interaction with a distance of 4.7 Å between long alkyl chain of butyl group and branched alkyl chain of ILE249 residue. (iv). Four  $\pi$ -alkyl interactions between (a)  $\pi$ -orbital of trimethoxy substituted 'B' phenyl ring and branched alkyl chain of ILE249 amino acid residue (bond distance: 5.22 Å), (b)  $\pi$ -orbital of PHE294 amino acid residue and chlorophenyl moiety (4.86 Å), (c)  $\pi$ -orbital of chlorophenyl and cyclic alkyl chain of PRO293 amino acid residue (5.48 Å), and (d)  $\pi$ -orbital of chlorophenyl and branched alkyl chain of VAL297 amino acid residue (4.91 Å).

In the case of **7w92 protease**, **5d** and **5e** [Fig.4(ii)] exhibit good potentials and also identical affinity binding energy and (-6.3 kcal/mol) with an inhibition constant of 23.8200  $\mu$ M than that of **5a** (-6.2 kcal/mol, and 28.2048  $\mu$ M), **5c** (-6.0 kcal/mol, and 39.5446  $\mu$ M), and **5e** (-6.2 kcal/mol and 28.2048  $\mu$ M) compounds. The **5d** compounds have one  $\pi$ - $\pi$  T-shaped, three alky-alkyl, and two  $\pi$ -alkyl interactions. For example, (i) the  $\pi$ - $\pi$  T-shaped alky-alkyl has a bond distance of 4.93 Å between  $\pi$ -orbital of trimethoxy substituted 'A' phenyl ring and  $\pi$ -orbital of PHE565 amino acid residue. (ii) Three alky-alkyl interactions have a bond distance of 5.17 (between methyl moiety of piperidine and branched alkyl chain of LEU518 amino acid residue), 5.08 (between methyl moiety of piperidine and branched alkyl chain of LEU546 amino acid residue), and 4.85 Å (between branched alkyl chain of LEU546 amino acid residue and cyclic piperidine chain). (iii) Two  $\pi$ -alkyl interactions consist of a bond distance of 5.32 Å (between  $\pi$ -orbital of trimethoxy substituted 'B' phenyl ring and branched alkyl chain LEU517 amino acid residue) and 4.11 Å (between  $\pi$ -orbital of PHE565 amino acid residue and methyl moiety of piperidine unit).

Similarly, (i) the **5e** compounds have three carbon hydrogen bonds with distance of 3.59 (between H-donor of -OCH<sub>3</sub> group and H-acceptor of carbonyl oxygen ASN331 amino acid residue), 3.58 (between H-donor of -OCH<sub>3</sub> group and H-acceptor of carbonyl oxygen PRO521 residue), and 3.54 Å (between H-donor of PRO579 amino acid residue and H-acceptor of imine nitrogen moiety). Also, (ii) the **5e** compounds contain four alky-hydrophobic

interactions between, such as (a) methyl chain of piperidine and branched alkyl chain of LEU582 amino acid residue (bond distance: 4.95 Å), (b) linear butyl chain of piperidine and branched alkyl chain of LEU582 amino acid residue (bond distance: 4.58 Å), (c) branched alkyl chain of PRO521 amino acid residue and methyl moiety of chloromethylphenyl unit (4.38 Å), and (d) methyl moiety of chloromethylphenyl unit and cyclic piperidine unit (5.36 Å). Additionally, (iii) the **5e** compounds have three  $\pi$ -alkyl interactions, namely (a)  $\pi$ -orbital of chloromethylphenyl moiety and linear alkyl chain of ARG577 amino acid residue (5.16 Å), (b)  $\pi$ -orbital of chloromethylphenyl moiety and cyclic alkyl chain of PRO521 amino acid residue (5.04 Å), and (c)  $\pi$ -orbital of trimethoxy substituted 'B' phenyl ring and cyclic alkyl chain of PRO521 amino acid residue (bond distance: 4.15 Å).

For **7nx7glycoprotease**, the **5e**[Fig-4(iii)] compound show better affinity binding score of -6.4 kcal/mole with 20.1168  $\mu$ M inhibition constant due to two carbon hydrogen bonds, two alkyl-alkyl hydrophobic, three  $\pi$ - $\sigma$  hydrophobic, and one  $\pi$ -alkyl hydrophobic interactions. For example, (i) two carbon hydrogen bonds have a bond distance of 3.72 (between H-donor of methoxy moiety from 'B' ring and carbonyl oxygen moiety of GLU154 amino acid residue) and 3.57 Å (between H-donor of methoxy moiety from 'A' ring and carbonyl oxygen moiety of amide carbonyl oxygen moiety of GLN39 amino acid residue), (ii) two alkyl-alkyl hydrophobic interactions with a bond distance of 4.80 (between methyl moiety of chloromethylphenyl ring and cyclic alkyl chain of PRO155 amino acid residue) and 4.39 Å (between linear butyl chain of piperidine moiety and cyclic alkyl chain of PRO173 amino acid residue), (iii) three  $\pi$ - $\sigma$  hydrophobic interactions with a bond distance of 3.85 (between cyclic CH moiety of PRO41 amino acid residue and  $\pi$ -orbital of trimethoxy substituted 'B' phenyl ring), 3.71 (between open chain CH moiety of VAL92 amino acid residue and  $\pi$ -orbital of trimethoxy substituted 'A' phenyl ring) and 3.69 Å and (iv) one  $\pi$ -alkyl hydrophobic interaction of a bond distance of 4.46 Å (between cyclic alkyl chain of PRO41 amino acid residue and  $\pi$ -orbital of N-phenyl moiety).

Likewise, the **5a** compounds exhibit the best affinity binding score of -6.6 kcal/mole with a 14.3482  $\mu$ M inhibition constant against **omicron 7s0b protease**. For example, one hydrogen bonding interaction of a distance of 1.91 Å between H-Donor of LEU116:HN amino acid residue and H-Acceptor of trimethoxy substituted 'B' phenyl ring, two electrostatic interaction of a  $\pi$ -cation with a bond distance of 4.56 (between positive charge of LYS209:NZ amino acid residue and  $\pi$ -orbital of trimethoxy substituted 'A' phenyl ring) and a  $\pi$ -anion with a bond distance of 4.19 Å (between negative charge of A:GLU156:OE<sub>2</sub> amino acid residue and  $\pi$ -orbital of chlorophenyl ring), and two  $\pi$ -alkyl interactions with distance of 5.01 (between  $\pi$ -orbital of chlorophenyl ring and cyclic alkyl chain of PRO41 amino acid residue) and 4.96 Å (between  $\pi$ -orbital of trimethoxy substituted 'A' phenyl ring and cyclic alkyl chain of PRO157 amino acid residue).

## 6. Drug-likeness properties

The drug-likeness properties were analyzed by molinspiration servers where Lipinski's rule states that orally active drug must satisfy the following five criteria: (i) molecular weight, (ii) log, (iii) hydrogen bond donor, (iv) hydrogen bond acceptor, and (v) total polar surface area for the synthesis piperidine-4-imines of **5a-e** as depicted in **Table 3**.

**Table 3.** The drug-likeness properties of piperidine-4-imines of **5a-e**.

Piperidin-4-imines	<sup>a</sup> MW (<500Da)	<sup>b</sup> LogP (<5.6)	<sup>c</sup> HBD (<5)	<sup>d</sup> HBA (<10)	<sup>e</sup> TPSA (<140Å)
5a	611.18	7.71	1	8	79.80
5b	701.30	9.12	0	8	71.01
5c	684.90	8.79	0	8	71.01
5d	721.72	9.19	0	8	71.01
5e	652.83	8.70	0	8	71.01

<sup>a</sup>MW—Molecular weight, <sup>b</sup>LogP—octanol/water partition coefficient,

<sup>e</sup>HBD—Hydrogen bond donor, <sup>d</sup>HBA—Hydrogen bond acceptor, and e  
TPSA—Total polar surface area.

An orally active drug has to satisfy Lipinski's rule without violation of the following standards: (i) the lipophilicity or octanol/water partition coefficient (LogP) of a molecule should not be greater than 5, (ii) molecular weight of the compound must be 500 Da, (iii) the hydrogen bond donor should not be more than 5 and hydrogen bond acceptor should not be more than 10, and (iv) the total molecular polar surface must be greater or equal 140 Å. The addition of an oral drug can be absorbed TPSA value when it is greater than 60 Å. Hydrogen bonding correlation is significant for the bioactivity of **5a-e** piperidin-4-imines. The above obtained results clearly suggest that the designed and synthesized lead molecule violates molecular weight and LogP values alone. Also, Lipinski's rule does not predict if these compounds are pharmacologically active. Therefore, these lead molecules may have better change to use in the invitro level analysis for SARS CoV-2 and its mutations.

## 7. Spectral data of compounds 5a-5e

### 7.1(Z)-3-butyl-N-(2-chlorophenyl)-5-methyl-2,6-bis(3,4,5-trimethoxyphenyl)piperidin-4-imine (5a)

Yield: 78%; m.p: 173–174°C, IR (KBr) (cm<sup>-1</sup>): 3302 (N-H stretching), 2933 (aromatic C-H stretching), 1697 (C=C stretching), 1590 (N-H bending) 1342 (C-O stretching), 1231 (C-N stretching), 827 (C-Cl stretching), 707 (C-H out of plan bending), 675 (N-H wagging). <sup>1</sup>H NMR(400MHz,DMSO):δ7.02(m,ArH),3.7(s,OCH<sub>3</sub>),2.83.0(m,CH<sub>2</sub>),2.6(s,NH),0.8(t,CH<sub>3</sub>). <sup>13</sup>CNMR(400MHz,DMSO):11.34,14.36,22.63,29.80,39.34,40.18,51.71,72.14,105.55,137.15,153.13,210.85.

### 7.2(Z)-3-butyl-5-Methyl-N,1-diphenyl-2,6-bis(3,4,5-trimethoxyphenyl)piperidin-4-imine(5b)

Yield: 72%; m.p: 171–175°C, IR (KBr) (cm<sup>-1</sup>): 3310 (N-H stretching), 2937 (aromatic C-H stretching), 1698 (C=C stretching), 1592 (N-H bending) 1341 (C-O stretching), 1234 (C-N stretching), 828 (C-Cl stretching), 709 (C-H out of plan bending), 676 (N-H wagging). <sup>1</sup>H NMR(400MHz,DMSO):7.01(m,ArH),3.08(s,OCH<sub>3</sub>),2.81.0(m,CH<sub>2</sub>),2.03(s,NH),0.81(t,CH<sub>3</sub>). <sup>13</sup>CNMR(400MHz,DM SO):11.35,14.46,21.63,22.80,40.34,41.18,52.71,72.14,105.55,138.15,153.55,210.87.

### 7.3(Z)-2-((3-butyl-5-methyl-1-phenyl-2,6-bis(3,4,5-trimethoxyphenyl)piperidin-4-ylidene)amino)benzenethiol(5c)

Yield: 69%; m.p: 176–179°C, IR (KBr) (cm<sup>-1</sup>): 3311 (N-H stretching), 2933 (aromatic C-H stretching), 1694 (C=C stretching), 1591 (N-H bending) 1342 (C-O stretching), 1233 (C-N stretching), 827 (C-Cl stretching), 706 (C-H out of plan bending), 677 (N-H wagging). <sup>1</sup>H NMR(400MHz,DMSO):7.03(m,ArH),3.09(s,OCH<sub>3</sub>),2.82.0(m,CH<sub>2</sub>),2.04(s,NH),0.82(t,CH<sub>3</sub>). <sup>13</sup>CNMR(400MHz,DM SO):11.36,14.47,21.64,22.81,40.32,41.17,52.72,72.13,105.56,138.16,153.57,210.88.

### 7.4(Z)-3-butyl-N-(2,3-dichlorophenyl)-5-methyl-1-phenyl-2,6-bis(3,4,5-trimethoxyphenyl)piperidin-4-imine(5d)

Yield: 68%; m.p: 171–173°C, IR (KBr) (cm<sup>-1</sup>): 3314 (N-H stretching), 2931 (aromatic C-H stretching), 1695 (C=C stretching), 1593 (N-H bending) 1343 (C-O stretching), 1234 (C-N stretching), 828 (C-Cl stretching), 707 (C-H out of plan bending), 674 (N-H wagging). <sup>1</sup>H NMR(400MHz,DMSO):7.05(m,ArH),3.04(s,OCH<sub>3</sub>),2.81.0(m,CH<sub>2</sub>),2.08(s,NH),0.83(t,CH<sub>3</sub>). <sup>13</sup>CNMR(400MHz,DM SO):11.32,14.41,21.64,22.83,40.33,41.14,52.75,72.14,105.57,138.17,153.54,210.81.

### 7.5(Z)-3-butyl-N-(3-chloro-2-methylphenyl)-5-methyl-1-phenyl-2,6-bis(3,4,5-trimethoxyphenyl)piperidin-4-imine(5e)

Yield: 74%; m.p: 178–180°C, IR (KBr) (cm<sup>-1</sup>): 3311 (N-H stretching), 2934 (aromatic C-H stretching), 1692 (C=C stretching), 1595 (N-H bending) 1341 (C-O stretching), 1233 (C-N stretching), 821 (C-Cl stretching), 708 (C-H out of plane bending), 675 (N-H wagging). <sup>1</sup>H NMR(400MHz,DMSO):7.04(m,ArH),3.01(s,OCH<sub>3</sub>),2.82.0(m,CH<sub>2</sub>),2.01(s,NH),0.85(t,CH<sub>3</sub>).<sup>13</sup>CNMR(400MHz,DM SO):11.31,14.42,21.61,22.87,40.31,41.15,52.77,72.11,105.58,138.18,153.51,210.83.

## 8. Conclusion

In this summary, we would conclude that we have successfully synthesized 5 piperidin-4-imines compounds by condensation and cyclisation of aldehyde and ketone by following the Schiff base method. The electronic configuration of HOMO and LUMO had revealed that methoxy and imine units are the most reactive parts of the synthesized compounds. Similarly, molecular docking studies of SARS CoV-2 receptors and its four protease (6lu7, 7w92, tnx7 and 7s0b) were calculated for title compounds. Among these compounds, **5a**, **5d** and **5e** exhibited best binding energy and inhibition constant. The results of the drug-likeness properties also exposed that the title compounds violate only weight and LogP value. From all these observations, we conclude that piperidin-4-imines do not have the ability to inhibit SARS Covid-2 in host cell. However, additional in vitro research and in vivo research are necessary to verify the results.

## 9. References

1. World Health Organization (WHO). Pneumonia of unknown cause – China. Geneva: WHO; 2020. Available from: <https://www.who.int/csr/don/05-january-2020-pneumonia-of-unknown-cause-china/en/>
2. Huang C, Wang Y, Li X, Ren L, Zhao J, Hu Y, et al. Clinical features of patients infected with 2019 novel coronavirus in Wuhan, China. *Lancet*. 2020;S0140-6736(20)30183-5. [https://doi.org/10.1016/S0140-6736\(20\)30154-9](https://doi.org/10.1016/S0140-6736(20)30154-9) PMID: 31986261
3. World Health Organization (WHO). WHO Director-General's remarks at the media briefing on 2019-nCoV on 11 February 2020. Geneva: WHO; 2020. Available from: <https://www.who.int/dg/speeches/detail/who-director-general-s-remarks-at-the-media-briefing-on-2019-ncov-on-11-february-2020>
4. Huang C, Wang Y, Li X, Ren L, Zhao J, Hu Y, Zhang L, Fan G, Xu J, Gu X, Cheng Z. Clinical features of patients infected with 2019 novel coronavirus in Wuhan, China. *The lancet*. 2020 Feb 15;395(10223):497-506.
5. Alimohamadi Y, Sepandi M, Taghdir M, Hosamirudrsari H. Determine the most common clinical symptoms in COVID-19 patients: a systematic review and meta-analysis. *Journal of preventive medicine and hygiene*. 2020 Sep;61(3):E304.
6. Centers for Disease Control and Prevention (CDC). Coronavirus Disease 2019 (COVID-19). Atlanta: CDC; 2020. Available from: <https://www.cdc.gov/coronavirus/2019-ncov/about/symptoms.html>
7. Wu YC, Chen CS, Chan YJ. Overview of the 2019 novel coronavirus (2019-nCoV): The pathogen of severe specific contagious pneumonia (SSCP). *J Chin Med Assoc*. 2020; [Epub ahead of print]. <https://doi.org/10.1097/JCMA.000000000000270> PMID: 32049687
8. Li MY, Li L, Zhang Y, Wang XS. Expression of the SARS-CoV-2 cell receptor gene ACE2 in a wide variety of human tissues. *Infectious diseases of poverty*. 2020 Apr 1;9(02):23-9.
9. Rahman FI, Ether SA, Islam MR. The “Delta Plus” COVID-19 variant has evolved to become the next potential variant of concern: mutation history and measures of prevention. *Journal of Basic and Clinical Physiology and Pharmacology*. 2022 Jan 1;33(1):109-12.
10. Kumar A, Parashar R, Kumar S, Faiq MA, Kumari C, Kulandhasamy M, Narayan RK, Jha RK, Singh HN, Prasoon P, Pandey SN. Emerging SARS-CoV-2 variants can potentially break set epidemiological barriers in COVID-19. *Journal of Medical Virology*. 2022 Apr;94(4):1300-14.
11. Mohapatra RK, Sarangi AK, Kandi V, Azam M, Tiwari R, Dhama K. Omicron (B. 1.1. 529 variant of SARS-CoV-2); an emerging threat: current global scenario. *Journal of medical virology*. 2022 May;94(5):1780-3.
12. Li G, De Clercq E. Therapeutic options for the 2019 novel coronavirus (2019-nCoV). *Nature reviews Drug discovery*. 2020 Mar;19(3):149-50.
13. Yao X, Ye F, Zhang M, Cui C, Huang B, Niu P, Liu X, Zhao L, Dong E, Song C, Zhan S. In vitro antiviral activity and projection of optimized dosing design of hydroxychloroquine for the treatment of severe acute respiratory syndrome coronavirus 2 (SARS-CoV-2). *Clinical infectious diseases*. 2020 Jul 28;71(15):732-9.
14. Wang Y, Fan G, Salam A, Horby P, Hayden FG, Chen C, Pan J, Zheng J, Lu B, Guo L, Wang C. Comparative effectiveness of combined favipiravir and oseltamivir therapy versus oseltamivir monotherapy in critically ill patients with influenza virus infection. *The Journal of infectious diseases*. 2020 Apr 27;221(10):1688-98.
15. Taniguchi H, Ebina M, Kondoh Y, Ogura T, Azuma A, Suga M, Taguchi Y, Takahashi H, Nakata K, Sato A, Takeuchi M. Pirfenidone in idiopathic pulmonary fibrosis. *European Respiratory Journal*. 2010 Apr 1;35(4):821-9.

16. Zhu Z, Lu Z, Xu T, Chen C, Yang G, Zha T, Lu J, Xue Y. Arbidol monotherapy is superior to lopinavir/ritonavir in treating COVID-19. *Journal of Infection*. 2020 Jul 1;81(1):e21-3.
17. Zhu M, Zhou H, Ma L, Dong B, Zhou J, Zhang G, Wang M, Wang J, Cen S, Wang Y. Design and evaluation of novel piperidine HIV-1 protease inhibitors with potency against DRV-resistant variants. *European Journal of Medicinal Chemistry*. 2021 Aug 5;220:113450.
18. Rajput, A. P., and D. V. Nagarale. "Synthesis, characterization and antimicrobial study of piperidine-2, 6-diones derivatives." *Pharm. Chem 8* (2016): 182-186.
19. Khanum SA, Girish V, Suparshwa SS, Khanum NF. Benzophenone-N-ethyl piperidine ether analogues—Synthesis and efficacy as anti-inflammatory agent. *Bioorganic & medicinal chemistry letters*. 2009 Apr 1;19(7):1887-91.
20. Kankala S, Kankala RK, Balaboina R, Thirukovela NS, Vadde R, Vasam CS. Pd-N-heterocyclic carbene catalyzed synthesis of piperidine alkene-alkaloids and their anti-cancer evaluation. *Bioorganic & medicinal chemistry letters*. 2014 Feb 15;24(4):1180-3.
21. Carroll FI, Dolle RE. The Discovery and Development of the N-Substituted trans-3, 4-Dimethyl-4-(3'-hydroxyphenyl) piperidine Class of Pure Opioid Receptor Antagonists. *ChemMedChem*. 2014 Aug;9(8):1638-54.
22. Lei, Peng, Xuebo Zhang, Yan Xu, Gaoferi Xu, Xili Liu, Xinling Yang, Xiaohe Zhang, and Yun Ling. "Synthesis and fungicidal activity of pyrazole derivatives containing 1, 2, 3, 4-tetrahydroquinoline." *Chemistry Central Journal* 10, no. 1 (2016): 1-6.
23. Lv K, Tao Z, Liu Q, Yang L, Wang B, Wu S, Wang A, Huang M, Liu M, Lu Y. Design, synthesis and antitubercular evaluation of benzothiazinones containing a piperidine moiety. *European Journal of Medicinal Chemistry*. 2018 May 10;151:1-8.
24. Konwar M, Sarma D. Advances in developing small molecule SARS 3CLpro inhibitors as potential remedy for corona virus infection. *Tetrahedron*. 2021 Jan 1;77:131761.
25. Cannalire R, Cerchia C, Beccari AR, Di Leva FS, Summa V. Targeting SARS-CoV-2 proteases and polymerase for COVID-19 treatment: state of the art and future opportunities. *Journal of medicinal chemistry*. 2020 Nov 13;65(4):2716-46.
26. Casida ME, Chong DP, editors, *Recent developments in density functional theory*. Singapore: World Scientific; 1995;1:155–192.
27. Casida ME, Casida KC, Salahub DR. Excited-state potential energy curves from time-dependent density-functional theory: a cross section of formaldehyde's 1A1 manifold. *Int. J. Quantum Chem*. 1998;70:933–941.
28. Vankadari N. Structure of furin protease binding to SARS-CoV-2 spike glycoprotein and implications for potential targets and virulence. *The journal of physical chemistry letters*. 2020 Jul 28;11(16):6655-63.
29. Trott O, Olson AJ (2010) AutoDockVina: improving the speed and accuracy of docking with a new scoring function, efficient optimization, and multithreading. *J ComputChem* 31: 455-461. 1
30. Patil, Anil Kumar, and Sharanappa Godi Ganur. "Comparative study on the effect of nano additives with biodiesel blend on the performance and emission characteristics of a laboratory ci engine." *International journal of mechanical and production engineering research and development (ijmperd)* ISSN (p): 2249-6890.
31. Al-Fatlawi, A. L. A. H. U. S. A. E. E. N. "Effects of chlorine dioxide and some water quality parameters on the formation of THMs in water treatment plants." *International Journal of Civil, Structural, Environmental and Infrastructure Engineering Research and Development (IJCSEIERD)* 4.2 (2014): 73-86.
32. DOSH, RUKIA JABER, et al. "Energy and some atomic properties for excited state of AR ion using Hartree-Fock method." *International Journal of Mechanical and Production Engineering Research and Development* 8.6 (2018): 827-830.
33. Nandhini, D., S. Subashchandrabose, and P. RAMESH. "Synthesis, characterization and computation of potassium doped calcium hydroxide nanoparticles and nanotubes." *International Journal of Mechanical and Production Engineering Research and Development (IJMPERD)* 9.1 (2019): 441-448.
34. Benmekhbi, L., et al. "Inhibition Study By Molecular Docking Of Dihydrofolate Reductase Of Escherichia Coli With Some Chalcone Molecules." *International Journal of Applied, Physical and Bio-Chemistry Research* 4.6 (2014): 17-24.
35. Singh, Neha, et al. "Awareness Towards Covid-19 Pandemic among Farm Women and its Technological Strategies." *International Journal of Agricultural Science and Research (IJASR)* 10 (2020): 151-158.



## Outlier Detection using Fuzzy Approach

S. Rajalakshmi<sup>1</sup> and P. Madhubala<sup>2\*</sup>

<sup>1</sup>Guest Lecturer, Department of Computer Science, Government Arts College for Women, Krishnagiri, and Research Scholar, Periyar University, Salem, Tamil Nadu, India.

<sup>2</sup>Assistant Professor, Don Bosco College, Dharmapuri, and Research Supervisor, Periyar University, Salem, Tamil Nadu, India.

Received: 25 Mar 2022

Revised: 24 Apr 2022

Accepted: 22 May 2022

### \*Address for Correspondence

#### P. Madhubala

Assistant Professor,  
Don Bosco College, Dharmapuri, and  
Research Supervisor, Periyar University,  
Salem, Tamil Nadu, India.  
Email: madhubalasivaji@gmail.com



This is an Open Access Journal / article distributed under the terms of the **Creative Commons Attribution License** (CC BY-NC-ND 3.0) which permits unrestricted use, distribution, and reproduction in any medium, provided the original work is properly cited. All rights reserved.

### ABSTRACT

Through the wisdom of free open text data, Data Analytics helps businesses grow and make decisions by revealing some fascinating patterns and trends in knowledge discovery. Customers' perspectives express sensible opinions that are not always true. We present a strong fuzzy based circle clustering strategy to find positive-definite outliers in this work. Text data from free handlers gives prior knowledge about the product opinion, which can be used to find knowledge discovery and pattern trends. Positive-definite reviews and comments on the internet encourage consumers and sellers to work together. Negative consequences may yield valuable insights for business, individuals, and government development. There are two parts to this paper: Data preprocessing, a circle-generating technique for clusters, and outlier detection using fuzzy logic. The engaging and fascinating experimental examination of the positive-definite outlier opinion yields accurate and appropriate conclusions with a degree of ambiguity in the mathematical model.

**Keywords:** fuzzy, outliers, opinion, clusters, free text handlers.

## INTRODUCTION

Data mining, also known as non-trivial extraction of implicit data, is a collection of techniques that includes classification, clustering, data summarization, change analysis, and anomaly detection. It uncovers hidden patterns and combines machine learning, deep learning, and statistical methodologies. It also looks for global patterns, decision support, estimating, forecasting, and novel correlation patterns, among other things. However, Data Mining



**Rajalakshmi and Madhubala**

must meet certain criteria, such as innovation, repository trends, understandability, veracity, and interest. Estimation, prediction, classification, association, and grouping are just some of the jobs and procedures it may perform. To create comprehensive records of the target variable and categorical predictor variable, estimation delivers the approximate value of a numeric variable. Point estimation, confidence interval estimation, simple linear regression and correlation, and multiple regression are some of the estimate methods available. The future holds predictions that are similar to classification and estimation. For example, using KNN, you can forecast the price of a stock for the next three months and the winners of a cricket team for the next ten years. The target variable is categorical rather than numeric in classification, which is similar to estimation. It is based on a predetermined set of predictor and target variables. Affinity analysis (or market basket analysis) uses association rules to determine which traits "go together." It also aims to discover the principles of association between two or more traits with a degree of confidence and support. Clustering is a grouping of records that are similar but have no target variable. It may not attempt to categorise, estimate, or forecast the value of a target variable. Within the cluster, record similarity is maximised, while outside the cluster, it is minimised. Clustering is a useful exploratory data analysis technique for detecting outliers. Clustering is an unsupervised learning technique that uses unlabeled training data to uncover classes within the data. A cluster are similar that contains collection of data objects. It's organised based on how similar it is. Clustering is widely employed in real-world issues for a variety of purposes. It is used in applications like as market research, pattern identification, data analysis, image processing, and the medical industry to simplify enormous datasets in order to uncover something new. The homogeneous 'n' data points correspond to the 'c' clusters of the partitioning matrix 'U.' Cluster Analysis uses class labels to help create taxonomies without analysing data items. The data objects are grouped using the maximization of intraclass similarity and minimization of interclass similarity principles. Section 2 describes outlier analysis, Section 3 describes related work, Section 4 includes various aspects of outlier detection, Section 5 includes applications of outlier detection , Section 6 includes clustering, Section 7 includes fuzzy clustering and Section 8 describes experimental results and discussion.

**OUTLIER ANALYSIS**

Outlier analysis is a methodology for detecting uncommon patterns that arise as a result of computational error, wrong input, sampling error, exceptional of true mistake, and native data modifiability. In a nutshell, it's the process of identifying patterns in a dataset that don't follow the predicted pattern. Anomalies, oddities, aberrations, discordant item, an exception, a surprise, and aberrant behaviour are all terms used to describe outliers. Both phrases are used interchangeably in the context of outlier discovery to transfer significant positive-definite data to other domains. The data analyst is fascinated by the common characteristics that exist across all application domains. Outlier detection relies heavily on the "interestingness" of real-world relevance. Data analysts are uninterested in noise and regard it as a barrier to outlier detection. Global, contextual, and collective outliers are the three sorts of outliers. Fraud detection, intrusion detection, image processing, health care informatics, surveillance, medical diagnosis, predictive maintenance, cyber-intrusion, and other applications are among its capabilities. It is necessary to recognise outliers in order to accept the uncertain and imprecise. To detect it, first cluster the data, then compute the centroid and distance using the Euclidean distance approach, then compute OF (objective function) and proclaim it as an outlier if it falls below a certain threshold.

Several variables make detecting outliers difficult in general. a)It's not always easy to distinguish between normal and abnormal behaviour. The anomalous point is close to the normal zone, which operates normally and appears to be more difficult to solve. It may lead to the induction of factors based on labelled data, data kind, anomaly type, and so on. b)In the future, the current concept of actual behaviour may not be well reflected. For each domain, the definition of abnormal behaviour may be different. For example, in medical diagnostics, changes in body temperature may be close to normal when evaluating the patient's therapy, and malevolent enemies may be considered typical behaviour. In the stock market, oscillations in the rise or fall in the value of a stock may be close to the normal zone, with outlier points being considered typical. c)Training labels and validating critical models is a difficult task. d)Noise is difficult to partition and eliminate since it is identical to true outliers. Data points that deviate from the norm are known as outliers. Some statistical tests, such as density-based and distance-based approaches, can be used to detect it. Data preprocessing, fuzzy clustering, and outlier analysis are the three sections





**Rajalakshmi and Madhubala**

of this research. The capacity to deal with noise and high dimensionality are the obstacles. Here are some questions to consider when we try to spot outliers.

- a) "Are all of the patterns interesting?"
- b) "How does the pattern appeal to you?"
- c) "Can a data mining system come up with the most interesting ones?"
- d) "It's finally novel?"

**RELATED WORK**

Outliers have been examined in the statistical field since the 19th century [21]. Anomaly observations were used to test a statistical model for noise accommodation through immunization [33]. For several research commodities, several application fields for detecting outliers have been researched [10]. In [6][3][43], a survey of statistics on outlier detection was conducted. For anomaly identification, [44] looked at a complete survey of statistics research. Noise accommodation is a structured robust analysis on linear regression for identifying outliers, noise removal is removing unwanted objects before analysis, Teng et al [68], identifying theft in credit card fraud detection and novelty detection is detecting novel patterns and outliers [48][49]. The study of sensitive data being sent to an unauthorised machine [41]. [25] investigates surprising observations in spacecraft sensors. The study looks at a survey of cyber-intrusion detection [51] as well as a study on intrusion detection [18]. [9] and [31] both conducted surveys on anomaly detection. [6] conducted a review on identifying anomalies in numeric and symbolic data. The investigation of outliers detection in various strategies is shown in Table 1.

In general, different aspects such as the nature of data input, label availability, types of anomalies, and the output of the application domain driven by requirements and limitations establish a distinct formulation of the problem. We evaluated the size of the structure and its worth as an extra element.

The type of data input is classified according to the type of data instance. Sequence data (time series, protein sequences, genome sequences, data sequences), geographical data (ecological data, vehicular traffic data), and graph data are all examples of data types (connect with edges to other vertices). It is dependent on the type of data, which can be univariate or multivariate. Different statistical models were employed to analyse data instances that were categorised as binary, categorical, and continuous. In [66]; Point, contextual, and collective anomalies are the three categories of anomalies. "Point anomalies" are defined as "data points that are aberrant in relation to other data points." Point anomalies are the simplest, and the outlier point is located outside the normal region's boundaries. For example, in credit card fraud detection, the anomaly is defined as a large amount spent in comparison to usual spending. ii) "Contextual anomalies" are defined as "data objects that stray significantly from a certain context." Contextual is also known as conditional because it is reliant on a choice. [63] It has two types of attributes: environmental and behavioural. The neighbourhood of a data instance is determined by contextual attributes, which are based on geographic and time series data. Non-contextual data characteristics are determined by behavioural attributes. The context is regarded as an oddity, while the behaviour is regarded as usual. As a result, the data instance's key property is categorised as anomalous in context and normal in behaviour attributes. iii) "Collective anomalies" are defined as "a data object that is abnormal in relation to the complete data set." Sequence data, graph data, and spatial data are all used. The types of anomaly detection are summarised in Table 2.

**VARIOUS ASPECTS OF OUTLIER DETECTION**

In general, different aspects such as the nature of data input, label availability, types of anomalies, and the output of the application domain driven by requirements and limitations establish a distinct formulation of the problem. We evaluated the size of the structure and its worth as an extra element. The type of data input is classified according to the type of data instance. Sequence data (time series, protein sequences, genome sequences, data sequences), geographical data (ecological data, vehicular traffic data), and graph data are all examples of data types (connect with edges to other vertices). It is dependent on the type of data, which can be univariate or multivariate. Different statistical models were employed to analyse data instances that were categorised as binary, categorical, and



**Rajalakshmi and Madhubala**

continuous. In [66]; Point, contextual, and collective anomalies are the three categories of anomalies. "Point anomalies" are defined as "data points that are aberrant in relation to other data points." Point anomalies are the simplest, and the outlier point is located outside the normal region's boundaries. For example, in credit card fraud detection, the anomaly is defined as a large amount spent in comparison to usual spending. ii) "Contextual anomalies" are defined as "data objects that stray significantly from a certain context." Contextual is also known as conditional because it is reliant on a choice. [63] It has two types of attributes: environmental and behavioural. The neighbourhood of a data instance is determined by contextual attributes, which are based on geographic and time series data. Non-contextual data characteristics are determined by behavioural attributes. The context is regarded as an oddity, while the behaviour is regarded as usual. As a result, the data instance's key property is categorised as anomalous in context and normal in behaviour attributes. iii) "Collective anomalies" are defined as "a data object that is abnormal in relation to the complete data set." Sequence data, graph data, and spatial data are all used. The types of anomaly detection are summarised in Table 2.

To evaluate if a data instance is anomalous or typical, a data label that encompasses all sorts of behaviour is typically costly and correct. Through the labelling mechanism, a significant amount of human work is required to obtain labelled training data sets. It records a labelled set of unusual data instances that are more challenging to understand than regular behaviour. Airline safety mechanism, for example, where unusual behaviour leads to rare events. When it comes to spotting outliers, there are three types of data labels: supervised, unsupervised, and semi-supervised. Two fundamental challenges in supervised anomaly detection are rather difficult. First, when compared to typical class instances, the anomalous class instance is extremely rare. As a result, an uneven distribution of class instances is discovered when compared to the predictive model. Second, to represent the label training dataset, several false anomalous data points are created. Unsupervised anomaly detection does not require training data labels, so an implicit assumption is made for anomalous instances that are close by and normal instances that are far away. Only the normal class has training data of labelled cases in semisupervised anomaly detection. Labeled instances are not required for the Anomaly class. Fault detection in spacecraft, for example. It's tough to spot outliers in test data if the engine is malfunctioning. As a result, the anomalous model is constructed in the same way as normal behaviour. Table 3 describes the various approaches of outlier detection.

Outliers in score and labels must be reported as part of the detection process. Using scoring algorithms, an Outlier Score is assigned to each instance that is dependent on degree. Using a threshold value, the data analyst selects the top outliers. They assign labels to each instance's control parameters for each approach.

**APPLICATIONS OF OUTLIER DETECTION**

Many applications detect outliers, including intrusion detection, fraud detection, medical health analysis detection, quality control, financial applications, web log-based analytics, Earth science applications, satellite image analysis, anti-terrorism, pharmaceutical research, data leakage prevention, time series monitoring, and more. Image processing detection [61], Text data outlier detection [64], Industrial damage detection [39], Novelty detection in robots [15], Sensor networks detection, [12], criminal activities detection [46], video monitoring detection, astronomical data detection [20], Management of customer complaints[29] are discussed.

**CLUSTERING**

" Clustering is an unsupervised learning technique that involves collecting similar objects and analysing them." There are several types of clustering methods, including partitioning methods (k-means, k-medoids), grid-based methods (Wavecluster, clique, sting), hierarchical methods (divisive, dendrogram, agglomerative), model-based methods, and density-based methods (denclue, optics, dbscan). It is widely used in many fields such as data mining, digital image processing, statistics, biology, deep learning, and machine learning, and is widely used in many applications such as data analysis, pattern recognition, market research, and image processing using software packages such as R programming, Python, and SPSS. Clustering aids the business sector in grouping customers based on common patterns. It also aids in economic market research, insurance forecasting, home planning, earthquake analysis, document classification, and geographic data analysis. It works with a wide range of properties,





**Rajalakshmi and Madhubala**

as well as arbitrary forms, noise, outliers, data object scalability, constraint-based grouping, and interpretability. Clustering tendency, non-uniform distribution solved by Hopkins test as null hypothesis (H0), and alternate hypothesis (H1) are used to evaluate clusters (Ha) ii) Clustering quality, which is determined by metrics like the intrinsic measure-silhouette, Fig(14)(15), and the extrinsic measure. iii) Number of optimal clusters (k), as determined by i) empirical and elbow methods, and ii) domain knowledge approach, as shown in granularity Fig(11). iii) statistical approach: the value of the gap statistic corresponds to clusters. Figure 1 depicts many cluster types.

Cluster validity indices are used to compare clustering algorithms or two cluster sets in terms of compactness and connectivity. It determines whether or not there is a cluster owing to noise. Internal cluster validation, external cluster validation, and relative cluster validation are all methods for determining cluster validity. The inter-cluster distance  $d(a, b)$  can be one of the following: a) single linkage distance, b) complete linkage distance, c) average linkage distance, or d) centroid linkage distance. Complete diameter linkage distance, average diameter linkage distance, and centroid diameter linkage distance are all examples of intra-cluster distance  $D(a)$ . Figure 2 depicts both well-separated and poorly-separated clustering.

J. C. Dunn proposed the Dunn index in 1974 as an internal metric for evaluating clustering techniques. It's used to distinguish compact, well-separated clusters within cluster variance. When the Dunn index is high, clustering is good, and the DI maximisation is used to determine the optimal number of clusters. In equation(1), the dunn index is defined as

$$\text{Dunn index}(U) = \min_{1 \leq i \leq k} \left\{ \min_{1 \leq j \leq k, j \neq i} \left\{ \frac{\delta(X_i, X_j)}{\max_{1 \leq k \leq k} \{\Delta(X_k)\}} \right\} \right\} \tag{1}$$

Where  $X_i$  and  $X_j$  are the cluster's intercluster distances.  $X_k$  is the cluster's intracluster distance.

The Davies–Bouldin index was created in 1979 by David L. Davies and Donald W. Bouldin to evaluate clustering techniques internally. The dataset's size and characteristics are assessed. Clustering is beneficial if the DB index value is low. In equation(2), the DB index is defined as follows:

$$\text{DB index}(U) = 1/k \sum_{i=1}^k \max_{j \neq i} \left\{ \frac{\Delta(X_i) + \Delta(X_j)}{\delta(X_i, X_j)} \right\} \tag{2}$$

Where,  $X_i$  and  $X_j$  denote the cluster's intercluster distance.  $X_k$  represents the cluster's intracluster distance.

Measuring the distances between two clusters' similarity is significant and vital. Euclidean and Manhattan distances are the two methodologies used. B. The equation for calculating Euclidean distance is as follows: (3)

$$J(U, V) = \sum_{i=1}^n \sum_{j=1}^c (\mu_{ij})^m \|x_i - v_j\|^2 \tag{3}$$

The pearson correlation distance, Eisen cosine correlation distance, and Spearman correlation distance are all correlation-based distances that may be calculated using equation(4) (5). The average dissimilarity between clusters is measured as average distance. The average silhouette of all rows is called Average Silhouette. The number of clusters that maximises this value is used.

$$J(U, c_1, \dots, c_c) = \sum_{i=1}^c J_i = \sum_j^c \sum_j^n u_{ij}^m d_{ij}^2 \tag{4}$$





**Rajalakshmi and Madhubala**

$$c_i = \sum_{j=1}^n u_{ij}^m x_j / \sum_{j=1}^n u_{ij}^m \tag{5}$$

**Summary of clustering types:**

J.A. Hartigan and M.A. Wong created the k-means algorithm to create a small number of clusters from a large number of data with no outliers. Discrete data, as an example. The fundamental goal is to partition n observations with p dimensions into k clusters with the lowest possible sum of squares. This approach locates a "local" optimal solution. Each row of the kth cluster has p variables and contains n and k observations. The jth row of the kth group provides a missing value for ith variable. It is normalised by subtracting the mean from the total and dividing by the standard deviation, which is indicated by zij.

**Algorithm 1: K-means clustering**

1. Decide on the number of clusters you want to use.
2. Choose k cluster centres.
3. Assign all data objects to the cluster centre that is the closest to you.
4. In each cluster, calculate new cluster centres.
5. Repeat the procedure until the cluster centre calculation remains unchanged.

**Algorithm 2: Hierarchical clustering**

1. Determine the smallest element dij in each of the n clusters.
2. Combine clusters i and j into a single new cluster, k (nk=ni+nj).
3. Use the distance formula to calculate distances.
4. Go through the instructions again. N-1 iterations are required for 1 to 3 objects.

Agglomerative hierarchical clustering algorithms are represented by a dendrogram, which is a tree diagram. The objects are never separated as the two clusters are combined into a single new cluster. The distance between clusters is defined by the horizontal axis, while the cluster items are represented by the vertical axis. The dij of n items represents the distance between i and j clusters. Figure 3 depicts an example dendrogram as well as the procedures involved in hierarchical clustering.

**FUZZY CLUSTERING**

Jim Bezdek invented soft clustering in 1981. It is the data object that contains members of all clusters with membership degrees ranging from 0 to 1. It has a high degree of membership that is close knit and a low degree of membership that is dispersed. Cluster prototype and membership degree are used to build the matrix. where 'n' denotes the number of data points 'vj' denotes circle centre cluster, 'm' denotes index of fuzziness index,  $m \in [1, \dots]$ , 'c' denotes cluster centre, 'ij' denotes membership degree, and 'dij' denotes Euclidean distance in equation(1)(2)(3). Figure (4) depicts the fuzzy membership function, which is given by equation (6)(7)(8).

$$\sum_{i=1}^c u_{ij} = 1, \forall j = 1, \dots, n \tag{6}$$

$$\mu_{ij} = 1 / \sum_{k=1}^c (d_{ij} / d_{ik})^{(2/m - 1)} \tag{7}$$

$$v_j = ( \sum_{i=1}^n \mu_{ij} )^m x_i / ( \sum_{i=1}^n ( \mu_{ij} )^m ), \forall j = 1, 2, \dots, c \tag{8}$$

Membership degree, =0,.....,1, is the fuzzy indication of similarity in fuzzy sets. If the membership degree is equal to





**Rajalakshmi and Madhubala**

1, the object belongs to the set completely, and if it is equal to 0, the object does not belong to the set at all. Clusters with comparable values have a higher possibility of belonging to a set. The following equation ( 9) can be used to calculate fuzzy clustering, goal function, cluster centre, and membership degree (10)

$$u_{ij} = 1 / \sum_{k=1}^c (d_{ij} / d_{kj})^2 / (m - 1) \tag{ 9 }$$

Where,

$$d_{ij} = \|c_i - x_j\| \tag{10}$$

clustering that is a little fuzzy Partially categorising clusters is possible using partition clustering algorithms. Each individual is a member of only one cluster in regular clustering.

**ALGORITHM OVERVIEW**

The algorithm's major criteria include efficiency, scalability, performance, and optimization. There are a variety of algorithms for reducing (or eliminating) outliers. However, it is possible that some critical buried data will be lost. The approach is first preprocessed to decrease noise and then partitioned using fuzzy set theory, a linear model, and the mean of clusters. Outliers are recognised using an objective function once the next circle generation process has been overrun. Outliers are often dismissed as exceptions (or) noise by many data mining tools.

**FUZZY CIRCLE BASED – (CENTROID) CLUSTERING PROPOSED**

Free text handlers opinions are clustered into two categories as positive definite and negative opinions. Fig (5) shows how blobby clusters are based on degree of fluidity and defined as "blobbiness clusters" which are proportional to the corresponding degree. The following equation (11) follows how to structure the clusters. The opinions of free text handlers are divided into two groups: positive definite opinions and negative definite opinions. Blobby clusters are characterised as "blobbiness clusters" that are proportionate to the relevant degree of fluidity, as seen in Fig (5). The structure of the clusters is determined by the following equation (11):

$$f(x, y, z) = \sum_{k=0}^n b_k \cdot e^{-ak} r^{2k} - T \tag{11}$$

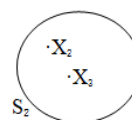
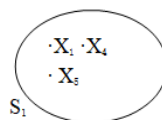
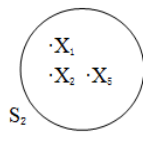
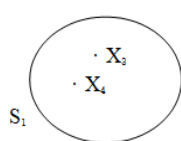
Where x,y,z are the parameters, T is the threshold, a and b are the blobby adjustments, and e and k are negative values. Let X= X1, X2, X3, X4, X5 be separated into two subsets, each of which is a non-empty matrices with each element belonging to a single Clustering

$$U1 = \begin{matrix} & \begin{matrix} X_1 & X_2 & X_3 & X_4 & X_5 \end{matrix} \\ \begin{matrix} S_1 \\ S_2 \end{matrix} & \begin{bmatrix} 0 & 0 & 1 & 1 & 0 \\ 1 & 1 & 0 & 0 & 1 \end{bmatrix} \end{matrix}$$

$$U2 = \begin{matrix} & \begin{matrix} X_1 & X_2 & X_3 & X_4 & X_5 \end{matrix} \\ \begin{matrix} S_1 \\ S_2 \end{matrix} & \begin{bmatrix} 1 & 0 & 0 & 1 & 1 \\ 0 & 1 & 1 & 0 & 0 \end{bmatrix} \end{matrix}$$

$$S_1 = \{X_3, X_4\}, S_2 = \{X_1, X_2, X_5\}$$

$$S_1 = \{X_1, X_4, X_5\}, S_2 = \{X_2, X_3\}$$





### Rajalakshmi and Madhubala

#### Algorithm 3: Circle generating algorithm

1.  $r, (x_c, y_c)$
2.  $p_0 = 1 - r$
3.  $p_k < 0, p_{k+1} = 2x_{k+1} + 1$
4.  $p_k > 0, p_{k+1} = 2x_{k+1} - 2y_k + 1$
5.  $2x_{k+1} = 2x_k + 2$
6.  $2y_{k+1} = 2y_k + 2$

#### Condition:

$$\text{fuzzycircle}(x,y) = x^2 + y^2 + 1$$

If  $\text{fcircle}(x,y) < 0 \rightarrow (x,y)$ , inside circle cluster

If  $\text{fcircle}(x,y) = 0 \rightarrow (x,y)$ , on circle cluster

If  $\text{fcircle}(x,y) > 0 \rightarrow (x,y)$ , outside circle cluster

Using the aforesaid approach, we have created new cluster centroids. Using the Euclidean distance between data points and every circle centroid, a new centroid value is produced until the threshold value is less than 0.

#### Pseudocode

1. Initialize membership matrix U
2. Calculate fuzzy cluster circle center C
3. Find the distance between different circle centers using Euclidean distance.
4. Calculate OF until the value is below threshold.
5. Otherwise, Fix a random point 'p', to get optimum value—repeat from step 2

#### Objective

The goal of employing a fuzzy based circle generating clustering algorithm to find outliers and identify influential factors in opinion mining.

#### Points to Remember

1. IQR is calculated when data is normalised with a Z-score (-3 to +3). (Inter Quartile Range)
2. Preparation of Data is done by a) Graphical Method b) Numerical Method
3. Research Methodology a) High Average Point b) Influential Observations c) Simple Linear Regression
4. Methods of Assessment - Algorithms for fuzzy clustering and generating circles
5. Outliers: LOF 1, (No consistent data point)  
No Outliers: LOF > 1 (consistent data point)

#### Idea

To discover top dissimilar clusters, choose n data points and k clusters.

1. Identify data that is incongruent (cluster the data)
2. Look for outliers in your data (calculate the centroid of each cluster)
3. Methodology: A distance-based strategy
4. Compare the distance around the outlier object assumption to the distance around the non-outlier object assumption (finding the distance)
5. Using the circle-generating technique, make the circle significantly equivalent to the distance between neighbours (To decide anomaly).

**Note:** Before detecting outliers, noise must be eliminated.



**Rajalakshmi and Madhubala****DISCUSSION OF EXPERIMENT RESULTS**

By using R programming version 3.6.1 and installing the basic package “ppclust” (23rd July 2019). Our technique has been tested on two datasets: Advertising and stock data. We are confident that our system will find internal coincidence quality outliers in a high proportion of cases. When the aforementioned two datasets are compared using the proposed method, the stock data dataset has a higher quality % than the Advertising dataset. Fig (6) shows the boxplot of outliers. Fig (7) shows the membership degree of stock\_data dataset. Fig (8)(9)(10)(11)(12) shows the fuzzy membership calculations. Fig (13) displays the optimal number of clusters. Fig (14) displays rows and columns of Advertising dataset. Fig (15)(16) shows the silhouette with 3 clusters and 2 clusters.

**CONCLUSION**

By 2025, our corporate economy will have matured due to customer-specific requirements. The competition between various pressures will be eliminated, and a successful outcome will lead to customer satisfaction. The suggested technique addresses the uncertainty, noise, and incompleteness of data in a networked context, enhancing the power of discovery patterns. The product's interestingness measurements are determined by pattern constraint and pattern evaluation in opinion mining based on user beliefs (or) expectations. The views of free text handlers (customers) are useful in determining the style of marketing that will result in an increasing profit for a specific product. We can better comprehend the targeted strategy. Fuzzy clustering is a great way to boost business growth. Our method appears to be effective based on the outcomes of our tests. When applied to the stock data dataset, the revised suggested technique produces positive results. In the future, the research will concentrate on fuzzy-genetic outlier detection.

**REFERENCES**

1. N. Abe, B. Zadrozny, J. Langford, Outlier Detection by active learning, *ACM Press*. (2006), pp. 504-509.
2. D. Agarwal, An empirical Bayes approach to detect anomalies in dynamic multidimensional arrays, *Proceedings of 5<sup>th</sup> IEEE international conference on data mining*. (2005), pp. 26-33.
3. Z. Bakar, R. Mohamad, A. Ahmad, M. Deris, A Comparative study for outlier detection techniques in data mining, *Cybernetics and Intelligent systems*. (2006), pp. 1-6.
4. V. Barnett, T. Lewis, Outliers in statistical data. *John wiley and sons*. (1994).
5. P. Barson, N. Davey, S. D. H. Field, R. J. Frank, Mcaskie, The detection of fraud in mobile phone networks, *Neural networks*. (1996).
6. R. J. Beckman, R. D. Cook, Outlier Technometrics 25 2 pp. 119-149.
7. R. Bolton, D. Hand, Unsupervised profiling methods for fraud detection, *Credit scoring and credit control VII*, (1999).
8. R. Brause, T. Langsdorf, M. Hepp, Neural data mining for credit card fraud detection. *Proceedings of IEEE International conference on tools with artificial intelligence*. (1999), pp. 103-106.
9. V. Chandola, A. Banerjee, V. Kumar, Anomaly Detection: A Survey. *ACM computing survey*. (2009), pp. 1-72.
10. D. M. Chapman, Hall, Hawkins, Identification of Outliers, *Springer*. (1980).
11. Charu C Aggarwal, Outlier Analysis, *Springer*. (2016).
12. V. Chatzigiannakis, S. Papavassiliou, M. Grammatikou, B. Maglaris, Hierarchical anomaly detection in distributed large-scale sensor networks. *In ISCC'06: Proceedings of the 11<sup>th</sup> IEEE symposium on computers and communications*. (2006), pp. 761-767.
13. N. V. Chawla, N. Japkowicz, A. Kotcz, Ed: Special issue on learning from imbalanced data sets, *SIGKDD Explorations*. (2004), 6 1 pp. 1-6.
14. K. C. Cox, S.G. Eick, G. J. Wills, R. J. Brachman, Visual data mining: Recognizing telephone calling fraud, *Journal of data mining and knowledge discovery*. (1997), pp. 225-231.





**Rajalakshmi and Madhubala**

15. P. A. Crook, S. Marsland, G. Hayes, Nehmzow, A tale of two filters on line novelty detection, *In Proceedings of International conference on Robotics and Automation*. (2002), pp. 3894-3899.
16. D. Dasgupta, N. Majumdar, Anomaly detection in Multidimensional data using negative selection algorithm, *In Proceedings of the IEEE Conference on Evolutionary Computation*. (2002), pp. 1039-1044.
17. D. Dasgupta, F. Nino, A Comparison of negative and Positive selection algorithms in novel pattern detection, *In Proceedings of the IEEE International Conference on Systems, Man and Cybernetics*. (2000), vol 1, pp. 125-130.
18. D. E. Denning, An intrusion detection model, *IEEE transactions of software engineering*. (1987), 13 2, pp. 222-232.
19. R. O. Duda, P. E. Hartv, D. G. Stork, Pattern classification, *Wiley interscience*. (2000).
20. H. Dutta, C. Giannella, K. Borne, H. Kargupta, Distributed top k outlier detection in astromomy catalogs using the demac system, *In Proceedings of 7<sup>th</sup> SIAM International Conference on Data mining*.
21. F. Y. Edgeworth, On discordant observations, *Philosophical Magazine*. (1887), 23 5, pp. 364-375.
22. T. Fawcett, F. Provost, Activity monitoring : noticing interesting changes in behaviour, *Proceedings of 5<sup>th</sup> ACM SIGKDD international conference on knowledge discovery and data mining*. (1999).
23. S. Forrest, C. Warrender, B. Pearlmuter, Detecting intrusions using system calls: Alternate data models, *In proceedings of the 1999 IEEE ISRSP*. (1999), pp. 133-45.
24. S. Forrest, S. A. Hofmeyr, A. Somayaji, T. A. Longstaff, A Sense of self for unix processes, *In Proceedings of the ISRSP96*. (1996), pp. 120-128.
25. R. Fujimaki, T. Yairi, K. Machida, An approach to spacecraft anomaly detection problem using kernel feature space, *In Proceedings of the eleventh ACM SIGKDD international conference on knowledge discovery in data mining*. (2005).
26. S. Ghosh, D. L. Reilly, Credit card fraud detection with a neural-network, *Proceedings of 14<sup>th</sup> annual computer security applications conference*. (1994).
27. R. Gwadera, M. J. Atallah, W. Szpankowski, Detection of significant sets of episodes in event sequences, *Proceedings of 4<sup>th</sup> IEEE International conference on data mining*. (2004), pp. 3-10.
28. R. Gwadera, M. J. Atallah, W. Szpankowski, Reliable Detection of episodes in event sequences, *Knowledge and information systems*. (2005b), pp. 415-437.
29. Z. He, X. Xu, J. Z. Huang, S. Deng, Mining class outliers: Concepts, algorithms. (2004b), pp, 588-589.
30. Z. He, X. Xu, S. Deng, Discovering Cluster-based local outliers, *Pattern Recognition letters*. (2003), pp. 1641-1650.
31. V. Hodge, J. Austin, A survey of Outlier Detection Methodologies. *Artificial Intelligence Review*22, (2004), 2 pp. 85-126.
32. S. A. Hofmeyr, S. Forrest, A. Somayaji, Intrusion detection using sequence of system calls, *Journal of computer security*. (1998), 6 3 pp.151-180.
33. P. Huber, Robust statistics, *Wiley*. (1974).
34. Irad Ben Gal, Outlier detection. Data mining and knowledge handbook: A complete guide for practitioners and researchers, *Kluwer academic publishers*. (2005).
35. A. K. Jain, R. C. Dubes, Algorithms for clustering data. (1988).
36. I. T. Jolliffe, Principal Component Analysis, Second edition, *Springer*. (2002).
37. M. V. Joshi, R. C. Agarwal, V. Kumar, Mining Needle in a haystack: Classifying rare classes via two-phase rule induction, *Proceedings of the 2001 ACM SIGMOD international conference on Management of data.ACM*. (2001).
38. M. V. Joshi, R. C. Agarwal, V. Kumar, Predicting rare classes can boosting make any weak learner strong, *Proceedings of the 8th ACM SIGKDD international conference on Knowledge and data mining. ACM press*. (2002).
39. E. Keogh, S. Lonardi, B. Y. Chiu, Finding surprising patterns in a time series database in linear time and space. *In Proceedings of eighth ACM SIGKDD international conference on knowledge discovery and data mining.ACM press*. (2002), pp, 550-556.
40. Y. Kou, C. T. Lu, D. Chen, Spatial weighted outlier detection, *In Proceedings of SIAM conference on Data Mining*. (2006).
41. V. Kumar, Parallel and Distributed Computing for Cybersecurity. *Distributed systems online, IEEE* (2005), 6 10.
42. T. Lane, C. E. Brodley, Temporal sequence learning and data reduction for anomaly detection. *ACM Transactions on information systems and security*. (1999), 2 3, pp, 295-331.
43. A. M. Leroy, P. J. Rousseeuw , Robust regression and outlier detection, (1987).







### Rajalakshmi and Madhubala

44. T. Lewis, Barnett, Outliers in Statistical Data, *Wiley & Sons*. (1984).
45. M. Li, P. M. B. Vitanyi, An Introduction to Kolmogorov complexity and its applications, *Springer-verlag*. (1993).
46. S. Lin, D. E. Brown, An outlier-based data association method for linking criminal incidents. *In Proceedings of 3<sup>rd</sup> SIAM data mining conference*. (2003).
47. Manish Gupta, Jing Gao, Charu C Aggarwal, Jiawei Han, Outlier Detection for Temporal data: A Survey, *IEEE Transactions on knowledge and data engineering*. (2014).
48. M. Markou, S. Singh, Novelty Detection: A review part 1: Statistical Approaches. *Signal Processing*.(2003a), 83 12, pp. 2481-2497.
49. M. Markou, Singh, Novelty Detection: A review part 2: Neural Network based approaches, *Signal Processing*.(2003b), 83 12, pp. 2481-2497.
50. C. C. Noble, D. J. Cook, Graph based anomaly detection, *In Proceedings of the 9<sup>th</sup> ACM SIGKDD international Conference on knowledge discovery and data mining*. *ACM Press*. (2003), pp. 631-636.
51. A. Patcha, J. M. Park, An overview of anomaly detection techniques: Existing solutions and latest technological trends, *Computer Networks*. (2007), 51 12, pp. 3448-3470.
52. V. V. Phoha, The springer internet security dictionary, *Springer-verlag*.
53. C. Phua, D. Alahakoon, V. Lee, Minority report in fraud detection : Classification of skewed data, *SIGKDD explorer newsletter*. (2004), pp. 50-59.
54. S. Rajalakshmi, P. Madhubala, A study of Outlier detection method using clustering approach, *LFS-Literacy findings*. ISSN:2278-2311, (2019), pp. 89-93.
55. S. Rajalakshmi, P. Madhubala, Outlier Detetion: a research and modified method using fuzzy clustering, *International journal of Innovative technology and Exploring Engineering*. ISSN:2278-3075, vol 9, Issue-3s, (2020), pp. 427-431.
56. S. Rajalakshmi, P. Madhubala, Auto detecting Perpetual outliers using efficient modified fuzzy clustering approach. *International journal of creative Research thoughts*. Vol 9, Issue 5 May 2021. ISSN:2320-2882. (2021).
57. S. Rajalakshmi, P. Madhubala, A Novel Analysis on Outliers. *Proceedings in International conference on research and development in science, engineering and technology*. (2021), pp. 71-755. (<https://stannescet.ac.in/ICRDSET2021>).
58. S. Salvador, P. Chan, Learning states and rules for time-series anomaly detection, *Tech.Rep*. (2003) .
59. S. L. Scott, Detecting network intrusion using a markov modulated non homogeneous poisson process, *Journal of American statistical association*. (2001).
60. S. Shekhar, C. T. Lu, P. Zhang, Detecting Graph based spatial outliers :Algorithms and applications, *In Proceedings of the 7<sup>th</sup> ACM SIGKDD international conference on knowledge discovery and data mining*. *ACM press*. (2001), pp. 371-376.
61. S. Singh, M. Markou, An approach to novelty detection applied to the classification of image regions, *IEEE Transactions on knowledge and data engineering* . (2004), pp. 396-407.
62. D. Snyder, Online intrusion detection using sequences of system calls, M.S.thesis, Department of computer science, Florida state university, (2001).
63. X. Song, M. Wu, C. Jermaine, S. Ranka, Conditional anomaly detection, *IEEE Transactions on knowledge and data engineering* 19. (2007), pp. 631-645.
64. A. Srivastava, Enabling the discovery of recurring anomalies in aerospace problem reports using high-dimensional clustering techniques, *Aerospace Conference. IEEE*. (2006), pp. 17-34.
65. I. Steinwart, D. Hush, C. Scovel, A Classification framework for anomaly detection, *Journal of Machine Learning Research* 6. (1996), pp. 211-232.
66. P. N. Tan, M. Steinbach, V. Kumar, Introduction to data mining, *Addison-wesley*. (2005).
67. M. Taniguchi, M. Haft, J. Hollmn, V. Tresp, Fraud detection in communications networks using neural and probabilistic methods, *Proceedings of IEEE international conference in acoustics, speech and signal processing*. (1998), pp. 1241-1244.
68. H. Teng, K. Chen, S. Lu, Adaptive real-time anomaly detection using inductively generated sequential patterns, *In Proceedings of IEEE Computer Society Symposium on Research in security and Privacy*. *IEEE Computer Society Press*. (1990), pp. 278-284.





**Rajalakshmi and Madhubala**

69. J. Theiler, D. M. Cai, Resampling approach for anomaly detection in multispectral images, *In Proceedings of SPIE 5093*. (2003), pp. 230-240.

70. R. Vilalta, S. Ma, Predicting rare events in temporal domains, *In Proceedings of the 2002 IEEE International Conference on Data Mining. IEEE Computer Society*. (2002).

71. A. S. Weigend, Mangeas, A. N. Mand Srivastava, Nonlinear gated experts for time-series –discovering regimes and avoid overfitting, *International journal of Neural systems*. (1995), pp. 373-399.

72. G. M. Weiss, H. Hirish, Learning to predict rare events in event sequences, *Proceedings of 4<sup>th</sup> International Conference on Knowledge Discovery and Data mining. AAAI press*. (1998), pp. 359-363.

73. Saihua Cai, An efficient outlier detection approach on weighted data stream based on minimal rare pattern mining, *China communications*. (2019).

74. Saihua Cai, MiFI-outlier: Minimal infrequent itemset-based outlier detection approach on uncertain data stream, *Knowledge based systems*. (2020).

75. Saihua Cai, Minimal weighted infrequent itemset mining based outlier detection approach on uncertain data stream, *Neural networks*. (2020).

76. Mikaeel Mokhtari, Interval type-2 fuzzy least-squares estimation to formulate a regression model based on a new outlier detection method using a new distance, *Computational and applied Mathematics*. (2021).

**Table 1: A study on Outlier detection Techniques.**

Techniques	References
Clustering based	[35][29][30]
Classification based	[66][19]
Information Theoretic	[45]
Statistical based	[4]
Spectral based	[36]
Hierarchical clustering	[11]
DB-SCAN	
Density based	
Fuzzy Clustering	

**Table 2: Types of Anomaly Detection**

Types of anomaly			Example	References
Point			Credit card – Fraud detection	[9]
Contextual	i)Contextual attributes	Spatial data	Latitude and Longitude of a location- rainfall	[40] [60]
	ii)Behavioral attributes	Time series data	Weather forecasting, Medical diagnosis	[71][58]
Collective	Sequence data		Event log management system	[23][24]
	Graph data		Rainfall in a month	[50]
	Spatial data		Temperature in a particular region	[60]

**Note:** “By incorporating the context information, both the types-point and collective-are transformed to contextual.”

**Table 3: Modes of Outlier Detection**

Modes of Data Label	References	Description
Supervised	[72] [37][38] [70] [69] [13] [65] [1]	Training data is required
Unsupervised	[9]	No training data label is required
Semi-supervised	[24] [17] [16] [25]	Combination of supervised and unsupervised technique

**Note:** The Semi supervised model is an unsupervised model with low outliers in test data and high robustness in training data.





**Rajalakshmi and Madhubala**

**Table 4: Applications of Outlier Detection**

Applications	Key Challenge	Techniques Studied	References
Host based Intrusion Detection System	<ul style="list-style-type: none"> <li>✓ Large amount of data, results in false alarm rate.</li> <li>✓ Collective anomaly.</li> <li>✓ No point anomaly.</li> <li>✓ Semi-supervised and Unsupervised</li> </ul>	<ul style="list-style-type: none"> <li>✓ Neural Networks</li> <li>✓ Rule-based systems</li> <li>✓ Statistical Profiling – Histograms</li> <li>✓ Mixture of models</li> </ul>	[52] [18] [32] [42][62] [24] [16]
Network based Intrusion Detection System	<ul style="list-style-type: none"> <li>✓ Anomalies change over time</li> <li>✓ To evade real time intrusion by outside hackers</li> <li>✓ Point anomaly</li> </ul>	<ul style="list-style-type: none"> <li>✓ Parametric and Non-Parametric modelling</li> <li>✓ Neural networks</li> <li>✓ Clustering based system</li> <li>✓ Support vector machine</li> <li>✓ Rule-based systems</li> <li>✓ Bayesian networks</li> <li>✓ Nearest Neighbor based</li> <li>✓ Statistical profiling-Histograms</li> </ul>	[27][28]
Credit card Fraud Detection	<ul style="list-style-type: none"> <li>✓ Immediate Online detection to track the credit card fraudulent transaction</li> <li>✓ Only Profiling and clustering techniques are used</li> <li>✓ Very critical to handle the geometric position at the earliest to track.</li> </ul>	<ul style="list-style-type: none"> <li>✓ Statistical profiling-Histograms</li> <li>✓ Information-Theoretic</li> </ul>	[26] [8] [7]
Mobile Phone Fraud Detection	<ul style="list-style-type: none"> <li>✓ Requires large accounts of calling activity</li> <li>✓ May be continuous or discrete</li> <li>✓ Unfavour destinations</li> </ul>	<ul style="list-style-type: none"> <li>✓ Parametric statistical modelling</li> <li>✓ Rule-based</li> <li>✓ Neural networks</li> <li>✓ Statistical profiling-Histograms</li> </ul>	[2][59][53][67][5][22][14].

**Table 5: Comparative Result analysis of dataset**

Algorithm	Dataset	No of records	No of clusters	Result percentage
FCM	Advertising	200	3	44.06%
	Stock_data	3000	3	52.52%
Fuzzy circle based clustering approach	Advertising	200	3	61.92%
	Stock_data	3000	3	69.48%





Rajalakshmi and Madhubala

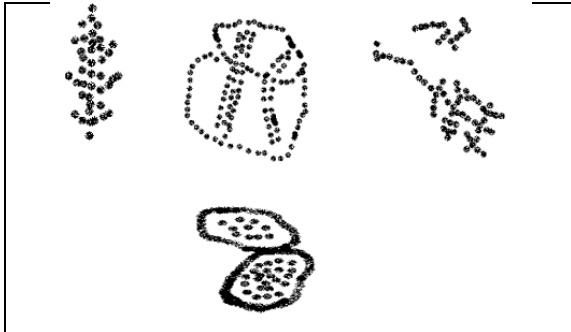


Figure 1: Different forms of clusters

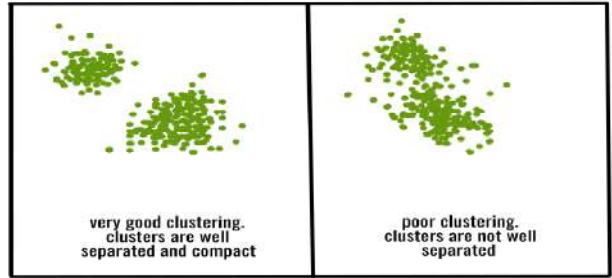


Figure 2: Good Clustering and Bad Clustering

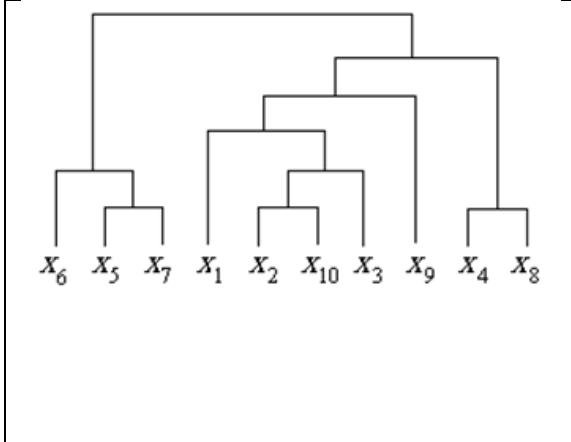


Figure 3: A Sample Dendrogram

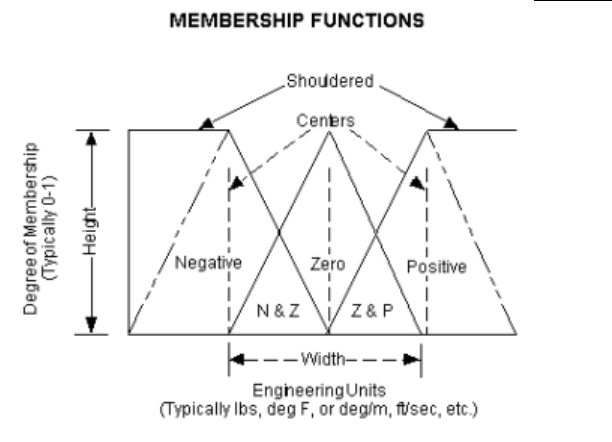


Figure 4: Fuzzy Membership function

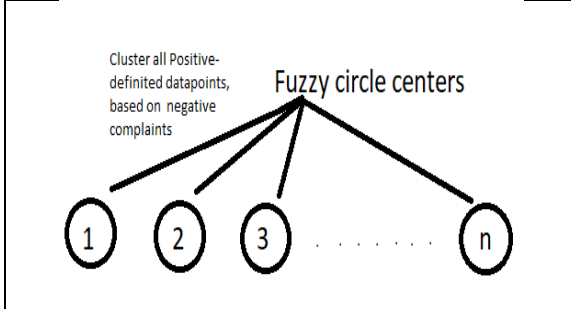


Figure 5: Bloby clusters are identified and circled

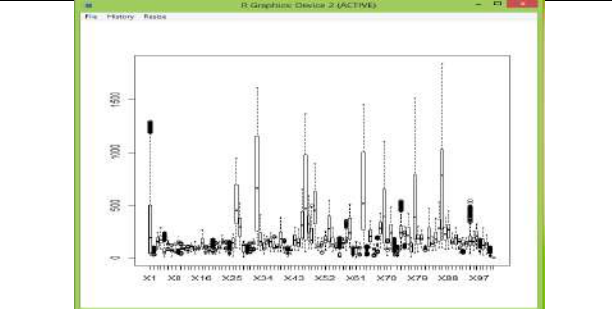


Figure 6: Boxplot of stock\_data dataset

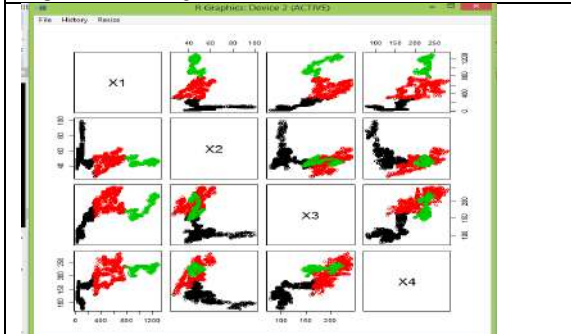


Figure 7: Crisp fuzzy membership degree

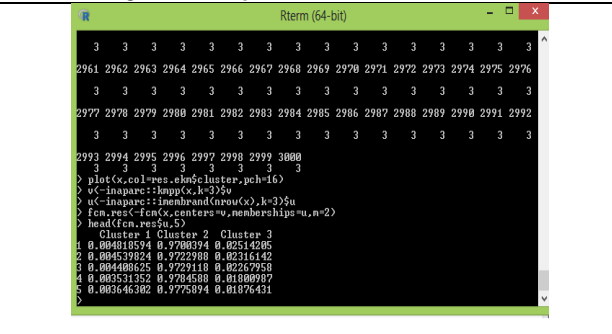


Figure 8: Fuzzy membership degree -Advertising





Rajalakshmi and Madhubala

```

Rterm (64-bit)
Cluster 1 Cluster 2 Cluster 3
1 0.004818594 0.97009394 0.02514285
2 0.004539824 0.97222988 0.02316142
3 0.004408625 0.9729118 0.02267958
4 0.003531352 0.9704588 0.01808987
5 0.003646302 0.9775994 0.01876431
> fcm.res<-fcm(X.centers=v, memberships=u,n=2,eta=2)
> head(fcm.res$u,5)
Error in head(fcm.res$u, 5) : object 'fcm.res' not found
> fcm.res<-fcm(X.centers=u, memberships=u,n=2,eta=2)
> head(fcm.res$u,5)
Cluster 1 Cluster 2 Cluster 3
1 0.004818597 0.9700939 0.02514287
2 0.004539827 0.9722297 0.02316144
3 0.004408627 0.9729118 0.02267959
4 0.003531354 0.9704588 0.01808988
5 0.003646303 0.9775994 0.01876432
> head(fcm.res$t,5)
[,1] [,2] [,3]
[1,] 1.075341e-05 0.0002983240 3.633884e-05
[2,] 1.056617e-05 0.0003034911 3.491231e-05
[3,] 1.060636e-05 0.0003139095 3.533728e-05
[4,] 1.045245e-05 0.0003081859 3.456843e-05
[5,] 1.054681e-05 0.0003722214 3.515887e-05

```

Figure 9: Fuzzy membership degree -- stock\_data

```

Rterm (64-bit)
2990 4.209040e-03 0.0117465543 0.9840443980
2991 2.540029e-03 0.0072610399 0.9910197315
2992 2.222362e-03 0.0171677798 0.9765188586
2993 3.138367e-03 0.0141544859 0.9806691857
2994 9.046303e-03 0.0248893267 0.9668643707
2995 6.579101e-03 0.0170505585 0.9755776307
2996 9.459298e-03 0.0283978927 0.9455267972
2997 1.123995e-02 0.0294657572 0.9582949200
2998 1.058502e-02 0.0278941195 0.9615208606
2999 1.153396e-02 0.0306763340 0.9581648085
3000 1.005452e-02 0.0408609435 0.9430045379
> res.fcm$u
      N1      N2      N3      N4
Cluster 1  81.0985 49.7688 114.3768 142.3949
Cluster 2  584.5254 46.45844 208.2517 289.1970
Cluster 3 1070.3881 45.23795 104.4906 226.7794
> summary(res.fcm$cluster)
      Min. 1st Qu.  Median    Mean 3rd Qu.    Max.
1.000    1.000    1.000    1.523    2.000    3.000
> summary(res.fcm)
Number of data objects: 3000
Number of clusters: 3

```

Figure 10: clusters of stock\_data dataset

```

Rterm (64-bit)
2990 0.010605802 0.02709412 0.9615209
2991 0.01153982 0.03027540 0.9581646
2992 0.01605452 0.04086094 0.9430045
Description statistics for the membership degrees by clusters
      Size      Min      Q1      Mean      Median      Q3      Max
Cluster 1 1775 0.4852531 0.9606384 0.9389110 0.9853685 0.9886370 0.9984530
Cluster 2  881 0.4821615 0.6691426 0.0850412 0.0289596 0.9475412 0.9765757
Cluster 3  344 0.4755421 0.0421608 0.0870861 0.7331659 0.9699499 0.9996957
Dunn's Fuzziness Coefficients:
Dunn_coeff normalized
0.8587654 0.7611548
Within cluster sum of squares by cluster:
 1  12124911 19628933 7963354
(Between_SS / total_SS = 89.48%)
Available components:
 [1] "u"      "u0"     "u00"    "u01"    "u02"    "u03"
 [6] "cluster" "csize"  "sumsqrs" "k"      "n"
 [11] "iter"    "best.start" "func.val" "comp.time" "inpargs"
 [16] "algorithm" "call"
> summary(res.fcm$cluster)
      Min. 1st Qu.  Median    Mean 3rd Qu.    Max.
1.000    1.000    1.000    1.523    2.000    3.000
> summary(res.fcm)
 [1] 44.06
> res.fcm$func.val
 [1] 29823503
> res.fcm$iter
 [1] 88
> res.fcm$comp.time
 [1] 44.06
> res.fcm$best.start
 [1] 1

```

Figure 11: coefficients of stock\_data dataset

```

Rterm (64-bit)
Within cluster sum of squares by cluster:
 1  12124911 19628933 7963354
(Between_SS / total_SS = 89.48%)
Available components:
 [1] "u"      "u0"     "u00"    "u01"    "u02"    "u03"
 [6] "cluster" "csize"  "sumsqrs" "k"      "n"
 [11] "iter"    "best.start" "func.val" "comp.time" "inpargs"
 [16] "algorithm" "call"
> summary(res.fcm$cluster)
      Min. 1st Qu.  Median    Mean 3rd Qu.    Max.
1.000    1.000    1.000    1.523    2.000    3.000
> summary(res.fcm)
 [1] 44.06
> res.fcm$func.val
 [1] 29823503
> res.fcm$iter
 [1] 88
> res.fcm$comp.time
 [1] 44.06
> res.fcm$best.start
 [1] 1

```

Figure 12: computation time of stock\_data dataset

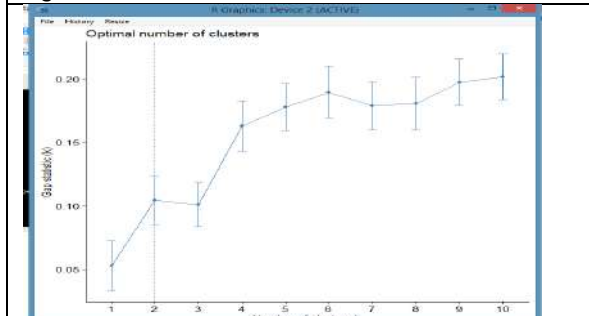


Figure 13: Displaying Optimal number of clusters

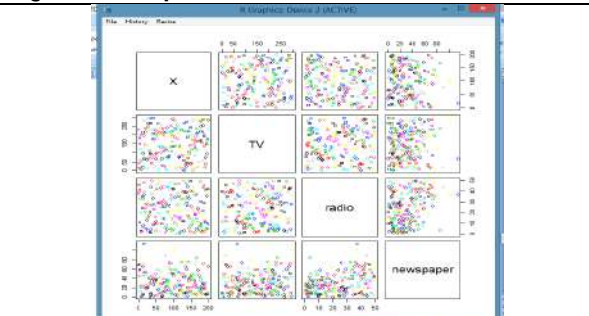


Figure 14: Displaying –Advertising dataset

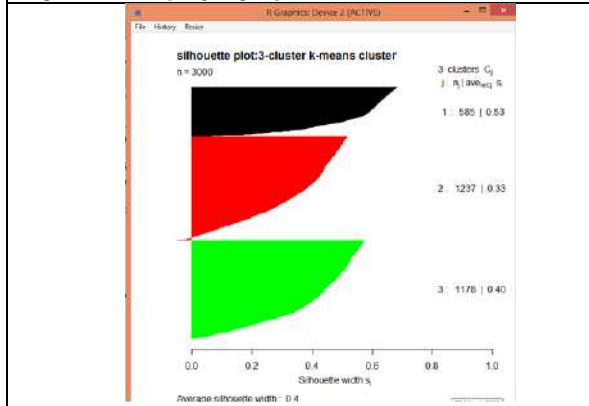


Figure 15: Silhouette with 3 clusters

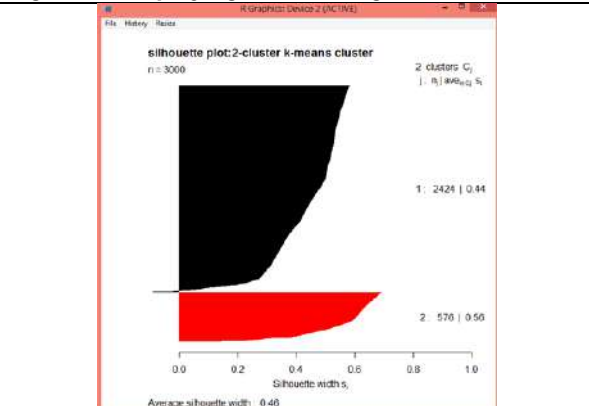


Figure 16: Silhouette with 2 clusters



# Gaussian Projection Deep Extreme Clustering and Chebyshev Reflective Correlation based Outlier Detection

S. Rajalakshmi<sup>1</sup>

Research Scholar

Department of Computer Science  
Periyar University, Salem, Tamilnadu, India

Dr. P. Madhubala<sup>2</sup>

Research Supervisor

Department of Computer Science  
Periyar University, Salem, Tamilnadu, India

**Abstract**—Outlier detection or simply the task of point detection that are noticeably distinct and different from data sample is a predominant issue in deep learning. When a framework is constructed, these distinctive points can later lead to model training and compromise accurate predictions. Owing to this reason, it is paramount to recognize and eliminate them before constructing any supervised model and this is frequently the initial step when dealing with a deep learning issue. Over the recent few years, different numbers of outlier detector algorithms have been designed that ensure satisfactory results. However, their main disadvantages remain in the time and space complexity and unsupervised nature. In this work, a clustering-based outlier detection called, Random Projection Deep Extreme Learning-based Chebyshev Reflective Correlation (RPDEL-CRC) is proposed. First, Gaussian Random Projection-based Deep Extreme Learning-based Clustering model is designed. Here, by applying Gaussian Random Projection function to the Deep Extreme Learning obtains the relevant and robust clusters corresponding to the data points in a significant manner. Next, with the robust clusters, outlier detection time is said to be reduced to a greater extent. In addition, a novel Chebyshev Temporal and Reflective Correlation-based Outlier Detection model is proposed to detect outliers therefore achieving high outlier detection accuracy. The proposed approach is validated with the NIFTY-50 stock market dataset. The performance of the RPDEL-CRC method is evaluated by applying it to NIFTY-50 Stock Market dataset. Finally, we compare the results of the RPDEL-CRC method to the state-of-the-art outlier detection methods using outlier detection time, accuracy, error rate and false positive rate evaluation metrics.

**Keywords**—Outlier detection; clustering; Gaussian random projection; deep extreme learning; Chebyshev distance; temporal; reflective correlation

## I. INTRODUCTION

Outliers are nothing but considered as data points or observations that plunge extraneous of an anticipated distribution or pattern and hence considered as the most-hottest topics as far as data mining is concerned. For example, if we were to perform data approximation with a Binomial distribution, then the outliers are the findings that do not emerge to go along with the pattern of a Binomial distribution. It discover anomalous data objects and are said to be of high use in several applications like detecting network intrusion, detecting fraudulent activities concerning credit card

management, outlier detection in stock market to mention few. In the area of outlier detection, the ground truth is found to be seldom missing and hence machine learning techniques are extensively utilized in outlier detection research.

Most of the prevailing research works concentrates on outlier detection for categorical or numerical attribute data. A fuzzy rough set (FRSs) was proposed in [1] to detect outlier in mixed attribute data based on fuzzy rough granules. Initially, the granule outlier degree (GOD) was designed with the objective of characterizing the outlier degree of fuzzy rough granules via fuzzy approximation accuracy.

Followed by which, the outlier factor on the basis of fuzzy rough granules was designed by integrating GOD and respective weights to measure outlier degree of objects using fuzzy rough granules-based outlier detection (FRGOD) algorithm. With this both precision and recall were said to be improved. Despite improvement observed in terms of precision and recall, the time and space complexity were relatively high. To address on this aspect, Gaussian Random Projection-based Deep Extreme Learning-based Clustering model is first designed and then the outliers are detected. With this process, the time and space complexity involved in outlier detection will be reduced to a greater extent.

Iterative ensemble method with distance-based data filtering was proposed in [2] based on an iterative approach with the purpose of detecting outliers present in unlabeled data. The ensemble method was utilized in clustering the unlabeled data. Then, with the clustered data potential outliers were filtered in an iterative manner employing cluster membership threshold. This was performed in an iterative manner until Dunn index score for clustering was said to be maximized.

On the other hand, the distance-based data filtering eliminated the prospective outlier clusters from post-clustered data on the basis of the distance threshold utilizing the Euclidean distance measure from majority cluster as filtering factor. With this the improvement were found to be observed in terms of both precision and f-score value. Despite improvement observed in terms of both precision and f-score, by detecting possible outlier clusters based on weighted method, the false positive rate can be reduced to a greater extent. With this objective, Chebyshev Temporal and Reflective Correlation-based Outlier Detection model is

designed so that using Chebyshev distance based temporal factor obtains highly correlated data points, therefore reducing the false positive rate to a greater extent.

#### A. Objective and Contributions

The main objective of this research is to propose a novel cluster-based outlier detection method that performs clustering process and outlier detection separately in a significant manner. This clustering-based outlier detection method addresses the limitations of the earlier outlier detection methods by its multi-factor i.e., deep clustering and correlative outlier detection model. Further, the contributions of this paper include the following.

- To propose a novel Gaussian Random Projection-based Deep Extreme Learning-based Clustering algorithm to minimize a composite objective function, i.e., outlier detection time along with the improvement in error rate. The model minimizes the outlier detection time and reduces error rate during outlier detection via two different functions, Gaussian Random Projection and square gradient function.
- To design a new Chebyshev Temporal and Reflective Correlation-based Outlier Detection algorithm based on Chebyshev Temporal function and Reflective Correlative function that ensures accurate outlier detection.
- The proposed Random Projection Deep Extreme Learning-based Chebyshev Reflective Correlation (RPDEL-CRC) method has provided improved results for outlier detection time, accuracy, error and false positive rate as performance evaluation measures.

#### B. Organization of the Paper

The rest of the paper is organized as: The discussion about the obtainable modern outlier detection techniques is presented in Section II. In Section III, the proposed Random Projection Deep Extreme Learning-based Chebyshev Reflective Correlation (RPDEL-CRC) method has been discussed. In Section IV, Chebyshev temporal and reflective correlation-based outlier detection model is discussed. The discussion about the experimental setup and comparative analysis with an elaborate discussion is described in Section V and finally, the conclusions are presented in Section VI.

## II. RELATED WORKS

The issue of outlier detection consists of detecting and eliminating malicious inferences from data. This problem is found to take place in several applications. However, outliers are frequently equipped by data stream that in turn influence the accuracy of data-based predictions. Hence, there arises an acute requirement to identify the outliers so as to enhance the data reliability.

A novel method to identify trajectory outlier group from large trajectory database using different types of algorithms was proposed in [3]. First, algorithms based on data mining were designed to identify the correlations between trajectory data and identify abnormal trajectories. Second, machine learning algorithms were applied to identify the group of

trajectory outliers. Finally, convolution deep neural network were used to learn distinct different features to determine group of trajectory outliers, therefore enhancing runtime and accuracy performance.

Conventional outlier detection method however does not take into consideration the subset occurrence frequency and hence, the outliers being detected do not fit the definition of outliers. To address on this aspect, a two-phase minimal weighted rare pattern mining-based outlier detection method, called MWRPM-Outlier [4] was proposed to efficiently detect outliers based on the weight data stream.

A novel methodology to identify conjunct unusual human behaviors from large pedestrian data in smart cities was proposed in [5]. First, data mining was used followed by which convolution deep neural networks was explored that in turn identified distinct features to determine collective abnormal human behavior. With this both runtime and accuracy were said to be improved.

Despite several outlier detection algorithms are said to exist for scenarios necessitating numerical data, only a few prevailing methods can control categorical data. Moreover, the methods outlined for categorical data severely endure from two issues, low detection precision and high time complexity. Two novel outlier detection mechanisms for categorical data sets were proposed in [6]. First an entropy based method using Outlier Detection Tree (ODT) was designed followed by which second simple if-then rules were utilized for outlier detection. With these two integrated mechanisms both precision and computational complexity were improved to a greater extent.

Outlier detection has received paramount significance in the domain of data mining owing to the requirement to detect unusual events in different types of applications, to name a few being, fraud detection, intrusion detection and so on. Different types of outlier detection algorithms have been proposed in the recent past for utilization on static data sets employing a finite number of samples.

Probabilistic deep autoencoder was proposed in [7] with the objective of reconstructing measurements of power system that in turn can be employed in outlier detection. First, nonparametric distribution estimation method was utilized for obtaining information pertaining to uncertainty. Second, confidence intervals were acquired from estimated distribution and were further utilized as input. Finally, based on the multilayer encoding and decoding processes, the measurement intervals were reconstructed, with which outlier detection were made in an accurate manner.

Outlier detection methods employing machine learning are said to be receiving greater attention in the past few years in several domains. But, an ensemble of such outlier detection methods could improve the overall detection performance. An algorithm called, Average Selection and Ensemble of Candidates for Outlier Detection (DASEC-OD) was proposed in [8] for high dimensional data. A review of unsupervised outlier detection methods focusing on multi-dimensional data was investigated in [9].

With the exponential requirement in analyzing high speed data streams, the job of outlier detection becomes more

demanding as the conventional outlier detection method can no longer presume all data for processing. In [10], a Memory-efficient incremental Local Outlier (MiLOF) was proposed for large data streams, therefore ensuring accuracy to a greater extent.

Nowadays, there prevail very huge types of outlier detector methods that bestow satisfactory results. But their major disadvantage remains in their unsupervised characteristic in conjunction with the hyper parameters that has to be appropriately assigned for acquiring better performance.

An improved content-based outlier detection method was proposed in [11]. In [12], a novel supervised outlier estimator was designed. This was performed by pipelining an outlier detector in such a manner that the targets involved in the outlier detector were obtained in an optimal manner. However, these methods did not perform in a satisfactory manner in case of utilization of the complex datasets and hence suffer from noise introduced by outliers, specifically when the ratio of outlier was found to be high. To address this aspect, a framework called, Transformation Invariant AutoEncoder (TIAE) was proposed in [13] that in turn attained not only stability but also ensured high performance on outlier detection. A comprehensive review of outlier detection techniques were investigated in [14].

In several practical classification issues, a portion of outliers are said to exist in datasets that in turn would have heavy influence on the constructed model performance. A group method of data handing (GMDH) using neural network in outlier detection was proposed in [15]. A novel robust outlier detection method (RiLOF) based on Median of Nearest Neighborhood Absolute Deviation (MoNNAD) was designed in [16] that employed median of local absolute deviation of the samples to attain high detection performance.

Monitoring data including the significant information of monitored object forms the fundamentals for data mining and analysis. However, the data being monitored suffers from outlier pollution therefore causing negative influence on corresponding data processing. To address on this aspect, an outlier detection method based on stacked autoencoder (SAE) was proposed in [17]. The proposed SAE had the significant potentiality of feature extraction and heavily maintained the indigenous information of data to a greater extent.

Accuracy and time involved in outlier detection was not focused. To address this aspect, a Neighbor Entropy Local Outlier Factor was presented in [18] that with the aid of self organizing feature map not only improved accuracy but also reduced the execution time to a greater extent. Moreover, semantic information was focused on [19] for outlier detection employing meta path based outlier detection. Outlier detection based on the multivariable panel data was designed in [20] via correlation coefficient that in turn indicated high accuracy detection ability.

Motivated by the above mentioned techniques in this work, a novel cluster-based outlier detection method called, Random Projection Deep Extreme Learning-based Chebyshev Reflective Correlation is proposed (RPDEL-CRC). The

elaborate description of RPDEL-CRC method is presented in the following sections.

### III. RANDOM PROJECTION DEEP EXTREME LEARNING-BASED CHEBYSHEV REFLECTIVE CORRELATION (RPDEL-CRC)

The proposed Random Projection Deep Extreme Learning-based Chebyshev Reflective Correlation method concentrates on the detection of outliers based on clustering. Methods designed based on cluster detect the outliers by placing data objects into distinct clusters. Here, the data objects in a data set are initially clustered. To design cluster-based outlier detection, the RPDEL-CRC method is split into two parts. Fig. 1 shows the block diagram of RPDEL-CRC method.

As illustrated in the figure below, the first part models robust cluster by means of Gaussian Random Projection-based Deep Extreme Learning. Here, the clustering based outlier detection initiates the outlier detection process by clustering the given input dataset, Nifty 50 Stock Market Data (2000 – 2021). Hence, to be more specific outliers are considered as data points within deviating clusters or the data points that deviate to the formed clusters. The second part uses the Chebyshev Temporal and Reflective Correlation-based Outlier Detection algorithm to detect outlier with minimum falsification. In this section, we first explain all prerequisites of the proposed method with a system model, and then finally we describe the proposed method.

#### A. System Model

Let  $P \in R^{(m*n)}$  represent a matrix with 'm' rows and 'n' columns of real numbers  $P_{ij} \in R$ . The matrix 'P' denotes a dataset 'DS' that includes the data for outlier analysis. The 'n' columns are called features and on the other hand, the 'm' are referred to as data points. Then, vector  $[DP]_i \in R^n$  refers to the data point, which is a row in 'P'. The matrix 'P' then consists of 'm' data points  $DP = \{ [DP]_1, DP_2, \dots, [DP]_n \}$ . Then, with the aid of the outlier detection algorithm the outliers present in the dataset 'DS' are detected. Finally, the overall feature space represents the vector space defined by the given features that in turn estimates the characteristics of the examined occurrence or event. Inliers are detected in subsets of the overall feature space and referred to as normal regions or normal data points. To be more specific, inliers are considered to as the data points in the normal regions. On the other hand, an outlier is a data point that does not belong in the normal region.

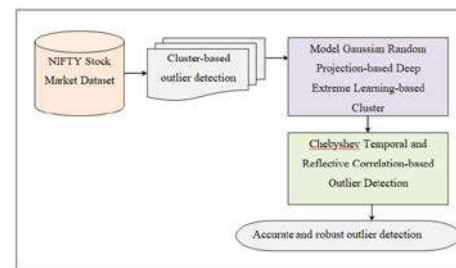


Fig. 1. Block Diagram of Random Projection Deep Extreme Learning-based Chebyshev Reflective Correlation Method.



### B. Case Analysis of Outlier Detection Accuracy

To detect outliers based on the cluster in a given dataset, the data has to be initially clustered. In this paper, Gaussian Random Projection-based Deep Extreme Learning model is first employed for clustering. The objective behind the design of Gaussian Random Projection-based Deep Extreme Learning model remains in training feed forward network from a raw training data set with ‘N’ samples, ‘{P,Q}={P<sub>i</sub>,Q<sub>i</sub> }<sub>(i=1,2,3, … ,N)</sub>’, with ‘P<sub>i</sub> ∈ R<sup>d</sup>’ and ‘Q<sub>i</sub>’ represents ‘M-dimensional’ binary vector where one entry denotes ‘1’ representing the cluster that ‘P<sub>i</sub>’ belongs to. Fig. 2 shows the block diagram of Gaussian Random Projection-based Deep Extreme Learning-based Clustering model.

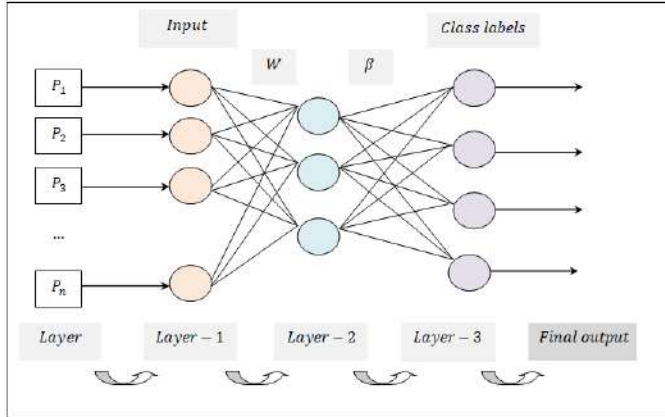


Fig. 2. Block Diagram of Gaussian Random Projection-based Deep Extreme Learning-based Clustering Model.

As shown in the above figure, the training process of GRP-DEL includes two steps. In (1), the hidden layer with ‘K’ nodes employing distinct numbers of neurons are constructed. Next, for the ‘i-th’ hidden layer node, a ‘d-dimensional’ vector ‘x<sub>j</sub>’ and a metric ‘y<sub>j</sub>’ are generated in an arbitrary manner. Then, for each input vector ‘P<sub>i</sub>’, the pertinent output on the ‘i-th’ hidden layer node is obtained by utilizing Sigmoid activation function. This is mathematically stated as given below.

$$g(P_i, x_j, y_j) = \frac{1}{1 + \exp[-(x_j^T * P_i + y_j)]} \quad (1)$$

Then, using the resultant value of the above Sigmoid activation function, the hidden layer outputs the matrix as given below.

$$H = \begin{bmatrix} g(P_1, x_1, y_1) & \dots & g(P_1, x_K, y_K) \\ \dots & \dots & \dots \\ g(P_N, x_1, y_1) & \dots & g(P_N, x_K, y_K) \end{bmatrix}_{N \times K} \quad (2)$$

In (2), an ‘M-dimensional’ binary vector ‘α<sub>j</sub>’ represents the output weight that associates the ‘j-th’ hidden layer with the resultant output node. Here, a random projection is applied that states that if points associating the ‘j-th’ hidden layer in a vector space are of sufficiently high dimension, then the ‘j-th’ hidden layer may be projected into a lower-dimensional space in such a manner that it preserves the distances between points (therefore minimizing dimensionality). With original input vector being ‘P<sub>i</sub>(K\*M)’, using a random ‘K\*d’ matrix dimensional matrix ‘R’, then the projection of data on to a

lower dimensional subspace is mathematically formulated as given below.

$$P_{K \times M} = R_{K \times d} P_{d \times M} \quad (3)$$

Then, with the above lower dimensional subspace random projection dimensionality of set of points and output matrix ‘Q’ is mathematically stated as given below.

$$H \cdot \alpha = Q \quad (4)$$

$$\alpha = \begin{bmatrix} \alpha_1 \\ \alpha_2 \\ \dots \\ \alpha_K \end{bmatrix}_{K \times M}; Q = \begin{bmatrix} Q_1 \\ Q_2 \\ \dots \\ Q_N \end{bmatrix}_{N \times M} \quad (5)$$

Next, with the resultant matrices ‘H’ and ‘Q’, the objective of GRP-DEL model remains in solving the output weights ‘α’ by reducing the losses of prediction errors, leading to the following equation.

$$\alpha_i(n) = \alpha_i(n-1) - \beta_i(n) \frac{MA_i(n)}{\sqrt{G_i(n)}} \quad (6)$$

From the above (6), ‘[[MA]]<sub>i</sub>(n)’ symbolizes the moving average of feature or attribute ‘i’ at iteration ‘n’, with square gradient denoted by ‘G<sub>i</sub>(n)’ and learning rate ‘β<sub>i</sub>(n)’ respectively.

$$MA_i(n) = \gamma_n MA_i(n-1) + (1 - \gamma_n) \quad (7)$$

$$G_i(n) = \theta_n G_i(n-1) + (1 - \theta_n) \quad (8)$$

$$\beta_i(n) = \beta_i(n-1) \frac{\sqrt{(1-\theta_n)^n}}{(1-\gamma_n)^n} \quad (9)$$

From the above (7), (8) and (9) the factors ‘γ<sub>n</sub>’ and ‘θ<sub>n</sub>’ are utilized in fine tuning the decay rates of moving averages close to one (i.e., ‘γ<sub>n</sub>=0.85’ and ‘θ<sub>n</sub>=0.9’). The pseudo code representation of Gaussian Random Projection-based Deep Extreme Learning-based Clustering is given below.

Algorithm 1: Gaussian Random Projection-based Deep Extreme Learning-based Clustering

**Input:** Dataset ‘DS’, data points ‘DP = {DP<sub>1</sub>, DP<sub>2</sub>, …, DP<sub>n</sub>}’  
**Output:** obtain cluster ‘Q<sub>i</sub>’ corresponding to ‘P<sub>i</sub>’ in computationally efficient and precise manner

- 1: **Initialize** ‘m’ rows and ‘n’ columns
- 2: **Begin**
- 3: **For** each Dataset ‘DS’ with data points ‘DP’ and input vector ‘P<sub>i</sub>’
- 4: Obtain pertinent output on the ‘i-th’ hidden layer employing Sigmoid activation function as in (1)
- 5: Obtain output matrix via hidden layer as in (2)
- 6: Evaluate Gaussian Random Projection as in (3)
- 7: Estimate hidden layer output and calculate the output matrix as in (4) and (5)
- 8: **Repeat** (training of neural networks)
- 9: Solve output weights by minimizing prediction loss error as in (6)
- 10: Treat each row of ‘Q’ as a point and cluster them into ‘K’ clusters
- 11: Estimate learning rates for cluster parameter as in (7), (8) and (9)
- 12: **Until** (first-order gradients for neural networks is arrived at)
- 13: **Return** ‘Q’
- 14: **End for**
- 15: **End**

As given in the above Gaussian Random Projection-based Deep Extreme Learning-based Clustering algorithm, with the objective of reducing the outlier detection time along with the improvement in precision, two different functions are employed. First, by employing Gaussian Random Projection the dimensionality of data is said to be reduced by projecting original input space (i.e., the raw data) with the aid of a sparse random matrix. Second, by estimating the learning rate by means of square gradient minimizes the error involved during the process of clustering to a greater extent. As a result, with these two function, clusters are formed both in a computationally efficient and precise manner.

#### IV. CHEBYSHEV TEMPORAL AND REFLECTIVE CORRELATION-BASED OUTLIER DETECTION MODEL

Outlier detection remains to be one of the primary step in data mining tasks. The motive behind the outlier detection strategy here is to identify the features or parameters that are counterfeit from several other features. Different types of outlier detection models are said to exist. In order to determine the perpetual temporal outliers, we obtain outliers based on distance measures by analyzing temporal values of the objects employing Chebyshev Temporal and Reflective Correlation-based Outlier Detection model. Fig. 3 shows the block diagram of Chebyshev Temporal and Reflective Correlation-based Outlier Detection model.

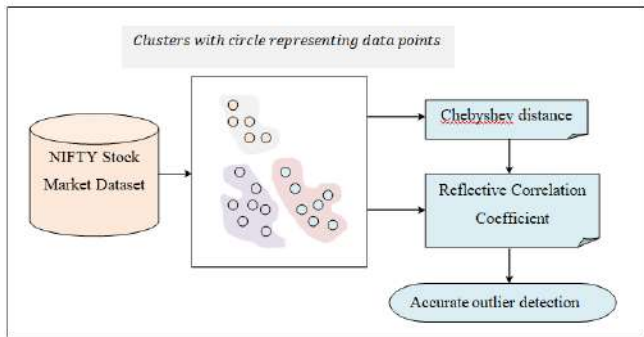


Fig. 3. Block Diagram of Chebyshev Temporal and Reflective Correlation-based Outlier Detection Model.

As shown in the above figure, with the obtained clusters for the given dataset ‘DS’, in a ‘d-dimensional’ vector, with data point denoted by ‘DP={DP[1],DP[2],...DP[d]}’ at time instance ‘T’, distance between two points ‘[[DP]]\_i’ and ‘DP\_j’ employing Chebyshev distance is mathematically, expressed as given below.

$$Dis(DP_i, DP_j) = Max(|DP_i - DP_j|) \quad (10)$$

From the above (10), by employing the Chebyshev distance measure ‘Dis ([[DP]]\_i, DP\_j)’, the greatest difference between two vectors (i.e., the data points) along any coordinate dimension (i.e., the cluster) is evaluated based on the maximum ‘Max(|[[DP]]\_i - [[DP]]\_j|)’ distance along one axis. To be more specific, based on the principle of chessboard distance as the minimum number of moves required by a king to go from one square to another is utilized; by means of Chebyshev distance, the overall outlier detection accuracy is said to be improved. Next, with the assumption of ‘m’ clusters

‘[[CI]]\_1, [[CI]]\_2,..., [[CI]]\_m’ the centroid data point ‘CP’ is then measured as given below.

$$Cl_i CP [i] = \frac{\sum_{P \in Cl_i} DP[i]}{|Cl_i|} \quad (11)$$

With the above determination of the centroid (11), with the assumption that in a cluster ‘CI’ most of the normal data points are hardly encircling the centroid data point of cluster ‘CI’, the abnormal data points or the outlier are those generally farther from the centroid data point. Then the updated weight of a centroid data point is mathematically stated as given below.

$$W(DP) = \frac{Dis(DP, Cl_i CP [i])}{\sum_{S \in Neigh(DP)} Dis(S, Cl_i CP [i])} \quad (12)$$

From the above (12), the weight of data point ‘DP’ in cluster ‘[[CI]]\_i’ is estimated based on the neighbors of ‘Neigh(DP)’ in ‘[[CI]]\_i’. Finally, to reflect the robustness and direction of linear correlation between two data points and minimizing the false positive cases, Reflective Correlation Coefficient is applied. RCC function is employed to evaluate the amount of dependency between two distributions of normalized scores ‘G\_i^Norm (DP), G\_j^Norm (DP)’ and is mathematically stated as given below.

$$RCC(DP_i, DP_j) = \frac{W(DP_i)W(DP_j)}{\sqrt{(\sum DP_i)^2 (DP_j)^2}} \quad (13)$$

From the above (13), reflective correlation coefficient ‘RCC’ is obtained based on the weighted data points ‘W([[DP]]\_i)’ and ‘W([[DP]]\_j)’ respectively. The final form of the objective function for minimizing the false positive cases of the ‘j-th detector’ is mathematically stated as given below.

$$Res_j = [G_j^{Norm}(DP)] - [G_j^{Norm}(DP_o)] \quad (14)$$

From the above (14) ‘G\_j^Norm’ forms the normalized score function of the ‘j-th detector’, ‘DP’ denoting the data points with contaminated dataset and ‘[[DP]]\_o’ denoting the outliers. The pseudo code representation of Chebyshev Temporal and Reflective Correlation-based Outlier Detection is given.

#### Algorithm 2 Chebyshev Temporal and Reflective Correlation-based Outlier Detection

<b>Input:</b> Dataset ‘DS’, data points ‘DP = {DP <sub>1</sub> , DP <sub>2</sub> , ..., DP <sub>n</sub> }’
<b>Output:</b> Accurate Outlier Detection
1: <b>Initialize</b> time instance ‘T’
2: <b>Begin</b>
3: <b>For</b> each Dataset ‘DS’ with data points ‘DP’ and cluster ‘Q <sub>i</sub> ’
4: Evaluate distance between data points ‘DP <sub>i</sub> ’ and ‘DP <sub>j</sub> ’ as in (10)
5: <b>For</b> each cluster ‘Q <sub>i</sub> ’
6: Evaluate centroid data point as in (11)
7: Evaluate weight of data point as in (12)
8: Estimate Reflective Correlation Coefficient as in (13)
9: Obtain final form of the objective function of the ‘j - th detector’ as in (14)
10: <b>Return</b> (outliers ‘DP <sub>o</sub> ’)
11: <b>End for</b>
12: <b>End for</b>
13: <b>End</b>

As given in the above Chebyshev Temporal and Reflective Correlation-based Outlier Detection algorithm, with the objective of improving the outlier detection accuracy with minimum falsification, two different functions are employed. First with the obtained clusters based on the data points, Chebyshev distance function is applied to estimate the difference between two data points along any cluster. Based on the minimum number of positioning between clusters, according to time, results are obtained, therefore ensuring outlier detection accuracy. Second by employing the Reflective Correlation Coefficient function dependency between two distributions or data points are obtained therefore reducing the false positive rate to a greater extent. Finally, the outliers are obtained.

V. EXPERIMENTAL SETUP

In this section, experimental analysis of the Random Projection Deep Extreme Learning-based Chebyshev Reflective Correlation (RPDEL-CRC) method for outlier detection in data mining is presented. In this section, the performance of the proposed RPDEL-CRC is compared with the state-of-the-art methods, fuzzy rough granules-based outlier detection (FRGOD) [1] and Iterative ensemble method with distance-based data filtering [2] using NIFT-50 Stock Market Dataset (<https://www.kaggle.com/datasets/rohanrao/nifty50-stock-market-data>). Simulations are performed in R Programming language. Fair comparison between proposed RPDEL-CRC method and existing fuzzy rough granules-based outlier detection (FRGOD) [1] and Iterative ensemble method with distance-based data filtering [2] are made for evaluating different parameters like, outlier detection time, outlier detection accuracy, false positive rate and error for different iterations.

A. Case Analysis of Outlier Detection Time

The first metric significant for cluster based outlier detection is the time consumed in detecting the outlier. To be more specific, outlier detection time refers to the time consumed in detecting the outliers. Lower the outlier detection time more efficient the method is said to be because earlier the time consumed in detecting the outlier is more efficient the method is. The outlier detection time is mathematically stated as given below.

$$OD_{time} = \sum_{i=1}^n Samples_i * Time [Res_j] \tag{15}$$

From the above (15), the outlier detection time ‘[[OD]]\_time’ is measured based on the samples involved in the simulation process ‘[[Samples]]\_i’ and the time consumed in detecting the outliers ‘Time [[Res]]\_j’. It is measured in terms of milliseconds (ms). Table I given below shows the results of outlier detection time observed for three different methods, RPDEL-CRC, FRGOD [1] and Iterative ensemble method with distance-based data filtering [2].

Fig. 4 illustrated above shows the outlier detection time with respect to 50000 different numbers of samples obtained at different intervals from different companies stock values between years 2007 and 2021. These curves are plotted with increasing cardinality of training samples ranging between 5000 and 50000. With the increasing cardinality, the number of

samples involved in analysis for outlier detection increases and therefore an increase in the outlier detection time is observed. However, simulations with 5000 samples observed ‘250ms’ for detecting outliers with respect to single stock sample using RPDEL-CRC, ‘350ms’ for detecting outliers with respect to single stock sample using [1] and ‘450ms’ for detecting outliers with respect to single stock sample using [2]. From this analysis it is inferred that the outlier detection time using RPDEL-CRC is comparatively lesser than [1] and [2]. The reason behind is the incorporation of Gaussian Random Projection-based Deep Extreme Learning-based Clustering model. By applying this model, dimensionality of data or data points are said to be reduced using Gaussian Random Projection based on projecting original input space (i.e., the raw data) with the aid of a sparse random matrix. With this, data points considered to be outliers are obtained that in turn assist in detecting the outliers altogether. Therefore, the outlier detection time using RPDEL-CRC method is found to be reduced by 20% compared to [1] and 37% compared to [2].

TABLE I. TABULATION FOR OUTLIER DETECTION TIME

Samples	Outlier detection time (ms)		
	RPDEL-CRC	FRGOD	Iterative ensemble method with distance-based data filtering
5000	250	350	450
10000	295	395	555
15000	355	435	635
20000	410	485	680
25000	435	535	745
30000	485	625	795
35000	525	685	835
40000	595	745	890
45000	685	800	920
50000	735	835	955

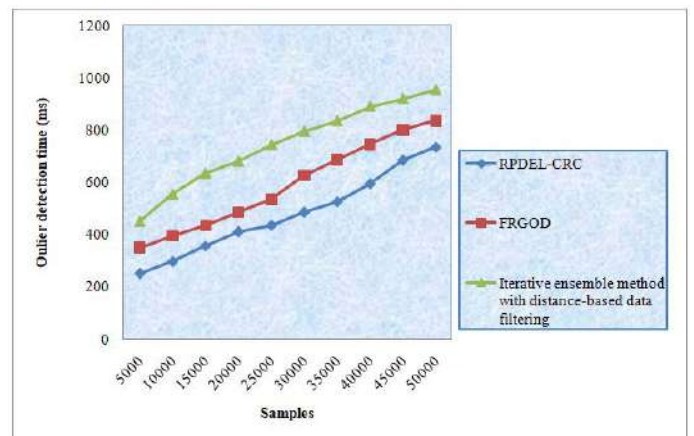


Fig. 4. Graphical Representation of Outlier Detection Time.

B. Case Analysis of Outlier Detection Accuracy

The second parameter of significance for cluster based outlier detection is the accuracy rate. In other words, the outlier detection accuracy is measured based on percentage ratio

between the samples involved in simulation process ‘ $\llbracket$  Samples $\rrbracket_i$ ’ and the actual samples accurately detected with outliers ‘ $\llbracket$  Samples $\rrbracket_{ODC}$ ’. This is mathematically stated as given below.

$$OD_{acc} = \sum_{i=1}^n \frac{Samples_{ODC}}{Samples_i} * 100 \quad (16)$$

Table II given shows the results of outlier detection accuracy observed for three different methods, RPDEL-CRC, FRGOD [1] and Iterative ensemble method with distance-based data filtering [2].

Fig. 5 illustrates the outlier detection accuracy for 50000 different stock samples obtained from the NIFTY-50 stock dataset at different time instances. From the figure it is inferred that the outlier detection accuracy is found to be inversely proportional to the stock samples involved in the simulation process. In other words, increasing the stock samples for detecting the outlier causes an increase in the overall data points involved in the process and this in turn minimizes the outlier detection accuracy. However, sample simulations performed with 5000 samples 4845 samples were accurately detected with outliers as it is using RPDEL-CRC, 4755 samples using [1] and 4695 samples using [2]. With this the overall accuracy using the three methods were found to be 96.90%, 95.1% and 93.9% respectively. The overall accuracy was found to be improved using RPDEL-CRC upon comparison with [1] and [2]. The reason behind the outlier detection accuracy improvement was owing to the application of Chebyshev distance function. By applying this distance function, the difference between two data points along any cluster was first evaluated. Then, on the basis of the minimum number of positioning between clusters, according to time, results were obtained, i.e., outliers were detected, therefore ensuring outlier detection accuracy. This in turn improved the outlier detection accuracy using RPDEL-CRC method by 3% compared to [1] and 7% compared to [2].

### C. Case Analysis of False Positive Rate

False positive rate is measured as the ratio between the numbers of negative events (i.e., negative outliers) wrongly categorized as positive (i.e., outliers) and the total number of actual negative events (i.e., actual outliers). This is mathematically stated as given below.

$$FPR = \frac{FP}{FP+TN} \quad (17)$$

From the above (17), the false positive rate ‘FPR’ is measured based on the false positive samples ‘FP’ (i.e., actually the data are not outliers) and the true negative samples ‘TN’ (i.e., outliers detected as outliers) respectively. Table III given shows the results of false positive rate observed for three different methods, RPDEL-CRC, FRGOD and Iterative ensemble method with distance-based data filtering [2].

TABLE II. TABULATION FOR OUTLIER DETECTION ACCURACY

Samples	Outlier detection accuracy (%)		
	RPDEL-CRC	FRGOD	Iterative ensemble method with distance-based data filtering
5000	96.9	95.1	93.9
10000	95.35	94.35	91.15
15000	94.15	92.85	90.35
20000	94.05	91.55	88.15
25000	93.85	91	88
30000	93.25	90.85	87.35
35000	93	90.25	86
40000	92.55	89.85	85.25
45000	92.15	89.15	84.35
50000	92	89	83

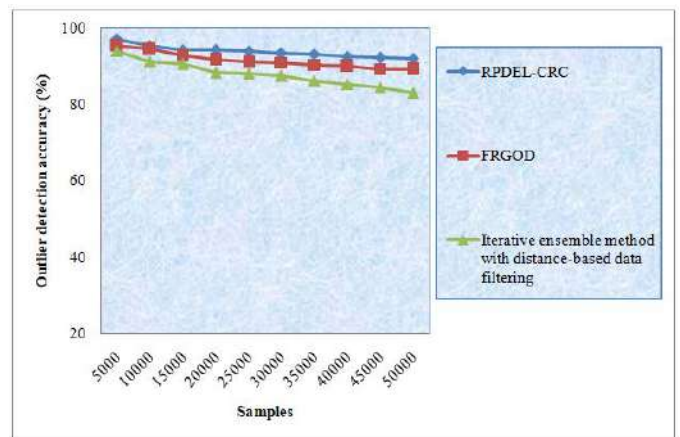


Fig. 5. Graphical Representation of Outlier Detection Accuracy.

TABLE III. TABULATION FOR FALSE POSITIVE RATE

Samples	False positive rate (%)		
	RPDEL-CRC	FRGOD	Iterative ensemble method with distance-based data filtering
5000	0.007	0.015	0.025
10000	0.015	0.018	0.026
15000	0.018	0.025	0.028
20000	0.02	0.028	0.033
25000	0.022	0.031	0.035
30000	0.025	0.032	0.036
35000	0.027	0.035	0.038
40000	0.029	0.037	0.042
45000	0.035	0.039	0.044
50000	0.038	0.042	0.048

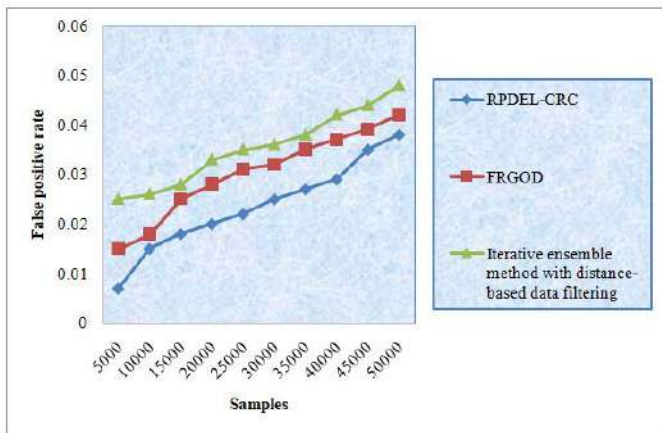


Fig. 6. Graphical Representation of False Positive Rate.

Fig. 6 given depicts false positive rate for different stock samples. From the figure, it is inferred that the false positive rate also increases with the increase in the number of stock samples involved in the simulation and hence the false positive rate is found to be directly proportional to the stock samples or samples. However, simulations conducted for 5000 samples show a false positive rate of 0.007 using RPDEL-CRC, 0.015 using FRGOD [1] and 0.025 using Iterative ensemble method with distance-based data filtering [2]. From this, it is observed that the false positive rate is comparatively lesser using RPDEL-CRC when compared to [1] and [2]. The reason behind is the application of Chebyshev Temporal and Reflective Correlation-based Outlier Detection algorithm. By applying this algorithm, dependency between two distributions of data points or data are separated. First, according to different weight of data points, i.e., based on the neighbors or data points in cluster, updated weight of a centroid data point is obtained. Next, with the identified updated weight of a centroid data point, outliers are detected based on the linear correlation between data points. Hence, by applying different updated weight of a centroid data point for each cluster, false positive rates are significantly reduced using RPDEL-CRC method by 24% compared to [1] and 36% compared to [2].

#### D. Case Analysis of Error Rate

Finally, the error rate involved in outlier detection is discussed in this section. The error rate is one of the significant parameters involved in the outlier detection process. This is owing to the reason that while clustering certain data points are said to be misplaced in the adjoining clusters, therefore resulting in error. This error rate is mathematically stated as given below.

$$ER = \left( \frac{V_{actual} - V_{expected}}{V_{expected}} \right) * \% \quad (18)$$

From the above (18), the error rate ‘ER’ is measured based on the actual value ‘V\_actual’ or the actual data point positioning and the expected value ‘V\_expected’ or the expected data positioning. It is measured in terms of percentage (%). Finally, Table IV lists the error rate obtained using the (18).

Finally, Fig. 7 illustrates the error rate observed during the process of outlier detection. From the figure, an increasing

trend is found to be observed using all the three methods, RPDEL-CRC, FRGOD [1] and Iterative ensemble method with distance-based data filtering [2] increasing the stock samples. This is due to the reason that with the increase in the stock samples provided as input obtained during different time instances from different companies, first, clusters are performed. While performing the clustering based on data points certain data points due to temporal instances cause a small shift in the positioning of clusters. This in turn results in the deviation and therefore error. However, simulations conducted with 5000 samples with actual data positioning observed to be 53, the expected data positioning using the three methods were observed to be 48, 45 and 43. Hence, the error rate were found to be 9.4%, 15.09% and 18.86% respectively using the three methods, therefore reducing the error with RPDEL-CRC method. The reason behind the minimization of error using RPDEL-CRC method was due to the application of Gaussian Random Projection-based Deep Extreme Learning-based Clustering algorithm. By applying this algorithm, the learning rate for solving the output weights were estimated by means of square gradient. As a result, the error rate using RPDEL-CRC was said to be reduced by 28% compared to [1] and 45% compared to [2].

TABLE IV. TABULATION FOR ERROR RATE

Samples	Error rate (%)		
	RPDEL-CRC	FRGOD	Iterative ensemble method with distance-based data filtering
5000	9.4	15.09	18.86
10000	9.75	16.15	21.32
15000	10.35	16.35	22
20000	10.85	17.25	22.85
25000	11.35	17.85	24.35
30000	13.15	18.35	24.85
35000	15.25	20	25
40000	17.35	21.35	28
45000	19.55	22.45	29.35
50000	21.25	23	30

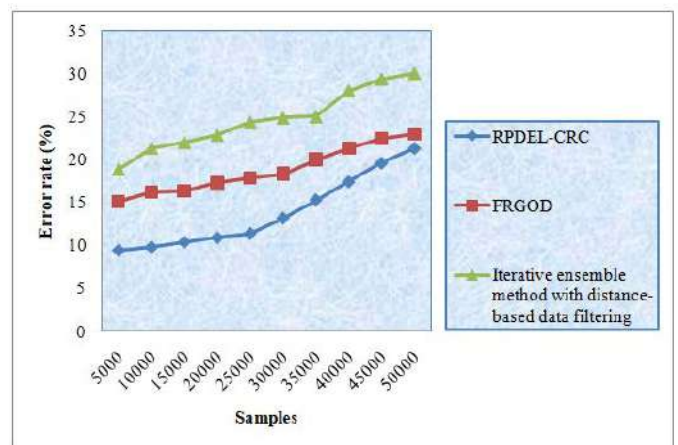


Fig. 7. Graphical Representation of Error Rate.

## VI. CONCLUSION

In spite of the fact that there has been an improvement in outlier detection, nevertheless mushrooming outliers are still found in its disastrous intents. In this day and age, it has become a big ultimatum that the behavior of outliers has to be monitored in many data mining tasks. In this paper, we proposed a new outlier detection method, called, Random Projection Deep Extreme Learning-based Chebyshev Reflective Correlation (RPDEL-CRC). The main contributions of our proposed RPDEL-CRC method is to the field of outlier detection that reduces the outlier detection time, error and false positive rate involved with maximum accuracy. The proposed method reduces the outlier detection time and error for operating the outlier detection via Gaussian Random Projection-based Deep Extreme Learning model that initially performs the clustering process by means of Gaussian Random Projection function. Next, with behavior grouping and clustering using Deep Extreme Learning, false positive rate is reduced in a timely manner. Third, the actual outlier detection process based on the clustering results is performed by means of Chebyshev Temporal and Reflective Correlation-based Outlier Detection model. Simulations were performed to evaluate the performance of RPDEL-CRC, FRGOD and Iterative ensemble method with distance-based data filtering method. Simulation results revealed that the proposed RPDEL-CRC method outperforms, FRGOD and Iterative ensemble method with distance-based data filtering method implementations, in terms of outlier detection time, accuracy, error rate and false positive rate.

### REFERENCES

- [1] Zhong Yuan, Hongmei Chen, Tianrui Li, Binbin Sang, and Shu Wang, "Outlier Detection Based on Fuzzy Rough Granules in Mixed Attribute Data," *IEEE Transactions on Cybernetics*, May 2021 [fuzzy rough granules-based outlier detection (FRGOD)].
- [2] Bodhan Chakraborty, Agneet Chatterjee, Samir Malakar, and Ram Sarkar, "An iterative approach to unsupervised outlier detection using ensemble method and distance-based data filtering," *Springer Complex & Intelligent Systems*, Feb 2022, [Iterative ensemble method with distance-based data filtering].
- [3] Asma Belhadi, Youcef Djenouri, Djamel Djenouri, Tomasz Michalak, and Jerry Chun-Wei Lin, "Deep Learning Versus Traditional Solutions for Group Trajectory Outliers," *IEEE Transactions on Cybernetics*, Dec 2020.
- [4] Saihua Cai, Ruizhi Sun, Shangbo Hao, Sicong Li, and Gang Yuan, "An Efficient Outlier Detection Approach on Weighted Data Stream Based on Minimal Rare Pattern Mi," *IEEE Xplore*, Oct 2019.
- [5] Asma Belhadi, Youcef Djenouri, Gautam Srivastava, Djamel Djenouri, Jerry Chun-Wei Lin, and Giancarlo Fortino, "Deep learning for pedestrian collective behavior analysis in smart cities: A model of group trajectory outlier detection," *Information Fusion*, Elsevier, Feb 2021.
- [6] Hongwei Du, Qiang Ye, Zhipeng Sun, Chuang Liu, and Wen Xu, "FAST-ODT: A Lightweight Outlier Detection Scheme for Categorical Data Sets," *IEEE Transactions of Network Science and Engineering*, Oct 2020].
- [7] You Lin, and Jianhui Wang, "Probabilistic Deep Autoencoder for Power System Measurement Outlier Detection and Reconstruction," *IEEE Transactions on Smart Grid*, Jul 2019.
- [8] N. Jayanthi, Burra Vijaya Babu, and N. Sambasiva Rao, "An ensemble framework based outlier detection system in high dimensional data using Tree Technique," *Materials Today: Proceedings*, Elsevier, Nov 2020.
- [9] Atiq ur Rehman, and Samir Brahim Belhaouari, "Unsupervised outlier detection in multidimensional data," *Journal of Big Data*, Springer, Jun 2021.
- [10] Mahsa Salehi, Christopher Leckie, James C. Bezdek, Tharshan Vaithianathan and Xuyun Zhang, "Fast Memory Efficient Local Outlier Detection in Data Streams," *IEEE Transactions on Knowledge and Data Engineering*, Nov 2016.
- [11] Huiping Li, BinWang, and Xin Xie, "An improved content-based outlier detection method for ICS intrusion detection," *EURASIP Journal on Wireless Communications and Networking*, Springer, Aug 2020.
- [12] Ángela Fernández, Juan Bella, and José R. Dorronsoro, "Supervised outlier detection for classification and regression," *Neurocomputing*, Springer, Feb 2022.
- [13] Zhen Cheng, En Zhu, Siqi Wang, Pei Zhang, and Wang Li, "Unsupervised Outlier Detection via Transformation Invariant Autoe," *IEEE Access*, Mar 2021.
- [14] Hongzhi Wang, Mohamed Jaward Bah, and Mohamed Hammad, "Progress in Outlier Detection Techniques: A Survey," *IEEE Access*, Aug 2019.
- [15] Xie Ling, Jia Yanlin, Xiao Jin, Gu Xin, and Huang Jing, "GMDH-Based Outlier Detection Model in Classification Problems," *Journal of Systems Science and Complexity*, Springer, Feb 2020.
- [16] Ali Degirmenci and Omer Karal, "Robust Incremental Outlier Detection Approach Based on a New Metric in Data Streams," *IEEE Access*, Nov 2021.
- [17] Fangyi Wan, Gaodeng Guo, Chunlin Zhang, Qing Goo, and Jie Liu, "Outlier Detection for Monitoring Data Using Stacked Autoencoder," *IEEE Access*, Nov 2019.
- [18] Ping Yang, Dan Wang, Zhuojun Wei, Xiaolin Du, and Tong Li, "An Outlier Detection Approach Based on Improved Self-Organizing Feature Map Clustering Algorithm," *IEEE Access*, Aug 2019.
- [19] Lu Liu, and Shang Wang, "Meta-path-based outlier detection in heterogeneous information network," *Frontiers of Computer Science*, Springer, Nov 2019.
- [20] Jintao Song, Shengfei Zhang, Fei Tong, Jie Yang, Zhiquan Zeng, and Shuai Yuan, "Outlier Detection Based on Multivariable Panel Data and K-Means Clustering for Dam Deformation Monitoring Data," *Advances in Civil Engineering*, Hindawi, Dec 2021.



SACRED HEART RESEARCH PUBLICATIONS

# Journal of Computing and Intelligent Systems

Journal homepage: [www.shcpub.edu.in](http://www.shcpub.edu.in)



ISSN: 2456-9496

## Hit of Fit: A Moral Analysis of Detecting Outliers using Clustering-Based Approach

Rajalakshmi<sup>#1</sup>, P. Madubala<sup>#2</sup>

Received on 25 APR 2022, Accepted on 15 JUN 2022

**Abstract** —Researchers are becoming increasingly interested in odd behaviour as machine learning and data analytics develop. The goal of this work is to improve the estimation of numerous factors that hide outliers and produce the best clustering results. In the real-time environment, outlier detection is an important research area. To deal with the overwhelming amount of uncertainty, the following factors make the approach difficult: a) defining the boundary between normal and abnormal behaviour b) cluster size distributed over space; c) stabilising the centroid point; d) model validation; e) difficult to distinguish noise; f) modifying unnormalized data into robust data; g) estimating fuzzy function point metric that gives more insight to imbalanced data in outliers using fuzziness. The primary goal of the first stage is to reduce noise. The data is clustered using fuzzy clustering in the second stage. To stabilise the centroid, the third stage uses a variety of algorithms, including numerous rounds of k-means, fuzzy clustering, and an improved method. After that, determine the fuzzy-fp metric, fuzzy variable index, and utilisation factor to complete the outcome analysis. Using the silhouette, Pseudo-F-Statistic, and Constellation methods, the cluster goodness is verified in the last stage. The benefits and drawbacks of this strategy are effectively listed. In a huge dataset, the outcome reveals a higher performance that identifies the factor by a high performance score and adds insight to provide a balanced view of the data.

**Keywords**– Clustering and Fuzzy.

### I. INTRODUCTION

In a variety of sectors, data mining is becoming increasingly popular. Researchers are tremendously interested in uncovering unexpected behaviour across large datasets. In data mining, outlier detection is intensively investigated and developed for specific application domains, while others are generic in nature. It's one of the most significant and hotly debated topics in science, and it's facing a slew of new difficulties. Changes in system behaviour, mechanical faults, human error, natural variations, and instrumental error all includes in it. Due to technological advancements, it aids in the comprehension of numerous dimensions that are used in various substantive fields. An outlier is a rare occurrence in a dataset that could be caused by a variety of factors. Finding and eliminating outliers from a data sample using simple univariate statistics such as standard deviation and interquartile range improve predictive modelling performance from a training dataset. The technique of finding outliers in a

dataset is known as outlier detection. They defy the dataset's usual patterns. Outliers are predicted by a goal variable, but the rest of the points are typical. A clustering technique is used to find outliers, which skews the model's representation. Noise can take many forms, including incorrect data entry, mechanical faults, experimental failure, and natural diseases.

### II. OUTLIER DETECTION TYPES

- necessary.
- Unsupervised :There is no need to label the training data.
- Semi-supervised : an approach that combines supervised and unsupervised techniques

#### A. Applications

Detection of Fraud, Detecting the intrusion into the network Monitoring system activity and network performance, evaluating satellite photos, Keeping track of the passage of time, Data Leakage Prevention, Medical Report Diagnosis, Criminal Actions in E-Commerce, Video Surveillance, Anti-Terrorism, Pharmaceutical Research, recognising novelties, etc.

### III. OBJECTIVE OF THIS PAPER

All Patterns that do not fit into a well-defined definition of normal behaviour are referred to as outliers. Anomalies, abnormalities, deviants, discordants, extreme data points, and other terms for outliers are all used to describe them. The phrases Outlier and Anomaly are interchangeable when it comes to revealing important information about a typical features. The following reasons make the technique extremely difficult: a) defining the line between normal and abnormal behaviour; b) model validation c) separating noise. b) cluster size distributed over space; c) stabilising the centroid point f) modifying unnormalized data into robust data;

**\*Corresponding author:**

**E-mail:**<sup>1</sup>rajaylakshmiravi7@gmail.com,<sup>2</sup>madhubalasivaji@gmail.com

<sup>1</sup>Research Scholar, Department of computer science, Periyar University, Salem, Tamilnadu

<sup>2</sup>Research Supervisor, Department of computer science, Periyar University, Salem, Tamilnadu

g) estimating fuzzy function point metric that gives more insight to imbalanced data in outliers using fuzziness

### A. Organization of the Paper

The Outlier detection (also known as anomaly detection) is a crucial and difficult task in data mining for a variety of applications, including credit card fraud detection, intrusion detection, and image processing. They analyse the datasets in a meaningful and entertaining way. This study describes a method for detecting outliers that is both accurate and efficient. Outlier detection and prediction are inextricably linked. Outlier detection in its various forms is used in a variety of fields to identify intrusion, recognise anomalies, and so on. Detecting occurrences in credit card transactions that are fraudulent analysing system network traffic, diagnosing medical reports executing the legislation change, hastening the damage figuring out textual anomaly detection in the industrial sector figuring out how to detect textual irregularity in the industrial sector etc., This study suggests that instead of deleting outliers, they should be worked with to fit within the boundary if necessary, as well as enhancing the estimation of various parameters that mask outliers during clustering.

An outlier in a dataset is an uncommon occurrence that can be caused by a multitude of circumstances. Simple univariate statistics such as standard deviation and interquartile range can help forecast model performance by identifying and removing outliers from a data sample. Compare typical and anomalous observations before declaring a datapoint as "outlier." Outlier is a term that refers to the intrinsic diversity of observation. Two types of outliers are possible. a) Excessive values (correct entry can not fit within cluster) b) Errors ( wrong entry in the right place). The statistical analysis is hampered by missing values and null values, which lead to errors and disruptions. Error metrics is the most important phase in detecting the error from the prediction of evaluation.

### B. Related Works

Unsupervised techniques of mixed data are studied in [1]. Applications, techniques in various domains are studied in [2]. A survey about outliers are studied in [3]. Cluster centroid stability using fuzzy is studied in [4]. Multivalued data streams using clustering is studied in [5].

### C. Fuzzy clustering

Clustering is the process of identifying comparable groupings of data in a dataset. Clustering is a strategy for unsupervised learning that is subjective in nature. Soft clustering, often known as fuzzy clustering, is a type of clustering that has a tendency to be fuzzy. Simple implementation with dependable performance creates uncertainty in the model. In 1981, Jim Bezdek came up with the idea that for each member in the dataset, it discovers known variants using the membership  $[0,1]$  and prototype matrix.

The membership grade (or degree of membership) is calculated using Euclidean distance and statistical features of clusters.

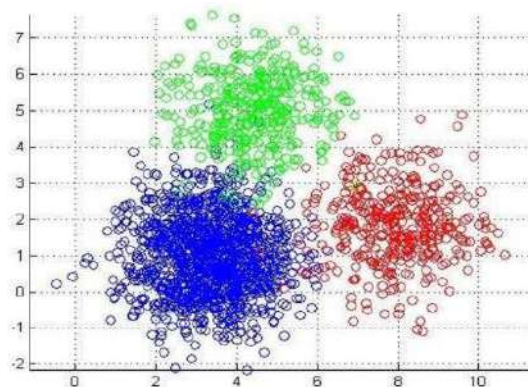


Fig. 1. Fuzzy Clustering

Consider a set  $S$  with a subset  $A(x)$  and elements defined as  $A(x) = 1$  if membership degree is subset value 0, and  $A(x) >$  subset value if membership degree is  $>$  subset value. The fuzzy membership ranges from 0 to 1. Each data point is assigned membership, and the distance between the data point and the cluster centre is determined. The centroid centre, rather than the borders, has a high degree of membership for the data objects. A membership value of one corresponds to each data point.

### D. Pseudocode of Fuzzy

1. Set up the membership matrix  $U$ .
2. Find the centre of the fuzzy cluster circle  $C$ .
3. Using Euclidean distance, calculate the distance between distinct circle centres.
4. Continue to calculate OF until it falls below the threshold.
5. Otherwise, To acquire the best value, fix a random point 'p' and repeat step 2 again.

### E. Proposed Methodology

"There won't be any intruders among the outliers." They have a variety of effects on the regression line, including the appearance of normal predictor values, atypical predictor values following the line, and unusual predictor values not following the line. Outliers can be caused by a variety of factors, including incorrect entry, misreporting, sample error, and a rare but genuine value. a) Discarding b) Winsorizing c) Variable transformation d) Fit various models are some of the common methods for dealing with outliers. e) Dropping but not forgetting f) Non-parametric approaches.



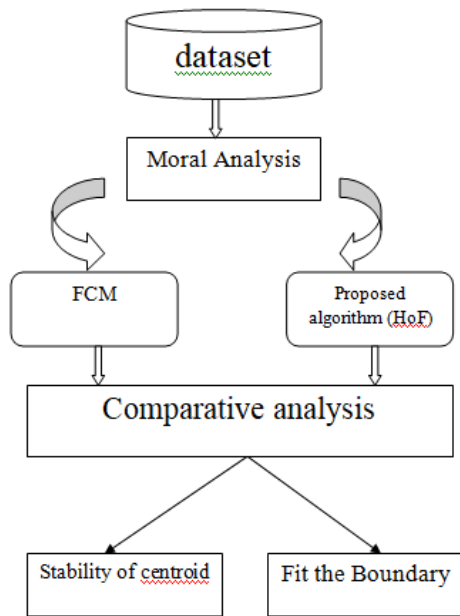


Fig. 2. The Framework of HoF Analysis

Outliers are points that are distinct from the rest of the data and provide useful information for the analysis. 1.data turns out to be skewed format 2.changes the overall statistical distribution of data in terms of mean,variance 3.Leads to obtain a bias in the accuracy level of the model. Figure 2 shows the framework of HoF.

**F. System Model**

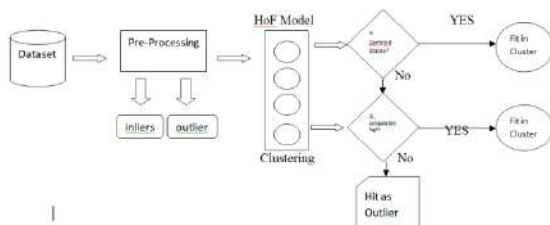


Fig. 3. Block Diagram of Proposed model (HoF)

**G. Proposed Algorithm (HoF : Hit of Fit)**

To create an objective function, run FCM. [HOF]

To find outliers, divide the data into tiny groups.

The remaining details (not in step 2)

Begin  
 Sum=0.5  
 Remove one point from each Pi point in the set.  
 Calculate HOFi using Pi

$DOFi = \frac{(HOF - HOFi)}{2}$  is the formula for calculating DOFi.

Sum =DOFi+Sum  
 Do Avg DOF=sum/n and return Pi.  
 Pi is equal to each point  
 Do If (DOFi> T) and return if point pi is an outlier.  
 Otherwise, come to a halt.

**H. Experimental setup**

**Case analysis of Outlier Detection - centroid stability**

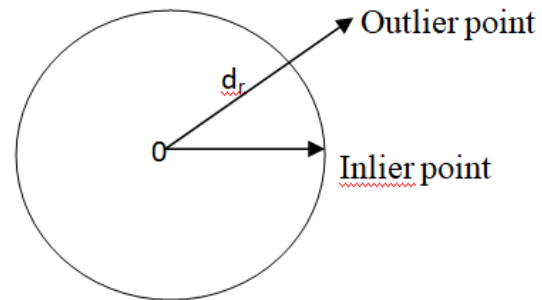


Fig.4 Stabilizing centroid point of the cluster

Consider a Dataset 'ds' with 'dpi' datapoints as inliers, 'dpo' datapoints as outliers and 'dr' as distance with reachability time. If reachability time is minimum, computational efficiency is high. From Fig. (3),

If dpi < threshold boundary, so called inliers

If dpo < threshold boundary, so called outliers.

**TABLE 1 CENTROID STABILY**

Dataset	Samples	FCM (outliers detected)	HoF(outliers detected)	No of iterations
Stock	3000	yes	yes	250
Advertising	200	No	yes	250

**TABLE 2 COMPUTATIONAL EFFICIENCY**

Dataset	Sample s	FCM (outliers detected)	HoF(outliers detected)	No of iterations
Stock	3000	yes	yes	250
Advertising	200	No	yes	250

From Table 1 and 2 it is clear that HoF algorithm works well in aspect of cluster centroid stability and high computational efficiency.

1. When data is normalised with a Z-score (-3 to +3), an IQR is calculated. (IQR) (Interquartile Range) (Interquartile Range) (Interquartile Range)

2. Data is prepared using one of the following methods:  
a) Graphical Method b) Numerical Method

3. Analysis Techniques a) High Leverage Point b) Influential Observations c) Simple Linear Regression a) High Leverage Point b) Influential Observations c) Simple Linear Regression a) High Leverage  
4. Assessment Methods - Algorithms for fuzzy grouping and calculating centroid

#### IV. COMPARATIVE ANALYSIS

Before clustering consider the following points, i) determine the number of clusters to be stated. ii) Know how to optimize (k=3) and solve a problem before creating the method. iii) Understand why your data should be grouped into a certain number. Following table shows the comparative analysis.

**TABLE 3**  
COMPARATIVE ANALYSIS OF DATASETS

Algorithm	Dataset	No of records	No of clusters	Result percentage
FCM	Advertising	200	3	44.06%
	Stock_data	3000	3	52.52%
Proposed algorithm (HoF)	Advertising	200	3	61.92%
	Stock_data	3000	3	69.48%

Thus from fig (4) and table 3 shows that proposed system works well for stock dataset in an efficient manner.

#### V. Conclusions

We obtain subjective knowledge and observation of the data through analysing. The proposed approach is compared with existing method by considering advertising and stock dataset to prove stability of the centroid and high computational efficiency.

#### ACKNOWLEDGMENT

I sincerely thank my research supervisor who encourages to complete my work a great success.

#### REFERENCES

- [1] AtiqurRehman, Samir BrahimBelhaouari, "Unsupervised outlier detection in multidimensional data," Journal of Big data, 2021.
- [2] Xiaodan Xu, Huawei Liu, Minghai Yao, "Recent Progress of Anomaly Detection," Hindawi, 2019.
- [3] Hongzhi Wang, Mohamed Jaward Bah, Mohamed Hammad, "Progress in Outlier Detection Techniques: A Survey," IEEE, 2019.
- [4] ErindBedalli, EneaMancellari, OzcanAsilkan, "A heterogeneous cluster ensemble model for improving the stability of fuzzy cluster analysis," Elsevier, 2016.
- [5] Agnieszka Duraja, Piotr S.Szczepaniaka, "Outlier Detection in Data Streams - A Comparative study of selected methods", Elsevier, 2021.

# ENHANCED LION SWARM OPTIMIZATION ALGORITHM WITH CENTRALIZED AUTHENTICATION APPROACH FOR SECURED DATA TRANSMISSION OVER WSN

S. Silambarasan<sup>1</sup> and M. Savitha Devi<sup>2</sup>

<sup>1</sup>Department of Computer Science, Periyar University, India

<sup>2</sup>Department of Computer Science, Periyar University Constituent College of Arts and Science, India

## Abstract

*Securing data accuracy in WSNs (Wireless Sensor Networks) is a major problem. Aggregation techniques for improving accuracy in data processing have been gaining attention of scholars, recently. Existing security systems using singular paths for transmission of data have delays in transmissions while being open to intrusions. Moreover, increased computational overheads and processing time increases the delay of data transmission in the given networks. To overcome these issues, this work proposes ELSOA-CA (Enhanced Lion Swarm Optimization Algorithm and Centralized Authentication) method. This method focuses on an optimal, faster and energy efficient data transmissions while ensuring accurate decisions on tomato crops. Multipath routing introduced in the proposed method ensures faster data transmissions by selecting optimal forwarder nodes which satisfy the constraints of delay and energy. Optimal forwarder node selection is done using ELOSA algorithm. Data transmissions are secured by centralized authentication involving third party nodes. Each and every node in a region gets registered with the authentication node where a node's genuineness is checked the node is allowed into the forwarder node list, used for data routing. CA (Centralized Authentication) enhances the security level of data transmissions over WSN multi path routing. ELSOA-CA framework's simulation results provide higher throughputs, reduced energy consumptions, improved network lifetimes PDRs (Packet Drop Ratios) and lesser delay times.*

## Keywords:

*Wireless Sensor Networks, Enhanced Lion Swarm Optimization Algorithm, Centralized Authentication Approach, Secured Data Transmission, Multipath Routing*

## 1. INTRODUCTION

WSNs are made of thousands of sensor nodes which communicate amongst themselves and are used in environment monitoring like humidity, temperature, air pollution and seismic event detections. WSN sensor nodes have processing, sensing and communication units. They transmit data using radio transceivers to a centralized collection point called Base Station (BS) [1] [2]. WSN nodes are powered by non-rechargeable batteries and their energy resources are limited. Though the distance between the sink and nodes is long, high node density and multi-hop models compensate this distance during communications. Each node passes collected information to neighboring nodes in the network.

Harvested energy is not-based on a time factor and varies thus predicting energy is a crucial task. The low energy levels of sensor nodes can cause serious impacts such as packet drop, data reliability and network lifetime. Many approaches have proposed management of node activities like node's sampling rate or energy harvests for effectively improving network lifetimes and performances [3]. WSN routings approaches-based on energy harvests have been widely proposed. For Example, an intelligent

approach-based on harvested energy using maximum point tracking algorithm powered by solar power was proposed in [4], while the study in [5] presented Harvesting Aware Speed Selection (HASS) by implementing an iterative process with dynamic voltage scaling to maintain the network energy consumption levels and saving harvested energy. Similarly, geographical routing-based approaches have also been adopted widely in which 1-hop neighbor nodes are selected for data transmissions.

The study in [6], presented Easy-Go approach using geographical routing-based packet forwarding for energy management. Duty-cycle-based approaches have also been introduced to improve the network lifetime [7]. The aforementioned techniques are-based on the different type of forwarding schemes. Schemes-based on packet forwarding, sleep-awake scheduling etc. have been addressed using cross-layer-based communication [8]. Though these schemes provide better lifetime performances, maintaining energy consumptions and harvesting energy is important and hence development of harvested energy management is a crucial task

In general, the energy harvesting process is mainly categorized into two main categories as energy harvesting from natural resources such as wind, thermal and vibration and energy-rich sources using wireless energy transfer mechanism. As discussed before, WSNs adopted for various applications can use energy harvesting techniques for improving network lifetime as energy harvesting techniques provide a continuous supply of energy to the sensor nodes, keeping them alive [9].

This assumption culminated in [10] where energy harvesting was used for packet forwarding. The study's proposed scheme created gradient-based node's relative position. This clustering model chose cluster heads-based on a value computed using storage and relative distances. The model also proposed a distribution of energy where the cluster heads shared traffic loads amongst themselves. Their scheme reduced cluster head reformation frequencies by reducing overheads. The Fig.1 depicts the structure of a WSN.

Current WSNs use multi-path schemes to enhance network performances as they can be accomplished by efficient utilization of resources. These schemes have also been formulated in wired and WSNs for reliability/fault-tolerant data transmissions, QoS (Quality of Service) and congestion controls. Multi-path routing schemes need to consider several constraints like power limitations, minimized computational capability and low memory resources. Moreover, the limitations in short-range radio communications like fading effects and interferences add challenges to multi-path protocol designs [11]. Existing multi-path schemes of traditional WSNs like Ad hoc networks have issues directly-based on low energy resources.

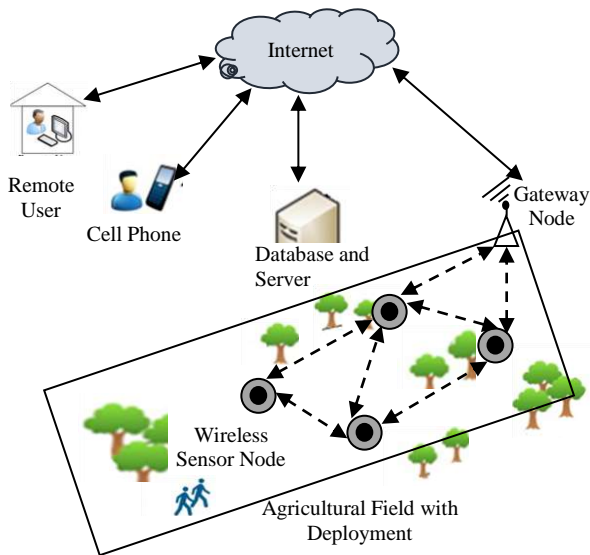


Fig.1 Structure of WSN

Due to the aforesaid reasons, the main aim of this work is optimizing the routing in WSNs with quick data transmissions. The next section is a review of related literature while section three discusses the proposed ELSOA-CA framework. Experimental results and the proposed scheme's performance are analyzed in section four. The paper concludes with section five.

## 2. RELATED WORK

Nguyen et al. [12] discussed the advantages of the WSN and the contribution of energy-harvesting schemes to improve the communication performance of the network. The authors focused on the advantages of energy harvesting schemes for IoT (Internet of Things)-based applications. The main advantage of the energy harvesting technique is that the energy source replacement issues can be resolved by providing the continuous power supply with the help of ambient sources of energy. Various types of approaches have been introduced recently to overcome the issue of energy harvesting such as the development of an efficient model for power generation and energy-aware routing protocols etc. The hardware implementation can cause a higher cost of implementation hence routing protocols are considered as a promising solution to address these issues. In this work, authors focused on the energy harvesting and developed energy-harvesting-aware-routing for heterogeneous IoT-based WSN applications.

Tang et al. [13] also focused on the IoT-based application scenario for energy-harvesting in WSN. In this work, a Trust-Based Secure Routing approach is developed which helps to improve the security and maximizes the available energy for energy-harvesting for sensor networks. According to this process, source and sink communicate using disjoint paths and hence the data can be verified separately to ensure the security. Furthermore, a traceback approach is also implemented which uses a probability-based approach to identify the malicious node. This probability-based approach helps to cop-up the issue of security and battery levels.

Fractional clustering was used by Sirdeshpande et al. [14] in their study. Their optimization algorithm called Fractional Lion

(FLION) used clustering for finding energy efficient routing paths. Their proposed schema improved network's lifetime and energy in their rapid selection of Cluster Heads (CHs). Their proposed FLION clustering algorithm used a fitness function for computing intra/inter cluster distances, CH energy, delays and node's energy while formulating multi-paths for routing. Their fitness function quickly identified cluster centroids for efficiency in discovering routing paths. They evaluated their proposed FLION clustering with other clustering algorithms like Fractional LSDAR, Low Energy Adaptive Clustering Hierarchy (LEACH), Artificial Bee Colony (ABC) and Particle Swarm Optimization (PSO)-based clustering algorithms. Experimentations of FLION showed that the scheme maximized WSN's lifetime.

Conditions conducive to routing were specified by Arya et al. [15]. The study detailed on ideal conditions required for feasible bandwidth usage. Their bandwidth estimations were optimized for saving energy using Ant Colony Optimization (ACO). Their work showed the performances of energy aware routing protocols without optimizations to compute WSN energy utilizations with estimated bandwidths. ACO optimized energy consumptions and computed optimized bandwidths for routing paths. Network performance was analyzed using bit error rates. Their experimental results showed ACO optimizations provided feasible and efficient routing solutions that improved WSN's lifetime.

Lion Swarm Optimization (LSO) was used by Guo et al. [16] in their work which attempted to improve global exploration capabilities using multi-agent structures. Their scheme combined LSO and multi-agent system for improving efficiency and accuracy in searches and by using group/environment information in a recursive fashion for economic load distribution of power. Their experimentation results showed that their proposed system significantly improved efficiency and robustness of power distribution, proving its effectiveness.

The work by Chang et al. [17] used Elliptic Curve Cryptography (ECC) in WSNs for improving authentications for protocols. The proposal initialized systems, registered nodes and authenticated nodes. A multiplication operation and sensor ID hash value were used for authenticating nodes. Nodes also authenticated other nodes using the scheme to enhance WSN security.

ECC was also used by Shankar et al. [18] to implement data exchanges or secure distribution of keys which paralleled RSA security with a lesser key size. The scheme also proposed mutual authentications between sink nodes and base station servers. The sink's ID, a random registered and timestamp values were used for the bi-authentication mechanism. The proposed scheme could detect replay attacks and enhanced security in healthcare-based WSN devices.

## 3. PROPOSED METHODOLOGY

The proposed methodology is aimed at helping agriculture by proposing ELSOA-CA framework which ensures accuracy of decisions regarding tomato crops using WSN sensor data. The overall methodology of ELSOA-CA framework is depicted in Fig.2.

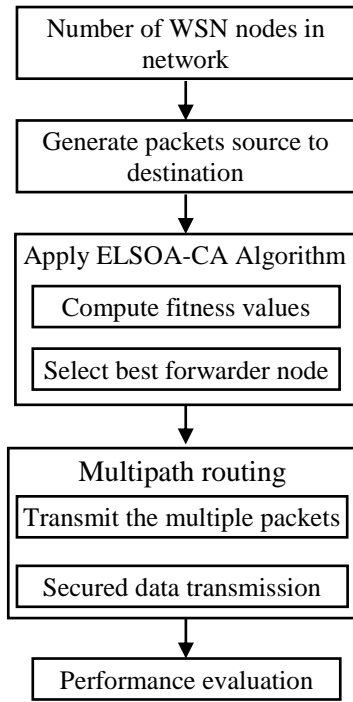


Fig.2. ELSOA-CA Framework - Block Diagram

### 3.1 SYSTEM MODEL

In this scenario, WSN is composed of N different sensor nodes, which can sense, observe and obtain data. Each node in the given network are immobile and power controlled [19]. All WSN nodes execute sensing tasks regularly with constant information transmissions to the BS which handles nodes within/outside its range. Nodes can be CHs or plain sensor nodes. The network formation is shown in Fig.3.

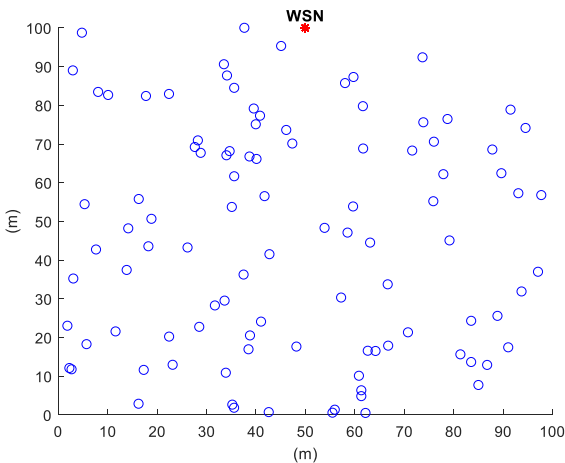


Fig.3. Network Formation

#### 3.1.1 Energy Model:

The proposed framework analyzes energy of nodes. Assuming each node has an initial energy,  $E_i$ , then the energy gets depleted when a node  $i$ , replies or broadcasts to another node  $j$ . The power consumed in transmissions is  $P_T$  while  $P_R$  the power utilization of  $i$  while receiving data unit from  $j$ . Again, assuming that a sink node has unlimited energy and constantly moves till end of network lifetime (from the start till it is dead), then the objective

of optimization narrows down to finding optimality in routing strategies and CH selections which can enhance network lifetime. Linear programming models can maximize network lifetimes. The Power consumed while transmitting  $L$  bits for distance  $D_i$  is shown in Eq.(1),

$$P_T = \begin{cases} P_{cons} * L * P_{amp} * D_i^2 & \text{if } D_i < D_0 \\ P_{cons} * L * P_{amp} * D_i^2 & \text{if } D_i \geq D_0 \end{cases} \quad (1)$$

$$P_R = P_{cons} * L \quad (2)$$

where

$E_{amp}$  is power dissipated.

$P_T$  is power consumption while transmission of packets

$L$  is bits

$P_{amp}$  is power amplification

$D_i$  is distance among nodes

$D_0$  is threshold distance

$P_R$  is power consumption while receiving the packets

The power consumption is reduced significantly in the node further while the data transmission and shortest routing path can be ensured effectively.

#### 3.1.2 Mobility Model:

This model is for IoTs nodes in a system. The model is based on device location, speed and connectedness. Let  $n_1$  and  $n_2$  be IoT nodes at locations  $(u_1, v_1)$  and  $(u_2, v_2)$ , respectively. Assuming the nodes travel to a new position  $(u'_1, v'_1)$  and  $(u'_2, v'_2)$  for an association, then the Euclidean distance between them can be expressed as

$$d(0) = |u_1 - u_2|^2 + |v_1 - v_2|^2 \quad (3)$$

WSN-based IoT node distances at time  $l$  and their positions can be computed as:

$$d(l) = |u'_1 - u'_2|^2 + |v'_1 - v'_2|^2 \quad (3)$$

where  $(u'_1, v'_1)$  and  $(u'_2, v'_2)$  are new locations of  $n_1$  and  $n_2$ .

#### 3.1.3 Objective Model:

In this research, the objective model is considered such as energy, and delay on the given WSN network. In this research, ELSOA algorithm is introduced to select best forwarder node that develops the optimal solutions for scalable network. Then apply CA framework for multipath data transmission over the WSN network. The formula is defined for delay, hop count, energy and lifetime is given below:

$$delay(d) = \frac{\sum_{i=1}^n (t_{ri} - t_{si})}{n}$$

where,  $T_{ri}$  -  $i^{\text{th}}$  packet receipt time,  $T_{si}$  -  $i^{\text{th}}$  packet sending time and  $n$  - total packets count.

$$Energy(e) = [(2 * p_i - 1)(e_t + e_r)]d \quad (6)$$

where,  $p_i$  - data packet,  $e_t$  - transmission energy of packet  $i$ ,  $e_r$  - energy for receiving packet  $i$  and  $d$  - distance between source and destination node.

The objective model  $O_M$  can be derived as:

$$O_M = n(M_e * L_d) \quad (7)$$

where,  $N$  - nodes count with optimal energy, and delay values,  $M_e$  - Minimum energy consumption node and  $L_d$  - Less delay.

It is further used to select the multiple optimal forwarder node selection and multipath routing through the ELWOA\_CA approach.

### 3.2 OPTIMAL FORWARDER NODE SELECTION USING ELSOA

The proposed ELSOA algorithm selects the best forwarder node for faster network transmissions. The selection of a forwarder node is a complex issue. Each source node exists with a group of neighbors. Forwarder node selections are based on many parameters: their residual energy; physical distances and available link quality. Forwarded data packets stay for a specific period of time in forwarder nodes based on transmission distance/range, speed of sound propagation, remaining energy, avoiding packet collisions and avoiding redundancy in transmissions. The node that holds packets for a minimal time based on the above said factors is the best forwarding node. When a node finds overheard packets, the packets are dropped while other packets remain in the buffer until forwarded.

Metrics considered for forwarder node selection directly impact routing protocol's performance where residual energy metric helps in balancing node energies. Link quality is also an important metric that impacts node's energy consumptions and PDRs (Packet Delivery Ratio) [20]. Depth metric usage reduces energy consumptions as they compute local depths while physical distances are computed using sink's beacon messages. Thus, it becomes mandatory for a forwarder node selection algorithm to consider multiple metrics for energy efficiency and reliability of forwarder nodes.

Forwarder nodes chosen with selected metrics transmit packets while other nodes hold the data packets. These nodes also forward when their holding time is exhausted and do not overhear. Thus, shortest path selection is a basic issue that impacts transmissions and network's lifetime based on energy [21]. It is common to select nodes which have lesser depth than the sender for reducing transmissions and forwarder node selections.

This work uses stochastic optimization in its proposed ELSOA for forwarder node selection. Lion Optimization Algorithm (LOA) is a meta-heuristic and capable of generating multiple solutions in each of its iterations. Lions, the strongest of the mammals live in groups with females being resident. Their social living area or territory is guarded by Lions and cubs [22]. A wandering Lion is engaged in a fight by the territorial lion and the victor stays as the territorial lion and drives out the loser. If the wanderer is the victor then the territorial lion's cubs are also killed and female is forced to mate. Cubs reaching puberty also challenge the territorial lion for holding the territory.

Lion's social behavior can be that of residents or nomadic where these behaviors. LOA searches for optimality in solving problems based on social behavior of lions which can be expressed as defense or takeover. The Fig.4 shows the nature of LOA

- **Territorial Defense:** Resident lions/cubs fight with nomadic males for controlling territory. LOA evaluates current solution (territorial) with a new solution (nomad). If the

nomad is better it replaces the territorial lion or existing solution.

- **Territorial Takeover:** LOA, while exhibiting this behavior stores only the best male/female solutions while removing existing solutions.

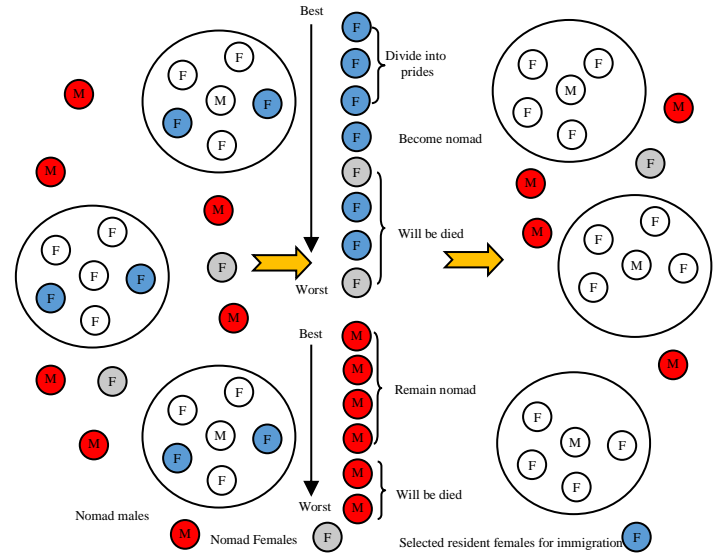


Fig.4. Nature of LOA

**Initialization:** LOA initialization starts with random generation of Lion population which is stored in a matrix form as the solution space where lions are solutions represented by:

$$Lion = [x_1, x_2, \dots, x_{N_{var}}] \quad (8)$$

where  $x_{N_{var}}$  are the generic forwarder nodes selected. Randomly generated nomad lion ratio is denoted by %N while the rest are resident lions. The solution required for selecting the best forwarder node from inputs is executed using LOA which can search and identify hidden relationships between individual elements of a network.

**Fitness Computations:** An objective function evaluates the fitness values of lions in the sorted and saved matrix

$$f(Lion) = f(x_1, x_2, \dots, x_{N_{var}}) \quad (9)$$

Fitness values are based on energy and delay or optimality of emergency message forwards effectively by the forwarder node. Most required parameters for this fitness function involve delay and reduced energy consumption given in:

$$Fitness = \text{Min} \frac{\sum_{i=1}^N (P_{energy\_consumption}^i + P_{delay}^i)}{2} \quad (10)$$

where,  $P_{energy\_consumption}^i$  - node consumption energy while receiving packets and  $P_{delay}^i$  - delays of nodes for selection.

The mathematical formulation for delay and energy consumption is given in Eq.(5) and Eq.(6).

On computing fitness values, they are updated as solutions where hunting, mating, roaming, defense are the operations used. Female lions search for prey inside their territory, thus hold the optimal solution within the territory. This work's selection of forwarder nodes is based on the above described fitness function values and subsequent updates.

**Hunting Operation:** There are three classes of hunters. Hunter with best fitness value is the center while the other two forms its left and right. Randomly chosen hunters attack dummy preys which escape when hunter's fitness improves and is updated to a new location.

**Movements Towards Safety:** Only selected female lions hunt for prey while others stay in safe territory. The best positions for each territory are computed and saved. High victory count indicates that the lions have moved away from the optimum point. Lower values indicate lions are roaming for enhancement and hence assessment of competitions indicates achievements.

**Roaming of Lions:** Roaming is a difficult operation and restricts searches of lions. LOA uses this to hunt in a search space and find an enhanced solution. Lions move by  $n$  units towards their preferred territory.

$$n \sim U(0, 2 * d)$$

where  $n$  is a random number with uniform distributions and  $d$  is a male lion's distance from selected territory. Nomad lions also move randomly in the search space

**Mating:** Mating is primary for lion survival and the process of creating new generations. On identifying suitable female and male lions, cubs are produced. This process produced new and best solutions from existing solutions using crossovers and mutations. Elimination of weak lions ensures best solutions are derived.

**Defense:** This behavior is important to lions. Matured males engage other lions in a battle. Losers turn into nomads or get out of the territory. Nomadic lions winning a battle take control of the loser's territory. Thus, LOA operates defense in two modes namely defending lions against new matured resident males and nomadic males. Thus, the strongest lion in the group is found by LOA.

**Migration:** This process is a relocation process where randomly chosen females turn into nomads and fitness values determine their rearrangement where the fittest females replace positions of females which turned nomads.

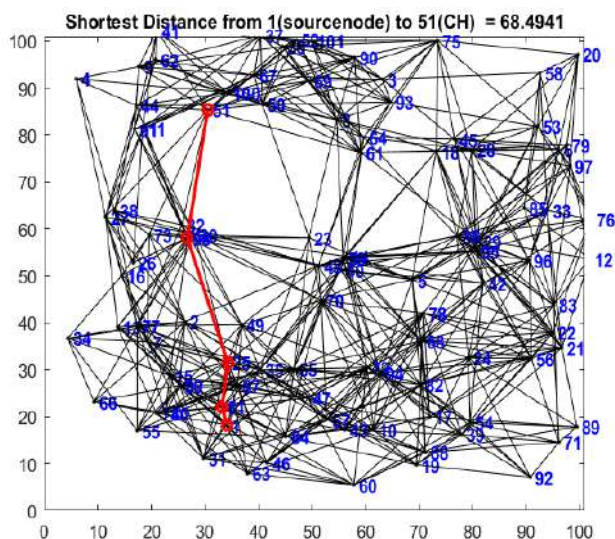


Fig.5. Shortest distance between nodes using ELSOA algorithm

**Population Equilibrium of Lions:** Every iteration ends in an equilibrium point or position of stability in the lion's population where a count for maximum lions per gender is assessed. Lions

with low fitness values are eliminated from the population. Fig.5 displays shorter distances between nodes. Found by ELSOA, the distances are lower for CHs near the BS while they increase as CHs get away from BS.

**Criteria for Termination:** The proposed terminates when more iterations achieve best fitness values. The partition with highest fitness values is the best partition and is selected for broadcasting messages. The territorial takes over operation keeps replacing lions with lower fitness values by higher fitness lions. Thus, only the solutions including males and females are saved while other solutions are discarded.

In ELSOA, ant's position updates are based on random walks around the ant-lions and selected by Roulette wheel where the best particle is preserved. Hence, ELSOA has advantages in terms of quick speed calculations, effective convergence and high efficiency [23]. Premature convergence and local optimum are issues for complex optimizations and improvements proposed for overcoming these issues for selection of forwarder nodes is presented below.

$$Ant = (R_A + R_E) / 2 \quad (11)$$

where,

$Ant$  - new position,

$R_A$  - ant-lion's random walk as selected by Roulette wheel,

$R_E$  - random walk around the elite. An ant's new position is modified if does not fit into the bounded area.

#### Algorithm 1: ELSOA

**Input:** Nodes from a network

**Output:** Best forwarding node

**Step 1:** Begin

**Step 2:** Random position initialization

**Step 3:** Initialization of normal and nomadic lion positions

**Step 4:** Assess the fitness value of each lion using Eq.(10)

**Step 5:** Select hunting females and move others to a safer position

**Step 6:** Select hunting nomadic females and move the rest to safety

**Step 7:** Remember the best solution

**Step 8:** For each lion do

**Step 9:** Try mating

**Step 10:** End for

**Step 11:** Update the position of pride and nomad lion (11)

**Step 12:** Merge new mature male and old male

**Step 13:** Sort all males according to their fitness

**Step 14:** Weakest male drives out and remained male become pride

**Step 15:** If terminating criteria fulfilled then

**Step 16:** Return the best forwarder node selection

**Step 17:** Else

**Step 18:**  $t = t + 1$

**Step 19:** Until  $t > \text{Max\_Iteration}$

**Step 20:** Return the best forwarder node selection

**Step 21:** Stop the algorithm

The algorithm 1 explains LOA and to summarize lions, strongest mammals exhibit a social behavior that can be residential or nomadic. Lions switch between these behaviours. Resident lions live in a territory where they mate to produce an offspring. Nomadic lion movements are sporadic and move alone or in pairs where outclassed males move in pairs.

### 3.3 SECURED DATA TRANSMISSION USING CA

In this work, secured data transmission is executed using CA with third party node for increasing the trust level. Each node within a region is registered with the authenticating node which checks genuineness of a node before allowing the node to be a part of forwarder node list. Authentications confirm a user’s entry into a system-based on identity or is a control system for users to be on the system.

Any user logging onto a system is authenticated and in case of two logins, user is authenticated twice. This process grows in complexity as entries into multiple systems require multiple authentications. Users have to keep track of multiple usernames and passwords which complicate the matter for both systems and users. A centralized authenticating server-based credential helps in avoiding this complexity.

Further, these types of servers eliminate redundancy and hence this work uses CA. When a BS receives packets that are encrypted, it decrypts the packets. This ensures the wireless carriers transmit data safely while the use of CA releases the network from the burdens of authentications. Application without CA’s grows in complexity with added contents [24].

The study [25] introduced a multipath routing protocol for energy-efficient communications by balancing network traffic in multiple paths. The study’s significant metric was the energy of a route in the route discovery phase. The study failed to achieve much as it did not consider wireless interferences and assumed links were free from errors.

This work is interference aware where the multipath routing protocol has three stages namely initialization, route discovery/establishment and route maintenance. Each node obtains neighborhood information in the first stage which is then used by the second stage to discover routes. In route establishment, the best next-hop node towards the sink is found. The second stage is triggered on an event detection with the outcome of discovering multiple paths between the source and sink with minimized interferences for data transmissions.

WSN-based agricultural experiments enhance growth and quality of tomatoes [26]. Hence, this work combines WSNs with agriculture in assessing event-based experimentations using tomato crops. The crop’s growth in a greenhouse does not cross 100 days for maturity or harvest.

## 4. SIMULATION RESULT

ELSOA-CA performances are reported and evaluated with other methods in this section. Methods considered for comparisons include Ant Colony Optimization (ACO), Light Weight Structure-based Data Aggregation Routing (LSDAR) and the proposed ELSOA which were simulated using NS-2 simulator. The metrics used for comparisons include end to end

delays, throughput, energy consumptions, and network lifetimes. Simulation parameters used is listed in Table.1.

Table.1. Simulation Parameters

Parameter	Values
No. of Nodes	100
Area Size	1100×1100 m
Mac	802.11
Radio Range	250m
Simulation Time	60 sec
Packet Size	80 bytes

### 4.1 PERFORMANCE EVALUATION

- **End-to-End Delay:** The average time taken by a packet to get transmitted from a source to a destination in a network.

$$\text{End-to-end delay} = \frac{\sum_{i=1}^n (t_{ri} - t_{si})}{n} \quad (12)$$

where  $t_{ri}$  –  $i^{\text{th}}$  packet receipt time,  $t_{si}$  – time the  $i^{\text{th}}$  packet was sent and  $n$  - total packets.

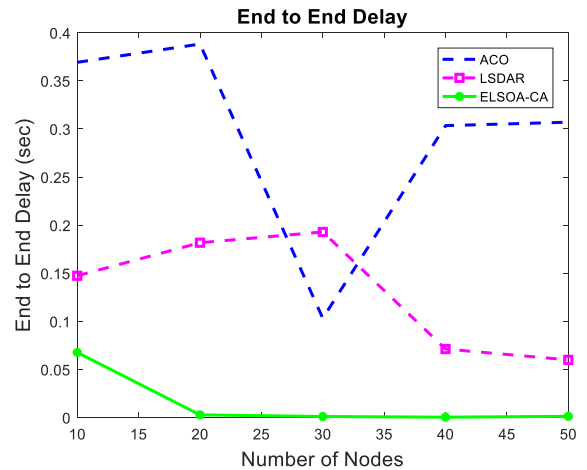


Fig.6. End-to-end delay comparison

The Fig.6 depicts evaluation comparisons in terms of end to end delay performance, where nodes are in x-axis and y-axis represents their end to end delay values. Methods compared are ACO, LSDAR and proposed ELSOA-CA algorithm which shows lesser end to end delays. Thus, the proposed ELSOA-CA system selects superior forwarder nodes-based on ELSOA fitness values.

- **Throughput:** The rate in which the data packets are successfully transmitted over the network.

$$\text{Throughput} = \frac{\text{total number of packets sent}}{\text{time}} \quad (13)$$

The Fig.7 depicts evaluation comparisons in terms of throughput performance, where nodes are in x-axis and y-axis represents their throughput values. Methods compared are ACO, LSDAR and proposed ELSOA-CA algorithm which shows higher throughputs. Thus, the proposed ELSOA-CA system selects superior forwarder nodes-based on ELSOA fitness values.



- **Energy Consumption:** Energy consumption is the average energy necessary for transmission of a packet to a node in the network in a specific period of time.

$$Energy(e)=[(2*pi-1)(e_t+e_r)]d \tag{14}$$

where,  $p_i$  - data packet,  $e_t$  - packet  $i$ 's transmission energy,  $e_r$  - energy required for receiving packet  $i$  and  $d$  - distance between transmission and destination nodes.

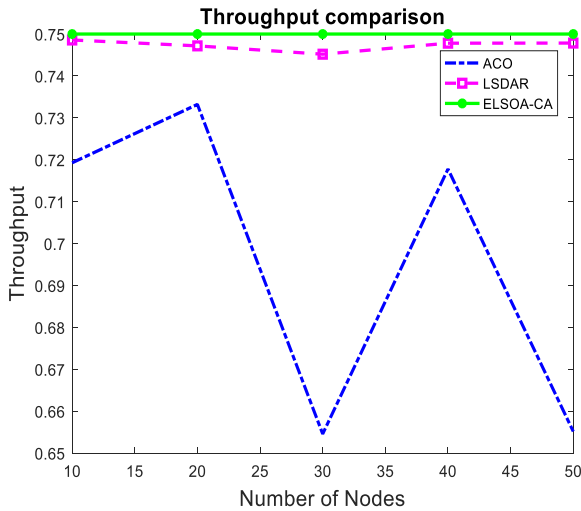


Fig.7. Throughput comparison

unused energy till the network dies and  $\mathbb{E}[E_r]$  – reported energy consumption of nodes.

The Fig.9 depicts evaluation comparisons in terms of network lifetime performance, where nodes are in x-axis and y-axis represents their network lifetime values. Methods compared are ACO, LSDAR and proposed ELSOA-CA algorithm which shows higher network lifetime. Thus, the proposed ELSOA-CA system selects superior forwarder nodes-based on ELSOA fitness values.

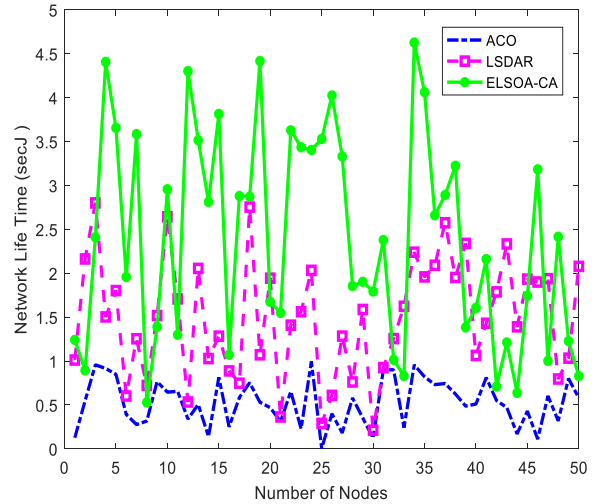


Fig.9. Network lifetime

- **PDR:** represents the ratio of the number of lost packets to the total number of sent packets

$$Packet\ loss\ ratio = \frac{N^{tx} - N^{rx}}{N^{tx}} \times 100\% \tag{16}$$

where,  $N^{tx}$  - transmitted packets,  $N^{rx}$  - received packets. This evaluation was done by extracting all real-time packet sizes that were transmitted and received.

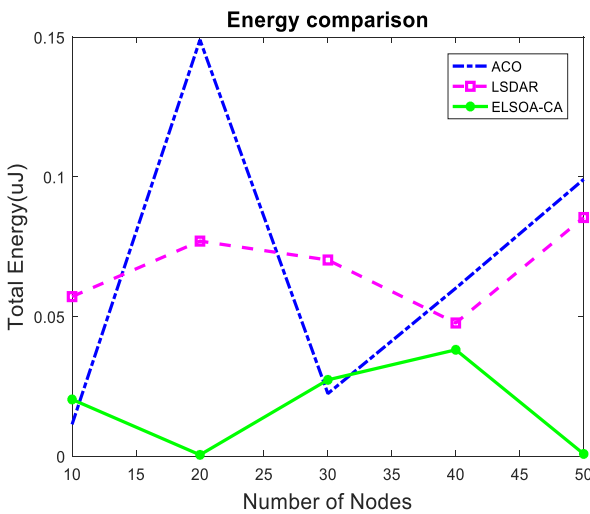


Fig.8. Energy consumption comparison

The Fig.8 depicts evaluation comparisons in terms of energy consumption performance, where nodes are in x-axis and y-axis represents their energy consumption values. Methods compared are ACO, LSDAR and proposed ELSOA-CA algorithm which shows lower energy consumptions. Thus, the proposed ELSOA-CA system selects superior forwarder nodes-based on ELSOA fitness values.

- **Network Lifetime:** The lifetime of a network.

$$Lifetime\ \mathbb{E}[L] = \frac{\epsilon_0 - \mathbb{E}[E_w]}{P + \lambda \mathbb{E}[E_r]} \tag{15}$$

where,  $P$  - constant power consumption of network and continuous,  $\epsilon_0$  - total non-rechargeable initial energy,  $\lambda$  - average sensor reporting rate,  $\mathbb{E}[E_w]$  – anticipated wasted energy or

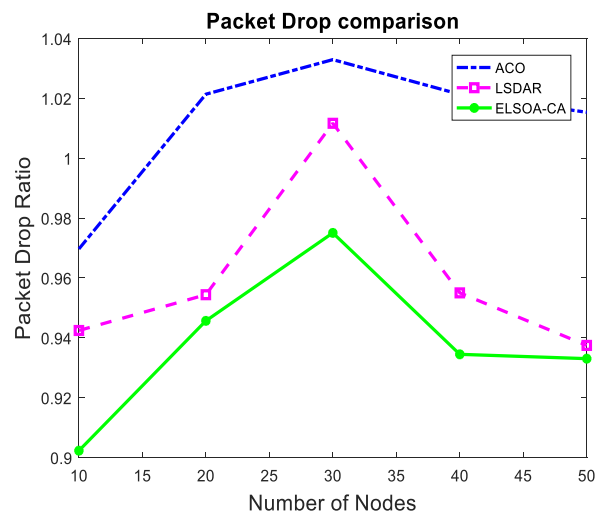


Fig.10. Packet drop ratio

The Fig.10 depicts evaluation comparisons in terms of PDR performance, where nodes are in x-axis and y-axis represents their PDR values. Methods compared are ACO, LSDAR and proposed ELSOA-CA algorithm which shows lower PDR. Thus, the

proposed ELSOA-CA system selects superior forwarder nodes based on ELSOA fitness values.

## 5. CONCLUSION

This work has proposed and demonstrated a new ELSOA-CA approach for optimizing selection of forwarder nodes in a WSN. The proposed ELSOA, selects the best forwarding node by reducing hops and choosing nodes with best fitness values. This work produces optimal solution for the forwarder node selection by considering residual energy and end to end delay which are computed using a fitness function. The CA is focused to improve the secured multipath data transmission using route discovery and route maintenance function for increasing the WSN performance. The result concludes that the proposed ELSOA-CA algorithm provides higher throughput, network lifetime, and lower end to end delay, packet drop ratio, energy consumption than the existing approaches. In future work, the hybrid LOA and novel encryption algorithm can be developed for dealing with computational complexity issues prominently.

## REFERENCES

- [1] Ghassan Samara and Mohammad Aljaidi, "Efficient Energy, Cost Reduction, and QoS based Routing Protocol for Wireless Sensor Networks", *Proceedings of International Conference on Electrical and Computer Engineering*, pp. 496-504, 2019.
- [2] Ramin Yarinezhad, "Reducing Delay and Prolonging the Lifetime of Wireless Sensor Network using Efficient Routing Protocol based on Mobile Sink and Virtual Infrastructure", *Ad Hoc Networks*, Vol. 84, pp. 42-55, 2019.
- [3] K. Srihari and G. Dhiman, "An IoT and Machine Learning-based Routing Protocol for Reconfigurable Engineering Application", *IET Communications*, Vol. 33, No. 2, pp. 1-18, 2021.
- [4] Y. Li and R. Shi, "An Intelligent Solar Energy-Harvesting System for Wireless Sensor Networks", *EURASIP Journal on Wireless Communications and Networking*, Vol. 20, No. 1, pp. 1-12, 2015.
- [5] B. Zhang, R. Simon and H. Aydin, "Harvesting-Aware Energy Management for Time-Critical Wireless Sensor Networks with Joint Voltage and Modulation Scaling", *IEEE Transactions on Industrial Informatics*, Vol. 9, No. 1, pp. 514-526, 2013.
- [6] S. Peng, T. Wang and C.P. Low, "Energy Neutral Clustering for Energy Harvesting Wireless Sensors Networks", *Ad Hoc Networks*, Vol. 28, pp. 1-16, 2015.
- [7] C. Liu, D. Fang, Y. Hu and H. Chen, "EasyGo: Low-Cost and Robust Geographic Opportunistic Sensing Routing in a Strip Topology Wireless Sensor Network", *Computer Networks*, Vol. 143, pp. 191-205, 2018.
- [8] G. Han, Y. Dong and D. Wu, "Cross-Layer Optimized Routing in Wireless Sensor Networks with Duty Cycle and Energy Harvesting", *Wireless Communications and Mobile Computing*, Vol. 15, No. 16, pp. 1957-1981, 2015.
- [9] R.J.M. Vullers and H.J. Visser H J, "Energy Harvesting for Autonomous Wireless Sensor Networks", *IEEE Solid-State Circuits Magazine*, Vol. 2, No. 2, pp. 29-38, 2020.
- [10] D. Wu, J. He, H. Wang and C. Wang, "A Hierarchical Packet Forwarding Mechanism for Energy Harvesting Wireless Sensor Networks", *IEEE Communications Magazine*, Vol. 53, No. 8, pp. 92-98, 2015.
- [11] M. Maimour, "Maximally Radio-Disjoint Multipath Routing for Wireless Multimedia Sensor Networks", *Proceedings of ACM Workshop on Wireless Multimedia Networking and Performance Modeling*, pp. 26-31, 2008.
- [12] T.D. Nguyen, J.Y. Khan and D.T. Ngo, "An Effective Energy-Harvesting-Aware Routing Algorithm for WSN-based IoT Applications", *Proceedings of IEEE International Conference on Communications*, pp. 1-6, 2017.
- [13] J. Tang, A. Liu, J. Zhang and T. Wang, "A Trust-Based Secure Routing Scheme using the Traceback Approach for Energy-Harvesting Wireless Sensor Networks", *Sensors*, Vol. 18, No. 3, pp. 751-756, 2018.
- [14] N. Sirdeshpande and Vishwanath Udipi, "Fractional Lion Optimization for Cluster Head-Based Routing Protocol in Wireless Sensor Network", *Journal of the Franklin Institute*, Vol. 354, No. 11, pp. 4457-4480, 2017.
- [15] Rajeev Arya and S.C. Sharma, "Energy Optimization of Energy Aware Routing Protocol and Bandwidth Assessment for Wireless Sensor Network", *International Journal of System Assurance Engineering and Management*, Vol. 9, No. 3, pp. 612-619, 2018.
- [16] A.S. Nandhini and P. Vivekanandan, "A Survey on Energy Efficient Routing Protocols for Manet", *International Journal of Advances in Engineering and Technology*, Vol. 6, No. 1, pp. 370-382, 2013.
- [17] Ying Guo and Mingyan Jiang, "Power System Optimization Based on Multi-agent Structure and Lion Swarm Optimization", *Journal of Physics: Conference Series*, Vol. 1575, No. 1, pp. 1-13, 2020.
- [18] Yong Ping Zhang and Lin-Lin Qin, "A Node Authentication Protocol based on ECC in WSN", *Proceedings of International Conference on Computer Design and Applications*, pp. 1-9, 2010.
- [19] Shashi Kant, Anurag Singh Tomar and Gaurav Kumar Tak, "Secure Medical Data Transmission by using ECC with Mutual Authentication in WSNs", *Procedia Computer Science*, Vol. 70, pp. 455-461, 2015.
- [20] R. Amuthavalli and R.S. Bhuvaneshwaran, "Detection and Prevention of Sybil Attack in WSN Employing Random Password Comparison Method", *Journal of Theoretical and Applied Information Technology*, Vol. 67, No. 1, pp. 236-246, 2014.
- [21] N. Chakchouk, "A Survey on Opportunistic Routing in Wireless Communication Networks", *IEEE Communications Surveys and Tutorials*, Vol. 17, pp. 2214-2241, 2015.
- [22] G. Gowrishankar and P. Senthil Kumar, "A Trust based Protocol for Manets in IoT Environment", *International Journal of Advanced Science and Technology*, Vol. 29, No. 7, pp. 2770-2775, 2020.
- [23] Maziar Yazdani and Fariborz Jolai, "Lion Optimization Algorithm (LOA): A Nature-Inspired Metaheuristic Algorithm", *Journal of Computational Design and Engineering*, Vol. 3, No. 1, pp. 24-36, 2016.
- [24] N. Vukovic, Z. Miljkovic and Z. Babic, "The Ant Lion Optimization Algorithm for Integrated Process Planning and

- Scheduling”, *Applied Mechanics and Materials*, Vol. 834, pp. 187-192, 2016.
- [25] Eugene Shablygin and Mikhail Vysogorets, “Centralized Authentication System with Safe Private Data Storage and Method”, U.S. Patent No. 826, pp. 1-19, 2014.
- [26] Lu Yeming and V.W.S. Wong, “An Energy-Efficient Multipath Routing Protocol for Wireless Sensor Networks”, *International Journal of Communication Systems*, Vol. 20, No. 7, pp. 1-14, 2007.
- [27] Vimla Devi, Kavi Kumar Khedo and Vishwakalyan Bhoyroo, “A Flexible and Reliable Wireless Sensor Network Architecture for Precision Agriculture in a Tomato Greenhouse”, *Proceedings of International Conference on Information Systems Design and Intelligent Applications*, pp. 119-129, 2019.



# Hybrid Simulated Annealing with Lion Swarm Optimization Algorithm with Modified Elliptic Curve Cryptography for Secured Data Transmission Over Wireless Sensor Networks (WSN)

S. Silambarasan

Department of Computer Science, Periyar University, Salem, Tamil Nadu, India  
silambus82@gmail.com

M. Savitha Devi

Department of Computer Science, Periyar University Constituent College of Arts and Science, Harur, Dharmapuri, Tamil Nadu, India  
savithasanma@gmail.com

Received: 27 April 2022 / Revised: 14 May 2022 / Accepted: 30 May 2022 / Published: 28 June 2022

**Abstract** – The security of data processing has become an important factor in the present scenario due to the rapid growth of the internet. Especially, Wireless Sensor Networks (WSNs) face complicated challenges in their vulnerable corrupted sensor nodes. In the earlier work, Enhanced Lion Swarm Optimization Algorithm and Centralized Authentications (ELSOA-CAs) scheme has been proposed for achieving ideal, quicker, and energy efficient data transmissions. But, in the earlier work, a congestion-aware multipath routing mechanism is not considered. Moreover, for the bigger file, the security is not still strong. This security issue is addressed in the proposed work by using Hybrid Simulated Annealing with Lion Swarm Optimization and Centralized Authentication (HSALSO-CA) mechanisms. In the proposed technical work, optimum, quicker, and energy-efficient data transmission is highlighted to guarantee that the decision-making regarding tomato crops is achieved with accuracy. In this research work, multipath routing is presented to ensure that the data transmission is accelerated. In this work, rapid multipath routing is formulated by choosing the best forwarder nodes that meet limitations such as delay and energy. Optimal Forwarder Node Selection employing Hybrid Simulated Annealing with Lion Swarm Optimization Algorithm (HSALSOA) is used. The Simulated Annealing algorithm is hybridized as it emphasizes optimal local and global search capability for the bigger network. Secured data transmission employing Modified Elliptic Curve Cryptographies (MECCs) algorithm guarantees increased security for congestion-sensitive multipath routing mechanisms. It is proven from the simulation outcomes that the proposed ELSOA-CA model yields superior performance in terms of enhanced throughputs, elongated network lives with reduced utilization of energies, and delays in contrast to available techniques.

**Index Terms** – Aggregation, Security, Lion Swarm Optimization, Forwarder Nodes, Centralized Authentication, Secured Data Transmission.

## 1. INTRODUCTION

When nodes of WSNs deployed in distant accesses deliver sensor inputs to users, WSNs confront serious authentication and security challenges. Various concerns and risks can be addressed depending on protocol levels. WSNs are made up of a large number of SNs that sense, gather, and distribute data in places where traditional networks are ineffective due to environmental and/or strategic factors [1]. They serve crucial roles in a wide range of applications including military surveillance and monitoring forest fire. They can also be used for monitoring building security shortly. These installed SNs can monitor very large areas where operational circumstances are hostile or difficult. Since, these kinds of networks exist in distant locations and are left unattended, protecting them against threats like node acquisitions, physical tamperers, and threats including eavesdropping and DOSs (denial of services) becomes imperative.

In WSNs, the primary concerns include authentication and Security, involving nodes in the network responsible for sending the sensor inputs to the user positioned remotely. Depending on the level of the protocol, the different challenges and risks are dealt with. There are several security concerns identical in both WSNs and wireless ad-hoc networks, and these form the basic dissimilarities between the architecture and objectives of the two kinds of networks [1].

**RESEARCH ARTICLE**

Even though the cost incurred in WSNs is less, their computational complexity hinders them to be directly applied in the current highly robust conventional wireless security mechanisms [2].

Conventional security standards of the wireless network are undesirable for sensor networks due to huge requirements of memory, energy, and high computational complexity [3]. One major problem of WSNs is that their SNs (sensor nodes) are not supervised when situated in hazardous environments exposed to limited energies, and undefined network architectures, making them vulnerable to numerous types of assaults including eavesdropping, compromised mote attacks, and traffic analyses, etc [4]. Quite diverse from the Internet, dispersed and energy-constrained WSNs have the frequent task of performing collaborative monitoring or managing one or more events in WSNs [5]. Before transmissions to data sinks that control SNs and collect their data, pre-processing or aggregations of event information at intermediary SNs is possible and even mandatory in certain cases [6]. Since conventional transport layers are not developed with no attention paid to these novel features of WSNs, better transport protocols are required [7]. Transport layers of WSNs perform two important functions namely information deliveries and control of congestions [8]. In cases of packet losses in multi-hop WSNs where few or entire packets are lost can be easily identified and lost data can be restored using suitable techniques when WSNs are robust [9]. Reliability is necessary when data is crucial for WSNs applications.

Congestions occur when SNs send their data to sinks creating traffic loads that networks struggle to handle [10]. If congestion occurs in WSN, nodes begin dropping the packets or the packet delay considerably goes above the needs of applications. Packet dropping happening often is a waste of energy and acts against any endeavor for gaining reliability. Excessive packet delay might result in data invalidity which is gathered by sensors [11].

Hence, in these devices, their constrained energy, limited processing power, less bandwidth, and communication capacity constitute the big setbacks on the processing strength and memory accessible for security depending on the executions. A vast variety of security approaches have been introduced to improve energy efficiency during the design of enhanced security protocols. It is understood that symmetric cryptography can be preferred for applications, which cannot address the computational complexity, which is a huge issue and is considered a problem identification of the research work. Therefore, the research goal is to develop effective cryptographic algorithms that are implemented optimally in terms of energy dissipation and computational complexity, and are pivotal in increasing the battery lifespan of SNs.

In this work, cache resources are allocated to diverse data flows based on their needs, and reliability and congestion-

aware data transfers are achieved. Data flows occurring in WSNs generate erratic resource allocations while monitoring those helps in better management. This is accomplished in this work by computing priority levels of multiple data flows and allocating large chunks of cache resources to data flows with the highest priority levels.

The technical work is organized as given. In this section, the need for addressing the congestion and reliability focus when carrying out the data transmission in the WSNs is studied in detail. Section 2 analyzes the different research approaches, which are presented to attain congestion-free, robust data transmission. Section 3 discusses the proposed research approach in detail with the appropriate diagrams and examples. Section 4 discusses the proposed research approach's performance examination based on the numerical evaluation. Lastly in section 5, the research study's conclusion is studied depending on the achieved findings.

## 2. RELATED WORKS

Rosset et al [12] introduced a new bio-inspired routing protocol called CB-RACO (Community-Based Routing with Ant Colony Optimization protocol) that combined meta-heuristic ACOs (Ant Colony Optimizations) with computationally inexpensive and distributed community detection methodologies LPs (Label Propagations). WSN communities are created by CB-RACO that reduces energy usage imbalance by routing the information within groups using swarm intelligence. Consequently, CB-RACO requires less memory and experiences less overhead concerning deployment and maintenance of routing paths.

Bhatia et al [13] introduced TRM-MAC, a TDMA-based reliable multicast MAC technology aimed toward WSNs. TRM-MAC protocol featured parametric components that could be used to trade off reliability and delay performances based on the application's demands. The TRM-MAC protocol was investigated for latencies and reliabilities of performances with various PLRs (packet loss rates) and contrasted with other findings.

Mohanty et al [14] developed the protocol ESDADs (Energy Efficient Structure-Free Data Aggregation and Deliveries), which aided in aggregating repeated data of intermediate nodes. Their recommended protocol computed packet waiting times at intermediary nodes in a reasonable manner, allowing data aggregations to be accomplished efficiently throughout routing paths. Sensitive data packets were broadcast to aggregation points. The proposed ESDADs protocol developed cost functions for structure-independent next-hop node selections and information aggregations near sources.

Faheem et al [15] recommended a new Energy Efficient and Reliable Data Gathering Routing Protocol for WSN-based smart grid applications. To achieve energy efficiencies and robust information aggregations from SGs (Smart Grids) in

**RESEARCH ARTICLE**

WSNs, the proposed solution employed software-oriented centralised controllers and many mobile sinks were the results of elaborate simulation carried out via EstiNet 9.0 revealed that the proposed approach performed better than available mechanisms and attained its specifies objectives for event-based applications in SGs.

Elappila et al [16] proposed survivable path routes in congested and interference sensitive energy efficient routing for WSNs. Their protocol was intended for networks with heavy traffic because as several sources tried to deliver their packets to the same destinations at the same time, typical scenarios of IoTs (Internet of Things) related to remote medical monitoring. In choosing next hop nodes, the approach used conditions i.e. functions made up of link's signals to interferences and noise ratios, element of path's survival, and congestion levels at next hop nodes.

Sharma et al [17] proposed a robust congestion-based approach that resulted in bi-directional dependability and rate modifications based on congestion controls. Their scheme used TOPSIS's (Technique for Order of Preference by Similarity to Ideal Solutions) for data transmissions as they select alternates i.e. least distances from optimal ones and greatest distances from negative ideal solutions. The degrees of congestion were determined based on ratios between average packet service times and average packet inter-arrival times were used.

Vinitha et al. [18] investigated energy issues of WSNs with their proposed Taylor C-SSAs (Taylor based Cat Salp Swarm Algorithms) where modified C-SSA were used with Taylor series. Their approach involved electing CHs (Cluster Heads) and data broadcasts at two levels for achieving multi-hop routing. For efficient information broadcasts, their scheme selected energy-efficient CHs based on LEACH protocol and SNs transmitted information over CHs that forwarded it to BSs (Base Stations) over selected best hops.

Devi et al [19] suggested cluster-based Data Aggregations for Latencies and Packet Loss Reductions. The study constructed Aggregation Trees and Slot Schedules in their proposed mechanisms. CHs used compressive aggregations to collect information from SNs while BSs constructed aggregate trees using MSTs (Minimum Spanning Trees). PLRs and latencies were taken into consideration while focusing on and allocating timeslots to SNs having collected information from them. The approach prevented unwanted rebroadcasts and waits that were found to be advantageous in improving WSN's network performances.

Rekha & Gupta (2021) [20] presented a secure confirmation and key organization approach based on ECCs (Elliptic Curve Cryptographies) which were used for ensuring WSN's transmission of information and images. Their scheme was found to be safe, reliable, and appropriate for developing

sensor-based IoTs and applications. The protocol was capable of defending the networks against hello flood, DOSs (Denial-of-Services), man-in-the-middle, and other attacks or security threats including mutual authentications, confidentiality, data integrities, perfect forward secrecies, and fair key agreements. Their proposed protocol was confirmed as safe against known threats in AVISPA simulations. Also, their performance evaluation proved the excellence of the proposed work when compared to other available approaches.

Qazi et al (2021) [21] primarily targeted security issues of WSNs by their unique authentications and data encryptions approach for communications between SNs. Their proposed scheme not only provided security for these communications but also accumulated memory spaces on nodes with the help of ECDSAs (Elliptic Curve Digital Signatures) cryptographic schemes in their key generations using times, counts of hello messages, and packet sizes. Additionally, their use of ASCWs (Algorithm for Wireless Secure Communications) allowed key managements with acceptable key lengths, thus assisting secure communications of nodes and efficient security of WSNs. Their ASCWs based authentications also reduced risk costs and security risks in comparison. Their creation of physical test beds using equipment and sensor motes were used for benchmarks for comparisons in terms of key generation times, counts of hello messages sent, and data packet sizes where findings demonstrated the appropriateness of ASCWs and implied that the new solution is used for safeguarding data on nodes during the WSN's connections.

Secure Data Communication and Enhance Sensor Reliability (SDER) based on ECCs were proposed by authors of [22]. ECC's Weierstrass functions tested the dependability of SNs while cryptography based on ECCs was used for network data security. The results of the study's simulation showed that the suggested SDER decreased both PLRs and network latencies.

Arya et al. [23] defined ideal conditions for routing. The work considered the best circumstances for bandwidth consumption where their predictions of bandwidths were enhanced by the use of ACOs for saving electricity. Their scheme demonstrated the use of energy-conscious routing protocols that can calculate energy utilization of WSNs from bandwidths without the use of optimizations. ACOs calculated optimum bandwidths for routing paths and energy consumption. Bit error rates were used to assess network performances where the study's findings indicated that optimizations based on ACOs provided practical and efficient routing strategies that increased the lifespan of WSNs.

The study in [24] described revolutionary LSDARs (light-weight structure-based Data Aggregation Routes) protocol for IoTs enables Networks that enhanced energy routing performances while protecting data at SNs against malicious attacks. The scheme divided networks into distinct clusters with varied radii to prevent energy gaps near BSs. This was

**RESEARCH ARTICLE**

followed by the creation of efficient and loop-free routes using A-star heuristics. Moreover, data security was provided by employing a mathematically unbreakable OTPs (one-time pads) encryption mechanism which safeguarded end-to-end communications and specifically from hostile SNs. Their simulation outcomes showed significant improvements when compared to other methods in terms of energy consumption, network lifespan, end-end delays, and PDRs (packet drop ratios).

ELSOA-CAs scheme was proposed for achieving ideal, quicker, and energy efficient data transmissions [25]. But, in the earlier work, the congestion-aware multipath routing mechanism is not considered. Moreover, for the bigger file, the security is not still strong. This is addressed in the proposed work by using HSALSO-CA (Hybrid Simulated Annealing with Lion Swarm Optimization and Centralized Authentication) mechanisms. In the proposed technical work, optimum, quicker, and energy-efficient data transmission is highlighted to guarantee that the decision-making regarding

tomato crops is achieved with accuracy.

**3. SECURED AND RELIABLE DATA TRANSMISSION IN WSN**

In the proposed research work, the focus is on optimum, quicker, and energy efficient data transmission that guarantees the decision-making on tomato crops with accuracy. In this research work, multipath routing is presented for making sure that the data transmission speed is high. In this, rapid multipath routing is ensured by choosing the optimum forwarder nodes that face limitations in energies and packet deliveries. Hence, this work employing the suggested HSALSOA selects Optimal Forwarding Nodes. The Simulated Annealing algorithm is a hybridized one as it achieves optimum local and global search potential for the bigger network. Data transmission with better security is ensured by utilizing the modified ECC algorithm that improves the security of congestion-aware multipath routing mechanism. The framework of the discussed work is illustrated in the following figure 1.

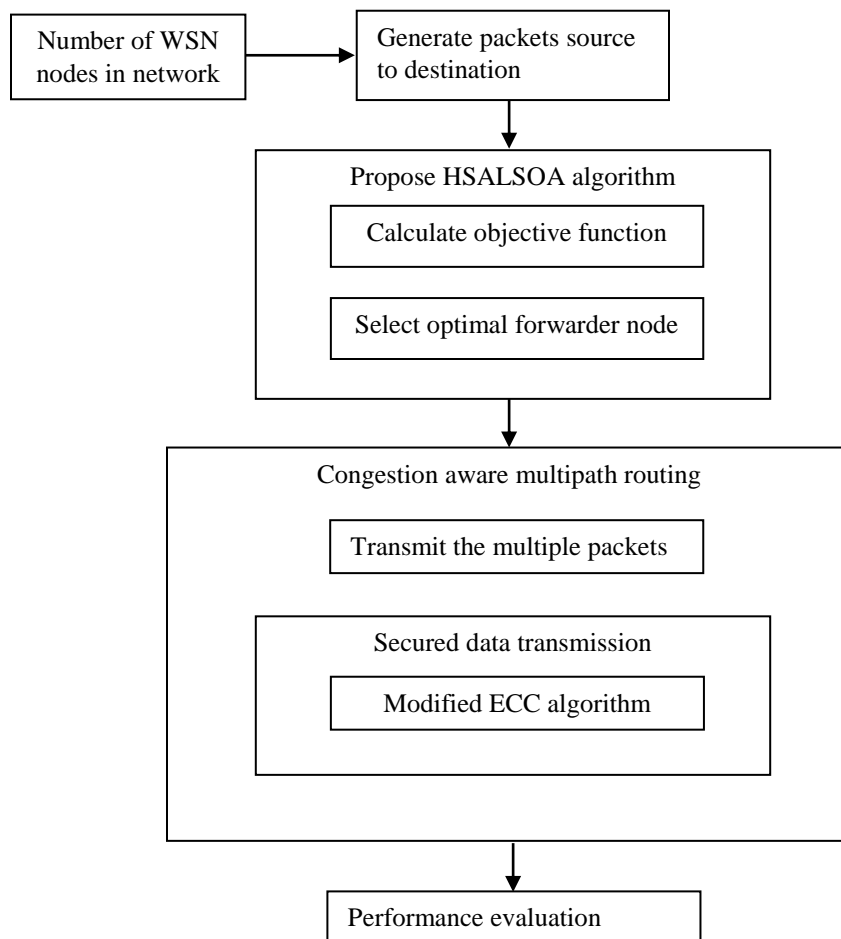


Figure 1 Architecture of Secured Data Transmission System

**RESEARCH ARTICLE**

3.1. System Model

WSNs used in this work consist of N number of SNs, used for sensing, observation, and acquisition of data. Every node in a particular network is stationery and power regulated. Entire WSN nodes help in the regular execution of sensing tasks with consistent data broadcast to BS that deals with nodes inside/external its range. Nodes could act as Cluster Head or simple sensor nodes [26] [27]. The proposed architecture of the network is depicted in Figure 2.

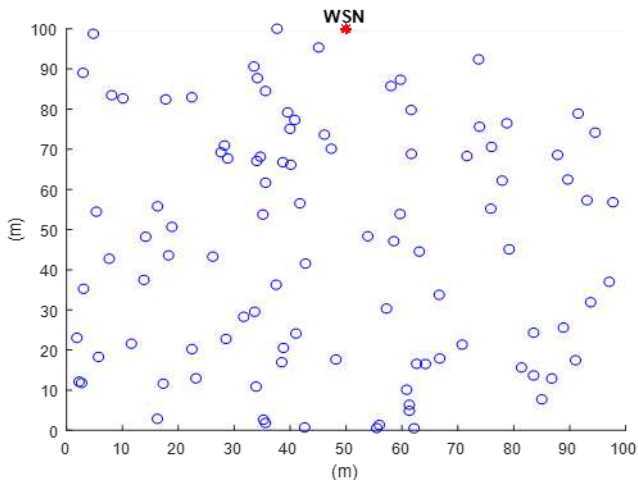


Figure 2 Network Formation

3.1.1. Energy Model

The proposed model helps in the energy analysis of nodes. Supposing that every node includes starting energy,  $E_i$ , then energy is exhausted once node  $i$ , responses or sends a broadcast to other node  $j$  [28]. Power depleted during broadcast is  $P_T$  when  $P_R$  indicates the power consumption of  $i$  when getting the data unit from  $j$ . Also presuming that the energy of a sink node is unconstrained and the node is on constant movement till completion of network lifespan (from beginning till dead), then goal of optimization is about achieving optimality in routing mechanisms and CH elections that improve network lifespan. Linear programming models increase the network lifespan [29] [30]. Power consumption during the transmission of  $L$  bits for distance  $D_t$  is given in Equation (1) and (2), where  $P_{amp}$  indicates the power consumed.

$$P_T = \begin{cases} P_{cons} * L * P_{amp} * D_t^2 & \text{if } D_t < D_0 \\ P_{cons} * L * P_{amp} * D_0^2 & \text{if } D_t \geq D_0 \end{cases} \quad (1)$$

$$P_R = P_{cons} * L \quad (2)$$

Where  $P_T$  refers to the power dissipation when transmitting the packets

$L$  stands for bits

$P_{amp}$  indicates power amplification

$D_t$  signifies the distance among nodes

$D_0$  refers to the threshold distance

$P_R$  indicates the power consumption during the receipt of the packets

The power dissipation is considerably decreased in the node further if it is made sure the data transmission and shortest routing path is achieved with efficiency.

3.1.2. Mobility Model

The model is intended for Internet of Things nodes existing in a system. This depends on device place, speed and how well it is connected. Let  $n_1$  and  $n_2$  refer to the IoT nodes at locations  $(u_1, v_1)$  and  $(u_2, v_2)$ , correspondingly. Presuming that the nodes move to a new position  $(u_1', v_1')$  and  $(u_2', v_2')$  for a correlation, then the Euclidean distance between them can be defined in eqn (3)

$$d(0) = |u_1 - u_2|^2 + |v_1 - v_2|^2 \quad (3)$$

WSNs based IoT node distances at time  $l$  and their location is measured through eqn (4)

$$d(l) = |u_1' - u_2'|^2 + |v_1' - v_2'|^2 \quad (4)$$

Where  $(u_1', v_1')$  and  $(u_2', v_2')$  indicate the new locations of  $n_1$  and  $n_2$ .

3.1.3. Objective Model

Here, objective model considers energy, and WSNs network delay. HSALSOA method is proposed to choose optimal of the forwarder nodes, yielding ideal results for flexible network. Next, CA system is used for multipath data broadcast over WSNs network. Expressions used for computing the delay, hop count, energy and lifespan can be defined in eqn (5).

$$delay(d) = \frac{\sum_{i=1}^n (T_{ri} - T_{si})}{n} \quad (5)$$

Where,  $T_{ri}$  -  $i$ th packet receipt time,  $T_{si}$  -  $i$ th packet sending time,  $n$  - number of total packets

The energy is calculated using eqn (6)

$$Energy(e) = [(2 * pi - 1)(e_t + e_r)d] \quad (6)$$

Where,  $pi$  - data packet,  $e_t$  - packet  $i$ 's transmission energy,  $e_r$  - receiving packet  $i$ 's energy,  $d$  - distance among source and destination node.

Objective model  $O_M$  is obtained through eqn (7):

$$O_M = n(M_e * L_d) \quad (7)$$

here  $N$  - total nodes with optimal energy and delay

$M_e$  - Minimum energy utilization node



**RESEARCH ARTICLE**

$L_d$ - Less delay

It is also utilized for choosing the numerous optimal forwarder node selection and multipath routing using HSALSOA mechanism.

### 3.2. Optimal Forwarder Node Selection using HSALSOA

The Suggested HSALSOA method chooses optimal forwarder nodes for rapid network broadcasts. Elections of forwarding nodes are quite complicated. A set of neighbors exists for source nodes and forwarding nodes where the latter are selected by considering their physical distances from BSs, remaining energy levels, and quality of networks. Depending on broadcast distances/ranges, sound propagation speeds, residual energies, packet collision preventions, and prevention of redundancies in broadcasts, the forwarded data packets remain in forwarder nodes for specified amounts of time. Based on the aforementioned factors, the best forwarding nodes are ones that hold packets for shorter periods. In case nodes discover overheard packets, then these packets are discarded while other packets are retained in buffers till they are forwarded. Measures taken into account for forwarder node selections have direct influences on the performance of routing protocols whereas residual energy metrics help create balances in node energies. Link qualities are primary measures as they affect the energy usage of SNs and PDRs. Measuring depths are useful in decreasing energy dissipations since the sink's beacon transmissions are used to compute local depths and physical distances. As a result, multiple parameters for energy efficacy and resilience of forwarder nodes need to be considered in the selection procedures of forwarder nodes. SNs other than selected forwarder nodes store data packets and when their holding times expire, they relay and do not spy. Hence, shortest path selections are an elementary challenge as they impact transmissions and lifespans of networks based on energy levels [31]. It is natural to choose SNs with minimized depths compared to senders so that broadcasts and elections of forwarder nodes are limited. This work has introduced HSALSOA for optimum forwarder node selection. The Simulated Annealing algorithm is hybridized as it encompasses ideal local and global search capability for the bigger network.

#### 3.2.1. LSOs (Lion Swarm Optimizations)

LSOs are bio-influenced metaheuristic algorithms for optimization problems. It was proposed in 2009 at Cambridge University [32]. LSOs rely on the natural split of labor amongst lion kings, lionesses, and lion cubs among lions pack have been put forward recently. The primary concept of LSOs is explained in Algorithm 1 [33]. At first, the method performs random initialization of the location of lions in search space, and the location having optimal fitness value is fixed as the lion king's location. Next, multiple lions are selected to be the hunting lions (also known as a lioness) and

coordinate with one another for hunting. If the prey is better compared to the lion king's prey, then the location of the prey would be taken by the lion king. So, cubs go behind the lioness so that they can study to hunt or eat close to the lion king, and would be sent out of the herd when they become adults. For survival, the lions which are sent out will attempt to get nearer to the optimal place that they have in memory. At first, as per labor division and cooperation, lions retain looking repetitively to obtain optimum data of objective function.

Steps of LSO algorithm:

Step 1: Initialize the position of every lion  $x_i, n, T, D, a_1, a_2$  and  $\beta$ .

Step 2: (1) compute the fitness value of every single lion and the value of nLeader

(2) Order the positions of lions based on their fitness value

(3) Find the lion king, lionesses and lion cubs. Record  $P_{best}$  and  $G_{best}$  and select  $P_{bestc}$  and  $P_{bestm}$ .

(4) Generate random number  $\gamma$  using normal distribution  $N(0,1)$ . Compute  $\alpha_f$  and  $\alpha_c$ .

Step 3: Update the position of lion king

Step 4: Update the position of lionesses

Step 5: Generate random number  $q$  and  $\gamma$  through  $U(0,1)$  and  $N(0,1)$ . Update the position of lion cubs.

(1) If  $q \leq 1/3$ , update the position of lion cubs

(2) If  $1/3 < q < 2/3$ , update the position of lion cubs

(3) If  $2/3 \leq q \leq 1$ , update the position of lion cubs

Step 6: (1) Compute the fitness values in accordance with the position of lion, and update  $p_{best}$ ,  $g_{best}$ ,  $P_{bestc}$  and  $P_{bestm}$ .

(2) verify if the algorithm meets the stop criterion.

(3) If the termination condition is attained, move to Step 8; else, move to Step 7.

Step 7: order is resorted for every constant number of iteration (nearly 10 times) to decide the position of the lion king, the lionesses and the lion cubs, and go to Step 3.

Step 8: Output the location of  $G_{best}$  to be best solution of optimization problem, terminate the iteration process.

---

#### Algorithm 1 LSOs

#### 3.2.2. Simulated Annealing

Simulated Annealing (SA) is one of the most predominant metaheuristic algorithms that have the capability of global

**RESEARCH ARTICLE**

optimizations [34]. SAs are trajectory based, arbitrary search strategies that mimic annealing processes that occur when metals are frozen too for crystals with the minimum usage of energies and achieving larger crystal sizes and thus minimizing limitations of metallic structures. The annealing procedure consists of careful temperature control and cooling rate, frequently known as the annealing schedule. SAs are used with success in different fields.

The method begins with the primary result and gets a close response for that result, and if there is no improvement in the objective function, it is taken with a probability  $p$ . here  $\Delta E$  refers to the difference between the objective function of the present response and the neighbor's response,  $T$  indicates temperature. At every temperature, multiple iterations are run, then the temperature is reduced gradually. In the initial stages, the temperature is maintained very high to improve the probability of getting worse responses.

The slow temperature reduction in last steps leads to possibilities of getting worse replies to reduce and therefore, method gets converged to best response. This method averts being restricted into local optimized locations resulting in movements towards reduced energies. The solution levels of  $x$  with fitness obtained using function  $f(x)$  based on its neighbours  $x'$ ,  $N(x)$ . The differences amongst objective functions of levels are given in eqn (8):

$$\Delta = f(x) - f(x') \tag{8}$$

$X'$  can be computed with the equation (9) below:

$$P_s = \exp\left(-\frac{\Delta}{T}\right) \tag{9}$$

Next, the probability of admitting a arbitrary value  $r \in (0,1)$  is then contrasted and  $x'$  becomes acceptable if  $P > r$ .  $T$  refers to temperature that the cooling plan controls. But, simulated annealing method consists of other factors like primary temperatures, varying temperatures, and cooling plans. The fundamental construction of SA method is provided Algorithm 2.

- 
- Choose a starting solution  $x$
  - REPEAT
  - Form the solution  $x'$  in neighborhood of  $x_0$
  - Compute  $\Delta$ , probability using Equation. (8)
  - Determine the new solution by  $P_s$
  - Remember optimal solution got till now
  - Decrease the temperature
  - UNTIL criteria are satisfied

---

Algorithm 2 Construction of SA Method

3.2.3. Hybrid Lion Swarm Optimization Using Simulated Annealing

This work introduces a novel approach to solving optimization problems. The proposed approach is a hybrid form of lion swarm optimization and a simulated annealing algorithm. Lion swarm optimization is population-driven. These algorithms exhibit a significant capability in global search, even though they are found to be not very strong in local searches. As mentioned in the earlier segment, the simulated annealing method consists of a procedure for neighbor search.

The procedure achieves an improved local search ability for the proposed technique; however, it executes strong global searches. Fusions of these methods help in global explorations search spaces with lion swarm methods and locally employing simulated annealing technique, thus exploiting benefits of both algorithms.

The proposed technique includes the generation of  $n$  primary population of the lion is initially done and the position of each lion is calculated. Then, every lion goes in the direction of the lion with maximum attraction. This work's produced solutions use simulated annealing approaches for local searches where its form can be generalized in Algorithm 3.

1. Starting initialization of lion swarm algorithm factors like total primary population  $N_{Pop}$ , total maximum replications, and coefficients of attraction.

2. Starting Initialization of simulated annealing process variables, such as total repetitions and main temperature ( $T$ ).

3. Creation of  $N_{Pop}$  lion (primary solution).

4. For every pair of lion (solutions) utilize subsequent steps:

4.1. When fitness of lion  $i$  is greater than lion  $j$  (or when fitness function  $i$  is comparably good than fitness function  $j$ ), lion  $i$  travels towards lion  $j$  as per following eqn (10):

$$\Delta x_i = \beta_0 e^{-\gamma r_{ij}^2} (x_j^t - x_i^t) + \alpha \epsilon_i \tag{10}$$

4.2. Modify the position based on the distance.

4.3. For every obtained solution  $x$ :

4.3.1. Get  $x$  neighbours.

4.3.2. when its energy is reduced  $\Delta E < 0$ , take solution, else admit it if  $\exp(-\Delta E/T)$

4.3.3. If the balance is not attained, temperature has to be reduced and move to step 4.3.1.

4.4. When the termination criterion of the method is not satisfied, go to step 4.

---

Algorithm 3 Simulated Annealing Approaches

**RESEARCH ARTICLE**

**3.3. Secured Routing Using Modified Elliptic Curve Cryptography**

When data transmissions are monitored during assaults, two metrics get measured namely delays and Packet Loss Ratios (PLRs). These variables determine if users meet their requirements of Quality of Services (QoSs). PLRs are defined as proportions of total dropped packets during flows to overall total packets of similar flows. Delays and PLRs are superior measures for assessments, specifically in the case of malicious user flows as the networks would face excessive delays. The aforementioned attacks can significantly impact QoSs including delays, throughputs, Packet Delivery Ration (PDRs), jitters, and energies.

ECC hybrid signcryption cryptographic approaches which create public/private encryption keys are used for recoveries after attacks. ECCs performs better than other encryption technique in terms of limited key lengths, stronger security, constrained memory spaces, enhanced speeds, computational costs, and forwarding privacies. Approaches of ECCs generate optimal private/public keys.

Hash padding, results of digital signatures are used in signcryption techniques. Hash padded data are then applied to encrypted hash functions with certificates received from digital signatures i.e. digitally signed. This implies authentication of data amongst neighbors. Subsequently, signed data packet are encrypted using CBCs (Cipher block chains) where plaintext blocks and earlier blocks of ciphertexts go through XOR operations prior to their encryptions. In this manner, every block of ciphertext relies on entire plaintext blocks that are handled till that point. For making every message distinct, an initialization vector has to be utilized in starting block. CBCs have remained a prominent method of analysis. The messages need to be padded in multiples of cypher block sizes, and only sequential encryptions are possible (they cannot be parallelized). One way of handling this obstacle is by using ciphertext stealing. Single bit variations in plaintexts or initialization vectors impact the following ciphertext blocks. IV, or starting variables are blocks of bits used by different modes to make encryptions random and hence offer separate ciphertexts even when comparable plaintexts are encrypted several times without requiring time-consuming re-keying procedures. The ultimate goal is to create the best signcryption possible, based on KEMs (Key Encapsulation Mechanisms) and DEMs (Data Encapsulation Mechanisms). KEMs are implemented using KDFs (Key Derivation Functions) and secure pseudo random number generation techniques [34]. KEMs transfer secret symmetric keys where extra keys are required to share secret keys for different cryptographic purposes like encryptions and integrity protections. KDFs are used to extract secret keys from other keys or known information using safe pseudo-random value methods where pseudo-random number

generations and KDFs are separate in KDFs. In traditional signcryption systems, DEMs are applied on basis of AES encryptions whereas in this suggested approach, AES methods are substituted with optimal ECCs.

Algorithm 4 shows how ECCs produce private and public encryption keys in signcryptions. ECCs increasing data security and ensure that keys generated are reliable. The functions in ECCs are specified in Prime and Binary fields where suitable fields with a finite big number of points are chosen for cryptography. The prime field procedure involves choosing prime integers and generating elliptic curves with points spanning from 0 to Z.

- Order the transmission of full data packets throughout a timed session.
- Use a digital signature (static) as the Initialization Vector for the XOR operation on plain text.
- To get Cipher Texts symmetric key encryptions are used along with CBCs.

Cipher\_texts1=CBCs

(Plain\_texts1 ⊕ Digital\_signature\_no)

- To perform XOR on subsequent packets, Cipher texts from the first packet are used.

Cipher\_texts2=CBCs (Plain\_texts2 ⊕ Cipher\_texts1)

- The procedures are iterated for all of session's packets.

Cipher\_texts<sub>i</sub>= CBCs (Plain\_textsi ⊕ Cipher\_textsi-1)

- Symmetric keys are padded with data packets during iterations.
- Data padded with keys are encrypted using Asymmetric Key Cryptography procedures of ECC's
- KEMs and D|E|Ms are used on data packets

Algorithm 4 ECC Based Signcryption Method

**4. RESULTS AND DISCUSSION**

Table 1 Simulation Factors

Factor	Values
Number of Nodes	100
Size of Area	1100 X 1100 m
Mac	802.11
Radio Range	250m
Simulation Time	60 sec
Packet Size	80 bytes

**RESEARCH ARTICLE**

The experiments on HSALSO-CA are carried out and its comparison analysis is performed with other techniques in this section. The techniques taken for assessments are ACOs (Ant Colony Optimizations), LSDAR (Light Weight Structure-based Data Aggregation Routing), ELSOA-CAs and suggested HSALSO-CA and the simulation is performed employing the NS-2 simulator. The measures taken for contrasts are E2E delay, throughput, energy dissipation, network lifetime. Simulation factors considered are mentioned in Table 1.

4.1. Performance Assessment

4.1.1. End to End Delays

These are the average times that packets consume while being transferred from sources to destinations in networks and based on Equation (11).

$$End - to - end\ delay = \frac{\sum_{i=1}^n (t_{ri} - t_{si})}{n} \tag{11}$$

Where  $t_{ri}$  – ith packet delivery time,  $t_{si}$  – time when ith packet was sent, n – number of packets.

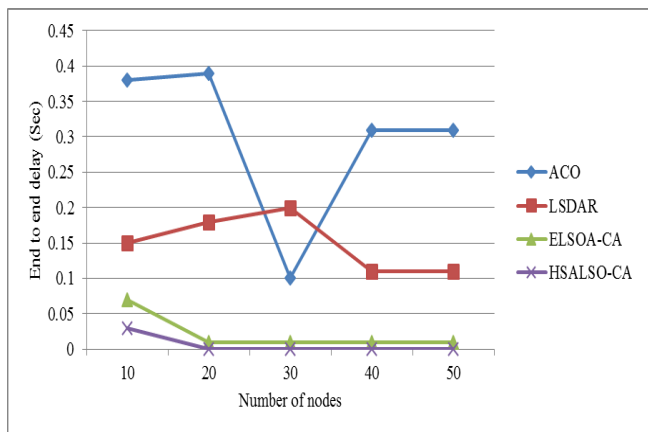


Figure 3 E2E Delay Comparison

Figure 3 shows comparative evaluations in terms of end-to-end delays where nodes form the x-axis while their corresponding delay values are plotted on the y-axis. Compared techniques include ACO, LSDAR, ELSOA-CAs, and the proposed HSALSO-CA algorithm which yields reduced E2E delays. Therefore, the proposed HSALSO-CA method chooses the best forwarder nodes by their HSALSO fitness values.

4.1.2. Throughputs

These are data packets sent against packets received effectively in networks and computed using Equation (12).

$$Throughputs = \frac{total\ number\ of\ packets\ sent}{time} \tag{12}$$

Figure 4 depicts comparison evaluations in terms of

throughput performance of ACOs, LSDAR, ELSOA-CAs, and the suggested HSALSO-CA algorithm where nodes form the x-axis while their corresponding throughputs are y-axis values. The suggested method of this work yields increased throughputs amongst the strategies studied for comparison. As a result, the proposed HSALSO-CA system selects the optimal forwarder nodes based on HSALSO fitness values.

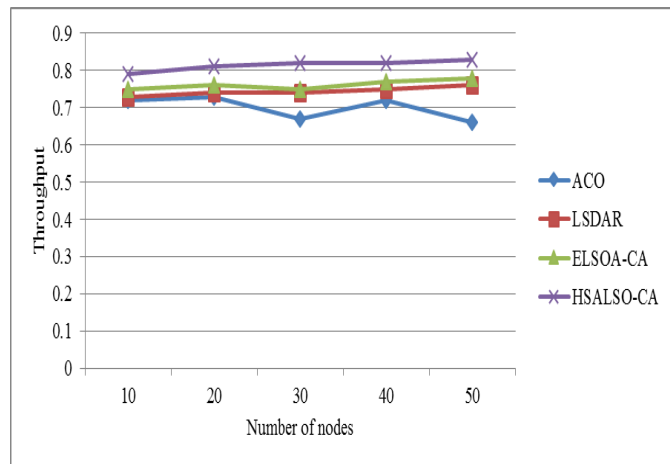


Figure 4 Comparison of Throughput

4.1.3. Energy Consumptions

This parameter implies average energies required by networks for transmissions of packets to SNs within a specified time frame and given as Equation (13)

$$Energy (e) = [(2 * pi - 1)(e_t + e_r)]d \tag{13}$$

Where  $pi$  - data packet,  $e_t$  - packet i's source energy,  $e_r$  - energy needed for the receipt of packet i, d - distance among source and destination nodes.

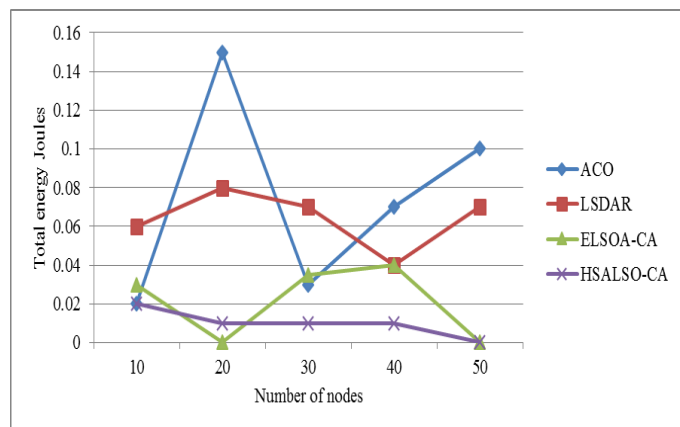


Figure 5 Energy Consumption Comparison

Figure 5 shows the comparative analysis concerning energy utilization performance, where nodes form the x-axis while their corresponding energy utilization is y-axis values.

**RESEARCH ARTICLE**

Compared techniques comprises of ACO, LSDAR, ELSOA-CAs, and the proposed algorithm HSALSO-CA dissipating less energy. Therefore, the proposed HSALSO-CA system helps in choosing the best of the forwarder nodes on the basis of HSALSO fitness data.

4.1.4. Network Lifespans

The life spans of networks can be computed using Equation (14)

$$Lifetime \mathbb{E}[L] = \frac{\epsilon_0 - \mathbb{E}[E_w]}{P + \lambda \mathbb{E}[E_r]} \quad (14)$$

Where P represents network’s constant power consumptions and a continuous value,  $\epsilon_0$  represents sum of non-rechargeable initial energy,  $\lambda$  stands for average reporting rates of sensors,  $\mathbb{E}[E_w]$  implies the expected energy wastages or non-utilized energies till the death of a network and  $\mathbb{E}[E_r]$  –reported energy consumption of nodes.

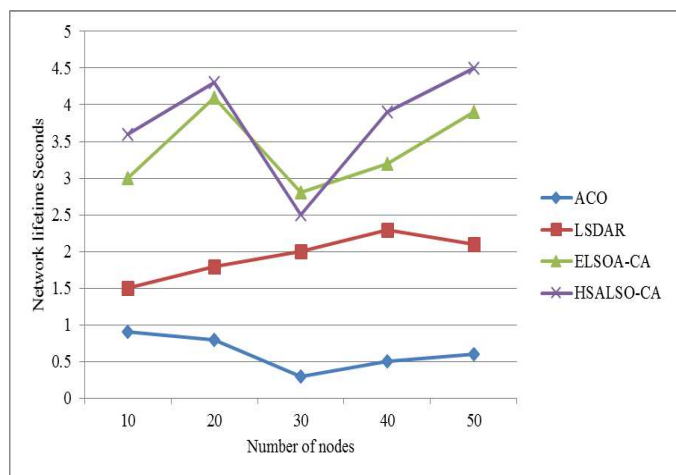


Figure 6 Network Lifetime

Figure 6 depicts a comparison analysis concerning the performance of network lifetime, where nodes form the x-axis while their corresponding network’s life spans are y-axis values. The methods used in comparisons include ACOs, LSDAR, ELSOA-CAs, and proposed HSALSO-CA which yields an increase in network lifetime. Therefore, the proposed HSALSO-CA selects the best of the forwarder nodes by HSALSO fitness values.

4.1.5. PDR

PDR indicates the proportion of total lost packets to overall sent packets can be expressed in eqn (15)

$$Packet \ loss \ ratio = \frac{N^{tx} - N^{rx}}{N^{tx}} \times 100\% \quad (15)$$

Where  $N^{tx}$  - transmitted packets,  $N^{rx}$  - received packets. This evaluation was carried out through the extraction of all real-time packet sizes, which are sent and obtained.

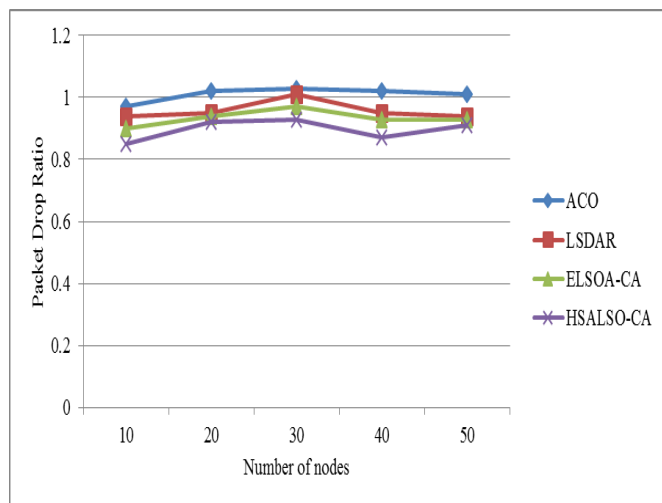


Figure 7 Packet Drop Ratio

Figure 7 shows the comparison evaluation concerning PDR performance, where nodes form the x-axis while their corresponding PDRs are y-axis values. Techniques taken for comparison include ACO, LSDAR, ELSOA-CAs, and the proposed HSALSO-CA algorithm which reveals reduced PDR. This way, the proposed HSALSO-CA system chooses the best forwarder nodes based on HSALSO fitness values.

5. CONCLUSION

In the proposed technical work, the focus is on optimum, rapid, and energy-efficient data broadcasting such that decisions on tomato crops are made with accuracy. In this research work, multipath routing is proposed for guaranteeing that the data transmission is faster. In this, rapid multipath routing is made sure by choosing the optimal forwarder nodes that handle limitations in delays and energies. Hence, optimal Forwarding Node selections are employed using the proposed HSALSOA scheme. The Simulated Annealing algorithm is hybridized as it encompasses both optimal local and global search capability for the bigger network. Secured data transmission employing modified ECC algorithm guarantees increased security for congestion-aware multipath routing mechanisms. In comparison to existing methodologies, simulation results demonstrate that the proposed ELSOA-CAs model delivers superior performance in terms of throughputs, network longevities, reduced energy usage, and end-to-end delays.

REFERENCE

- [1] Orhan, O. (2016). Energy neutral and low power wireless communications (Doctoral dissertation, Polytechnic Institute of New York University).
- [2] Li, J., Liu, W., Wang, T., Song, H., Li, X., Liu, F., & Liu, A. (2019). Battery-friendly relay selection scheme for prolonging the lifetimes of sensor nodes in the Internet of Things. *IEEE Access*, 7, 33180-33201.
- [3] Wang, C., He, Y., Yu, F. R., Chen, Q., & Tang, L. (2017). Integration of networking, caching, and computing in wireless systems: A survey,

**RESEARCH ARTICLE**

some research issues, and challenges. *IEEE Communications Surveys & Tutorials*, 20(1), 7-38.

[4] Shaf, A., Ali, T., Draz, U., & Yasin, S. (2018). Energy Based Performance analysis of AODV Routing Protocol under TCP and UDP Environments. *EAI Endorsed Transactions on Energy Web*, 5(17).

[5] Yang, L., Zhu, H., Kang, K., Luo, X., Qian, H., & Yang, Y. (2018, April). Distributed censoring with energy constraint in wireless sensor networks. In *2018 IEEE International Conference on Acoustics, Speech and Signal Processing (ICASSP)* (pp. 6428-6432). IEEE.

[6] Randhawa, S., & Jain, S. (2017). Data aggregation in wireless sensor networks: Previous research, current status and future directions. *Wireless Personal Communications*, 97(3), 3355-3425.

[7] Tomic, I., & McCann, J. A. (2017). A survey of potential security issues in existing wireless sensor network protocols. *IEEE Internet of Things Journal*, 4(6), 1910-1923.

[8] Kharb, K., Sharma, B., & Trilok, C. A. (2016). Reliable and congestion control protocols for wireless sensor networks. *International Journal of Engineering and Technology Innovation*, 6(1), 68.

[9] Anand, N., Varma, S., Sharma, G., & Vidalis, S. (2018). Enhanced reliable reactive routing (ER3) protocol for multimedia applications in 3D wireless sensor networks. *Multimedia Tools and Applications*, 77(13), 16927-16946.

[10] Kumaravel, K., & Anusuya, N. (2018). A SURVEY ON CONGESTION CONTROL SYSTEM IN WIRELESS SENSOR NETWORKS. *International Journal for Research in Science Engineering & Technology*, 5(9), 7-11.

[11] Harish, V. S. K. V., & Kumar, A. (2016). A review on modeling and simulation of building energy systems. *Renewable and sustainable energy reviews*, 56, 1272-1292.

[12] Rosset, V., Paulo, M. A., Cespedes, J. G., & Nascimento, M. C. (2017). Enhancing the reliability on data delivery and energy efficiency by combining swarm intelligence and community detection in large-scale WSNs. *Expert Systems with Applications*, 78, 89-102.

[13] Bhatia, A., & Hansdah, R. C. (2016). TRM-MAC: A TDMA-based reliable multicast MAC protocol for WSNs with flexibility to trade-off between latency and reliability. *Computer Networks*, 104, 79-93.

[14] Mohanty, P., & Kabat, M. R. (2016). Energy efficient structure-free data aggregation and delivery in WSN. *Egyptian Informatics Journal*, 17(3), 273-284.

[15] Faheem, M., Butt, R. A., Raza, B., Ashraf, M. W., Ngadi, M. A., & Gungor, V. C. (2019). Energy efficient and reliable data gathering using internet of software-defined mobile sinks for WSNs-based smart grid applications. *Computer Standards & Interfaces*, 66, 103341.

[16] Elappila, M., Chinara, S., & Parhi, D. R. (2018). Survivable path routing in WSN for IoT applications. *Pervasive and Mobile Computing*, 43, 49-63.

[17] Sharma, B., Srivastava, G., & Lin, J. C. W. (2020). A bidirectional congestion control transport protocol for the internet of drones. *Computer Communications*, 153, 102-116.

[18] Vinitha, A., & Rukmini, M. S. S. (2019). Secure and energy aware multi-hop routing protocol in WSN using Taylor-based hybrid optimization algorithm. *Journal of King Saud University-Computer and Information Sciences*.

[19] Devi, V. S., Ravi, T., & Priya, S. B. (2020). Cluster Based Data Aggregation Scheme for Latency and Packet Loss Reduction in WSN. *Computer Communications*, 149, 36-43.

[20] Rekha, & Gupta, Rajeev. (2021). Elliptic Curve Cryptography based Secure Image Transmission in Clustered Wireless Sensor Networks. *International Journal of Computer Networks and Applications*. 8. 67. 10.22247/ijcna/2021/207983.

[21] Qazi, R., Qureshi, K. N., Bashir, F., Islam, N. U., Iqbal, S., & Arshad, A. (2021). Security protocol using elliptic curve cryptography algorithm for wireless sensor networks. *Journal of Ambient Intelligence and Humanized Computing*, 12(1), 547-566.

[22] Uma Maheswari P, Ganeshbabu TR, P.Subramanian, Elliptic Curve Cryptography based Secure Data Communication and Enhance sensor Reliability in Wireless Sensor Network, *International Journal of Recent Technology and Engineering (IJRTE)*, 8(5), 2020.

[23] Rajeev Arya and S.C. Sharma, "Energy Optimization of Energy Aware Routing Protocol and Bandwidth Assessment for Wireless Sensor Network", *International Journal of System Assurance Engineering and Management*, 9(3), pp. 612-619, 2018.

[24] Haseeb, K., Islam, N., Saba, T., Rehman, A., & Mehmood, Z. (2020). LSDAR: A light-weight structure based data aggregation routing protocol with secure internet of things integrated next-generation sensor networks. *Sustainable Cities and Society*, 54, 101995.

[25] Silambarasan, S., & Devi, M. S. (2021). Enhanced Lion Swarm Optimization Algorithm With Centralized Authentication Approach for Secured Data Transmission Over WSN. *ICTACT Journal on Communication Technology*, 12(3), 2471-2479.

[26] W. B. Heinzelman, A. P. Chandrakasan, and H. Balakrishnan, "An application-specific protocol architecture for wireless microsensor networks," *IEEE Transactions on Wireless Communications*, vol. 1, no. 4, pp. 660-670, 2002.

[27] D. Kumar, T. C. Aseri, and R. B. Patel, "EEHC: energy efficient heterogeneous clustered scheme for wireless sensor networks," *Computer Communications*, vol. 32, no. 4, pp. 662-667, 2009.

[28] Lee, H.; Wicke, M.; Kusy, B.; Gnawali, O.; Guibas, L. Data Stashing: Energy-Efficient Information Delivery to Mobile Sinks through Trajectory Prediction. *Proceedings of the 9th ACM/IEEE International Conference on Information Processing in Sensor Networks*, Stockholm, Sweden, 12-16 April 2010; pp. 291-302.

[29] Tian, K.; Zhang, B.; Huang, K.; Ma, J. Data Gathering Protocols for Wireless Sensor Networks with Mobile Sinks. *Proceedings of the IEEE Global Telecommunications Conference (GLOBECOM 2010)*, Miami, FA, USA., 6-10 December 2010; pp. 1-6.

[30] Kusy, B.; Lee, H.; Wicke, M.; Milosavljevic, N.; Guibas, L. Predictive QoS Routing to Mobile Sinks in wireless sensor networks. *Proceedings of the IEEE International Conference on Information Processing in Sensor Networks (IPSN, 2009)*, San Francisco, CA, USA, 13-16 April 2009; pp. 109-120.

[31] Wang, M.; Heidari, A.A.; Chen, M.; Chen, H.; Zhao, X.; Cai, X. Exploratory differential ant lion-based optimization. *Expert Syst. Appl.* 2020, 159, 113548.

[32] Pierezan, J.; Coelho, L.d.S.; Mariani, V.C.; Goudos, S.K.; Boursianis, A.D.; Kantartzis, N.V.; Antonopoulos, C.S.; Nikolaidis, S. Multiobjective Ant Lion Approaches Applied to Electromagnetic Device Optimization. *Technologies* 2021,

[33] E. Aarts, J. Korst, and W. Michiels, "Simulated annealing," in *Search Methodologies: Introductory Tutorials in Optimization and Decision Support Techniques*, K Burke and G. Kendall, Eds., pp. 91-120, Springer US, Boston, Mass, USA, 2nd edition, 2014.

[34] Nishanth, R. B., Ramakrishnan, B., & Selvi, M. (2015). Improved signcrypton algorithm for information security in networks. *International Journal of Computer Networks and Applications (IJCNA)*, 2(3), 151-157.

**Authors**



**Silambarasan S** received the BCA (2004) from Periyar University, Salem, MCA (2008) from Anna University and M.Phil (2014) in Computer Science from the Vinayaka Missions University, Salem. He joined the Department of Computer Science and Applications at Don Bosco College, Dharmapuri in 2009, as an Assistant Professor. His research interests include Data Mining, Big Data, and Network Security.

**RESEARCH ARTICLE**

**Dr. M. Savitha Devi** completed her Ph.D in Mother Teresa Women's University, Kodaikanal. She done her M.C.A and M.Phil from Periyar University, Salem, and studied her PGM.Sc Computer Science in Vysya College, Salem where she got University 11<sup>th</sup> rank in the year 2003. She completed her under graduate course in Government Arts College, Salem-8. She began her carrier as Assistant Professor in Computer Science in AVS College, Salem in 2003 and


taught for 4 years and then joined in Don Bosco College, Dharmapuri and continued her teaching profession for 9 years as a Faculty, Head of the Department, Research Co-Ordinator, IQAC Co-Ordinator, Academic Council Member, Class Quality Cell Co-Ordinator as well as member in various committees. She also attended Faculty Development Programmes on "Total Quality Management" organised by CHRIST University, Bangalore and "Role of IQAC Towards Quality Assurance in Autonomous Colleges" organised by Sacred Heart College, Thirupattur. She has received a Best Co-Ordinator award by ARK Techno Solutions, IIT Chennai, chief faculty 2015 ROBOKART.com. She has completed a "Virtual Course for Teachers of Higher Education in International Distant Education Unit of DBI of Higher Education – Brazil" on Oct' 2009 to Apr'2010. She was a Board of Studies member for B.Sc Digital Print Media in Periyar University, Salem for 7 years. She acted as an External Expert Committee Member in MGR College, Hosur on 2013 for Visual Communication Course. On July 2017, she joined as an Assistant Professor and Head in Computer Science, Government Arts and Science College, Harur - 636903, Dharmapuri District, TamilNadu and continuing her admirable job in the 18<sup>th</sup> year.

**How to cite this article:**

S. Silambarasan, M. Savitha Devi, "Hybrid Simulated Annealing with Lion Swarm Optimization Algorithm with Modified Elliptic Curve Cryptography for Secured Data Transmission Over Wireless Sensor Networks (WSN)", International Journal of Computer Networks and Applications (IJCNA), 9(3), PP: 316-327, 2022, DOI: 10.22247/ijcna/2022/212557.



# Analyzing the efficiency of nanostructured Sm<sup>3+</sup>- and Gd<sup>3+</sup>-doped TiO<sub>2</sub> and constructing DSSCs using efficacious photoanodes

S. Bharathi Bernadsha<sup>1</sup>, V. Anto Feradrick Samson<sup>1,\*</sup> , N. J. Simi<sup>2</sup>, J. Madhavan<sup>1</sup>, and M. Victor Antony Raj<sup>1</sup>

<sup>1</sup>Department of Physics, Loyola College (University of Madras), Chennai, Tamil Nadu, India

<sup>2</sup>Department of Physics, Newman College, Thodupuzha, Idukki, Kerala, India

Received: 12 November 2021

Accepted: 20 January 2022

© The Author(s), under exclusive licence to Springer Science+Business Media, LLC, part of Springer Nature 2022

## ABSTRACT

The rare earth elements, gadolinium and samarium, are doped with TiO<sub>2</sub> by hydrothermal synthesis technique to study the photoconversion performance of a photoanode in a dye-sensitized solar cell (DSSC). The obtained materials are subjected to the characterizations XRD, HR-TEM, UV-Vis spectroscopy, and XPS. DSSCs are fabricated using N719 dye, redox electrolyte, and platinum counter electrode. Charge-transfer ability was investigated using electrochemical impedance spectroscopy (EIS) on DSSCs. The efficiencies of DSSCs are influenced by the electron transport within the TiO<sub>2</sub>-dye-electrolyte system. After the fabrication and simulation, among the two, Gd<sup>3+</sup>-doped TiO<sub>2</sub> gives the desired outcomes and higher efficiency (5.542%) than the pure and Sm<sup>3+</sup>-doped TiO<sub>2</sub> and thus it proves to be a superior solar cell anode material.

## 1 Introduction

According to the report of National Action Plan on Climate Change (NAPCC), those who use power also have the responsibility to maintain the environment cleaner. This statement calls for curtailing higher carbon dioxide emitting energy productions and to innovate alternative resources. Dye-sensitized solar cells (DSSCs) are being investigated intensively as potential alternatives for the next-generation solar cells. From the time Gratzel and his team reported the first DSSCs in the year 1991 and threw some light upon the increasing efficiency of solar cells with

minimized expenses, DSSCs have become the talk of the town. The features like low production cost, high power conversion efficiency (PCE), payback period, and ecofriendly production promote DSSCs superior to their older generation silicon solar cells [1, 2, 3].

Among all the semiconductor materials, TiO<sub>2</sub> nanoparticles are widely used as photoanode due to its large surface area-to-volume ratio, high PCE, and easy preparation in DSSCs [4]. Moreover, the conversion efficiency of TiO<sub>2</sub>-based DSSCs has energy losses by recombination and slow electron transportation as major predicaments [5, 6]. One of the most important parts of DSSCs is photoanode [7]. However, the

Address correspondence to E-mail: antofradrick@gmail.com



development of promising photoanode that exhibits better solar cell performance is still critical for the applications of DSSCs. Research works have been attempted on designing and preparing the highly efficient materials for DSSCs. Enhancing the DSSCs' performance using TiO<sub>2</sub> coupling with other materials is considered to be an important field of research [8]. Such an attempt is made by doping the rare earth elements (REEs) like samarium and gadolinium with TiO<sub>2</sub> and the characterizations were done to find the suitability of the synthesized material. TiO<sub>2</sub> is sensitive only to UV light by cause of its large bandgap, and it has low quantum efficiency, resulting from the fast recombination rate of photogenerated electron–hole pairs. Doping with metal and non-metal species is a popular technique which facilitates visible light activity of titanium dioxide. Moreover, the REE used for doping resulted in stronger absorption edge shift toward a longer wavelength. Red shift of this type can be attributed to the charge-transfer transition between rare earth ion's *f* electrons and the TiO<sub>2</sub> conduction or valence band. Introducing the orbitals between the conduction and valence band of TiO<sub>2</sub> reduces the bandgap. Samarium and gadolinium are also economic compared to other lanthanides and they improve the absorption in the visible light spectrum [9].

REEs-doped TiO<sub>2</sub> is synthesized through hydrothermal method and produced as an efficient photoanode. The effect of samarium (Sm<sup>3+</sup>) and gadolinium (Gd<sup>3+</sup>) on the surface and morphology of TiO<sub>2</sub> was investigated by characterizing the material with XPS, TEM, and XRD. The optical property was elucidated by UV spectroscopy. The *J*–*V* characteristics provide the data to calculate the efficiency of the fabricated DSSCs. Doping TiO<sub>2</sub> with transition metals is known to enhance their response in visible light region [10, 11]. Very few reports are available accounting for the improvement in the efficiency of TiO<sub>2</sub> toward visible light when doped with lanthanide ions/oxides [12]. Study on the comparison of doping Sm<sup>3+</sup> and Gd<sup>3+</sup> (2 wt%) with TiO<sub>2</sub> is not commonly available in works hence this work will pave path for the researchers to explore more.

## 2 Materials utilized

Samarium(III) oxide (powder, Sm<sub>2</sub>O<sub>3</sub>, 99.9%), gadolinium(III) oxide (powder, Gd<sub>2</sub>O<sub>3</sub>, 99.9%), and ethanol (99%) were purchased from Merck.

Titanium(IV) isopropoxide (liquid, Ti[OCH(CH<sub>3</sub>)<sub>2</sub>]<sub>4</sub>, anatase, 99.9%), platinum (liquid, 99.9%), and fluorine-doped tin oxide (FTO, 13 Ω/sq)-coated glass were received from Sigma-Aldrich. All chemical reagents were used without further purification as they were obtained from commercial sources with the highest purity.

## 3 Preparation technique

Solution reaction-based approach is carried out to synthesize nanomaterials and this method has good control over the compositions of the synthesized nanomaterials. Solution of pure TiO<sub>2</sub> and REE (Sm<sup>3+</sup>/Gd<sup>3+</sup>)-doped TiO<sub>2</sub> was synthesized using this widely employed technique. Titanium(IV) isopropoxide (anatase, 99.9%) and acetic acid were taken in 1:4 molar ratio. Drop by drop, 20 M of distilled water was added to the solution during magnetic stirring to get the solution. This process is allowed for 25 min to observe better results. The obtained solution was poured into a Teflon autoclave. The autoclave was placed in the furnace at 100 °C for 24 h. The product was exposed for 3 h at the heating rate of 5 °C/min to obtain TiO<sub>2</sub> nanoparticles by calcination at 400 °C. Following the same procedure of preparing undoped TiO<sub>2</sub>, RE<sup>3+</sup>-doped TiO<sub>2</sub> samples were synthesized. As mentioned above, after 25 min of stirring, the solution was added with samarium (2 wt%) in smaller quantities. After 25 min of stirring, the process was similar to that of preparing undoped TiO<sub>2</sub>. To get gadolinium-doped TiO<sub>2</sub>, the procedure of preparing samarium-doped TiO<sub>2</sub> is repeated by replacing samarium (2 wt%) with gadolinium (2 wt%).

## 4 Preparation of DSSC

The TiO<sub>2</sub> photoanodes were prepared by a modified version of the reported procedures mentioned by Jara et al. [13]. The FTO glass was sonicated for 20 min in ethanol, washed with acetone and Millipore water, and dried before use. 0.1 g of prepared material (undoped TiO<sub>2</sub>, Sm<sup>3+</sup>/Gd<sup>3+</sup>-doped TiO<sub>2</sub>) was added with a 0.25 ml of Triton-X 100 (4-octylphenol polyethoxylate) and ethanol (5 ml). Employing the prepared FTO glasses (20 mm × 20 mm) as substrates, the paste was dropped using pipette. Spin-

coating was carried out at 500 rpm for 30 s and 2000 rpm for 90 s. Then, it is left to dry at the ambient temperature. The schematic diagram of DSSC is provided in Fig. 1A.

On the anode FTO glass, 5 mmol of N719 dye was applied and left to spread evenly for 12 h. A few drops of liquid platinum were placed on another FTO glass and left to spread evenly. It was exposed to 350°C for 25 min to obtain the platinum (Pt) counter electrode. The two electrodes were sandwiched and a hole was made on the counter electrode.  $I^-/I_3^-$  taken as electrolyte was injected through the hole in the counter electrode. The arranged system was placed in the simulator to measure the activity of DSSC. At room temperature using a Keithley 2400 high current source power meter under white-light illumination from a 500 W xenon lamp (AM1.5G), current density–

voltage ( $J-V$ ) measurements were taken. The energy level diagrams of undoped and doped  $TiO_2$  are given in Fig. 1B.

## 5 Results and discussion

### 5.1 XRD

The prepared sample crystallographic phases were investigated using XRD. The XRD pattern of  $TiO_2$  and ( $Sm^{3+}$  and  $Gd^{3+}$ ) doped  $TiO_2$  is portrayed in Fig. 2b. The presence of strong diffraction peaks at  $2\theta \approx 25.2^\circ, 37.9^\circ, 48.1^\circ, 54.1^\circ, 54.9^\circ, 62.7^\circ, 68.9^\circ, 70.1^\circ,$  and  $75.1^\circ$  corresponding to the  $(hkl)$  reflections planes of (101), (004), (200), (105), (211), (204), (116), (220), and (215), respectively, (JCPDS card no. 21-1272). The

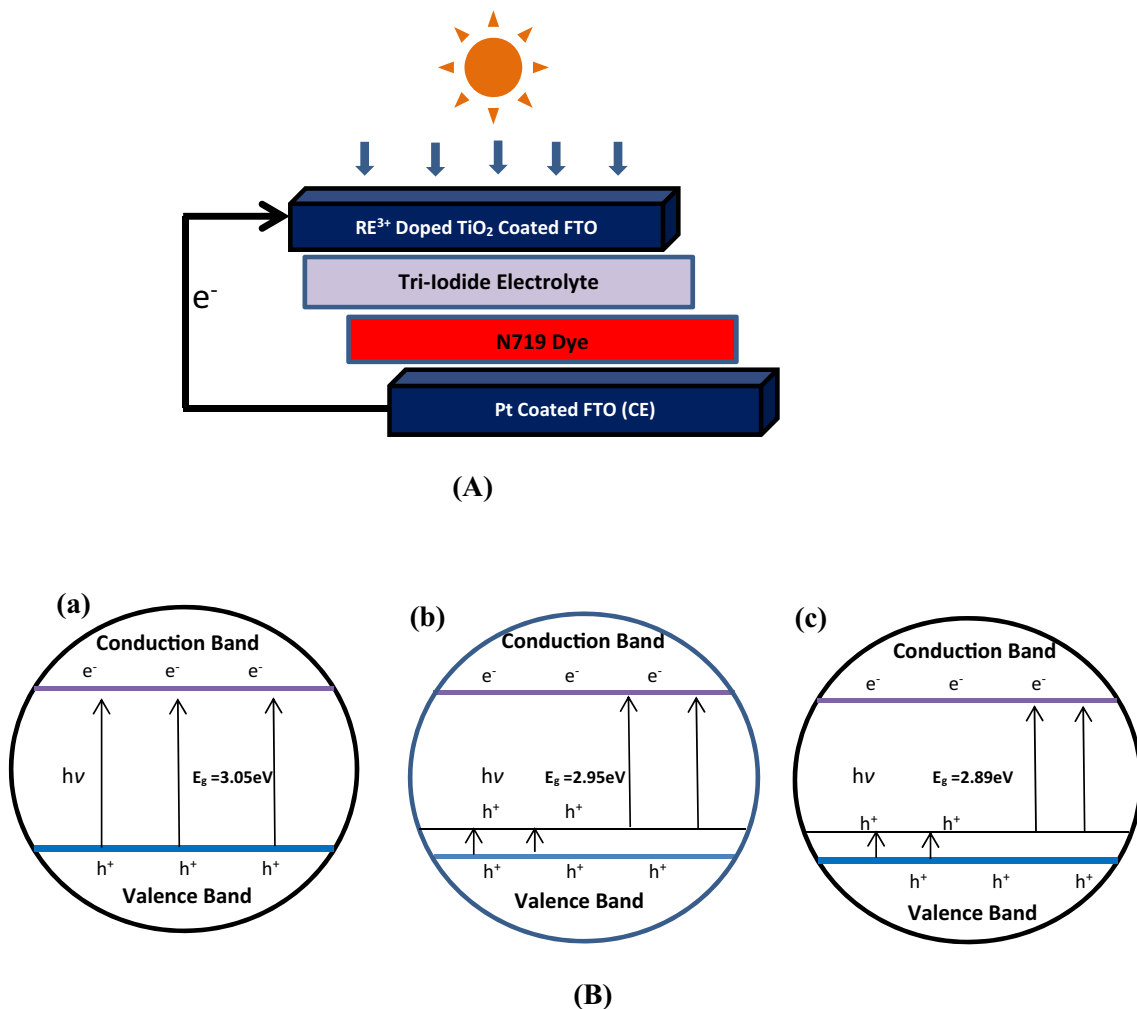


**Fig. 1** **A** Schematic diagram of fabrication of DSSC. **B** Energy level diagram of (a) undoped  $TiO_2$ , (b)  $Sm^{3+}$ -doped  $TiO_2$ , (c)  $Gd^{3+}$ -doped  $TiO_2$

obtained diffraction peaks indicate that anatase crystalline structure is present and the studies authenticate that there is no other impurity observed. Furthermore, peaks of  $\text{Sm}^{3+}$  and  $\text{Gd}^{3+}$  oxides are not seen in patterns. This situation can be ascribed to insertion of dopant ions into the crystal lattice of  $\text{TiO}_2$ . The average crystallite size of the  $\text{TiO}_2$  and  $\text{Sm}^{3+}$ - and  $\text{Gd}^{3+}$ -doped  $\text{TiO}_2$  sample grains was calculated from the prominent peak and the plane 101 utilizing Scherrer's equation. The obtained crystallite size is found to be 9.2, 8.74, and 8.77 for pure and  $\text{Sm}^{3+}$ - and  $\text{Gd}^{3+}$ -doped  $\text{TiO}_2$  samples. While doping with  $\text{Sm}^{3+}$  and  $\text{Gd}^{3+}$ , the crystallite size of the samples decreases. This can be attributed that dopant ions could go into the  $\text{TiO}_2$  lattice [14] and also the crystal growth of  $\text{TiO}_2$  nanoparticles was hindered by dopant ions resulting decreasing in crystal size [15]. From this XRD results,  $\text{Sm}^{3+}$ - and  $\text{Gd}^{3+}$ -doped  $\text{TiO}_2$  samples expected to have more surface area to adsorb large dye molecule into the  $\text{TiO}_2$  surface.

## 5.2 EDAX

Figure 3 provides the energy-dispersive X-ray analysis (EDAX) of Sm-doped, Gd-doped, and undoped  $\text{TiO}_2$ . EDAX is a systematic method utilized to analyze the elemental or chemical characterization of an area of the specimen under study. The elements corresponding to each of its peaks are analyzed. The elemental incorporations of Gd and Sm in the samples are confirmed through the spectrums obtained.

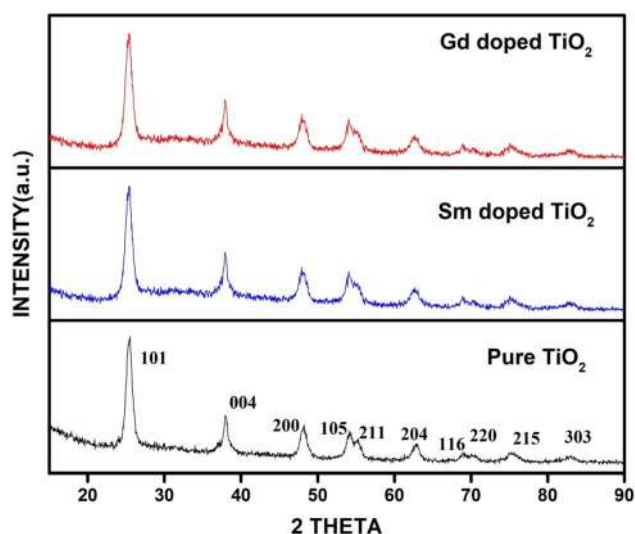


**Fig. 2** XRD images of (a) Gd-doped, (b) Sm-doped, and (c) undoped  $\text{TiO}_2$

Measure of the respective elements incorporated in the specimen is shown as the peak heights or areas are in Fig. 3. Table 1 shows the experimental mass percentage of the titanium, oxygen, gadolinium, and samarium as obtained from EDAX analysis of the compounds. From the spectrums, we observe that Ti peaks appear at + 0.6 keV, + 4.5, and + 5 keV. Samarium is detected at + 0.9, + 4.8, + 5.3, and + 6 keV. Gadolinium is found to be present at + 1, + 5.4, + 6.1 keV, and so on. Thus from the EDAX spectra, the presence of dopants, namely, samarium and gadolinium are seen and thus the doping has taken place as per the expected mass percentages into the  $\text{TiO}_2$  crystal lattice.

## 5.3 HR-TEM

Figure 4A represents the HR-TEM and SAED images of undoped and doped  $\text{TiO}_2$  materials. 2 wt% of doping REE ( $\text{Sm}^{3+}/\text{Gd}^{3+}$ ) ions cover the  $\text{TiO}_2$  nanoparticles to form uneven surface. A greater impact in preventing the growth of the grain and the creating reduction in the size was caused by the presence of samarium and gadolinium. The segregation of the doping ions at the grain boundary limits the grain growth by restricting direct contact of the grains.

Distinguishable crystal planes and well-defined spherical shapes are observed in both the samples. The sizes of the undoped and  $\text{Sm}^{3+}$ - and  $\text{Gd}^{3+}$ -doped samples were measured as 10.41, 9.26, and 9.32 nm, respectively. The lattice fringes are very clear and the interplanar distance is calculated as 0.276 nm for  $\text{Sm}^{3+}$ -doped  $\text{TiO}_2$ , 0.281 nm for Gd-doped  $\text{TiO}_2$ , and 0.269 nm for undoped  $\text{TiO}_2$ . The considerable waviness and expansion of fringes are attributed to the electrical stress might have been originated from earth ions doping [16, 17].

The reduction in the size of the particles was observed and in good agreement with XRD findings. Selected area electron diffraction patterns provide the information about the indices based on which we can calculate the  $d$ -spacing of the elements and the size of the materials is calculated from that measured  $d$ . These images prove that the materials possess properly formed poly crystalline structures. The planes are clear and distinct and easy to identify from the images. They are also in perfect agreement with the various planes present in XRD pattern. The cross-sectional image of undoped  $\text{TiO}_2$ , Sm-doped  $\text{TiO}_2$ ,

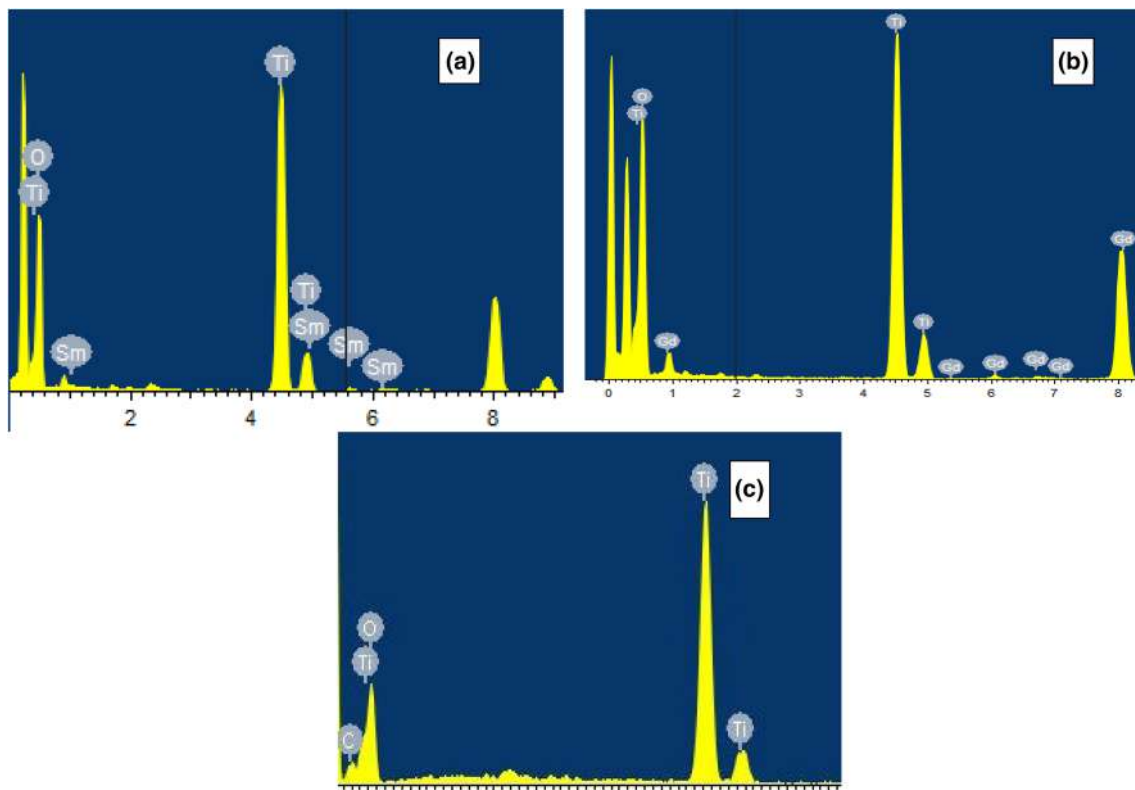


**Fig. 3** EDAX spectrum of **A** Sm-doped, **B** Gd-doped, and **C** undoped TiO<sub>2</sub>

**Table 1** Elemental composition and wt% of the synthesized materials

Materials	Element	Wt%
Samarium doped TiO <sub>2</sub>	O	36.52
	Ti	61.75
	Sm	01.73
Gadolinium doped TiO <sub>2</sub>	O	38.32
	Ti	59.83
	Gd	1.85
Pure TiO <sub>2</sub>	Ti	60.83
	O	39.16

and Gd-doped TiO<sub>2</sub> is shown in Fig. 4B and the thicknesses are measured to be 11.1 μm, 10.8 μm, and 11 μm, respectively.

#### 5.4 Absorption spectra

Optical properties and optic bandgap values of nanoparticles were investigated with UV-Vis spectroscopy. Figure 5A denotes the optical absorption spectra of undoped TiO<sub>2</sub>, Sm<sup>3+</sup>-doped, and Gd<sup>3+</sup>-doped TiO<sub>2</sub>, respectively. Doping achieved by

replacing the Ti<sup>4+</sup> cation with Sm<sup>3+</sup> and Gd<sup>3+</sup> cation. The main absorption wavelength of TiO<sub>2</sub> corresponds to the intrinsic absorption of anatase phase TiO<sub>2</sub>, whereas the optical absorption band of Sm<sup>3+</sup>-doped TiO<sub>2</sub> and Gd<sup>3+</sup>-doped TiO<sub>2</sub> exhibit bathochromic shift. Thus, upon optical excitation, the energy required for the electrons to transit from the valence band to the conduction band decreases leading to a bathochromic shift commonly known as red shift.

The bandgap energy ( $E_g$ ) estimated using Taucplot function shown in Fig. 5B–D. The observed 3.05 eV, 2.95 eV, and 2.89 eV are the optical bandgap values of pure TiO<sub>2</sub>, Sm<sup>3+</sup>-doped TiO<sub>2</sub>, and Gd<sup>3+</sup>-doped TiO<sub>2</sub>, respectively. The lowest optical bandgap energy is found for Gd<sup>3+</sup>-doped TiO<sub>2</sub> and is found to be the most efficient among other photoanodes because of high potential electron injection. The above results show that Gd-doped TiO<sub>2</sub> is more active in UV-A, UV-B, and visible spectrum compared to Sm-doped or undoped TiO<sub>2</sub> and absorbs maximum portion of solar light to enhance the photovoltaic conversion.

After doping of Sm<sup>3+</sup> and Gd<sup>3+</sup> cation, a major effect on the band structure and trap states of TiO<sub>2</sub> is

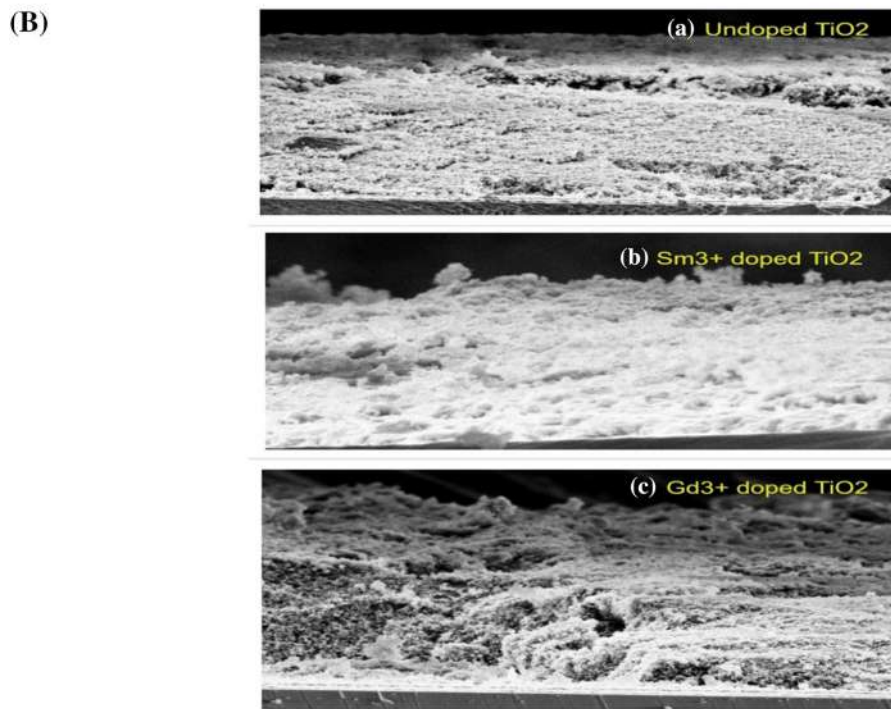
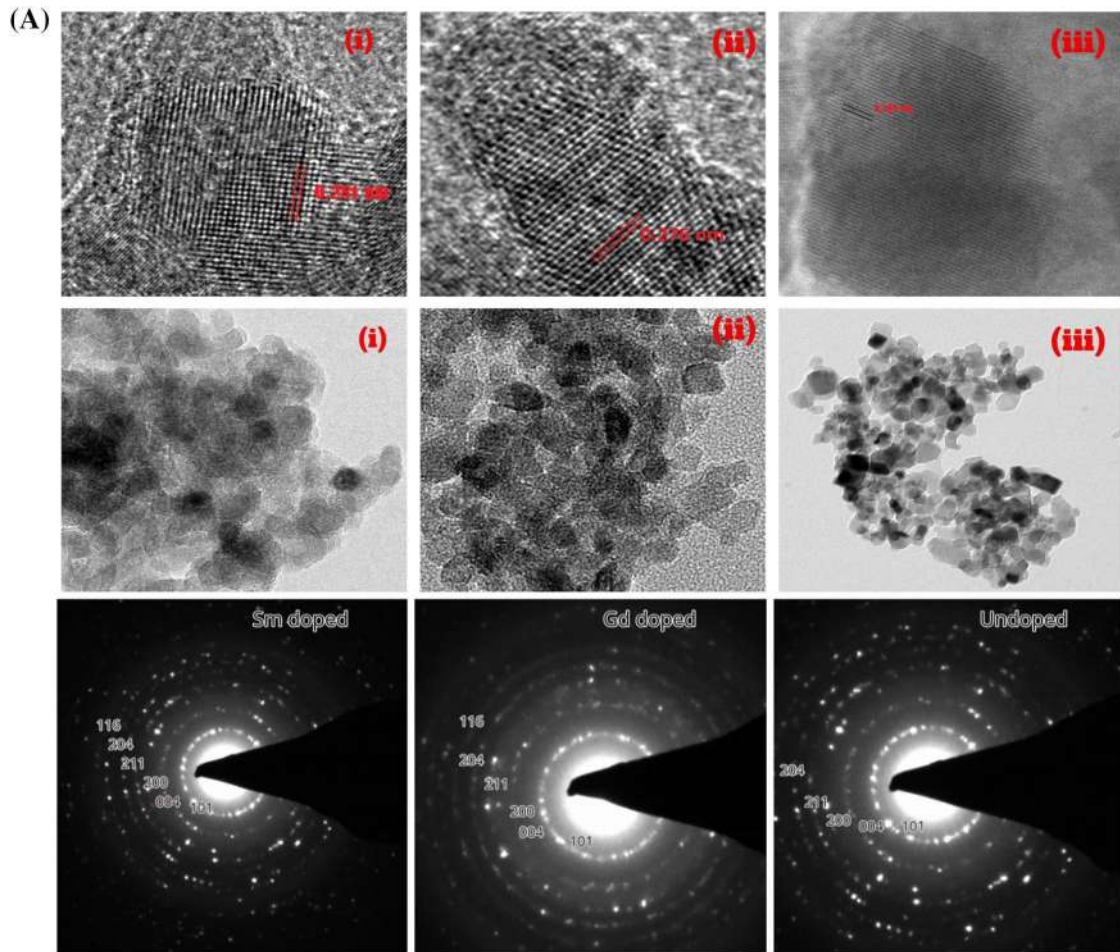


**Fig. 4** **A** High-resolution TEM images and SAED pattern of (i) Sm-doped, (ii) Gd-doped, and (iii) undoped TiO<sub>2</sub>. **B** Cross sectional images of (a) undoped TiO<sub>2</sub>, (b) Sm-doped TiO<sub>2</sub>, and (c) Gd-doped TiO<sub>2</sub>

seen and also the charge injection between photoanode and dye molecules should be fast to avoid recombination which benefits the possible enhancement in the photovoltaic activity for the fabrication of DSSCs.

### 5.5 X-ray photoelectron spectroscopy (XPS)

High-resolution XPS study was used to find the chemical states of Ti, Sm<sup>3+</sup>, and Gd<sup>3+</sup> of the synthesized samples given in Fig. 6A–C. After the baseline correction, the peaks were deconvoluted using Gaussian–Lorentzian line shapes. The survey

spectrum of Sm<sup>3+</sup>- and Gd<sup>3+</sup>-doped TiO<sub>2</sub> nanoparticles is shown in Fig. 6A, which assures the presence of Ti, C, O, Sm<sup>3+</sup>, and Gd<sup>3+</sup>; moreover, the impurities are not much evident here. The XPS spectra were charge corrected having C 1s peak at 284.6 eV as reference.

In Fig. 6B, the binding energy peak at 458.56 eV and 464.22 eV corresponds to the oxidation state of Ti 2p<sub>3/2</sub> and Ti 2p<sub>1/2</sub>, respectively. These findings are in conformity with the reference data results [4] and confirm that the tetravalent Ti atoms are consistent in TiO<sub>2</sub> lattice. O 1s configuration peaks, observed in Fig. 6C, are the results of oxygen presence on the surface in crystal lattice. The peaks are observed at 529.66 eV for Gd-doped TiO<sub>2</sub> and 529.71 eV in Sm<sup>3+</sup>-doped TiO<sub>2</sub> that confirm the presence of Sm 3d<sub>5/2</sub> and Gd 3d<sub>5/2</sub> states in the TiO<sub>2</sub> crystal lattice, which in turn narrowed the charge-transfer band. Hence,

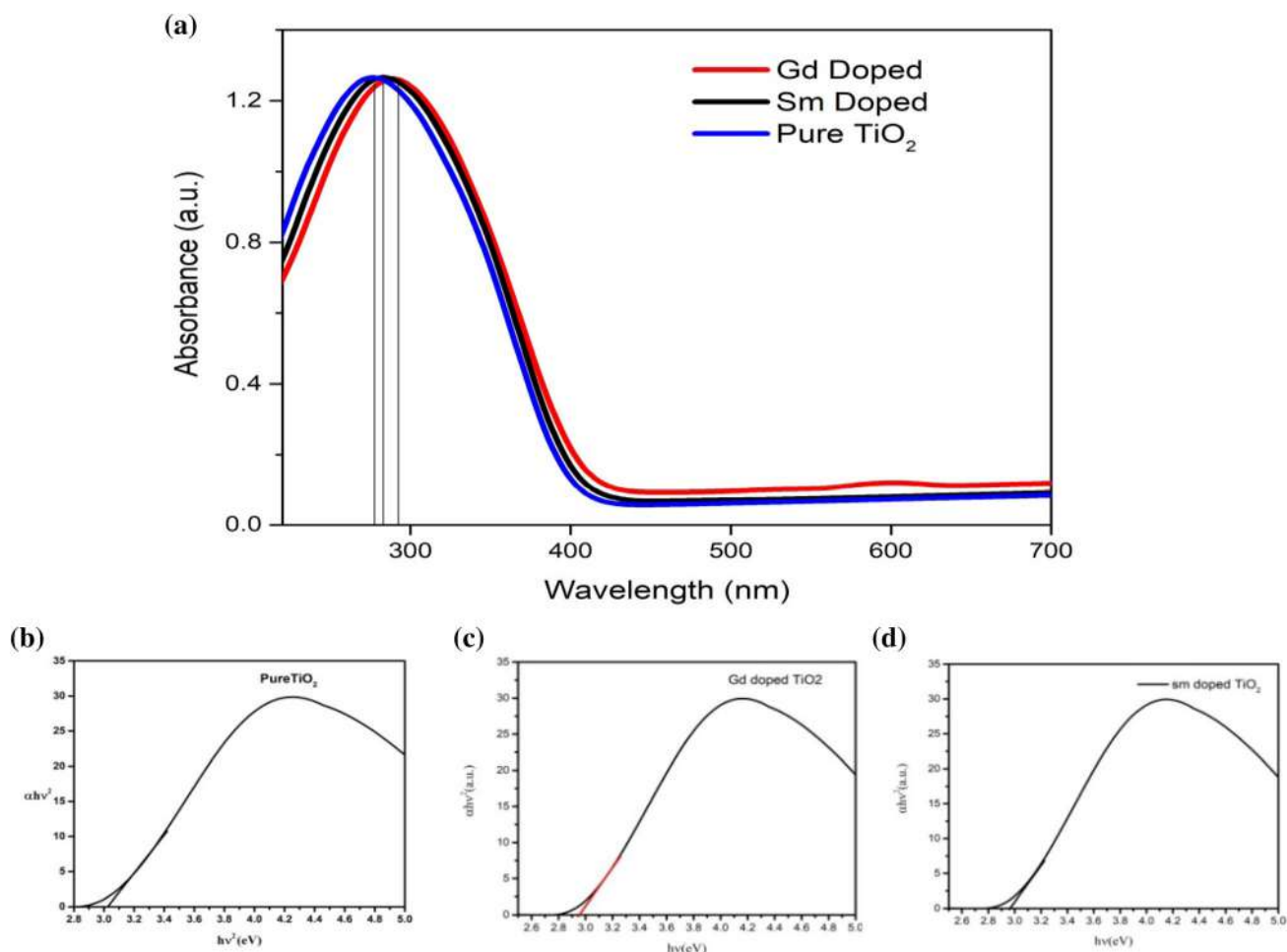


**Fig. 5** **A** Absorption spectra of Gd-doped, Sm-doped, and undoped TiO<sub>2</sub> bandgap of **B** undoped TiO<sub>2</sub>, **C** Gd-doped and **D** Sm-doped

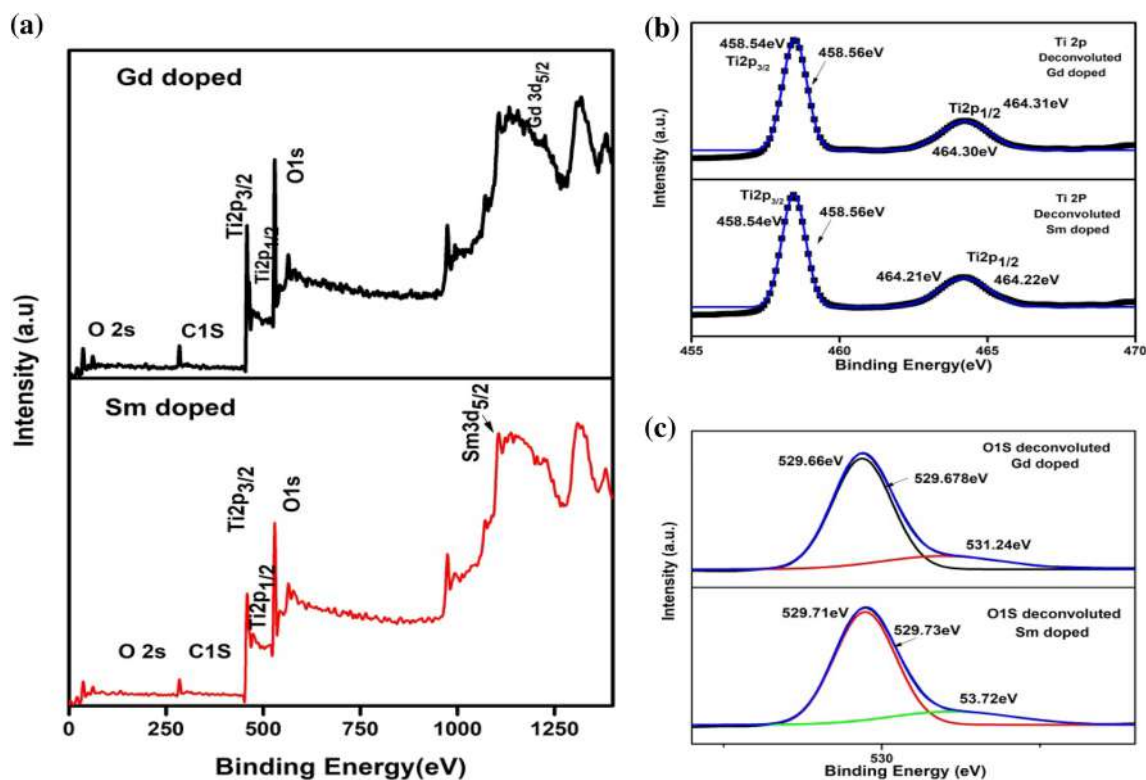


**Fig. 6** XPS spectra of Sm- and Gd-doped TiO<sub>2</sub>

XPS analysis indicates the successful doping of Sm<sup>3+</sup> and Gd<sup>3+</sup> ions into the TiO<sub>2</sub> crystal lattice.

## 5.6 Electrochemical impedance analysis (EIS)

EIS is used to further investigate the electrical conductivity and charge-transfer ability of the prepared photoanodes by Impedance spectra of the two identical symmetric dummy cells is shown in Fig. 7. The obtained experimental data were fitted with a Nyquist equivalent circuit including a series resistance ( $R_s$ ), charge-transfer resistance ( $R_{ct}$ ), and Nernst diffusion ( $Z_N$ ), respectively [18], where  $R_s$  is the resistance of FTO,  $R_{ct}$  is the resistance of interface between electrolyte, dye, and photoanode, and  $Z_N$  is corresponding to the resistance in the redox couple. In general, low  $R_{ct}$  is the salient factor to achieve fast electron transport mobility within photoanode/electrolyte interface. From EIS analysis,  $R_{ct}$  values are decreasing after doping with Sm<sup>3+</sup> and Gd<sup>3+</sup> ions, indicating faster electron generation within the photoanodes; and Gd<sup>3+</sup>-doped TiO<sub>2</sub> has low  $R_{ct}$  values compared with other photoanodes due to smaller crystallite size, which shows that electrolyte can

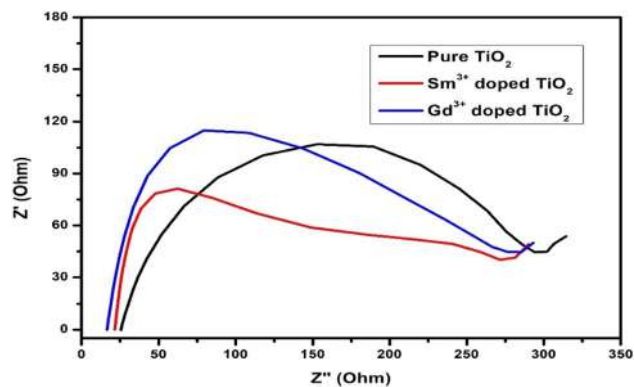


**Fig. 7** Electrochemical impedance spectra of pure TiO<sub>2</sub>, Sm- and Gd-doped TiO<sub>2</sub>

**Table 2** The impedance results of the photoanodes

Photoanodes	$R_s$ ( $\Omega$ )	$R_{ct}$ ( $\Omega$ )	$Z_N$ ( $\Omega$ )
TiO <sub>2</sub>	17.9	7.1	3.8
Sm <sup>3+</sup> doped TiO <sub>2</sub>	16.5	6.7	3.3
Gd <sup>3+</sup> doped TiO <sub>2</sub>	15.8	6.3	2.9

easily access into the photoanode to produce large electron ions. The measured EIS data are shown in Table 2.

**Table 3** Efficiency of DSSCs (pure TiO<sub>2</sub>, Sm-doped and Gd-doped TiO<sub>2</sub>)

Sample	$J_{sc}$ (mA/cm <sup>2</sup> )	$V_{oc}$ (V)	$J_{max}$	$V_{max}$	Fill factor (FF)	$\eta$ (%)
TiO <sub>2</sub>	17.24	0.56	0.3650	13.71	0.5183	5.003
Sm <sup>3+</sup> doped TiO <sub>2</sub>	17.25	0.58	0.3830	13.75	0.5263	5.265
Gd <sup>3+</sup> doped TiO <sub>2</sub>	17.25	0.605	0.3971	13.96	0.5311	<b>5.542</b>

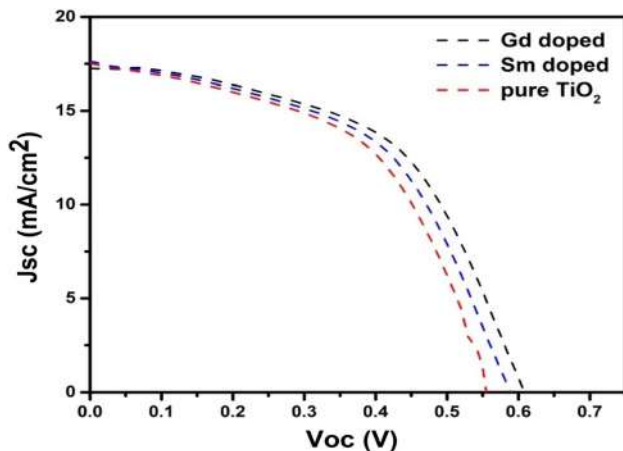


**Fig. 8**  $I$ - $V$  curve

### 5.7 $I$ - $V$ characteristics

The current density–voltage performances of pure, Sm<sup>3+</sup>- and Gd<sup>3+</sup>-doped TiO<sub>2</sub> DSSCs are provided in Table 3 and the curves are portrayed in Fig. 7. The conversion efficiency was high for Gd<sup>3+</sup>-doped TiO<sub>2</sub> compared to Sm<sup>3+</sup>-doped and pure TiO<sub>2</sub>. One of the salient factors for the enhancement of the efficiency is the increase in UV and visible region light absorption of the materials. Replacing Ti<sup>4+</sup> cation with Sm<sup>3+</sup>/Gd<sup>3+</sup> cations drives an effect on the trap states and band structure of TiO<sub>2</sub>. As the bandgap decreases, the conduction of Gd<sup>3+</sup>-doped TiO<sub>2</sub> increases (Fig. 8).

It results in the increase of absorption energy from a major portion of visible light as a result of reduction of its bandgap energy. It was found that employed dopant also affects dye adsorption owing to different binding strengths between the dye and the dopant. Since Gd<sup>3+</sup>-doped TiO<sub>2</sub> allows N719 to bind itself of the surface easily than Sm<sup>3+</sup>-doped and bare TiO<sub>2</sub> photoanodes, the efficiency table of fabricated DSSCs (Table 3) shows an increment in efficiency as Gd<sup>3+</sup>-doped TiO<sub>2</sub> > Sm<sup>3+</sup>-doped TiO<sub>2</sub> > undoped TiO<sub>2</sub>.

## 6 Conclusion

Sm<sup>3+</sup>- and Gd<sup>3+</sup>-doped TiO<sub>2</sub> were synthesized with hydrothermal technique. Morphological and optical properties of the materials were characterized. After the elaborate analysis, the prepared anode materials were converted into electrodes and respective DSSCs were fabricated. Among the samples, Gd<sup>3+</sup>-doped TiO<sub>2</sub> exhibited reduced size, 7.74 nm, minimized bandgap, 2.89 eV, greater absorption of solar light especially in UV-A, UV-B, and near visible region, and better efficiency, 5.542%. These results show that Gd<sup>3+</sup>-doped TiO<sub>2</sub> is an appropriate anode material for the assembling of DSSC.

## References

- Shibu Joseph, S. Jacob Melvin Bobby, D. Muthu Gnana Theresa Nathan, P. Sagayaraj, Investigation on the role of cost effective cathode materials for fabrication of efficient DSSCs with TiNT/TiO<sub>2</sub> nanocomposite photoanodes, *Sol. Energy Mater. Sol. Cells* **165** (2017)
- B. O'Regan, M. Graetzel, Low-cost, high efficiency solar cell based on dye-sensitized colloidal TiO<sub>2</sub> films. *Nature* **353**, 737 (1991)
- Y. Chiba, A. Islam, Y. Watanabe, R. Komiya, N. Koide, L. Han, Dye-sensitized solar cells with conversion efficiency of 11.1%. *Jpn. J. Appl. Phys.* **2** **45**, 638–640 (2006)
- P.A. Cormier, J. Dervaux, N. Szuwarski, Y. Pellegrin, F. Odobel, E. Gautron, M. Boujtita, R. Snyders, Single crystalline-like and nanostructured TiO<sub>2</sub> photoanodes for dye sensitized solar cells synthesized by reactive magnetron sputtering at glancing angle. *J. Phys. Chem. C* **122**, 20661–20668 (2018)
- Q. Huang, G. Zhou, L. Fang, L. Hu, Z.S. Wang, TiO<sub>2</sub> nano rod arrays grown from a mixed acid medium for efficient dye-sensitized solar cells. *Energy Environ. Sci.* **4**, 2145–2151 (2011)



6. M. Wang, Y. Wang, J. Li, ZnO nanowire arrays coating on TiO<sub>2</sub> nanoparticles as a composite photoanode for a high efficiency DSSC. *Chem. Commun.* **47**, 11246–11248 (2011)
7. A. Somdee, Improved photovoltaic efficiency of dye sensitized solar cells by decorating TiO<sub>2</sub> photoanode with barium titanate oxide. *J. Alloys Compd.* **777**, 1251–1257 (2019)
8. M. Bron, C. Roth, Chapter 10: new and future developments in catalysis, in *Fuel Cell Catalysis from a Materials Perspective* (Elsevier, Inc., Amsterdam, 2013)
9. J. Reszczyńska, T. Grzyb, J.W. Sobczak, W. Lisowski, M. Gazda, B. Ohtani, A. Zaleska, Lanthanide co-doped TiO<sub>2</sub>: the effect of metal type and amount on surface properties and photocatalytic activity. *Appl. Surf. Sci.* **307**, 333–345 (2014)
10. H. Kato, A. Kudo, Visible-light-response and photocatalytic activities of TiO<sub>2</sub> and SrTiO<sub>3</sub> photocatalysts codoped with antimony and chromium. *J. Phys. Chem. B* **106**, 5029–5034 (2002)
11. K. Kasinathan, J. Kennedy, M. Elayaperumal et al., Photodegradation of organic pollutants RhB dye using UV simulated sunlight on ceria based TiO<sub>2</sub> nanomaterials for antibacterial applications. *Sci. Rep.* **6**(1), 1–12 (2016)
12. J. Reszczyńska, D.A. Esteban, M. Gazda, A. Zaleska, Pr-doped TiO<sub>2</sub>. The effect of metal content on photocatalytic activity. *Physicochem. Probl. Miner. Process.* **50**, 515–524 (2014)
13. D.H. Jara, S.J. Yoon, K.G. Stamplecoskie, P.V. Kamat, Size-dependent photovoltaic performance of CuInS<sub>2</sub> quantum dot-sensitized solar cells. *Chem. Mater.* **26**, 7221–7228 (2014)
14. A.G. Niaki Ghanbari, A.M. Bakhshayesh, M.R. Mohammadi, Double-layer dye-sensitized solar cells based on Zn-doped TiO<sub>2</sub> transparent and light scattering layers: improving electron injection and light scattering effect. *Sol. Energy* **103**, 210–222 (2014)
15. H.G. Yang, C.H. Sun, S.Z. Qiao, J. Zou, G. Liu, S.C. Smith, H.M. Cheng, G.Q. Lu, Anatase TiO<sub>2</sub> single crystals with a large percentage of reactive facets. *Nature* **453**(7195), 638–641 (2008)
16. Z.L. Liu, Z.L. Cui, Z.K. Zhang, Structural phase transformation and UV–Vis characterization of Cr doped nanosized titanium dioxide. *Gongneng Cailiao/J. Funct. Mater.* **36**, 1404–1408 (2005)
17. D.O. Klenov, G.N. Kryukova, L.M. Plyasova, Localization of copper atoms in the structure of the ZnO catalyst for methanol synthesis. *J. Mater. Chem.* **8**(7), 1665–1669 (1998)
18. K. Subalakshmi, S. Jayaraman, Effect of fluorine-doped TiO<sub>2</sub> photoanode on electron transport, recombination dynamics and improved DSSC efficiency. *Sol. Energy* **171**, 914–928 (2018)

**Publisher's Note** Springer Nature remains neutral with regard to jurisdictional claims in published maps and institutional affiliations.



# Unravelling the necessity of conservation and recycling of rare earth elements from the perspective of global need

S. Bharathi Bernadsha

To cite this article: S. Bharathi Bernadsha (2022): Unravelling the necessity of conservation and recycling of rare earth elements from the perspective of global need, Canadian Metallurgical Quarterly, DOI: [10.1080/00084433.2022.2046901](https://doi.org/10.1080/00084433.2022.2046901)

To link to this article: <https://doi.org/10.1080/00084433.2022.2046901>



Published online: 07 Mar 2022.



Submit your article to this journal [↗](#)



View related articles [↗](#)



View Crossmark data [↗](#)

REVIEW



# Unravelling the necessity of conservation and recycling of rare earth elements from the perspective of global need

S. Bharathi Bernadsha

Department of Physics, Loyola College, (Affiliated to the University of Madras), Chennai, India

## ABSTRACT

Rare earth elements (REEs) play an indispensable role in the manufacturing of hybrid cars, wind turbines, compact fluorescent lights, flat screen televisions, mobile phones, disc drives, and defence technologies due to their varied chemical, magnetic, and luminescent properties. The unequal spreading of REE resources creates non-equilibrium in the utilisation and exploitation of them among the nations. They are implanted in most of the electronic and magnetic products and demand for them continues to increase in their production. Such dependency on REE poses serious risks to the dependant country's economy and military complex. It creates a great deal of harmful waste. Around 1% of the REE are recycled from end-products. Scientific interest of recycling REEs is constantly rising due to the increased use of REEs. This paper presents a comprehensive review of the distribution of REEs and various recycle methods.

## RÉSUMÉ

Les éléments de terres rares (ETR) jouent un rôle indispensable dans la fabrication de voitures hybrides, d'éoliennes, de lampes fluorocompactes, de téléviseurs à écran plat, de téléphones cellulaires, de lecteurs de disque et de technologies de défense en raison de leurs propriétés chimiques, magnétiques et luminescentes variées. Cependant, leurs gisements et leurs disponibilités ne sont pas uniformes sur la terre. Cette répartition inégale de ces ressources en ETR crée un déséquilibre dans l'utilisation et l'exploitation de ces éléments parmi les nations. Comme ces minéraux sont implantés dans la plupart des produits électroniques et magnétiques, leur demande continue d'augmenter dramatiquement dans leur production. Une telle dépendance vis-à-vis les ETR pose des risques sérieux pour l'économie et le complexe militaire du pays dépendant. Une grande quantité de minerai est requise pour les méthodes de production actuelles. Cela crée beaucoup de déchets nocifs pour une petite quantité de produits désirés. Les propriétés chimiques des éléments de terres rares les rendent difficiles à séparer du minerai et compliquent également le processus de purification. Environ 1% des ETR sont recyclés à partir des produits finis, le reste étant expulsé en déchet et retiré du cycle des matériaux. L'intérêt scientifique pour le recyclage des ETR est en constante augmentation en raison de l'utilisation accrue des ETR grâce à leur utilité. Cet article présente un compte-rendu détaillé de la distribution des ETR entre les pays et diverses méthodes de recyclage.

## ARTICLE HISTORY

Received 19 April 2020  
Accepted 21 February 2022

## KEYWORDS

Rare earth element; climate change; Reserve of REEs; e-waste; Ore and Mining; conservation; recycling; environment friendly

## 1. Introduction

The rare earths supply and demand was indefinite in 2021 due to pandemic, but most analysts remained optimistic about the sector's growth in 2022. Although they usually get less attention than gold, copper, and lithium, rare earth elements (REEs) are important metals for the global economy, especially in the twenty-first century [1]. Rare earth elements (REEs) are found to be indubitably important elements in the day today needs of human beings. Regarding the conservation and recycling, the papers have not dealt sufficiently in the recent past. This review aims at understanding the supply, conservation for the sustainability, and recycling of REE. The literature in various databases and websites, from

openly available materials, has been compiled and analysed critically.

The present world is more worried about the climate change and reliability of the fossil fuel supply [2]. So every researcher is vying to invent and discover new forms of supplements to alternate the depleting fossil fuels. Photovoltaic, fuel cells, wind turbines, and hydrothermal systems are some of the alternative methods to generate energy for various purposes of human beings [3]. It is likely that solar, wind energy, and electric vehicles will be considered as part of the solution for a more sustainable future. Present technologies for electric vehicles and wind turbines rely heavily on REEs like dysprosium (Dy) and neodymium (Nd) for rare

earth magnets [4]. REEs exhibit numerous peculiar physical and chemical properties, which ultimately arise from their distinctive electronic configurations [5]. Due to the above mentioned properties of REEs, they have been applied in various modern electronic industries, such as high-temperature superconductors, energy-saving lamps, flat screen monitors, and televisions, rechargeable batteries, and very strong permanent magnets [6]. All REEs are not available in pure metal form, although Promethium, the rarest, has unstable isotopes, only occurs in trace quantities in natural materials [7]. REEs are the elements that have become extremely important to our world of technology owing to their unique magnetic, phosphorescent, and catalytic properties. These elements are critical to technologies ranging from cell phones and televisions to LED light bulbs and wind turbines [8].

## 2. Rare earth elements and their applications

Rare earth elements (REEs) consist of Yttrium and the 15 Lanthanide elements, namely, Lanthanum, Cerium, Praseodymium, Neodymium, Promethium, Samarium, Europium, Gadolinium, Terbium, Dysprosium, Holmium, Erbium, Thulium, Ytterbium, and Lutetium [9]. The IUPAC includes Scandium also as one of the REEs. The name 'rare earth' was given by early chemists in reference to the difficulty in separation of the elements from each other [10]. For practical reasons, the REEs are divided into two major divisions: the Light Rare Earths (Lanthanum (La), Cerium (Ce), Praseodymium (Pr), Neodymium (Nd), and Samarium (Sm)) and the Heavy Rare Earths (Gadolinium (Gd), Europium (Eu), Terbium (Tb), Dysprosium (Dy), Thulium (Tm), Ytterbium (Yb), Lutetium (Lu), Yttrium (Y), Holmium (Ho), and Erbium (Er)) [11] (Figure 1 and Table 1).

REEs are used in catalysts, magnets, polishing powders, batteries, metallurgy, glass, ceramics, phosphors, and a host of other applications requiring very small amounts of material, including medical applications [12]. To state the fact, the REEs are not really rare in the earth comparing to the commonly used elements like gold or platinum [4]. They are abundant in the natural deposits, and more than 250 minerals contain these REEs in them are discovered [13]. Due to the leap in the technology especially in high-tech usages like mobile phones, defence technologies, flat screen televisions, sophisticated cars, consumer electronics, computers and networks, communications, clean energy, advanced transportation, health care and environmental mitigation, the need of REEs in the global market is increasing [14–18].

## 3. The availability of rare earth elements in the globe

The demand for mineral commodities is different from that of consumer goods. As the demand for the products keep on increasing, the need for REEs also increases. Hence, the countries hunt for the availability of the reserves of REEs in their own territories. As a result of those searches, some of the countries have identified the reserves, and some other countries are in search of them [19].

In nature, REEs do not exist as individual native metals such as gold, copper, and silver because of their reactivity, instead occur together in numerous ore/accessory minerals as either minor or major constituents. Though REEs are found in a wide range of minerals, including silicates, carbonates, oxides, and phosphates, they do not fit into most mineral structures and can only be found in a few geological environments [20]. The resources have been calculated using data on the percentage of rare earths found in various ore deposits [21]. Eu is the only rare earth element estimated to have less than 1000 years. The sustainability of the REEs has become a major concern as their demands are increasing every day. The increase in the modern industry, environmental issues, and other demands results in the reality that the REEs are depleting resources [22]. Thus, studying and obtaining the essential data about the sources, marketing, applications, recycling, and possibilities of responsible uses are to be given primacy. The countries are becoming careful in using their reserves. Several studies are carried out to investigate the resources of different countries.

Figure 2 depicts the reserves available in the countries measured in the year 2020. China is the leading country in having the major part of the reserves in the world. It has 44MMT (million metric ton) as their reserve followed by Vietnam (22MMT), Brazil (21MMT), Russia (12MMT), India (6.9MMT), Australia (4.9MMT), and US and Greenland together own (1.5MMT) [23].

Figure 3 gives the production of REEs from the reserves in major top 10 REE extracting countries (in metric ton) for the year 2018, 2019, and 2020 [23]. From the data, the graph is drawn, and it is found that the production of REEs was never stopped despite of facing the Corona epidemic and complete lockdown period. It is also clear that major exporters like china and Myanmar have increased their production. Except Australia, most of the countries either have increased the quantity of production or maintained the *status quo*.

In general, there are about 34 countries with rare earth deposits in the world. In Asia, fourteen countries have rare earth deposits. In Europe, six countries have been

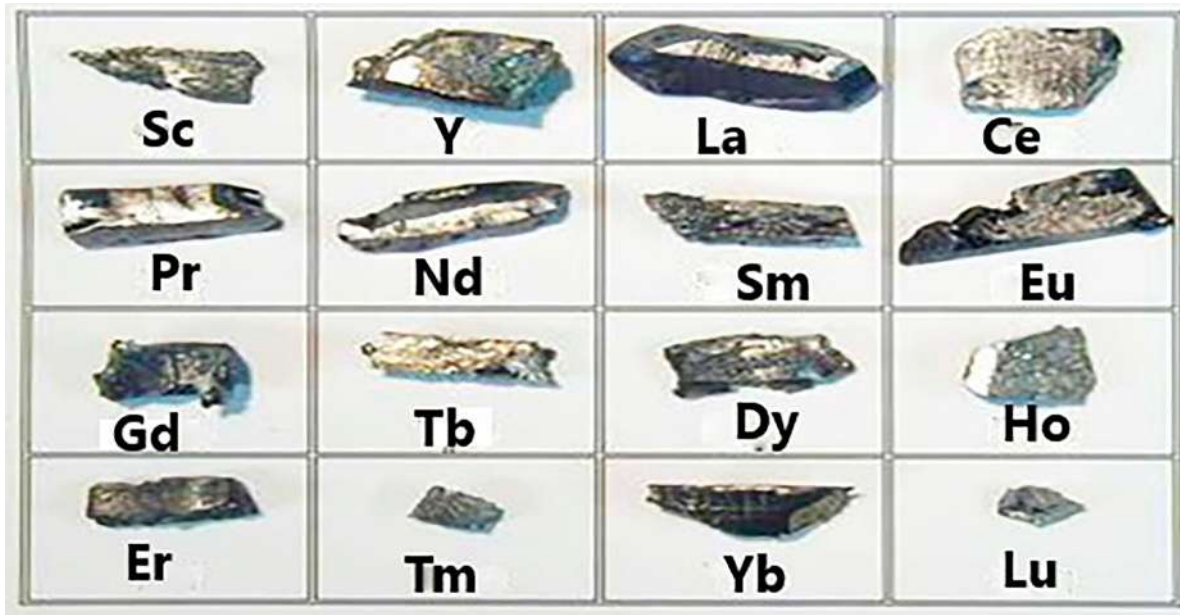


**Figure 1.** Images of rare earth elements (REEs).

found to have rare earths. There are plenty of rare earth reserves in Australia, but no processing plant could be built for environmental problems. The United States has its rare earth deposits. For Canada, there are many small-scale rare earth reserves with good heavy rare earth element contents for economic exploitation and have attracted many investors. One of its mining companies, the Great Western Group, is developing its rare earth production in South Africa. In South America, mainly in Brazil and in Africa, there are 10 countries [24–28] (Figure 4).

## 4. Rare earth element and major countries

### 4.1. China

Between 2010 and 2012, the Chinese government imposed export regulations on their rare earth minerals and semi-processed rare earth products [29,30]. These regulations created a disrupt between demand and supply. In 2012, against China, the US, Japan, and the Europe Union brought an allegation to WTO. After two years of serious arguments, the case was settled but did not favour China. As a consequence, China stopped its production of REEs by 2014. When China stopped its shipments in the year 2014, the entire world underwent the crucial time in manufacturing guided missile and hybrid cars to flat screen televisions and Black Berry phones. However, the countries put a lot of pressure on China, and thus the export licence on REEs was enforced in 2015 [31–35]. The Chinese producers also have issues

with environmental pollution resulting from poorly regulated mining operations [36,37].

### 4.2. United States of America

The United States need an adequate, stable, and reliable supply of REEs. In their national security, economic well-being, and industrial production, the REEs play an inevitable role [38]. The United States is a major dependent country which imports major part of its critical minerals. The Commerce Department says that US imports more than 50% of our annual consumption of 31 of the 35 minerals designated as critical by the Department of the Interior. The United States reliance on imports not only puts China's REE dominance in perspective, but also it points to potential vulnerability to cost in a world market seeing a demand surge for rare earths [39].

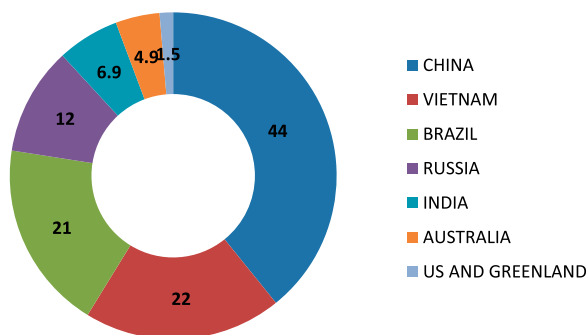
### 4.3 Europe Union

European Union (EU) have no mine supply of the REE, but it does have a number of areas of suitable geology with REE resources [40,41]. It is identified that the Europe Union also depends on China for the supply of REEs. Chinese supply of the raw materials runs the Europe Union's solar and wind energy producing industries. For their various needs, Tellurium, Gallium, Indium, Neodymium, and Dysprosium are imported by European countries [42]. Along with rest of the world, EU's production of materials and energy depends on the Chinese supply of REEs. Hence, the European Commission, to create pacts

**Table 1.** REEs Symbol, Atomic Number, and Applications.

S.No	Element	Symbol	Atomic No.	Applications
01.	Scandium	Sc	21	Aluminium–scandium alloys in aerospace industry [97], defence industry, and high intensity discharge light [98].
02.	Yttrium	Y	39	Alloys, lasers and glass, red phosphors [99], fluorescent lamps, metals [100], ceramics [36, 101].
03.	Lanthanum	La	57	Metal alloys, catalysts hybrid engines, [100] catalysis, phosphors [99], carbon-arc lamps [102, 103].
04.	Cerium	Ce	58	Catalysis particularly auto, petroleum refining, metal alloys [100], phosphors [99], corrosion protection, carbon-arc lamps, cigarette lighter flints [36, 102].
05.	Praseodymium	Pr	59	Magnets [100], optical fibres, carbon-arc lamps [102].
06.	Neodymium	Nd	60	Catalysis in petroleum refining [100], hard drives in laptops, headphones, Nd-Fe-B magnets [102].
07.	Promethium	Pm	61	Nuclear battery [102].
08.	Samarium	Sm	62	Sm-Co magnets, IR absorption in glass [102].
09.	Europium	Eu	63	Phosphors, red colour for TV and computer screens [100], green phosphor [99].
10.	Gadolinium	Gd	64	MRI, nuclear power, magnets, nuclear magnetic resonance imaging, phosphors [102].
11.	Terbium	Tb	65	phosphors [99], fluorescent lamps [102], magnets [100].
12.	Dysprosium	Dy	66	Magnets, hybrid engines, magnets [100, 102].
13.	Holmium	Ho	67	Neutron absorber, glass colouring agent, lasers [100].
14.	Erbium	Er	68	Red, green phosphors, amplifiers for optical fibres transmission, pink in glass melts, sunglasses [102].
15.	Thulium	Tm	69	Medical X-ray units – X-ray sensitive phosphors [102].
16.	Ytterbium	Yb	70	Catalysts, lasers, steel alloys – grain refiner [100, 102], stress sensors [102].
17.	Lutetium	Lu	71	Catalysts in petroleum refining, Ce-doped Lu-glass used in detectors for positron emission tomography [100].

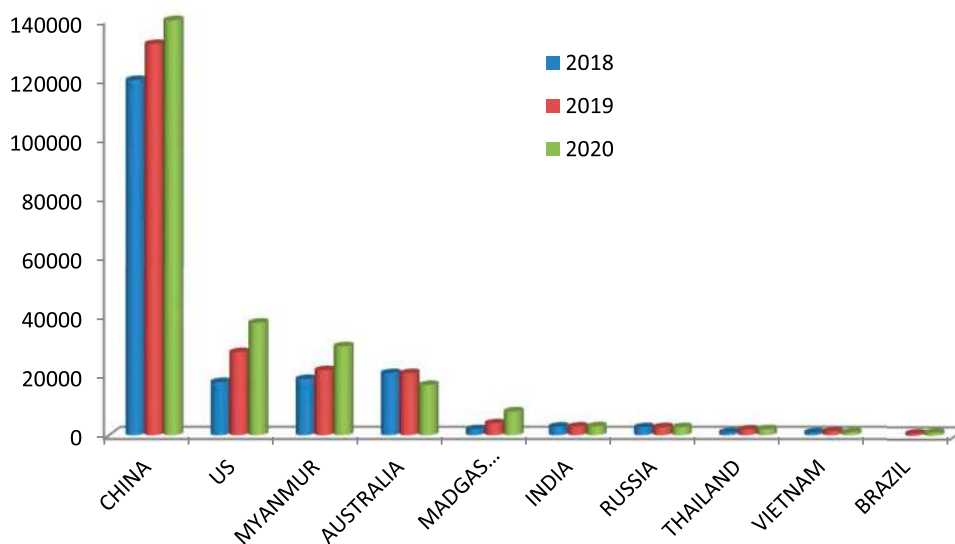
## RESERVE (MILLION METRIC TON)

**Figure 2.** Total reserves in the world (2020) (in million metric tons).

with other REE-producing countries especially African Countries, has instituted the association called ‘European Raw Materials Initiatives’ [43,44].

### 4.4 Japan

A notable characteristic of Japan’s oceans is depth [45]. Japan has the share of 23% of the global reserve of Neodymium material. Japan has been the most proactive country. Though Japan has the reserves, mining the reserves is not economically feasible. So, scientist of Japan explored the sea mud and found that as a good source of REEs [46]. At present, rare earths fall beyond the scope of Japanese law regulating mining. When the mining laws were originally written, policymakers did not foresee any domestic rare earth development. But

**Figure 3.** Production of REEs (in metric ton) from top 10 countries for years 2019 and 2020.

sediments containing high concentrations of rare earths have been discovered recently in coastal waters. By allowing JOGMEC (Japan Oil, Gas, and Metals National Corp) to finance refining at home, Japan seeks to mitigate supply-chain risks [47–49]. A major impact on the rare earth market occurred with the announcement of rare earth deposits at Jongju in North Korea which are being developed by Pacific Century Rare Earth Mineral and the North Korea government [50].

#### 4.5 India

India depends on imported minerals in spite of owning 6.9 million tonnes of rare earth metals. There is a need to develop a long-term strategic vision for REEs. The largest such global opportunity exists in the Indian Ocean region (IOR). Geologically, the entire region around the IOR is rich in REE formed by millions of years of natural concentrating process. Producing REE from these mineral sands is cheap [51].

#### 4.6 Canada

Until the discovery of the Jongju deposit(s), the Canadian deposit at Nechalacho in the North-West Territories was one of the most exciting rare earth developments [50]. Nechalacho is unique for a few reasons; Canada's only rare earth elements mining project was aiming to produce end-products that will ultimately be used in technology manufacturing. According to Natural Resources Canada, the most important use for rare earth elements is making magnets that can be used in cell phones, computers, wind turbines, and electric vehicles [52]. Nechalacho affords Canada the necessary capabilities to position itself along the length of the rare earth elements value chain, while attracting investment in other strategic downstream industries such as aerospace and defence, electric motor manufacture, advanced manufacturing and materials, renewable energy, and other clean technology [53].

The Joint Action Plan on Critical Minerals Collaboration, which was announced by the Canadian and US federal governments in January 2020, the Nechalacho mine looks set to play a key role in enabling Canada to assume an internationally strategic role as a supplier of critical minerals [54–58].

### 5. Need for the conservation of REEs

REE industries can produce serious health and environmental issues such as REE bioaccumulation [59] radiation exposure [60], species invasion [61], and biodiversity loss [62]. Many of these environmental issues are also present in other types of mining activities,

but radioactive pollution and REE toxicity are specific environmental risks associated with REE production that are attracting more attention [63]. The recent tightening of export quotas for REE by China has resulted in price spikes and supply issues for consumers around the world. Because of the widespread use of REE in a clean energy economy, in particular magnets for wind turbines, automobile magnets, rechargeable batteries, and phosphors for lighting, the US Department of Energy (DOE) has listed eight REEs in the critical range in the short term (2015) and five in the medium term (2025), both regarding the risk of supply and their importance to clean energy. Similarly, the European Union (EU) has also included the REE in their list of materials critical to its future development [64,65].

As the research institutions and countries express their ideas, the REE is becoming the bone of contention. The statements made by the leaders of the countries on the export and import of the REEs also give a feel that the nations are making use of the REE reserves as reason for subjugating other countries. So, the REE has to be conserved well by the countries that conservation of REE must result in the sharing of the resources.

### 6. Recycling rare earth elements

The wastes that serve as potential sources of REEs can be classified into three major categories: industrial wastes, mining wastes, and electronic wastes. The common industrial wastes that have been used for REE extraction include mineral processing wastes, namely phosphogypsum and red mud as well as coal processing waste (fly ash). Main mining waste sources for REEs include mine tailings and acid mine drainage sources. For electronic wastes, magnets, NiMH batteries, and phosphors are major REE sources [66]. Their combined crustal abundance is around 200 ppm. Rare earth elements are also found in high concentrations, i.e. higher than 10% rare earth oxide (REO), in over 70 minerals, with the most commercially significant being monazite, bastnaesite, and xenotime together with ion adsorption clays and apatite [67].

One option being explored is recycling rare earth metals from used products. You might think it would be easier to recover rare earths from products than extract them from the ground, but it is not as easy as it sounds. Given the importance of these products to modern living, governments around the world are funding research to make recycling a more feasible option. Some companies are already finding it worthwhile. The elements are present in small amounts in things like cell phones. As parts get smaller, so do the amounts of material used. In a touch screen, for example, the

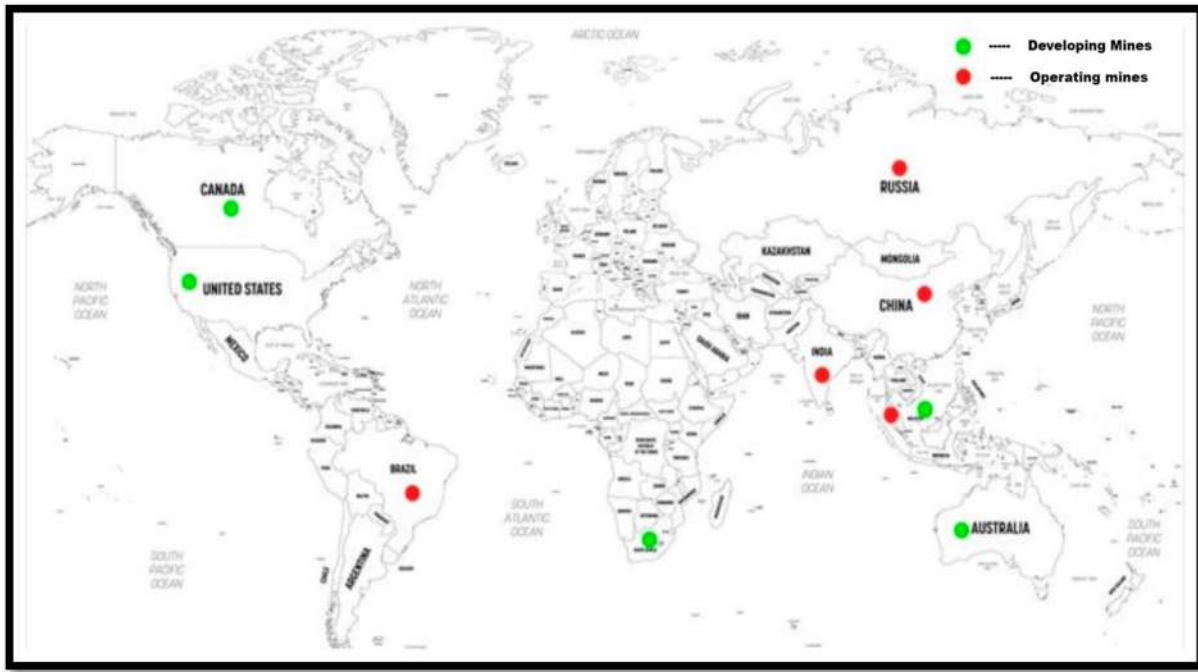


**Figure 4.** The presence of REE mines operating and developing over the globe [46].

elements are distributed throughout the material at the molecular scale. Since the electronic wastes are rich in REEs, their sustainable management includes REE extraction. The alumina production process generates waste residue known as ‘red mud’ which contains 0.041%, 0.014%, 0.011%, and 0.012% of Ce, La, Nd, and Sc, respectively [68] (Figure 5).

### 6.1 Industrial waste recycling

Phosphogypsum is a waste product from the fertiliser industry. It generally contains 0.1–2% of REEs. A

mixed culture of sulphur-oxidising bacteria has been reported to extract 55–70% of REEs from phosphogypsum after 30 days of incubation at pH 1.5–1.8 [69,70]. The slurry left after the extraction of aluminium from bauxite ore using the *Bayer process* is known as red mud. For each ton of alumina produced, 1–2 tons of red mud is generated [70]. Combustion of coal in thermal power plants leads to the generation of residue known as fly ash. The largest producer is China, followed by India, Europe, Africa, and the Middle East. It has been estimated that the highest e-waste is produced by China, followed by the United States, Japan,

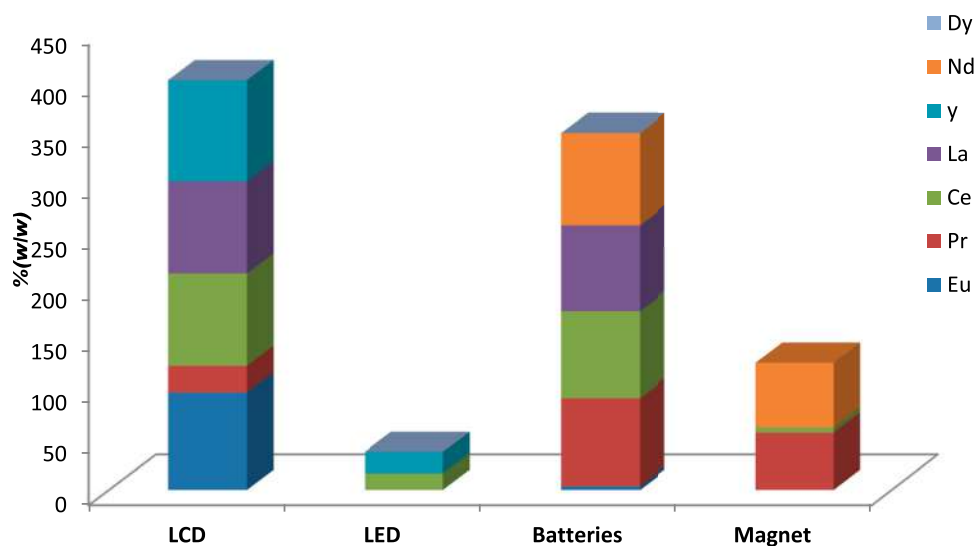


**Figure 5.** The recoverable REEs from LCDs, LEDs, batteries, and magnets [92–96].



India, and Germany. With COVID-19 keeping people indoors and on devices, the usage of electronic gadgets is only getting higher [71].

## 6.2 Mining wastes recycling

Rejects from mineral processing and water treatment plants are deposited in the mine tailings at mine sites. From an abandoned mine and its ability to accumulate REEs including Dy, Y, Nd, Eu, Tb, and Yb indicate another avenue for REE bio-recovery from mine tailings [72]. Acid mine drainages (AMD) are produced in large quantities. The AMD produced in Xingren coalfield mine, located in the southwestern Guizhou province of China, is reported to contain La, Ce, Pr, Nd, Sm, Eu, Gd, Tb, Dy, Ho, Er, Tm, Yb, and Lu, with total REE concentrations varying between 0.1 and 0.9 ppm [73]. Recycling them will be a good source of conserving and recycling the REE.

## 6.3 Electronic waste

One of the significant challenges in the recycling of electronic waste is the very low quantity of REEs in each device. The recovery of Europium and Yttrium from colour TV screens using sulphuric acid as the leaching agent is one of the ways of recycling. NiMH batteries contain approximately 10% REEs to improve hydrogen storage capacity of the battery. The content of La, Ce, and Nd in NiMH batteries has been reported to be 237, 67, and 36 ppm, respectively [74]. Different hydrometallurgical and pyrometallurgical processes have been adopted for the extraction of REEs from NiMH batteries [75]. The doping of Lithium Ion Battery cathodes with REEs such as La, Ce, Pr, Gd, and Dy is reported to enhance the structural stability and electrochemical performances of the batteries [76]. Electronic display and lighting products such as CRTs, LEDs, LCDs, and fluorescent lamps contain phosphors which serve as the major source of REEs in these items. The concentrations of La, Ce, Eu, Gd, Tb, and Y in phosphors derived from fluorescent lamps have been reported to be 3.8, 4.9, 4.4, 2.5, 2.7 and 112.1 ppm, respectively [77].

In the past 10 years, more research was carried out to recover REEs from a different end-of-life electronic wastes using conventional approaches such as precipitation, filtration, pyrometallurgy, hydrometallurgy, liquid-liquid solvent extraction, among others [78]. Dismantling/manual disassembly is the process in which hazardous material and other streams are removed from the components of electronic wastes such as screens, batteries, capacitors, PCB, computers CPU and RAM for the selective recovery of the REEs,

and other high-value products [79]. The processes used in REEs recovery and separation are bioleaching, biosorption, siderophores, hydrometallurgy, pyrometallurgy, and carbon-based material. Bioleaching is an effective technology of metal recovery from primary and secondary sources using microorganisms such as extremophiles, moderately thermophilic bacteria, and mesophiles. It is widely used in commercial recovery of metals especially molybdenum (Mo), copper (Cu), zinc (Zn), nickel (Ni), arsenic (As), cobalt (Co), antimony (Sb), gallium (Ga), palladium (Pd), platinum (Pt), and osmium (Os) from their ores [80].

Bioleaching can also be applied for the extraction of metals from electronic waste, mine, flay ashes, contaminated soils, sludge, and spent catalysts. Johnston et al. (2013) [81] investigated the extraction of REEs from electronic waste using bio-recovery, which includes bioreduction, acidolysis, biomineralisation, and cyanogenic bioleaching. The results showed that when compared with the other processes such as hydrometallurgy and pyrometallurgy, bio-recovery is a more cost-effective and environment friendly process.

Biosorption is one of the modern biological methods that get the most attention in the field of recovery of metals from electronic waste, due to unique properties such as high recovery efficiency for metals in low concentration, high regeneration, fast kinetics, and non-generation of secondary residues. It is cost-effective, can be efficiently operated and used in situ, shows high efficiency in the removal of contaminants from aqueous solution, and does not produce any chemical sludge. Moreover, it can be easily integrated with any system as compared with the conventional methods [82–84].

Siderophores are small, high-affinity iron-chelating compounds secreted by microorganisms such as bacteria, fungi, and grasses. The chelator molecules are produced to hunt Fe+3 from the environment to satisfy the microorganism's metabolic needs. They are known as the best ligands for ferric ions [85]. Siderophores have a high affinity towards desferrioxamine, which is abundant naturally. The recovery of REEs using siderophores is cost-effective, rapid, reversible, and an eco-friendly technology compared with conventional methods for the recovery of REEs which are available in small concentration from different end-of-life electronic wastes. It has a unique application for the recovery of REEs in the future and can be applied in a vast environmental field [86].

Pyrometallurgy is one of the known thermal treatments that can be used for the recovery of metals from electronic waste. This process includes smelting in a plasma arc furnace, blast furnace, or copper smelter,

incineration, and high heat roasting in the presence of selective gases to recover mainly nonferrous metals. Moreover, this process is characterised by high energy consumption. However, it has high efficiency for the recovery of selective REEs from electronic wastes. About 70% recovery of REEs are from electronic wastes [87].

Hydrometallurgy is a chemical method that can be used for the extraction of metals from electronic waste. In this process, gadolinium, yttrium, and lanthanum, are extracted from electronic waste using chloride solution [88] some drawbacks due to the generation of sludge, heavy metal pollution, and toxicity. However, Tuncuk et al. (2012) [89] showed that hydrometallurgical processes could achieve high efficacy for the recovery of metals from printed circuit boards. They have also reported the limitation of this method as it can recover only Li and Co metals, not other metals.

In greener physical treatment with supercritical water process, REEs are extracted from electronic waste by using supercritical water and acid leaching (HCl) [90]. Cryo-milling is another physical treatment approach, which is a green and novel technology for the recycling of REEs from electronic waste. In this process, electronic waste is degraded into nanoparticle sizes using a ball milling machine, which is operated at low temperatures. This leads to an increase in the efficiency of the separation of oxides, polymers, and meal constituents [91]. Moreover, this approach is an eco-friendly process due to the generation of small volumes of waste and the need for low temperatures, so that it is feasible to apply on a large scale.

## 7. Conclusion

The recent development of various novel technologies for sustainable and effective recovery of REEs from electronic and other mining wastes draws the attention of the rulers, researchers, and scientists. This paper highlights the presence of REE in different nations around the globe and their impact. Different processes for the recovery of REEs from electronic and mining wastes through bioleaching, biosorption, siderophores, hydrometallurgy, pyrometallurgy, and carbon-based material are mentioned. In addition to this efficient recycling when these technologies are employed well, they can help in achieving sustainable development goals and balance social, economic, and environmental sustainability.

Electronic waste is an emerging problem in developed and developing nations worldwide. The environment, particularly the aquatic environment, can be harmed if the wastes are not treated, stored, or recycled.

Moreover, they have high economic value and high content of the REEs. So, they must be recycled. An efficient recycling of rare earths requires the development of environmentally friendly dismantling, sorting, pre-processing, and pyro-, hydro-, and/or electrometallurgical processing steps to recover the REEs from magnets, batteries, lamp phosphors, and other applications. With respect to a number of other applications or residues containing rare earths, one has to be realistic about the recycling options. To conclude, considering the growing levels of REEs present in the sphere of technology, we need to plan and conserve the REE for the proper utilisation. It is evident that in addition to mitigating some of the supply risk, REE recycling can minimise the environmental challenges.

Innovative, cost-effective technologies, which can reduce the environmental impact of the overall recycling with respect to the primary mining route, should be further fine-tuned. Products could be designed in such a way that dismantling can be easier, and thus the components can be separated from each other easily. Researches can be carried out to replace the critical rare earths by less critical metals. Secondly, the supply risk can be mitigated by investing in sustainable primary mining from old or new rare earth deposits.

## Disclosure statement

No potential conflict of interest was reported by the author(s).

## References

- [1] <https://investingnews.com/daily/resource-investing/critical-metals-investing/rare-earth-investing/top-canadian-rare-earths-stocks>.
- [2] Welsby D, Price J, Pye S, et al. Unextractable fossil fuels in a 1.5°C world. *Nature*. 2021;597:230–234.
- [3] <https://www.twi-global.com/technical-knowledge/faqs/renewable-energy#TypesofRenewableEnergy>.
- [4] Alonso E, Sherman AM, Wallington TJ, et al. Evaluating rare earth element availability: A case with revolutionary demand from clean technologies. *Environ. Sci. Technol*. 2012;46:3406–3414.
- [5] Barrett SD, Dhesi SS. The structure of rare-earth metal surfaces. London: Imperial College Press; 2001.
- [6] Voncken JHL. The rare earth elements: an introduction. In the series: Springer briefs in earth sciences. Dordrecht: Springer Nature; 2016.
- [7] Castor SB, Hendrik JB. Rare earth elements. In: Kogel JE, Trivedi NC, Barker JM, et al, editors. *Industrial minerals and rocks: commodities, markets, and uses*, vol. 7. Society for Mining Mineralogy, United States; 2006. p. 769–792.
- [8] Zepf V. Rare earth elements: what and where they are. In: *rare earth elements*. Berlin, Heidelberg: Springer; 2013; pp. 11–39.


- [9] Pecharsky VK, Gschneidner KA. Rare-earth element. *Encyclopedia Britannica*. 17 Jan. 2019; Accessed 17 January 2022.
- [10] Chakhmouradian AR, Wall F. Rare earth elements: minerals, mines, magnets (and more). *Elements*. 2012;8:333–340.
- [11] Moldoveanu GA, Papangelakis VG. Recovery of rare earth elements adsorbed on clay minerals: I. desorption mechanism. *Hydrometallurgy*. 2012;117:71–78.
- [12] Goodenough KM, Wall F, Merriman D. The rare earth elements: demand, global resources, and challenges for resourcing future generations. *Nat Resour Res*. 2018;27:201–216.
- [13] Jordens A, Cheng YP, Waters KE. A review of the beneficiation of rare earth element bearing minerals. *Miner. Eng*. 2013;41:97–114.
- [14] Swift TK, Moore MG, Rose-Glowacki HR, et al. The economic benefits of the North American Rare Earths industry. *Rare Earth Technology Alliance*. 2014;1.
- [15] Goonan T G. Rare earth elements—End Use and recyclability, in *Scientific investigations report 2011–5094*. U.S. Department of the interior. U.S. Geological Survey. 2011;1.
- [16] Curtis N. (2010). Rare earths, we can touch them every day. Lynas Presentation in JP Morgan Australia Corporate Access Days, New York.
- [17] Jurd B, Nolde J, Curreri D. Lanthanum oxide product stewardship summary. W. R. Grace & Co. - Conn, Columbia, pg 1 3.
- [18] Yung Y, Bruno K. (2012). Low rare earth catalysts for FCC operations.
- [19] Zhou B, Li Z, Zhao Y, et al. Rare earth elements supply vs. clean energy technologies: new problems to be solve. *Gospodarka Surowcami Mineralnymi*. 2016;32(4):29–44.
- [20] Dostal J. Rare earth element deposits of alkaline igneous rocks. *Resources*. 2017;6(34):1–2.
- [21] Cordier DJ, Hedrick JB. Rare earths: U.S. Geological Survey Minerals Yearbook 2008. [http://minerals.usgs.gov/minerals/pubs/commodity/rare\\_earth/myb1-2008-raree.pdf](http://minerals.usgs.gov/minerals/pubs/commodity/rare_earth/myb1-2008-raree.pdf) (accessed on 27 December 2021).
- [22] Tkaczyk AH, Bartl A, Amato A, et al. Sustainability evaluation of essential critical raw materials: cobalt, niobium, tungsten and rare earth elements. *J Phys D: Appl Phys*. 2018;51(20):203001.
- [23] <https://www.usgs.gov/centers/national-minerals-information-center/rare-earths-statistics-and-information>.
- [24] Wenqing S. Research on development strategy of rare earth industry in inner Mongolia. *Journal of the Chinese Rare Earth Society* (in Chin.). 2005;23 (Suppl.):628.
- [25] Jianzhong C, Liping C. Current mining situation and potential development of rare earth in China. *Chinese Rare Earths* (in Chin.). 2010;31(2).
- [26] Cuixia X, Kai Z, Qizhi S. The summary of rare earths development. *Global Geology* (in Chin.). 1998;17(1).
- [27] Zonglin H. (2004). Rare Earth Resources, Exploitation, Application and Sustainable Development of China, *Yearbook of the Chinese Society of Rare Earths* (in Chin.).
- [28] Peishan Z. A study on genetic classification of rare earth mineral deposits of China. *Chinese Journal of Geology* (in China.). 1989;1.
- [29] Cordier DJ, Hedrick JB. Rare earths: U.S. Geological Survey Minerals Yearbook 2008.
- [30] Xinhua. China to introduce special invoice for rare earth sector to curb illegal mining. [http://news.xinhuanet.com/english/2010/china/2011-11/30/c\\_131279962.htm](http://news.xinhuanet.com/english/2010/china/2011-11/30/c_131279962.htm).
- [31] Han A, Ge J, Lei Y. An adjustment in regulation policies and its effects on market supply: Game analysis for China's rare earths. *Resour. Policy*. 2015;46:30–42.
- [32] Wang X, Lei Y, Ge J, et al. Production forecast of China's rare earths based on the generalized Weng model and policy recommendations. *Resour. Policy*. 2015;43:11–18.
- [33] Ge JL, Lei Y, Zhao L. China's rare earths supply forecast in 2025: a dynamic computable general equilibrium analysis. *Minerals*. 2016;6:95.
- [34] He C, Lei Y. Potential impact of U.S. Re-emerging rare earths industry on future global supply and demand. *Trend. Int. Bus. Res*. 2013;6:44–50.
- [35] Wang X, Ge J, Li J, et al. Market impacts of environmental regulations on the production of rare earths: A computable general equilibrium analysis for China. *J. Clean. Prod*. 2017;154:614–620.
- [36] MMTA. Minor Metals Trade Association, <http://www.mmta.co.uk/metals/Ce> (accessed on 17th January 2022).
- [37] [http://news.xinhuanet.com/english/china/2011-12/27/c\\_131329820.htm](http://news.xinhuanet.com/english/china/2011-12/27/c_131329820.htm).
- [38] Rare Earth Elements: The Global Supply Chain. Marc Humphries Specialist in Energy Policy, June 8, 2012.
- [39] Telger E. The U.S. Is trying To secure rare earth elements For national security. that goes beyond simple investment. *Forbes*. 21 February 2021.
- [40] Goodenough KM, et al. Europe's rare earth element resource potential: An overview of REE metallogenetic provinces and their geodynamic setting. *Ore Geol Rev*. 2016;72(Part 1):838–856.
- [41] Davris P, Balomenos E, Taxiarchou M, et al. Current and alternative routes in the production of rare earth elements. *Berg Huetttenmaenn Monatsh*. 2017;162:245–251.
- [42] Rabe W, Kostka G, Smith Stegen K. China's supply of critical raw materials: risks for Europe's solar and wind industries? *Energy Policy*. 2017;101:692–69936.
- [43] Tiess G. Minerals policy in Europe: some recent developments. *Resour. Policy*. 2010;35:190–198.
- [44] Han A, Ge J, Lei Y. An adjustment in regulation policies and its effects on market supply: Game analysis for China's rare earths. *Resour. Policy*. 2015;46:30–42.
- [45] "Japan pioneers extracting rare-earth elements from the deep sea,". <https://www.nature.com/articles/d42473-020-00524-y>. (Accessed on 18 January 2022).
- [46] Sachan D. Rush for rare earths: Countries explore sources of the metals to counter China, Down to Earth, <https://www.downtoearth.org.in/news/rush-for-rare-earths-33873>, 17 September 2015.
- [47] <https://asia.nikkei.com/Politics/Japan-to-limit-rare-earth-mining-to-protect-offshore-deposits>. (accessed on 22 December 2021).

- [48] <https://spectrum.ieee.org/us-and-japan-seeking-to-break-chinas-grip-on-rare-earths>. (accessed on 14 January 2022).
- [49] Seo H, Kim G. Rare earth elements in the East Sea (Japan Sea): distributions, behaviors, and applications. *Geochim Cosmochim Acta*. 2020;286:19–28.
- [50] [http://www.sec.gov/Archives/edgar/data/1362898/000114420413064890/v361732\\_ex99-1.htm](http://www.sec.gov/Archives/edgar/data/1362898/000114420413064890/v361732_ex99-1.htm).
- [51] Tewari M. The rare earth metal race: How India lost it to China, *Deccan Chronicle*, Published Aug 29, 2021, (accessed on 27 December 2021).
- [52] “Canada’s 1st rare earth mining project starts production”. <https://www.cbc.ca/news/canada/north/nechalacho-rare-earth-mine-starts-production-1.6104251>. (accessed on 19 January 2022).
- [53] <https://canada-next-best-place-to-home.ft.com/the-rare-earths-that-are-elemental-to-canadian-success> (accessed on 19th January 2022).
- [54] <https://canada-next-best-place-to-home.ft.com/the-rare-earths-that-are-elemental-to-canadian-success>.
- [55] Kiri S. “Canada Rare Earth Corporation emerging as a force to be reckoned with in the race to supply rare earths for electric vehicle production”, <https://ca.proactiveinvestors.com/companies/news/969214>.
- [56] [https://www.ourcommons.ca/Content/Committee/412/RNNR/WebDoc/WD6669744/412\\_RNNR\\_reldoc\\_PDF/RareEarthElements-Summary-e.pdf](https://www.ourcommons.ca/Content/Committee/412/RNNR/WebDoc/WD6669744/412_RNNR_reldoc_PDF/RareEarthElements-Summary-e.pdf).
- [57] Vaughan J, Tungpalan K, Parbhakar-Fox A, et al. Toward closing a loophole: recovering rare earth elements from uranium metallurgical process tailings. *JOM*. 2021;73:39–53.
- [58] Richardson DG, Birkett TC. Residual carbonatite-associated deposits. In: Eckstrand OR, Sinclair WD, Thorpe RI, editor. *Geology of Canadian mineral deposit types*. Geology of Canada no 8. Ottawa: Geological Survey of Canada; 1996. p. 108–119.
- [59] Li X, Chen Z, Chen Z, et al. A human health risk assessment of rare earth elements in soil and vegetables from a mining area in Fujian province, southeast China. *Chemosphere*. 2013;93(6):1240–1246.
- [60] Ault T, Krahn S, Croff A. Radiological impacts and regulation of rare earth elements in non-nuclear energy production. *Energies*. 2015;8(3):2066–2081.
- [61] Boojar MMA, Tavakkoli Z. Antioxidative responses and metal accumulation in invasive plant species growing on mine tailings in Zanjan. *Iran. Pedosphere*. 2011;21(6):802–812.
- [62] Degtjarenko P, Marmor L, Randle T. Changes in bryophyte and lichen communities on Scots pines along an alkaline dust pollution gradient. *Environ. Sci. Pollut. Res*. 2016;23:17413–17425.
- [63] Gwenzi W, Mangori L, Danha C, et al. Sources, behaviour, and environmental and human health risks of high-technology rare earth elements as emerging contaminants. *Sci. Total Environ*. 2018;636:299–313.
- [64] US Department of Energy: ‘Critical materials strategy summary’. (2011). Washington, US, Department of Energy.
- [65] European Commission: ‘Critical raw materials for the EU’, Report of the ad-hoc Working Group on defining critical raw materials; . (2010). Luxembourg.
- [66] Khanna R, Ellamparathy G, Cayumil R, et al. Concentration of rare earth elements during high temperature pyrolysis of waste printed circuit boards. *Waste Manage*. 2018;78:602–610.
- [67] Roskill Information Services Ltd. *The economics of rare earths and yttrium*, 12 edn. London: Roskill Information Services Limited; 2004.
- [68] Binnemans K, Jones PT, Blanpain B, et al. Towards zero-waste valorisation of rare-earth-containing industrial process residues: a critical review. *J. Cleaner Prod*. 2015;99:17–38.
- [69] Yang, F, Kubota, Y, Baba, N, Kamiya, M, Goto. Selective extraction and recovery of rare earth metals from phosphor powders in waste fluorescent lamps using an ionic liquid system. *J. Hazard. Mater*. 2013;254–255:79–88.
- [70] Binnemans K, Jones PT, Blanpain B, et al. Towards zero-waste valorisation of rare-earth-containing industrial process residues: a critical review. *J. Cleaner Prod*. 2015;99:17–38.
- [71] Mohan V. India third largest e-waste generator in the world, capacity limited to treat only one fourth of its waste, *The times of India*, 4 July 2020.
- [72] Horiike T, Yamashita M, New A. Fungal isolate, *Penidiella* sp. Strain T9, accumulates the rare earth element dysprosium. *Appl. Environ. Microbiol*. 2015;81:3062–3068.
- [73] Li X, Wu P. Geochemical characteristics of dissolved rare earth elements in acid mine drainage from abandoned high-As coal mining area, southwestern China. *Environ. Sci. Pollut. Res*. 2017;24:20540–20555.
- [74] Maroufi S, Nekouei RK, Hossain R, et al. Recovery of rare earth (i.e. La, Ce, Nd, and Pr) oxides from end-of-life Ni-MH battery via thermal isolation. *ACS Sustainable Chem. Eng*. 2018;6:11811–11818.
- [75] Xia Y, Xiao L, Tian J, et al. Recovery of rare earths from acid leach solutions of spent nickel-metal hydride batteries using solvent extraction. *J Rare Earths*. 2015;33:1348–1354.
- [76] Ding Y, Zhang P, Jiang Y, et al. Effect of rare earth elements doping on structure and electrochemical properties of LiNi<sub>1/3</sub>Co<sub>1/3</sub>Mn<sub>1/3</sub>O<sub>2</sub> for lithium-ion battery. *Solid State Ionics*. 2007;178:967–971.
- [77] Innocenzi V, Ippolito NM, Pietrelli L, et al. Application of solvent extraction operation to recover rare earths from fluorescent lamps. *J. Cleaner Prod*. 2018;172:2840–2852.
- [78] Sethurajan M, Van Hullebusch ED, Fontana D, et al. Recent advances on hydrometallurgical recovery of critical and precious elements from end of life electronic wastes—a review. *Crit Rev Environ Sci Technol*. 2019;49:212–275.
- [79] Lee CH, Chang CT, Fan KS, et al. An overview of recycling and treatment of scrap computers. *J. Hazard. Mater*. 2004;114:93–100.
- [80] Brierley CL, Brierley JA. Progress in bioleaching: part B: applications of microbial processes by the minerals industries. *Appl Microbiol Biot*. 2013;97:7543–7552.
- [81] Johnston CW, Wyatt MA, Li X, et al. Gold biomineralization by a metallophore from a gold-associated microbe. *Nat Chem Biol*. 2013;9:241.

- [82] Das N, Das D. Recovery of rare earth metals through biosorption: an overview. *J Rare Earths*. 2013;31:933–943.
- [83] Das N, Vimala R, Karthika P. (2008). Biosorption of heavy metals—an overview. <http://nopr.niscair.res.in/handle/123456789/1822>.
- [84] Xiong C, Chen X, Liu X. Synthesis, characterization and application of ethylenediamine functionalized chelating resin for copper preconcentration in tea samples. *Chem Eng J*. 2012a;203:115–122.
- [85] Chaturvedi KS, Hung CS, Crowley JR, et al. The siderophore yersiniabactin binds copper to protect pathogens during infection. *Nat Chem Biol*. 2012;8:731.
- [86] Christenson EA, Schijf J. Stability of YREE complexes with the trihydroxamate siderophore desferrioxamine B at seawater ionic strength. *Geochim Cosmochim Acta*. 2011;75:7047–7062.
- [87] Hsu E, Barmak K, West AC, et al. Advancements in the treatment and processing of electronic waste with sustainability: a review of metal extraction and recovery technologies. *Green Chem*. 2019;21:919–936.
- [88] Abdelbasir SM, El-Sheltawy CT, Abdo DM. Green processes for electronic waste recycling: a review. *J Sustain Metallurgy*. 2018;4:295–311.
- [89] Tuncuk A, Stazi V, Akcil A, et al. Aqueous metal recovery techniques from e-scrap: hydrometallurgy in recycling. *Miner Eng*. 2012;25:28–37.
- [90] Xiu FR, Qi Y, Zhang FS. Recovery of metals from waste printed circuit boards by supercritical water pre-treatment combined with acid leaching process. *Waste Manag*. 2013;33:1251–1257.
- [91] Tiwary CS, Kishore S, Vasireddi R, et al. Electronic waste recycling via cryomilling and nanoparticle beneficiation. *Mater Today*. 2017;20:67–73.
- [92] Zamprogno Rebello R, Weitzel Dias Carneiro Lima MT, Yamane LH, et al. Characterization of end-of-life LED lamps for the recovery of precious metals and rare earth elements. *Resour., Conser. Recycling*. 2020;153:104557.
- [93] Yao Y, Farac NF, Azimi G. Supercritical fluid extraction of rare earth elements from nickel metal hydride battery. *ACS Sustainable Chem. Eng*. 2018;6:1417–1426.
- [94] Pavon S, Fortuny A, Coll MT, et al. Improved rare earth elements recovery from fluorescent lamp wastes applying supported liquid membranes to the leaching solutions. *Sep. Purif. Technol*. 2019;224:332–339.
- [95] Deshmane VG, Islam SZ, Bhavne RR. Selective recovery of rare earth elements from a wide range of E-waste and process scalability of membrane solvent extraction. *Environ. Sci. Technol*. 2020;54:550–558.
- [96] Seon Hong H, Chul Jung H, Seo M, et al. A study on the efficient recovery and separation of the phosphor from CCFLs in end-of-life LCD units. *Curr. Nanosci*. 2014;10:138–142.
- [97] Ahmad Z. The properties and application of scandium-reinforced aluminium. *JOM*. 2003;55:35–39.
- [98] USGS. USGS Minerals Information. <http://minerals.usgs.gov/minerals/pubs/commodity/rare-earths> (accessed on 21 December 2021).
- [99] Lighting GE. Available online: <http://www.gelighting.com> (accessed on 11 December 2021).
- [100] Humphries M. Rare earth elements: The Global Supply Chain: congressional research service. Washington: The Library of Congress; 2010.
- [101] Hughes AE. Interfacial phenomena in Y<sub>2</sub>O<sub>3</sub>-ZrO<sub>2</sub>-based ceramics: A surface science perspective. *Mater. Sci. Monogr*. 1995;81:183–238.
- [102] Hurst C. (2010). China's Rare Earth Elements Industry: What Can the West Learn? Institute for the Analysis of Global Security: Fort Leavenworth, KS, USA.
- [103] <https://www.jstor.org/stable/pdf/resrep21146.14.pdf>.



# Analyzing the efficiency of nanostructured Sm<sup>3+</sup>- and Gd<sup>3+</sup>-doped TiO<sub>2</sub> and constructing DSSCs using efficacious photoanodes

S. Bharathi Bernadsha<sup>1</sup>, V. Anto Feradrick Samson<sup>1,\*</sup> , N. J. Simi<sup>2</sup>, J. Madhavan<sup>1</sup>, and M. Victor Antony Raj<sup>1</sup>

<sup>1</sup>Department of Physics, Loyola College (University of Madras), Chennai, Tamil Nadu, India

<sup>2</sup>Department of Physics, Newman College, Thodupuzha, Idukki, Kerala, India

Received: 12 November 2021

Accepted: 20 January 2022

© The Author(s), under exclusive licence to Springer Science+Business Media, LLC, part of Springer Nature 2022

## ABSTRACT

The rare earth elements, gadolinium and samarium, are doped with TiO<sub>2</sub> by hydrothermal synthesis technique to study the photoconversion performance of a photoanode in a dye-sensitized solar cell (DSSC). The obtained materials are subjected to the characterizations XRD, HR-TEM, UV-Vis spectroscopy, and XPS. DSSCs are fabricated using N719 dye, redox electrolyte, and platinum counter electrode. Charge-transfer ability was investigated using electrochemical impedance spectroscopy (EIS) on DSSCs. The efficiencies of DSSCs are influenced by the electron transport within the TiO<sub>2</sub>-dye-electrolyte system. After the fabrication and simulation, among the two, Gd<sup>3+</sup>-doped TiO<sub>2</sub> gives the desired outcomes and higher efficiency (5.542%) than the pure and Sm<sup>3+</sup>-doped TiO<sub>2</sub> and thus it proves to be a superior solar cell anode material.

## 1 Introduction

According to the report of National Action Plan on Climate Change (NAPCC), those who use power also have the responsibility to maintain the environment cleaner. This statement calls for curtailing higher carbon dioxide emitting energy productions and to innovate alternative resources. Dye-sensitized solar cells (DSSCs) are being investigated intensively as potential alternatives for the next-generation solar cells. From the time Gratzel and his team reported the first DSSCs in the year 1991 and threw some light upon the increasing efficiency of solar cells with

minimized expenses, DSSCs have become the talk of the town. The features like low production cost, high power conversion efficiency (PCE), payback period, and ecofriendly production promote DSSCs superior to their older generation silicon solar cells [1, 2, 3].

Among all the semiconductor materials, TiO<sub>2</sub> nanoparticles are widely used as photoanode due to its large surface area-to-volume ratio, high PCE, and easy preparation in DSSCs [4]. Moreover, the conversion efficiency of TiO<sub>2</sub>-based DSSCs has energy losses by recombination and slow electron transportation as major predicaments [5, 6]. One of the most important parts of DSSCs is photoanode [7]. However, the

Address correspondence to E-mail: antofradrick@gmail.com

development of promising photoanode that exhibits better solar cell performance is still critical for the applications of DSSCs. Research works have been attempted on designing and preparing the highly efficient materials for DSSCs. Enhancing the DSSCs' performance using TiO<sub>2</sub> coupling with other materials is considered to be an important field of research [8]. Such an attempt is made by doping the rare earth elements (REEs) like samarium and gadolinium with TiO<sub>2</sub> and the characterizations were done to find the suitability of the synthesized material. TiO<sub>2</sub> is sensitive only to UV light by cause of its large bandgap, and it has low quantum efficiency, resulting from the fast recombination rate of photogenerated electron–hole pairs. Doping with metal and non-metal species is a popular technique which facilitates visible light activity of titanium dioxide. Moreover, the REE used for doping resulted in stronger absorption edge shift toward a longer wavelength. Red shift of this type can be attributed to the charge-transfer transition between rare earth ion's f electrons and the TiO<sub>2</sub> conduction or valence band. Introducing the orbitals between the conduction and valence band of TiO<sub>2</sub> reduces the bandgap. Samarium and gadolinium are also economic compared to other lanthanides and they improve the absorption in the visible light spectrum [9].

REEs-doped TiO<sub>2</sub> is synthesized through hydrothermal method and produced as an efficient photoanode. The effect of samarium (Sm<sup>3+</sup>) and gadolinium (Gd<sup>3+</sup>) on the surface and morphology of TiO<sub>2</sub> was investigated by characterizing the material with XPS, TEM, and XRD. The optical property was elucidated by UV spectroscopy. The *J*–*V* characteristics provide the data to calculate the efficiency of the fabricated DSSCs. Doping TiO<sub>2</sub> with transition metals is known to enhance their response in visible light region [10, 11]. Very few reports are available accounting for the improvement in the efficiency of TiO<sub>2</sub> toward visible light when doped with lanthanide ions/oxides [12]. Study on the comparison of doping Sm<sup>3+</sup> and Gd<sup>3+</sup> (2 wt%) with TiO<sub>2</sub> is not commonly available in works hence this work will pave path for the researchers to explore more.

## 2 Materials utilized

Samarium(III) oxide (powder, Sm<sub>2</sub>O<sub>3</sub>, 99.9%), gadolinium(III) oxide (powder, Gd<sub>2</sub>O<sub>3</sub>, 99.9%), and ethanol (99%) were purchased from Merck.

Titanium(IV) isopropoxide (liquid, Ti[OCH(CH<sub>3</sub>)<sub>2</sub>]<sub>4</sub>, anatase, 99.9%), platinum (liquid, 99.9%), and fluorine-doped tin oxide (FTO, 13 Ω/sq)-coated glass were received from Sigma-Aldrich. All chemical reagents were used without further purification as they were obtained from commercial sources with the highest purity.

## 3 Preparation technique

Solution reaction-based approach is carried out to synthesize nanomaterials and this method has good control over the compositions of the synthesized nanomaterials. Solution of pure TiO<sub>2</sub> and REE (Sm<sup>3+</sup>/Gd<sup>3+</sup>)-doped TiO<sub>2</sub> was synthesized using this widely employed technique. Titanium(IV) isopropoxide (anatase, 99.9%) and acetic acid were taken in 1:4 molar ratio. Drop by drop, 20 M of distilled water was added to the solution during magnetic stirring to get the solution. This process is allowed for 25 min to observe better results. The obtained solution was poured into a Teflon autoclave. The autoclave was placed in the furnace at 100 °C for 24 h. The product was exposed for 3 h at the heating rate of 5 °C/min to obtain TiO<sub>2</sub> nanoparticles by calcination at 400 °C. Following the same procedure of preparing undoped TiO<sub>2</sub>, RE<sup>3+</sup>-doped TiO<sub>2</sub> samples were synthesized. As mentioned above, after 25 min of stirring, the solution was added with samarium (2 wt%) in smaller quantities. After 25 min of stirring, the process was similar to that of preparing undoped TiO<sub>2</sub>. To get gadolinium-doped TiO<sub>2</sub>, the procedure of preparing samarium-doped TiO<sub>2</sub> is repeated by replacing samarium (2 wt%) with gadolinium (2 wt%).

## 4 Preparation of DSSC

The TiO<sub>2</sub> photoanodes were prepared by a modified version of the reported procedures mentioned by Jara et al. [13]. The FTO glass was sonicated for 20 min in ethanol, washed with acetone and Millipore water, and dried before use. 0.1 g of prepared material (undoped TiO<sub>2</sub>, Sm<sup>3+</sup>/Gd<sup>3+</sup>-doped TiO<sub>2</sub>) was added with a 0.25 ml of Triton-X 100 (4-octylphenol polyethoxylate) and ethanol (5 ml). Employing the prepared FTO glasses (20 mm × 20 mm) as substrates, the paste was dropped using pipette. Spin-

coating was carried out at 500 rpm for 30 s and 2000 rpm for 90 s. Then, it is left to dry at the ambient temperature. The schematic diagram of DSSC is provided in Fig. 1A.

On the anode FTO glass, 5 mmol of N719 dye was applied and left to spread evenly for 12 h. A few drops of liquid platinum were placed on another FTO glass and left to spread evenly. It was exposed to 350°C for 25 min to obtain the platinum (Pt) counter electrode. The two electrodes were sandwiched and a hole was made on the counter electrode.  $I^-/I_3^-$  taken as electrolyte was injected through the hole in the counter electrode. The arranged system was placed in the simulator to measure the activity of DSSC. At room temperature using a Keithley 2400 high current source power meter under white-light illumination from a 500 W xenon lamp (AM1.5G), current density–

voltage ( $J-V$ ) measurements were taken. The energy level diagrams of undoped and doped  $TiO_2$  are given in Fig. 1B.

## 5 Results and discussion

### 5.1 XRD

The prepared sample crystallographic phases were investigated using XRD. The XRD pattern of  $TiO_2$  and ( $Sm^{3+}$  and  $Gd^{3+}$ ) doped  $TiO_2$  is portrayed in Fig. 2b. The presence of strong diffraction peaks at  $2\theta \approx 25.2^\circ, 37.9^\circ, 48.1^\circ, 54.1^\circ, 54.9^\circ, 62.7^\circ, 68.9^\circ, 70.1^\circ,$  and  $75.1^\circ$  corresponding to the  $(hkl)$  reflections planes of (101), (004), (200), (105), (211), (204), (116), (220), and (215), respectively, (JCPDS card no. 21-1272). The

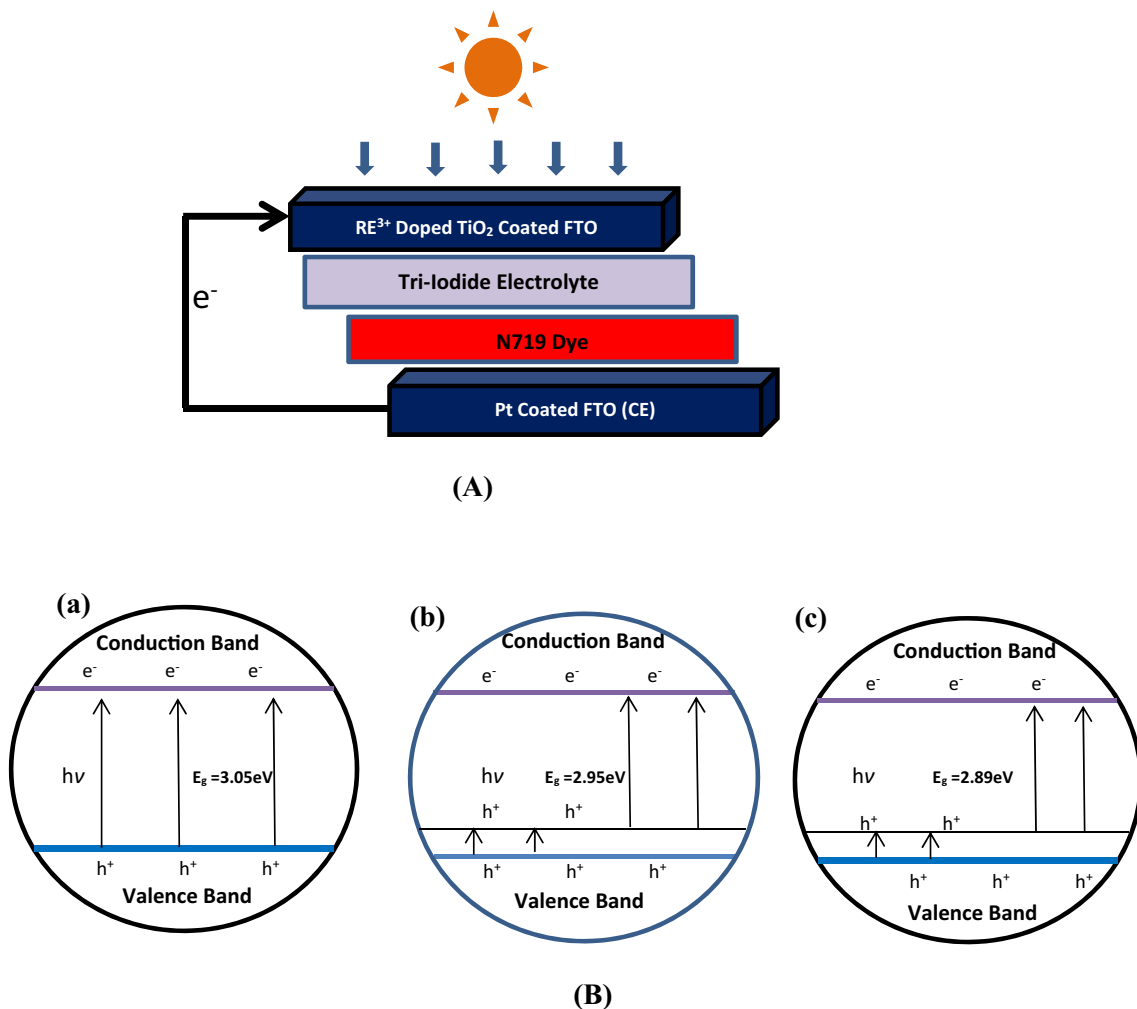


**Fig. 1** **A** Schematic diagram of fabrication of DSSC. **B** Energy level diagram of (a) undoped  $TiO_2$ , (b)  $Sm^{3+}$ -doped  $TiO_2$ , (c)  $Gd^{3+}$ -doped  $TiO_2$



obtained diffraction peaks indicate that anatase crystalline structure is present and the studies authenticate that there is no other impurity observed. Furthermore, peaks of  $\text{Sm}^{3+}$  and  $\text{Gd}^{3+}$  oxides are not seen in patterns. This situation can be ascribed to insertion of dopant ions into the crystal lattice of  $\text{TiO}_2$ . The average crystallite size of the  $\text{TiO}_2$  and  $\text{Sm}^{3+}$ - and  $\text{Gd}^{3+}$ -doped  $\text{TiO}_2$  sample grains was calculated from the prominent peak and the plane 101 utilizing Scherrer's equation. The obtained crystallite size is found to be 9.2, 8.74, and 8.77 for pure and  $\text{Sm}^{3+}$ - and  $\text{Gd}^{3+}$ -doped  $\text{TiO}_2$  samples. While doping with  $\text{Sm}^{3+}$  and  $\text{Gd}^{3+}$ , the crystallite size of the samples decreases. This can be attributed that dopant ions could go into the  $\text{TiO}_2$  lattice [14] and also the crystal growth of  $\text{TiO}_2$  nanoparticles was hindered by dopant ions resulting decreasing in crystal size [15]. From this XRD results,  $\text{Sm}^{3+}$ - and  $\text{Gd}^{3+}$ -doped  $\text{TiO}_2$  samples expected to have more surface area to adsorb large dye molecule into the  $\text{TiO}_2$  surface.

## 5.2 EDAX

Figure 3 provides the energy-dispersive X-ray analysis (EDAX) of Sm-doped, Gd-doped, and undoped  $\text{TiO}_2$ . EDAX is a systematic method utilized to analyze the elemental or chemical characterization of an area of the specimen under study. The elements corresponding to each of its peaks are analyzed. The elemental incorporations of Gd and Sm in the samples are confirmed through the spectrums obtained.

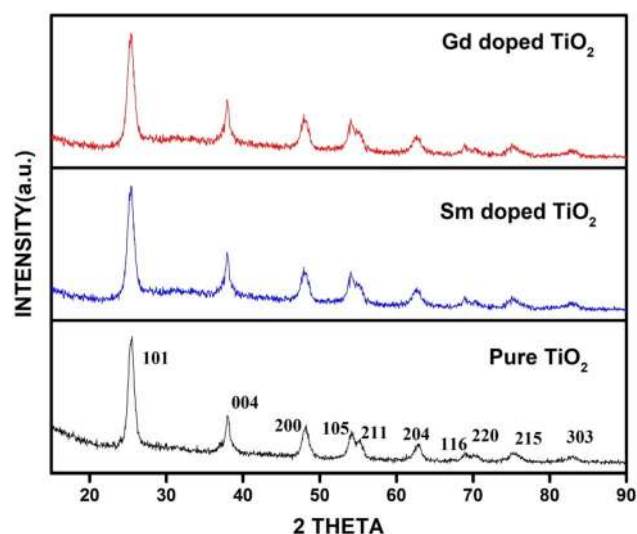


**Fig. 2** XRD images of (a) Gd-doped, (b) Sm-doped, and (c) undoped  $\text{TiO}_2$

Measure of the respective elements incorporated in the specimen is shown as the peak heights or areas are in Fig. 3. Table 1 shows the experimental mass percentage of the titanium, oxygen, gadolinium, and samarium as obtained from EDAX analysis of the compounds. From the spectrums, we observe that Ti peaks appear at + 0.6 keV, + 4.5, and + 5 keV. Samarium is detected at + 0.9, + 4.8, + 5.3, and + 6 keV. Gadolinium is found to be present at + 1, + 5.4, + 6.1 keV, and so on. Thus from the EDAX spectra, the presence of dopants, namely, samarium and gadolinium are seen and thus the doping has taken place as per the expected mass percentages into the  $\text{TiO}_2$  crystal lattice.

## 5.3 HR-TEM

Figure 4A represents the HR-TEM and SAED images of undoped and doped  $\text{TiO}_2$  materials. 2 wt% of doping REE ( $\text{Sm}^{3+}/\text{Gd}^{3+}$ ) ions cover the  $\text{TiO}_2$  nanoparticles to form uneven surface. A greater impact in preventing the growth of the grain and the creating reduction in the size was caused by the presence of samarium and gadolinium. The segregation of the doping ions at the grain boundary limits the grain growth by restricting direct contact of the grains.

Distinguishable crystal planes and well-defined spherical shapes are observed in both the samples. The sizes of the undoped and  $\text{Sm}^{3+}$ - and  $\text{Gd}^{3+}$ -doped samples were measured as 10.41, 9.26, and 9.32 nm, respectively. The lattice fringes are very clear and the interplanar distance is calculated as 0.276 nm for  $\text{Sm}^{3+}$ -doped  $\text{TiO}_2$ , 0.281 nm for Gd-doped  $\text{TiO}_2$ , and 0.269 nm for undoped  $\text{TiO}_2$ . The considerable waviness and expansion of fringes are attributed to the electrical stress might have been originated from earth ions doping [16, 17].

The reduction in the size of the particles was observed and in good agreement with XRD findings. Selected area electron diffraction patterns provide the information about the indices based on which we can calculate the  $d$ -spacing of the elements and the size of the materials is calculated from that measured  $d$ . These images prove that the materials possess properly formed poly crystalline structures. The planes are clear and distinct and easy to identify from the images. They are also in perfect agreement with the various planes present in XRD pattern. The cross-sectional image of undoped  $\text{TiO}_2$ , Sm-doped  $\text{TiO}_2$ ,

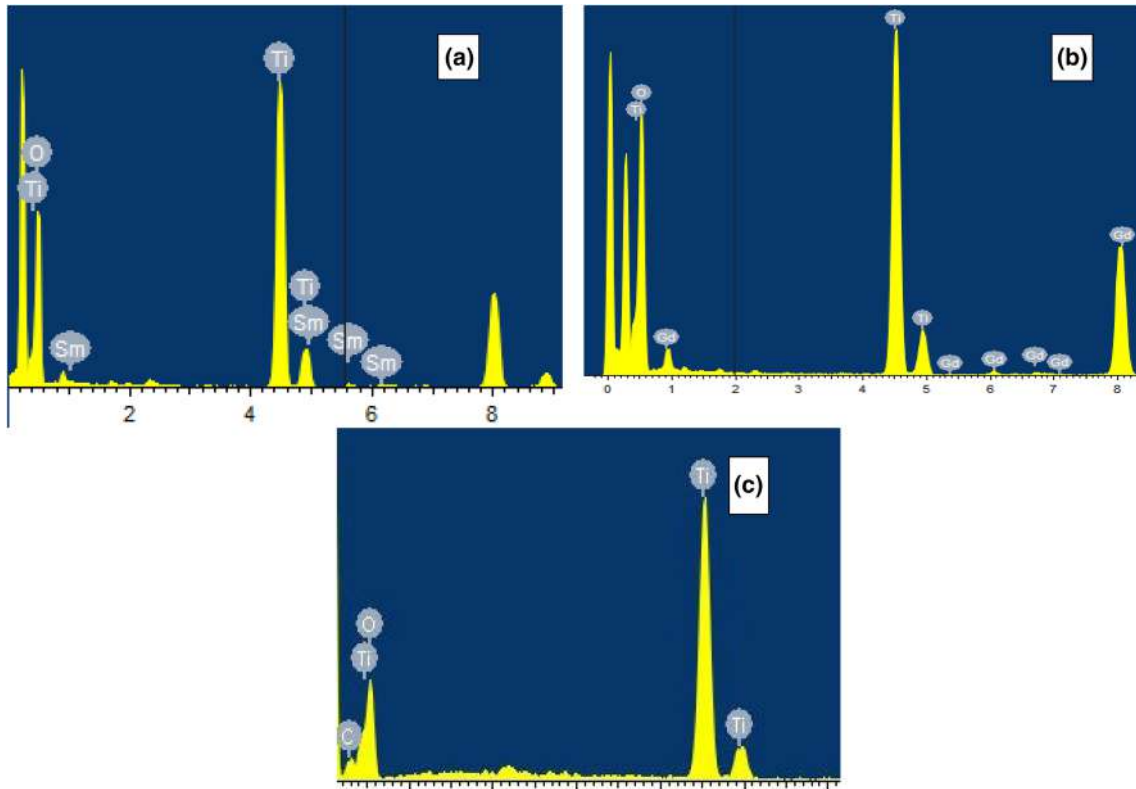


**Fig. 3** EDAX spectrum of **A** Sm-doped, **B** Gd-doped, and **C** undoped TiO<sub>2</sub>

**Table 1** Elemental composition and wt% of the synthesized materials

Materials	Element	Wt%
Samarium doped TiO <sub>2</sub>	O	36.52
	Ti	61.75
	Sm	01.73
Gadolinium doped TiO <sub>2</sub>	O	38.32
	Ti	59.83
	Gd	1.85
Pure TiO <sub>2</sub>	Ti	60.83
	O	39.16

and Gd-doped TiO<sub>2</sub> is shown in Fig. 4B and the thicknesses are measured to be 11.1 μm, 10.8 μm, and 11 μm, respectively.

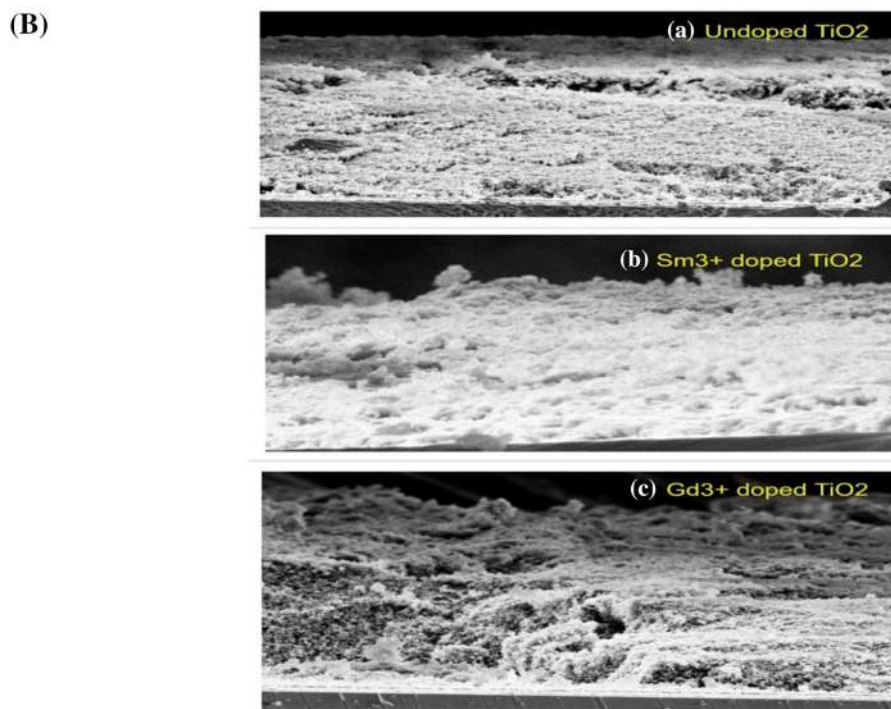
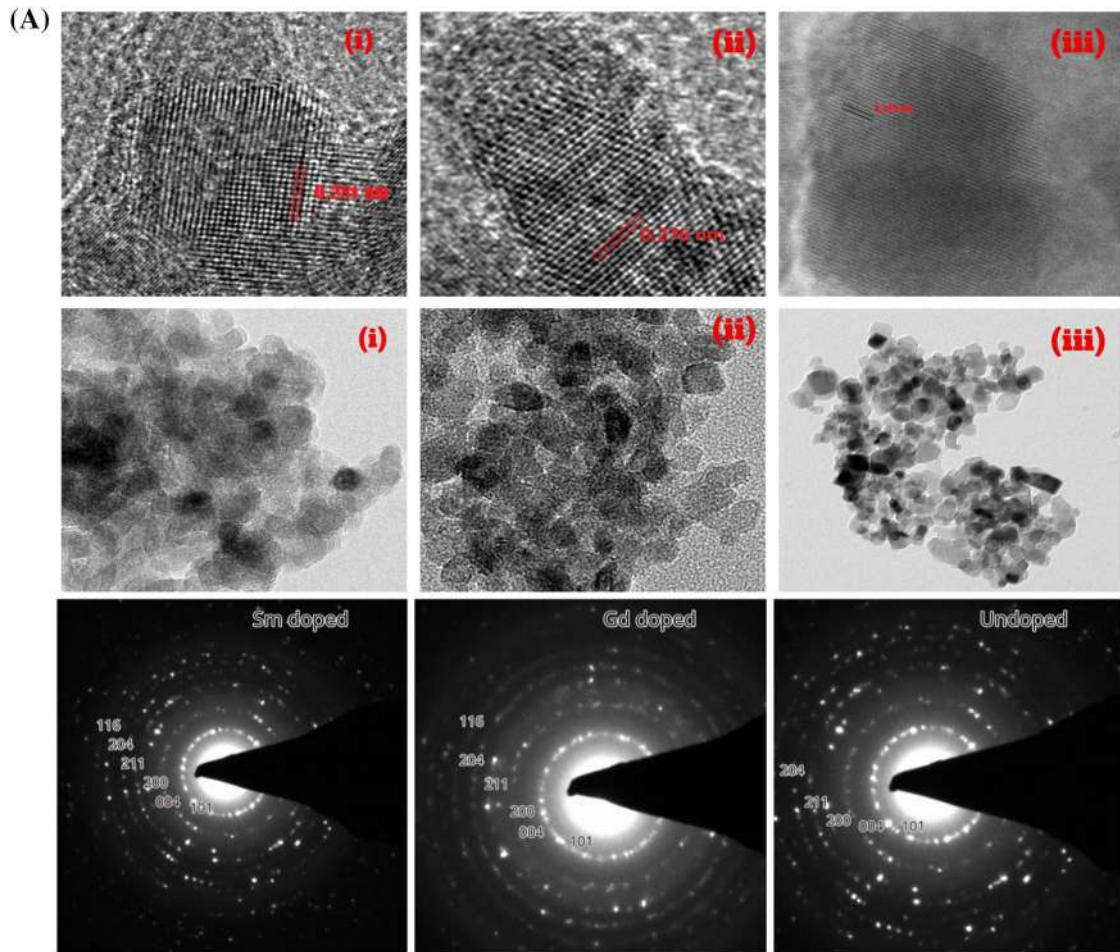
### 5.4 Absorption spectra

Optical properties and optic bandgap values of nanoparticles were investigated with UV-Vis spectroscopy. Figure 5A denotes the optical absorption spectra of undoped TiO<sub>2</sub>, Sm<sup>3+</sup>-doped, and Gd<sup>3+</sup>-doped TiO<sub>2</sub>, respectively. Doping achieved by

replacing the Ti<sup>4+</sup> cation with Sm<sup>3+</sup> and Gd<sup>3+</sup> cation. The main absorption wavelength of TiO<sub>2</sub> corresponds to the intrinsic absorption of anatase phase TiO<sub>2</sub>, whereas the optical absorption band of Sm<sup>3+</sup>-doped TiO<sub>2</sub> and Gd<sup>3+</sup>-doped TiO<sub>2</sub> exhibit bathochromic shift. Thus, upon optical excitation, the energy required for the electrons to transit from the valence band to the conduction band decreases leading to a bathochromic shift commonly known as red shift.

The bandgap energy (*E<sub>g</sub>*) estimated using Taucplot function shown in Fig. 5B–D. The observed 3.05 eV, 2.95 eV, and 2.89 eV are the optical bandgap values of pure TiO<sub>2</sub>, Sm<sup>3+</sup>-doped TiO<sub>2</sub>, and Gd<sup>3+</sup>-doped TiO<sub>2</sub>, respectively. The lowest optical bandgap energy is found for Gd<sup>3+</sup>-doped TiO<sub>2</sub> and is found to be the most efficient among other photoanodes because of high potential electron injection. The above results show that Gd-doped TiO<sub>2</sub> is more active in UV-A, UV-B, and visible spectrum compared to Sm-doped or undoped TiO<sub>2</sub> and absorbs maximum portion of solar light to enhance the photovoltaic conversion.

After doping of Sm<sup>3+</sup> and Gd<sup>3+</sup> cation, a major effect on the band structure and trap states of TiO<sub>2</sub> is



◀ **Fig. 4** **A** High-resolution TEM images and SAED pattern of (i) Sm-doped, (ii) Gd-doped, and (iii) undoped TiO<sub>2</sub>. **B** Cross sectional images of (a) undoped TiO<sub>2</sub>, (b) Sm-doped TiO<sub>2</sub>, and (c) Gd-doped TiO<sub>2</sub>

seen and also the charge injection between photoanode and dye molecules should be fast to avoid recombination which benefits the possible enhancement in the photovoltaic activity for the fabrication of DSSCs.

### 5.5 X-ray photoelectron spectroscopy (XPS)

High-resolution XPS study was used to find the chemical states of Ti, Sm<sup>3+</sup>, and Gd<sup>3+</sup> of the synthesized samples given in Fig. 6A–C. After the baseline correction, the peaks were deconvoluted using Gaussian–Lorentzian line shapes. The survey

spectrum of Sm<sup>3+</sup>- and Gd<sup>3+</sup>-doped TiO<sub>2</sub> nanoparticles is shown in Fig. 6A, which assures the presence of Ti, C, O, Sm<sup>3+</sup>, and Gd<sup>3+</sup>; moreover, the impurities are not much evident here. The XPS spectra were charge corrected having C 1 s peak at 284.6 eV as reference.

In Fig. 6B, the binding energy peak at 458.56 eV and 464.22 eV corresponds to the oxidation state of Ti 2p<sub>3/2</sub> and Ti 2p<sub>1/2</sub>, respectively. These findings are in conformity with the reference data results [4] and confirm that the tetravalent Ti atoms are consistent in TiO<sub>2</sub> lattice. O 1s configuration peaks, observed in Fig. 6C, are the results of oxygen presence on the surface in crystal lattice. The peaks are observed at 529.66 eV for Gd-doped TiO<sub>2</sub> and 529.71 eV in Sm<sup>3+</sup>-doped TiO<sub>2</sub> that confirm the presence of Sm 3d<sub>5/2</sub> and Gd 3d<sub>5/2</sub> states in the TiO<sub>2</sub> crystal lattice, which in turn narrowed the charge-transfer band. Hence,

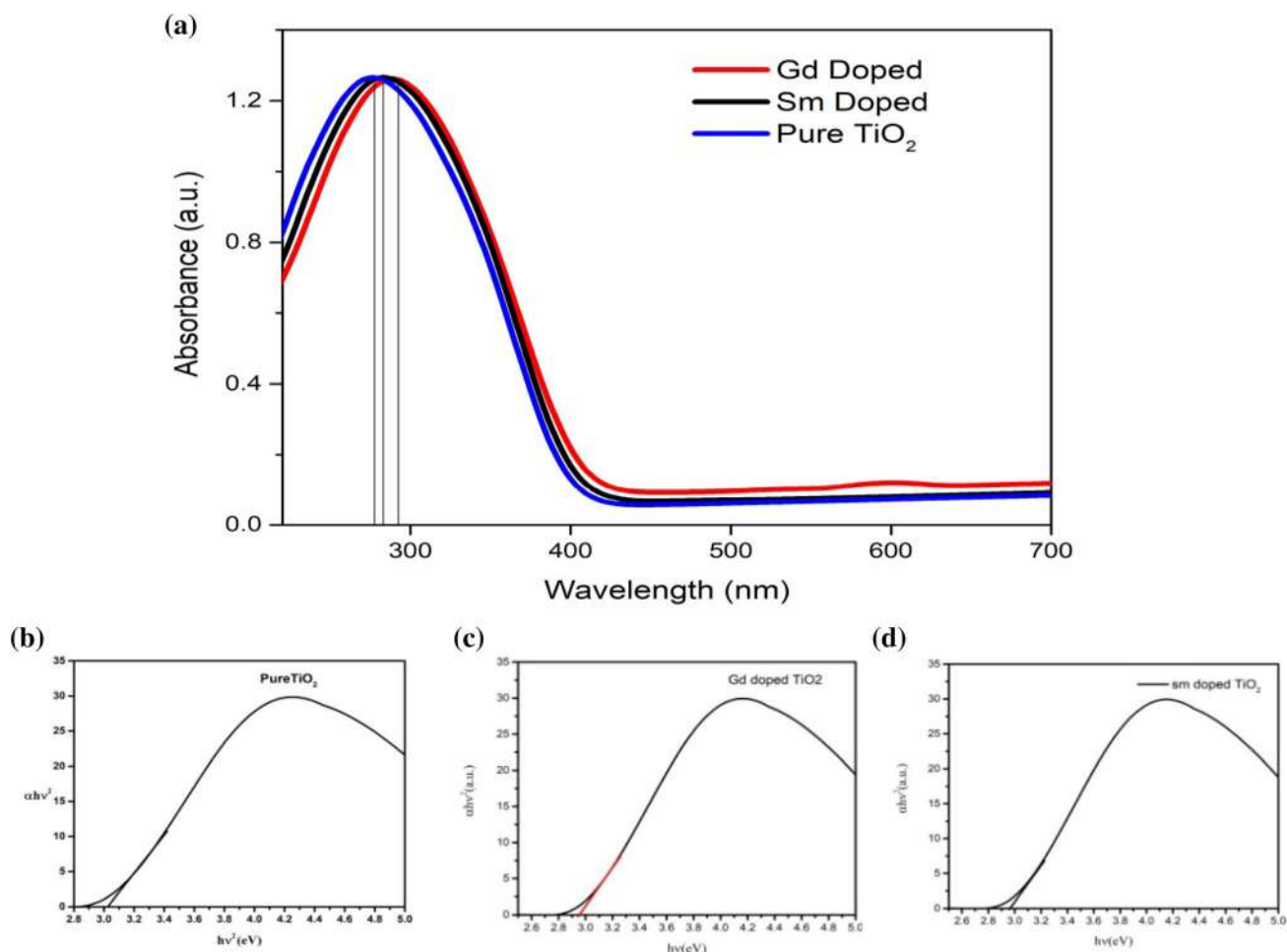


**Fig. 5** **A** Absorption spectra of Gd-doped, Sm-doped, and undoped TiO<sub>2</sub> bandgap of **B** undoped TiO<sub>2</sub>, **C** Gd-doped and **D** Sm-doped

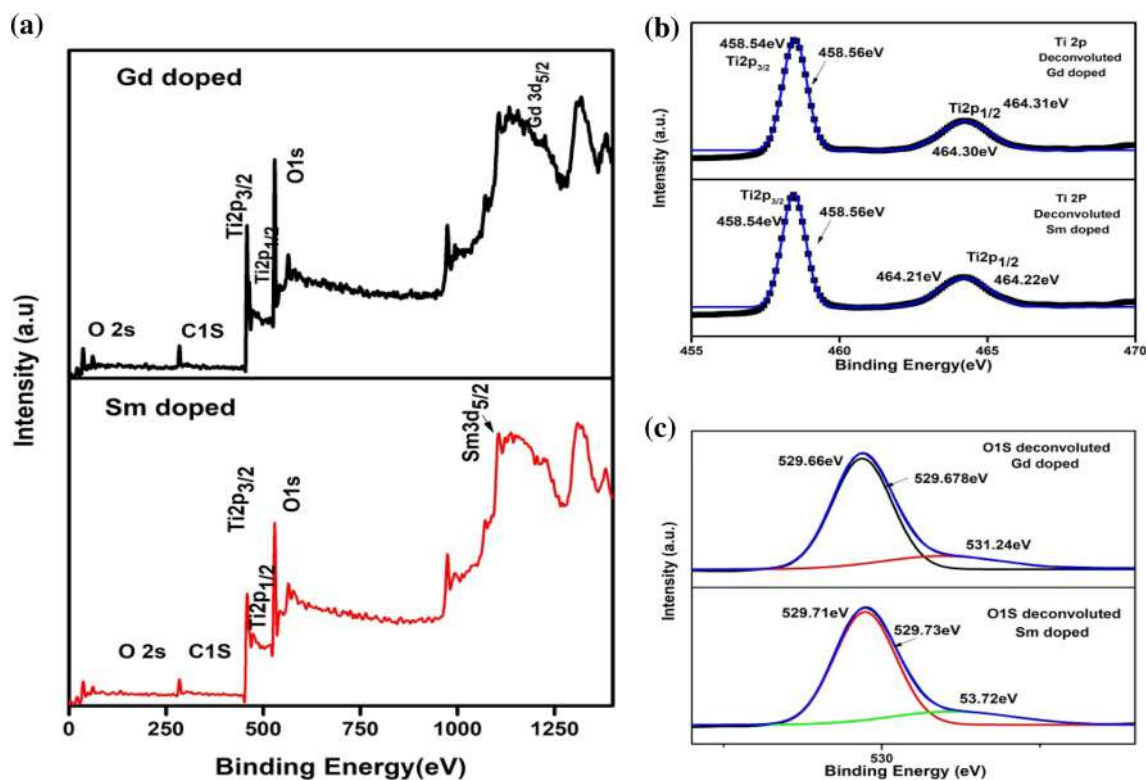


**Fig. 6** XPS spectra of Sm- and Gd-doped TiO<sub>2</sub>

XPS analysis indicates the successful doping of Sm<sup>3+</sup> and Gd<sup>3+</sup> ions into the TiO<sub>2</sub> crystal lattice.

## 5.6 Electrochemical impedance analysis (EIS)

EIS is used to further investigate the electrical conductivity and charge-transfer ability of the prepared photoanodes by Impedance spectra of the two identical symmetric dummy cells is shown in Fig. 7. The obtained experimental data were fitted with a Nyquist equivalent circuit including a series resistance ( $R_s$ ), charge-transfer resistance ( $R_{ct}$ ), and Nernst diffusion ( $Z_N$ ), respectively [18], where  $R_s$  is the resistance of FTO,  $R_{ct}$  is the resistance of interface between electrolyte, dye, and photoanode, and  $Z_N$  is corresponding to the resistance in the redox couple. In general, low  $R_{ct}$  is the salient factor to achieve fast electron transport mobility within photoanode/electrolyte interface. From EIS analysis,  $R_{ct}$  values are decreasing after doping with Sm<sup>3+</sup> and Gd<sup>3+</sup> ions, indicating faster electron generation within the photoanodes; and Gd<sup>3+</sup>-doped TiO<sub>2</sub> has low  $R_{ct}$  values compared with other photoanodes due to smaller crystallite size, which shows that electrolyte can

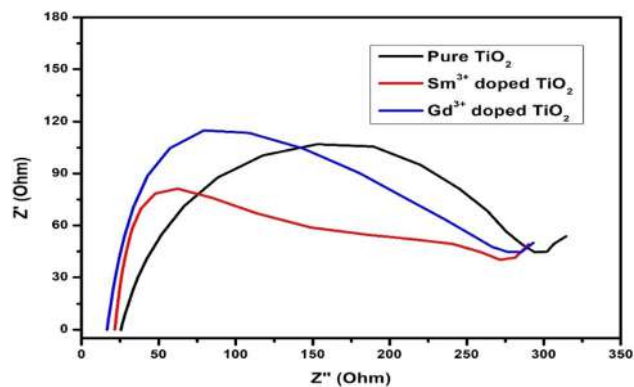


**Fig. 7** Electrochemical impedance spectra of pure TiO<sub>2</sub>, Sm- and Gd-doped TiO<sub>2</sub>

**Table 2** The impedance results of the photoanodes

Photoanodes	$R_s$ ( $\Omega$ )	$R_{ct}$ ( $\Omega$ )	$Z_N$ ( $\Omega$ )
TiO <sub>2</sub>	17.9	7.1	3.8
Sm <sup>3+</sup> doped TiO <sub>2</sub>	16.5	6.7	3.3
Gd <sup>3+</sup> doped TiO <sub>2</sub>	15.8	6.3	2.9

easily access into the photoanode to produce large electron ions. The measured EIS data are shown in Table 2.

**Table 3** Efficiency of DSSCs (pure TiO<sub>2</sub>, Sm-doped and Gd-doped TiO<sub>2</sub>)

Sample	$J_{sc}$ (mA/cm <sup>2</sup> )	$V_{oc}$ (V)	$J_{max}$	$V_{max}$	Fill factor (FF)	$\eta$ (%)
TiO <sub>2</sub>	17.24	0.56	0.3650	13.71	0.5183	5.003
Sm <sup>3+</sup> doped TiO <sub>2</sub>	17.25	0.58	0.3830	13.75	0.5263	5.265
Gd <sup>3+</sup> doped TiO <sub>2</sub>	17.25	0.605	0.3971	13.96	0.5311	<b>5.542</b>

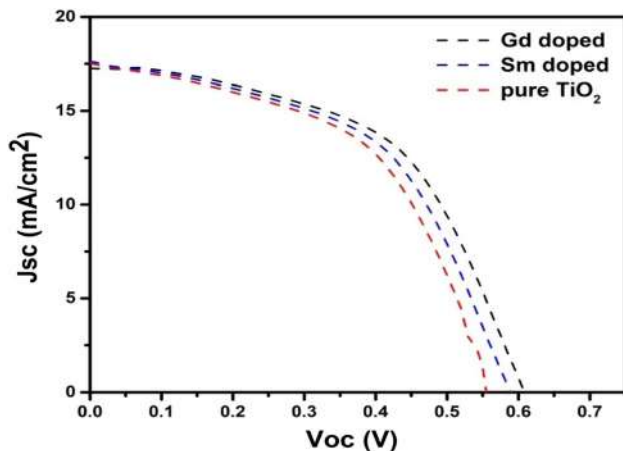


**Fig. 8** I–V curve

### 5.7 I–V characteristics

The current density–voltage performances of pure, Sm<sup>3+</sup>- and Gd<sup>3+</sup>-doped TiO<sub>2</sub> DSSCs are provided in Table 3 and the curves are portrayed in Fig. 7. The conversion efficiency was high for Gd<sup>3+</sup>-doped TiO<sub>2</sub> compared to Sm<sup>3+</sup>-doped and pure TiO<sub>2</sub>. One of the salient factors for the enhancement of the efficiency is the increase in UV and visible region light absorption of the materials. Replacing Ti<sup>4+</sup> cation with Sm<sup>3+</sup>/Gd<sup>3+</sup> cations drives an effect on the trap states and band structure of TiO<sub>2</sub>. As the bandgap decreases, the conduction of Gd<sup>3+</sup>-doped TiO<sub>2</sub> increases (Fig. 8).

It results in the increase of absorption energy from a major portion of visible light as a result of reduction of its bandgap energy. It was found that employed dopant also affects dye adsorption owing to different binding strengths between the dye and the dopant. Since Gd<sup>3+</sup>-doped TiO<sub>2</sub> allows N719 to bind itself of the surface easily than Sm<sup>3+</sup>-doped and bare TiO<sub>2</sub> photoanodes, the efficiency table of fabricated DSSCs (Table 3) shows an increment in efficiency as Gd<sup>3+</sup>-doped TiO<sub>2</sub> > Sm<sup>3+</sup>-doped TiO<sub>2</sub> > undoped TiO<sub>2</sub>.

## 6 Conclusion

Sm<sup>3+</sup>- and Gd<sup>3+</sup>-doped TiO<sub>2</sub> were synthesized with hydrothermal technique. Morphological and optical properties of the materials were characterized. After the elaborate analysis, the prepared anode materials were converted into electrodes and respective DSSCs were fabricated. Among the samples, Gd<sup>3+</sup>-doped TiO<sub>2</sub> exhibited reduced size, 7.74 nm, minimized bandgap, 2.89 eV, greater absorption of solar light especially in UV-A, UV-B, and near visible region, and better efficiency, 5.542%. These results show that Gd<sup>3+</sup>-doped TiO<sub>2</sub> is an appropriate anode material for the assembling of DSSC.

## References

- Shibu Joseph, S. Jacob Melvin Bobby, D. Muthu Gnana Theresa Nathan, P. Sagayaraj, Investigation on the role of cost effective cathode materials for fabrication of efficient DSSCs with TiNT/TiO<sub>2</sub> nanocomposite photoanodes, *Sol. Energy Mater. Sol. Cells* **165** (2017)
- B. O'Regan, M. Graetzel, Low-cost, high efficiency solar cell based on dye-sensitized colloidal TiO<sub>2</sub> films. *Nature* **353**, 737 (1991)
- Y. Chiba, A. Islam, Y. Watanabe, R. Komiya, N. Koide, L. Han, Dye-sensitized solar cells with conversion efficiency of 11.1%. *Jpn. J. Appl. Phys.* **2** **45**, 638–640 (2006)
- P.A. Cormier, J. Dervaux, N. Szuwarski, Y. Pellegrin, F. Odobel, E. Gautron, M. Boujtita, R. Snyders, Single crystalline-like and nanostructured TiO<sub>2</sub> photoanodes for dye sensitized solar cells synthesized by reactive magnetron sputtering at glancing angle. *J. Phys. Chem. C* **122**, 20661–20668 (2018)
- Q. Huang, G. Zhou, L. Fang, L. Hu, Z.S. Wang, TiO<sub>2</sub> nano rod arrays grown from a mixed acid medium for efficient dye-sensitized solar cells. *Energy Environ. Sci.* **4**, 2145–2151 (2011)

6. M. Wang, Y. Wang, J. Li, ZnO nanowire arrays coating on TiO<sub>2</sub> nanoparticles as a composite photoanode for a high efficiency DSSC. *Chem. Commun.* **47**, 11246–11248 (2011)
7. A. Somdee, Improved photovoltaic efficiency of dye sensitized solar cells by decorating TiO<sub>2</sub> photoanode with barium titanate oxide. *J. Alloys Compd.* **777**, 1251–1257 (2019)
8. M. Bron, C. Roth, Chapter 10: new and future developments in catalysis, in *Fuel Cell Catalysis from a Materials Perspective* (Elsevier, Inc., Amsterdam, 2013)
9. J. Reszczyńska, T. Grzyb, J.W. Sobczak, W. Lisowski, M. Gazda, B. Ohtani, A. Zaleska, Lanthanide co-doped TiO<sub>2</sub>: the effect of metal type and amount on surface properties and photocatalytic activity. *Appl. Surf. Sci.* **307**, 333–345 (2014)
10. H. Kato, A. Kudo, Visible-light-response and photocatalytic activities of TiO<sub>2</sub> and SrTiO<sub>3</sub> photocatalysts codoped with antimony and chromium. *J. Phys. Chem. B* **106**, 5029–5034 (2002)
11. K. Kasinathan, J. Kennedy, M. Elayaperumal et al., Photodegradation of organic pollutants RhB dye using UV simulated sunlight on ceria based TiO<sub>2</sub> nanomaterials for antibacterial applications. *Sci. Rep.* **6**(1), 1–12 (2016)
12. J. Reszczyńska, D.A. Esteban, M. Gazda, A. Zaleska, Pr-doped TiO<sub>2</sub>. The effect of metal content on photocatalytic activity. *Physicochem. Probl. Miner. Process.* **50**, 515–524 (2014)
13. D.H. Jara, S.J. Yoon, K.G. Stamplecoskie, P.V. Kamat, Size-dependent photovoltaic performance of CuInS<sub>2</sub> quantum dot-sensitized solar cells. *Chem. Mater.* **26**, 7221–7228 (2014)
14. A.G. Niaki Ghanbari, A.M. Bakhshayesh, M.R. Mohammadi, Double-layer dye-sensitized solar cells based on Zn-doped TiO<sub>2</sub> transparent and light scattering layers: improving electron injection and light scattering effect. *Sol. Energy* **103**, 210–222 (2014)
15. H.G. Yang, C.H. Sun, S.Z. Qiao, J. Zou, G. Liu, S.C. Smith, H.M. Cheng, G.Q. Lu, Anatase TiO<sub>2</sub> single crystals with a large percentage of reactive facets. *Nature* **453**(7195), 638–641 (2008)
16. Z.L. Liu, Z.L. Cui, Z.K. Zhang, Structural phase transformation and UV–Vis characterization of Cr doped nanosized titanium dioxide. *Gongneng Cailiao/J. Funct. Mater.* **36**, 1404–1408 (2005)
17. D.O. Klenov, G.N. Kryukova, L.M. Plyasova, Localization of copper atoms in the structure of the ZnO catalyst for methanol synthesis. *J. Mater. Chem.* **8**(7), 1665–1669 (1998)
18. K. Subalakshmi, S. Jayaraman, Effect of fluorine-doped TiO<sub>2</sub> photoanode on electron transport, recombination dynamics and improved DSSC efficiency. *Sol. Energy* **171**, 914–928 (2018)

**Publisher's Note** Springer Nature remains neutral with regard to jurisdictional claims in published maps and institutional affiliations.

Home More ▾

Article Full-text available

Synthesis of rNiCo Nanocomposite - As an Electrode Material for Supercapacitor Applications

Springer

August 2022 · *Journal of Inorganic and Organometallic Polymers and Materials* 32(35)DOI: [10.1007/s10904-022-02455-1](https://doi.org/10.1007/s10904-022-02455-1)J Fennyl Britto · Anto Feradrick Samson V · Bharathi Bernadsha S · [Show all 5 authors](#) · Victor Antony Raj

Research Interest Score	2.0
Citations	1
Recommendations	1
Reads	67

[Learn about stats on ResearchGate](#)

New

## The publisher of your research added a full-text

Springer Nature provided the most up-to-date published version of your research.  
This means:

- More people can discover and read your work, and it's easier for you to track its impact.
- If a publisher full-text was added, any reader with an institutional subscription to Springer Nature journals can now access your full-text on ResearchGate. Open access full-texts added by Springer Nature can be discovered and read by anyone.
- You can no longer edit the details of the publication page, nor remove a full-text added by a publisher.

You can learn more about the partnership between ResearchGate and the publisher [here](#).

## Abstract and figures

Reduced graphene oxide/nickel cobalt oxide (rNiCo) nanocomposites synthesized via one pot hydrothermal procedure were reported. The X-ray diffraction (XRD) and High Resolution-Transmission Electron Microscopy (HR-TEM) and High Resolution-Scanning Electron Microscopy (HR-SEM) results demonstrates the formation of rNiCo nanocomposites and their morphology. The rNiCo-30 sample exhibits large specific surface area 236.548 m<sup>2</sup>g<sup>-1</sup> along with highly open mesoporous structure. The electrochemical properties are investigated by employing Cyclic Voltammetry (CV), Galvanostatic Charge-Discharge (GCD) and Electrochemical Impedance Spectroscopy (EIS) techniques. The rNiCo-30 sample achieve specific capacitance of 962.96 Fg<sup>-1</sup> at current density 1 Ag<sup>-1</sup>, energy density 308.14 WhKg<sup>-1</sup> and excellent cycling stability (93.5%) for 5000 charge-discharge cycles at 3 Ag<sup>-1</sup>. The power density for the sample rNiCo-30 at different current densities 1, 2, 3, 4 and 5 Ag<sup>-1</sup> are 0.67, 0.76, 0.83, 0.88 and 0.94 KWKg<sup>-1</sup> respectively. The excellent electrochemical performance of rNiCo-30 electrode attributed to easy diffusion of electrolytes and availability of many electrochemical active sites. Moreover presence of rGO in the nanocomposite structure offered uniform porous structures which enables easy flow of electron transportation. These results suggest that prepared electrodes have a great potential for supercapacitor applications. The synthesized nanocomposites could be used as an electrode material for supercapacitor devices.



Share



More

+8

Content available from [Journal of Inorganic and Organometallic Polymers and Materials](#)

This content is subject to copyright. [Terms and conditions](#) apply.

 Publisher Full-text ①

 Springer  
Springer Nature added this full-text to your  
publication. · [Learn more](#)  
Publicly visible 

Content available from [Journal of Inorganic and Organometallic  
Polymers and Materials](#)  
This content is subject to copyright. [Terms and conditions](#) apply.

 Synthesis of rNiCo Nanocomposite ... ns.pdf 

Page 1

Share

More



# Synthesis of rNiCo Nanocomposite - As an Electrode Material for Supercapacitor Applications

J Fennyl Britto<sup>1</sup> · V Anto Feradrick Samson<sup>1</sup> · S Bharathi Bernadsha<sup>1</sup> · J Madhavan<sup>1</sup> · M Victor Antony Raj<sup>1,2</sup>

Received: 31 May 2022 / Accepted: 19 July 2022 / Published online: 17 August 2022

© The Author(s), under exclusive licence to Springer Science+Business Media, LLC, part of Springer Nature 2022

## Abstract

Reduced graphene oxide/nickel cobalt oxide (rNiCo) nanocomposites synthesized via one pot hydrothermal procedure were reported. The X-ray diffraction (XRD) and High Resolution-Transmission Electron Microscopy (HR-TEM) and High Resolution-Scanning Electron Microscopy (HR-SEM) results demonstrates the formation of rNiCo nanocomposites and their morphology. The rNiCo-30 sample exhibits large specific surface area  $236.548 \text{ m}^2\text{g}^{-1}$  along with highly open mesoporous structure. The electrochemical properties are investigated by employing Cyclic Voltammetry (CV), Galvanostatic Charge-Discharge (GCD) and Electrochemical Impedance Spectroscopy (EIS) techniques. The rNiCo-30 sample achieve specific capacitance of  $962.96 \text{ Fg}^{-1}$  at current density  $1 \text{ Ag}^{-1}$ , energy density  $308.14 \text{ WhKg}^{-1}$  and excellent cycling stability (93.5%) for 5000 charge-discharge cycles at  $3 \text{ Ag}^{-1}$ . The power density for the sample rNiCo-30 at different current densities 1, 2, 3, 4 and  $5 \text{ Ag}^{-1}$  are 0.67, 0.76, 0.83, 0.88 and  $0.94 \text{ KWKg}^{-1}$  respectively. The excellent electrochemical performance of rNiCo-30 electrode attributed to easy diffusion of electrolytes and availability of many electrochemical active sites. Moreover presence of rGO in the nanocomposite structure offered uniform porous structures which enables easy flow of electron transportation. These results suggest that prepared electrodes have a great potential for supercapacitor applications. The synthesized nanocomposites could be used as an electrode material for supercapacitor devices.

**Keywords** rNiCo · Nanocomposites · Hydrothermal synthesis · Supercapacitor

## 1 Introduction

Over the rapid depletion of fossil fuels and deteriorating environmental issues, research has been devoted for developing clean energy conversion and storage devices to address the global problems [1, 2]. Recently, the increasing demand for energy devices in our daily life has attracted great attention. The important key factor to overcome these circumstances is to develop efficient energy storage devices with high power and energy density along with long cyclic life and adequate safety [3]. Flexible devices and green energy storage have attained major attentiveness in science as well as in electronic technology. As yet batteries and

capacitors have been considered as two major features in advanced energy storage applications [4, 5].

Owing to, supercapacitors have a predominant role compared to any other energy storage device due to its storage property, high power density, long term stability and fast charge-discharging process [6, 7]. In this technological world, they have fascinated great attention towards the advanced technologies in the energy field. Supercapacitors have been categorised into two types. One is Electrochemical Double Layer Capacitance (EDLC) contains carbon materials and the other is Pseudocapacitance (PC) which contains transition metal oxides and conductive polymers [8, 9]. Basically, the electrochemical active materials were used as the electrode materials and the key index to specify their performance. Besides, many research have been focused on efficient diffusion and distribution of ions and electrons [10].

In such a way, various materials have been explored as supercapacitors such as carbon materials, conducting polymers and Transition Metal Oxides (TMO). Among them, binary transition metal oxide  $\text{NiCo}_2\text{O}_4$  has been considered

✉ M Victor Antony Raj  
vicvad2003@yahoo.co.in

<sup>1</sup> Department of Physics, Loyola College, 34 Chennai, India

<sup>2</sup> Loyola Institute of Frontier Energy (LIFE), Loyola College, 34 Chennai, India



Content courtesy of Springer Nature, terms of use apply. Rights reserved.

Share

More

is spinel structure formed by replacing Co with Ni in  $\text{Co}_3\text{O}_4$ . As a result,  $\text{NiCo}_2\text{O}_4$  exhibits better electrochemical activity and good electronic conductivity compared to bare counterparts of Nickel and Cobalt oxides [11]. However,  $\text{NiCo}_2\text{O}_4$  electrodes suffer from fast capacity fading and low cyclic stability during charge-discharge process due to their poor electrical conductivity [12]. To overcome these predicaments, developing a composite material with carbonaceous materials for the improvement of electrochemical properties of  $\text{NiCo}_2\text{O}_4$  electrode material is the need. Among the carbonaceous material, graphene is one of the best material. Graphene is a two dimensional crystal material endowed with large specific area, excellent electron transport, good electronic conductivity, chemical stability and flexibility.

Reduced graphene oxide (rGO) evinces with  $\text{NiCo}_2\text{O}_4$  will enhance the surface area and conductivity of the active material. Due to its high specific surface area and electronic conductivity, rGO sheets are expected to be outstanding electrode material for supercapacitor. rGO is widely put to use for the betterment of electrochemical performances compared with bare counterparts. Also the development of  $\text{NiCo}_2\text{O}_4$  between graphene sheets absolutely prevents the restacking of the graphene sheets and thus facilitates rapid electrolyte ion diffusion as well as fast electron transport [13]. Recently, irregular porous rGO/ $\text{NiCo}_2\text{O}_4$  composite was prepared by Luo et al. by using the spray pyrolysis technique and the composite exhibited high capacitance of  $777.1 \text{ Fg}^{-1}$  at a current density of  $5 \text{ Ag}^{-1}$ . Liu et al. prepared a mesoporous  $\text{NiCo}_2\text{O}_4$  nanoneedle grown on graphene networks and the composite delivered a high specific capacitance of  $970 \text{ Fg}^{-1}$  at  $20 \text{ Ag}^{-1}$  [14]. Wang et al. reported the electrostatically assembled nickel cobaltite-graphene sheets, showed an initial capacitance of  $835 \text{ Fg}^{-1}$  at a specific current of  $1 \text{ Ag}^{-1}$ . The results signifies the combining structures and the nature of the interactions between the different components plays the key factors to enhance the electrochemical performance of the rNiCo [15, 16]. In this work, by adopting a one-step approach to synthesis rNiCo nanocomposites by hydrothermal method. The electrochemical properties were evaluated by Cyclic Voltammetry (CV), Galvanostatic Charge-Discharge (GCD) and Electrochemical Impedance Spectroscopy (EIS) techniques. The influence of rGO in the nanocomposite material and their electrochemical behaviour of the rNiCo nanocomposites were studied and compared with the bare  $\text{NiCo}_2\text{O}_4$ .

## 2.1 Materials

All the chemicals and the reagents put to use for the synthesis of the present work are of analytical grade and used without any further purification. Nickel (II) nitrate hexahydrate ( $\text{Ni}(\text{NO}_3)_2 \cdot 6\text{H}_2\text{O}$ ), cobalt (II) nitrate hexahydrate ( $\text{Co}(\text{NO}_3)_2 \cdot 6\text{H}_2\text{O}$ ), Urea crystal ( $\text{CH}_4\text{N}_2\text{O}$ ), cetyltrimethylammonium bromide (CTAB) were all purchased from Merck and polyvinylidene fluoride (PVDF), activated carbon (AC) and ethanol were purchased from Sigma Aldrich. De-ionized water was deliberately used for the complete process and also for other application studies.

## 2.2 Preparation on rNiCo Nanocomposite

Graphene oxide (GO) and reduced graphene oxide (rGO) was prepared by natural graphite power via modified Hummer's method [17]. The rNiCo nanocomposite was synthesized by one pot hydrothermal method. Initially 10, 20 and 30 mg of GO was dispersed into 60 mL of distilled water via ultra-sonication for 30 min. In the experimental process.

1 mmol of  $\text{Ni}(\text{NO}_3)_2 \cdot 6\text{H}_2\text{O}$ , 2 mmol of  $\text{Co}(\text{NO}_3)_2 \cdot 6\text{H}_2\text{O}$ , 4 mmol of urea were dissolved separately in 20 ml deionised water under vigorous stirring. Then using CTAB as a surfactant for the hydrothermal method, 1 mmol of CTAB was added in 20 ml deionised water and stirred for 30 min. In order to obtain a uniform solution both the NiCo mixture and CTAB solution were mixed together and continued to stir for 20 min. Intending to obtain the final homogeneous solution, the mixture should be ultra-sonicated for 30 min. Then the prepared solution was transferred into a 100 ml Teflon lined stainless autoclave at  $120^\circ\text{C}$  for 10 h. Once the solution was cooled down to the room temperature, light purple colour precipitate was taken out and centrifuged repeatedly with DI water and ethanol. The obtained product was kept dried in the furnace at  $80^\circ\text{C}$  for 12 h. The purple colour nanopowder was grinded and kept for calcination at  $300^\circ\text{C}$  for 2 h and the nanocomposites are named as rNiCo-10, rNiCo-20 and rNiCo-30. The above steps were followed by the preparation of pure NiCo without adding Graphene Oxide (GO).

## 2.3 Materials characterization:

The structural and morphological analysis were investigated from X-ray diffraction XRD; Rigaku, D/MAX-2500/PC) using Cu Ka ( $40 \text{ kV}$ ,  $100 \text{ mA}$ ) in the range of  $10\text{--}70^\circ$  Transmission Electron Microscope (TEM ((JEM-2100). To calculate the specific surface area of the sample, Bhunauer-Emmett-Teller (BET) method (Micromeritics ASAP2020

 Springer

Content courtesy of Springer Nature, terms of use apply. Rights reserved.

Page 3

Share

More

size of the samples. The electrochemical measurements were put forth in an electrochemical workstation (VSP Biologic controlled by EC-lab software) in a typical three electrode configuration.

#### 2.4 Electrochemical measurements:

The three electrode configuration includes working electrode, counter electrode and reference electrode. The working electrode was prepared by mixing 80 wt % as synthesised sample, 10 wt % of activated carbon (AC) and 10 wt % of polyvinylidene fluoride (PVDF) is in the ratio of 8:1:1 were grinded in a mortar and a few drops of N-methyl-2-pyrrolidone (NMP) solution were added as a binding agent and altogether mixed well. The slurry was finally coated on a piece of nickel foil and dried at 60 degC for 12 h. Now the coated foil was placed in the three electrode configuration where the sample acts as working electrode, platinum as a counter electrode and Ag/AgCl as a reference electrode in an aqueous solution of 2 M Na<sub>2</sub>O<sub>4</sub> (sodium sulphate) electrolyte. Cyclic Voltammetry (CV) measurements were carried out at different scan rates. In order to accomplish the current densities, Galvanostatic Charge-Discharge studies (GCD) were conducted. Electrochemical Impedance Spectroscopy (EIS) test were performed at a frequency range of 1 MHz–0.1 Hz.

### 3 Results and discussions:

#### 3.1 X-Ray diffraction (XRD)

The crystalline structure of the samples were examined by XRD analysis. The crystalline structure of GO, rGO and the different compositions of NiCo, rNiCo-10, rNiCo-20 and rNiCo-30 were shown in Fig. 1 (a, b). In Graphene oxide, characteristic peak of 9.8° following to the plane (001) indicates the successful preparation of graphene oxide from graphite powder. For rGO, the diffraction peak of graphene oxide vanishes and a broad peak centered at 24.4° (002) is observed, which indicates the removal of most oxygen-containing functional group of GO occurred during the chemical reduction and successful formation of rGO. In Fig. 2(b) the diffraction planes of (111), (220), (311), (400), (511) and (440) reflect at 2θ values of 18.9°, 31.1°, 36.7°, 44.6°, 59.1° and 65.0° coincides with the standard diffraction data JCPDS card No.20–0781 denoting the formation of NiCo nanoparticles along with cubic spinel structure with fine quality [18]. For the nanocomposite structure of rNiCo-10, there is no disordered graphene oxide peaks were seen, which is due to the small amount of adding graphene

graphene planes is weak as compared to fine crystalline NiCo planes [19]. Furthermore, nanocomposite structure rNiCo-20 and rNiCo-30 the diffraction plane of rGO were appeared around 24.4° which is due to increasing the rGO content during the preparation. This results confirms that the reduced graphene oxide is successfully dispersed on the surface of NiCo nanoparticles and does not make any structural changes in the planes. Moreover, in the composite structure, the NiCo act as a spacer between rGO and stacking principals leads to the increment in accessible surface area and open channel for efficient electrolytic diffusion, which is the fundamental support for the electrochemical studies. From the XRD results, the average crystalline size of the nanoparticles calculated by the Scherer Eq. (1).

$$D = \frac{K\lambda}{\beta C \cos\theta} \quad (1)$$

Where, D is crystallite size, β represents full width half maximum, θ represents the diffraction angle, wavelength of CuKα radiation is shown by λ and K is the shape factor having constant value of 0.9 respectively. The obtained particle sizes for NiCo, rNiCo-10, rNiCo-20 and rNiCo-30 nanoparticles are 32.2, 28.71, 25.13 and 21.44 nm respectively. From XRD, rGO sheet is successfully dispersed on the surface of NiCo nanoparticles and brings high crystallinity cubic spinel structure.

#### 3.2 High resolution-scanning Electron microscope (HR-SEM)

The morphological features of the as-fabricated samples of NiCo, rNiCo-10, rNiCo-20 and rNiCo-30 were shown in Fig. 3 (a, b, c, d). It clearly indicates the formation of perfect cubic structure. Figure 3(a) shows it is evident that large amount of NiCo are deposited on the surface of rGO sheets. Figure 3(b, c, d) shows small agglomeration compared to NiCo. The interconnected porous structure between the cubic structures enhance better electron transportation and also ensures that each nanocrystalline cubic particles helps to enhance the electrochemical activity [20]. In addition, CTAB is also found to be effective in nanostructuring of NiCo nanocomposites. The rGO sheets are thin and not clearly seen whereas HR-TEM confirms the presence of rGO sheets.

 Springer

Content courtesy of Springer Nature, terms of use apply. Rights reserved.

Share

More

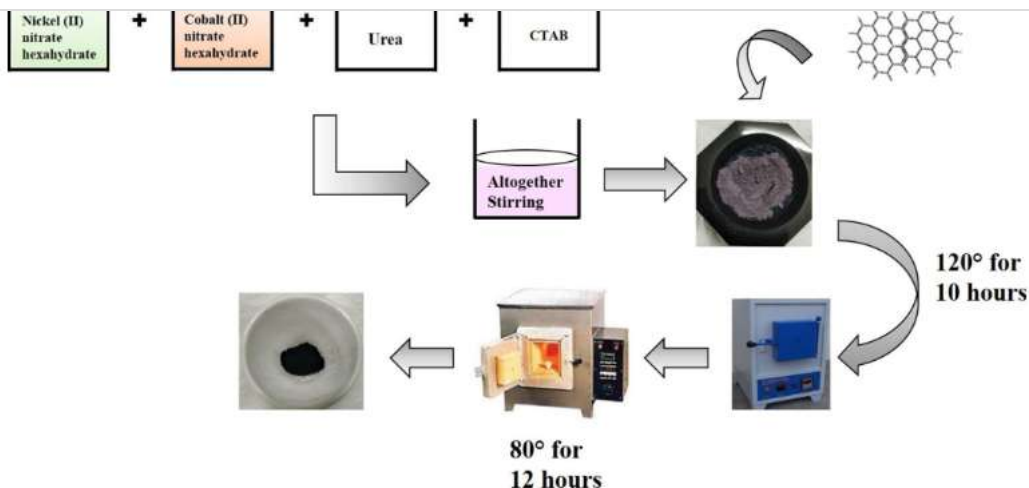


Fig. 1 Schematic representation of rNiCo synthesis procedure

### 3.3 High Resolution-Transmission Electron Microscopy (HR-TEM)

The surface morphologies of the as-synthesized samples were investigated by HR-TEM. The HR-TEM image of rGO has been shown in Fig. 4(a). It shows that characteristic sheet morphology with a small thickness signifying large surface defects of rGO [21]. Figure 4(c) shows the HR-TEM image of NiCo nanoparticles which exhibits cubic spinel shape in morphologies with smaller agglomeration [22]. In contrast, for the nanocomposite structure NiCo

nanoparticles are evenly attached on the external surface of rGO sheets shown in Fig. 4(e). Also we can see that the loosely assembled NiCo nanoparticles spread on both sides of rGO sheets, representing a multilayer structure, which develops an open channel for particle dispersion respectively [23]. It also seems to be porous structure so that it can deliver additional accessible area for ion exchange between the electrode and electrolyte to achieve high electrochemical performance. Figure 4(b) shows the selected area electron diffraction pattern of rGO, which confirms the amorphous nature of the sample. Figure 4(d and f) shows

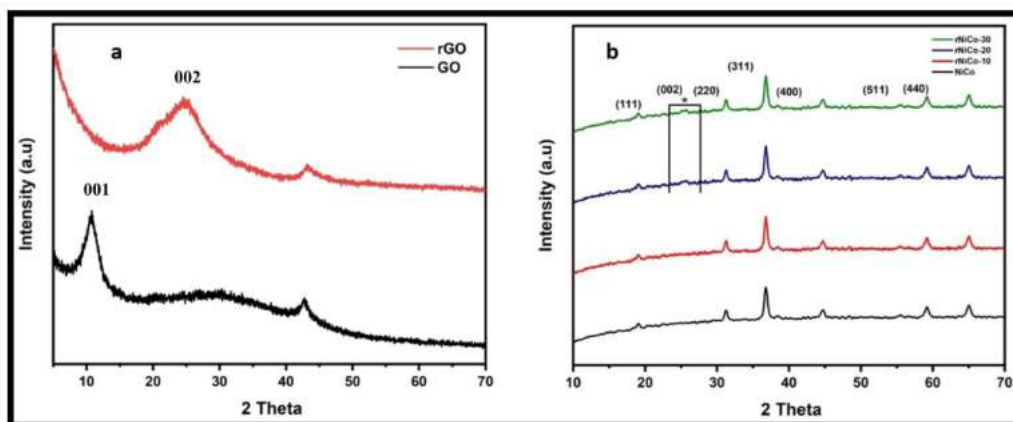


Fig. 2 XRD patterns of (a) GO, rGO and (b) NiCo, rNiCo-10, rNiCo-20 and rNiCo-30

Springer

Content courtesy of Springer Nature, terms of use apply. Rights reserved.

Share

More

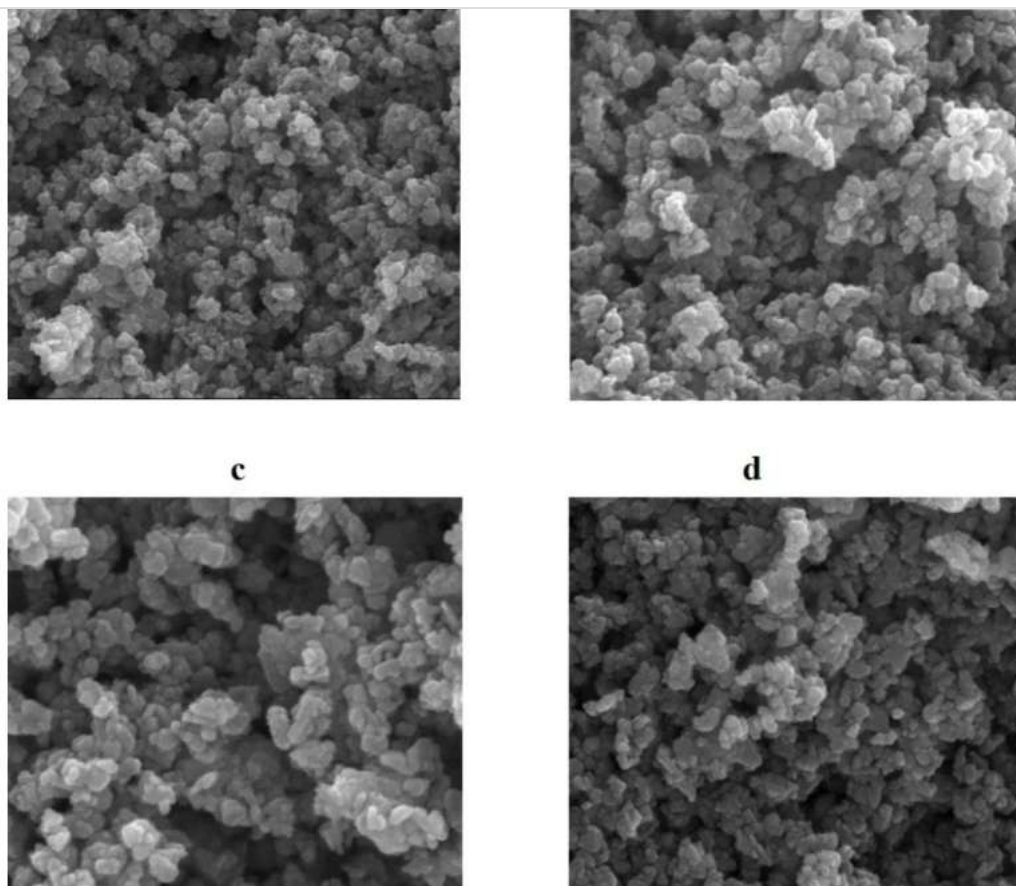


Fig. 3 h-SEM of (a) NiCo, (b) rNiCo-10, (c) rNiCo-20 and (d) rNiCo-30

the selected area electron diffraction of NiCo and rNiCo-30 which is consistent with the crystal plane of NiCo.

### 3.4 Brunauer-Emmett-Teller (BET)

The surface area and the porosity of the samples were investigated by BET studies. Figure 5(a, b, c and d) shows the absorption-desorption of  $N_2$  isotherms of NiCo, rNiCo-10, rNiCo-20 and rNiCo-30 samples respectively. As it can be seen from the adsorption-desorption graphs, all the samples shows the typical type IV isotherm along with hysteresis loop. This indicates that all the samples exhibits mesopores structure which exist in both samples [24, 25]. The high surface area with mesoporous structure are expected

to provide more accessible electrochemical active sites and efficient channel electron transport during the electrochemical studies. According to BET analysis, the total specific surface area of rNiCo-30 ( $236.548 \text{ m}^2\text{g}^{-1}$ ) is much larger than that of other samples (NiCo ( $161.287 \text{ m}^2\text{g}^{-1}$ ), rNiCo-10 ( $210.680 \text{ m}^2\text{g}^{-1}$ ) and rNiCo-20 ( $224.112 \text{ m}^2\text{g}^{-1}$ )) due to the addition of rGO and its secondary pores between NiCo nanoparticles enhances the surface area of the sample [26]. Paranthaman et al. had reported that the surface area of rGO as  $110.16 \text{ m}^2\text{g}^{-1}$  [27]. Thus, the nanocomposite structure may provide high surface area with more porosity to accelerate the ions adsorption and extraction. Inset Fig. 5(a, b, c and c) shows the BJH pore size distributions of the samples. The majority of the pore size were distributed in the range of

 Springer

Content courtesy of Springer Nature, terms of use apply. Rights reserved.

Share

More

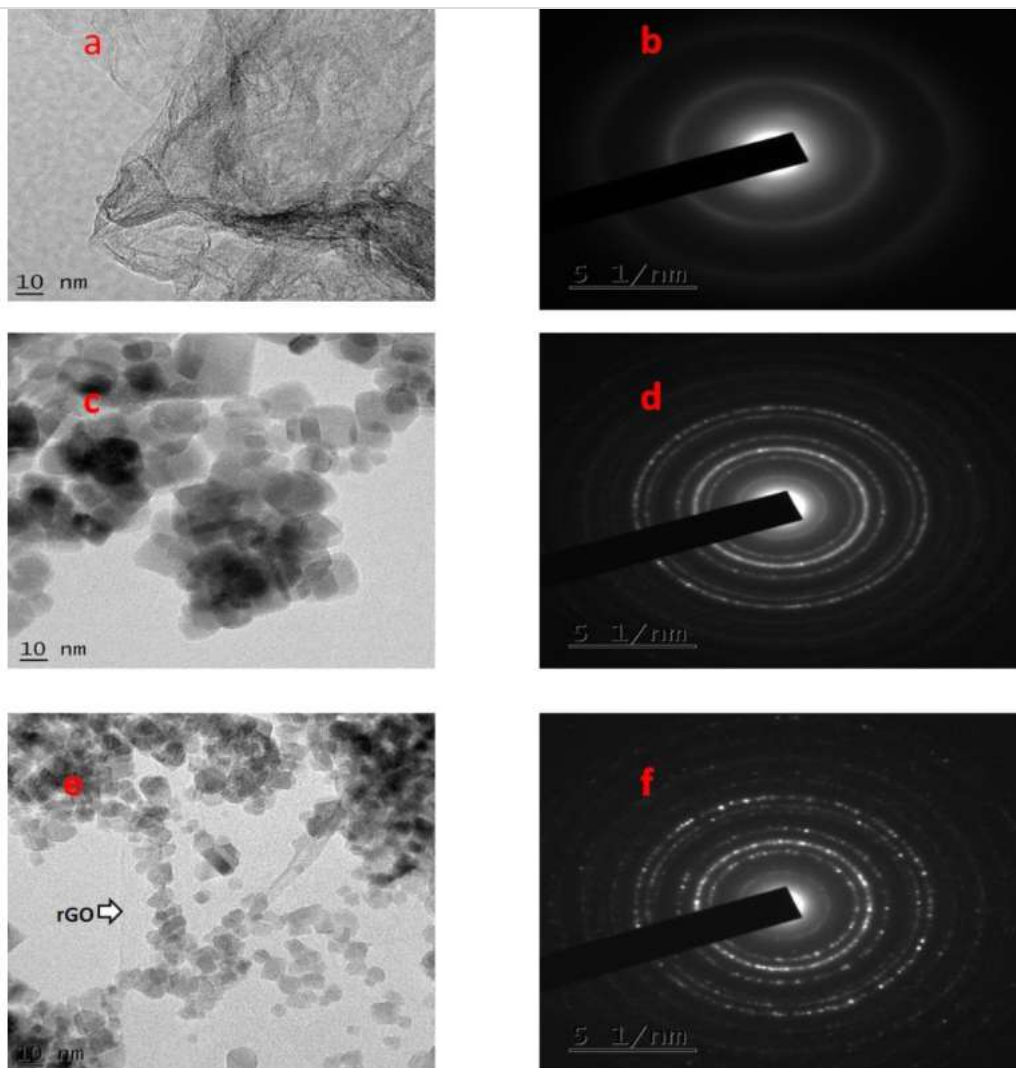


**Fig. 4** h-TEM images of (a), (b) rGO (c), (d) NiCo and (e), (f) rNiCo-30

2–10 nm that calculated from the adsorption branch of the isotherm. BET studies clearly reveals that the ion transport takes place in a smooth way from the electrode material to the electrolyte and produce more active sites which greatly improve the electrochemical performance.

### 3.5 Electrochemical characterization

#### 3.5.1 Cyclic Voltammetry (CV)

The electrochemical properties of the as-synthesised samples were explored by various techniques which involve CV, GCD and EIS [28]. Figure 6(a) shows CV graph of

 Springer

Content courtesy of Springer Nature, terms of use apply. Rights reserved.

Share

More

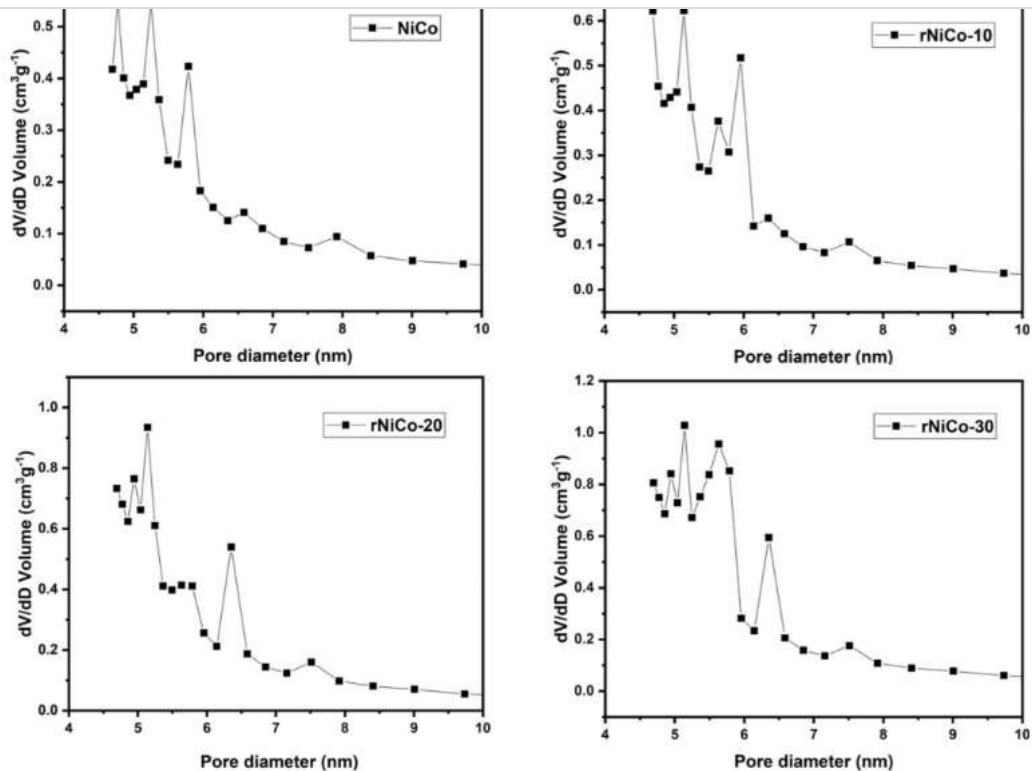


Fig. 5 Shows  $N_2$  adsorption-desorption isotherms of (a) NiCo (b) rNiCo-10 (c) rNiCo-20 (d) rNiCo-30

as-synthesised samples tested in 2 M  $Na_2SO_4$  electrolyte with scan rates  $10 \text{ mVs}^{-1}$  (potential window: 0-0.8 V). The shape of the recorded CV's curves displays the capacitance comes from the electric double-layer capacitance of rGO along with the pseudo capacitance of NiCo component. Compared to bare NiCo and rGO electrode, rNiCo nanocomposite electrodes shows a large CV area which indicates the superposition of electric double layer capacitance of rGO between NiCo and electrolyte. The CV curves of rNiCo-30 nanocomposites shows large CV area suggesting the predominant electric double layer capacitive behaviour of the electrode, which could be due to the presence of high carbon content in nanocomposites. Figure 6(b) shows the CV curves of rNiCo-30 electrode at various scan rates ranging from 10 to  $100 \text{ mVs}^{-1}$ . Owing to the increasing scan rate, there will be a shift on both the ends of curves but the shape does not change [29]. This phenomenon indicating the faster charge/discharge rates and stable electrochemical

response at high scan rate. The good electrochemical properties of the rNiCo-30 electrode attribute to its well-ordered hierarchical nanocomposite structure and the porosity of the material. This enables the fast reaction process and significantly reduce the diffusion time of sodium ions at the interface of the electrode. The above CV result demonstrates that the rNiCo-30 electrode can endure high current charge-discharge cycle performance with a good rate. The value specific capacitance ( $C_s \text{ Fg}^{-1}$ ) is calculated from the CV curves using the following Eq. (2)

$$C_s = \frac{1}{mv(V_e - V_a)} \int_{V_a}^{V_b} I dv \quad (2)$$

Where,  $C_s \text{ (Fg}^{-1}\text{)}$  is specific capacitance,  $V \text{ (Vs}^{-1}\text{)}$  is scan rate,  $V_c - V_a \text{ (V)}$  is potential window,  $I \text{ (A)}$  is current and  $m \text{ (g)}$  is mass of the material. The calculated specific

Springer

Content courtesy of Springer Nature, terms of use apply. Rights reserved.



Share

More

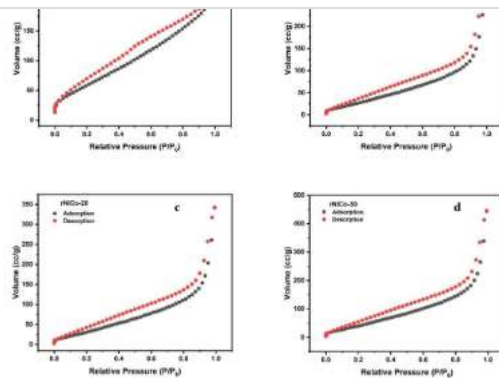


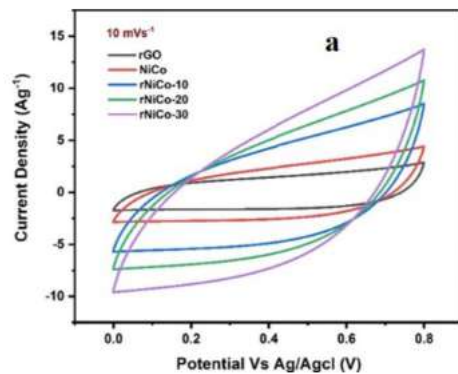
Fig. 5(e) Shows the enlarged graph of pore size distribution

capacitance ( $C_s \text{ Fg}^{-1}$ ) of the samples rGO, NiCo, rNiCo-10, rNiCo-20 and rNiCo-30 was found to be 204.53  $\text{Fg}^{-1}$ , 236.09  $\text{Fg}^{-1}$ , 499.84  $\text{Fg}^{-1}$ , 967.97  $\text{Fg}^{-1}$  and 1083.59  $\text{Fg}^{-1}$  at a scan rate of 10  $\text{mVs}^{-1}$  respectively.

### 3.5.2 Galvanometric Charge-Discharge (GCD)

To further, the galvanometric charge-discharge (GCD) of the electrode were measured at different current densities of 1, 2, 3, 4 and 5  $\text{Ag}^{-1}$  respectively. Figure 7(a, b, c, d and e) represents the charge- discharge profile of rGO, NiCo, rNiCo-10, rNiCo-20 and rNiCo-30 electrodes. The value of specific capacitance is calculated from GCD profile using to the following Eq. (3)

$$C_s = \frac{I \Delta t}{m \Delta V} \quad (3)$$



voltage difference ( $\Delta V$ ) and  $m$  is the mass of the active material. Based on charge discharge profile the value of specific capacitance ( $C_s$ ) is found to be 174.79  $\text{Fg}^{-1}$ , 220.42  $\text{Fg}^{-1}$ , 462.65  $\text{Fg}^{-1}$ , 805.96  $\text{Fg}^{-1}$  and 962.97  $\text{Fg}^{-1}$  for rGO, NiCo, rNiCo-10, rNiCo-20 and rNiCo-30 at the current density of 1  $\text{Ag}^{-1}$  respectively. The specific capacitance calculated at different current densities  $\text{Ag}^{-1}$  are summarized in Table 1. The specific capacitance of rNiCo-30 electrode is larger than that of other electrodes due to easy diffusion of electrolytes and availability of many active sites. Moreover presence of rGO offered large surface area by uniform porous structures enables easy flow of electrons transportation [30–32]. It is observed that decrease in specific capacitance at high current densities is due to diffusion of electrolyte ions. At lower scan rates, the electrolyte ions take sufficient time to access the active sites of the electrode materials, resulting in high specific capacitance. In opposition, the decrease in the specific capacitance at higher current densities can be regarded as only the outer surface active sites can be accessed in the electrochemical reaction. Table 2 shows the comparison of electrochemical parameters of NiCo based composites [33, 34].

The values for specific energy ( $E_s$ ) and specific power ( $P_s$ ) were calculated by the following Eqs. (4 & 5) [35, 36].

$$E_s = \frac{1}{2} C_s \Delta V^2 \quad (4)$$

$$P_s = \frac{E_s}{\Delta t} \quad (5)$$

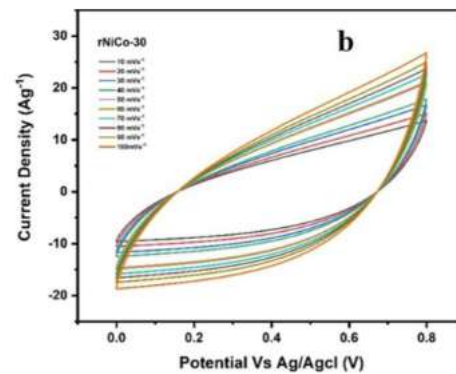


Fig. 6 (a) shows CV graph of as-synthesised samples at a scan rates 10  $\text{mVs}^{-1}$ , (b) shows the CV curves of rNiCo-30 electrode at various scan rates

Springer

Content courtesy of Springer Nature, terms of use apply. Rights reserved.

Share

More

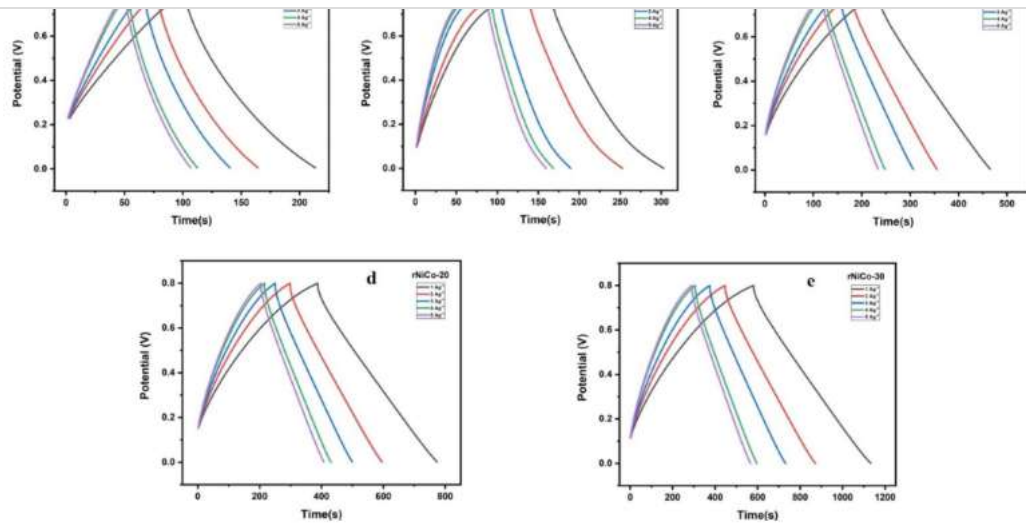


Fig. 7 GCD graph of (a) rGO (b) rNiCo (c) rNiCo-10 (d) rNiCo-20 and (e) rNiCo-30

**Table 1** Comparison of electrochemical parameters at various scan rates

Sample	Current Density ( $\text{Ag}^{-1}$ )				
	$1 \text{ Ag}^{-1}$	$2 \text{ Ag}^{-1}$	$3 \text{ Ag}^{-1}$	$4 \text{ Ag}^{-1}$	$5 \text{ Ag}^{-1}$
rGO	174.79	134.95	115.20	92.01	87.23
NiCo	220.42	184.98	140.35	124.10	117.90
rNiCo-10	462.65	373.93	334.93	291.07	280.32
rNiCo-20	805.96	666.60	593.07	534.73	524.12
rNiCo-30	962.96	767.34	658.53	554.64	530.70

Where,  $E_s$  is specific energy ( $\text{Whkg}^{-1}$ ),  $C_s$  is specific capacitance ( $\text{Fg}^{-1}$ ),  $\Delta V$  is potential window of discharge (V),  $P_s$  is specific power ( $\text{Wg}^{-1}$ ) and  $\Delta t$  is discharge time (s). The value of energy density and power density for rGO (55.93 and  $0.49 \text{ Whkg}^{-1}$ ), NiCo (43.18 and  $0.49 \text{ Whkg}^{-1}$ ), rNiCo-10 (36.86 and  $0.49 \text{ Whkg}^{-1}$ ), rNiCo-20 (29.44 and  $0.49 \text{ Whkg}^{-1}$ ) and rNiCo-30 (27.91 and  $0.50 \text{ Whkg}^{-1}$ ) at current density  $1 \text{ Ag}^{-1}$  respectively. The energy density is found to be decreased with respect to power density. The increasing trend of the power density indicates that the discharging

**Table 2** Comparison of electro-chemical parameters of NiCo based composites

Electrode material	Synthesis method	Electrolyte	Specific capacitance ( $\text{Fg}^{-1}$ )	Reference
$\text{NiCo}_2\text{O}_4/\text{rGO}$	Hydrothermal	2 M KOH	672.79	6
Porous $\text{NiCo}_2\text{O}_4/\text{rGO}$	Spray Pyrolysis	2 M KOH	726	7
$\text{NiCo}_2\text{O}_4/\text{rGO}$	Hydrothermal	1 M $\text{Na}_2\text{SO}_4$	709	10
Urchin like $\text{NiCo}_2\text{O}_4$	Hydrothermal	1 M KOH	636	22
$\text{NiCo}_2\text{O}_4$ microspheres	Hydrothermal	2 M $\text{Na}_2\text{SO}_4$	697.5	25
Porous $\text{NiCo}_2\text{O}_4/\text{rGO}$	Hydrothermal	3 M KOH	947	27
$\text{NiCo}_2\text{O}_4/\text{rGO}$	Thermal treatment	6 M KOH	835	28
rGO/NiCo	Hydrothermal	1 M $\text{Na}_2\text{SO}_4$	962.96	This work

**Table 3** Shows the energy density and power density values at different current densities

Sample	Energy Density ( $\text{WhKg}^{-1}$ )					Power Density ( $\text{KWKg}^{-1}$ )				
	$1 \text{ Ag}^{-1}$	$2 \text{ Ag}^{-1}$	$3 \text{ Ag}^{-1}$	$4 \text{ Ag}^{-1}$	$5 \text{ Ag}^{-1}$	$1 \text{ Ag}^{-1}$	$2 \text{ Ag}^{-1}$	$3 \text{ Ag}^{-1}$	$4 \text{ Ag}^{-1}$	$5 \text{ Ag}^{-1}$
rGO	55.93	43.18	36.86	29.44	27.91	0.49	0.50	0.51	0.53	0.55
NiCo	70.53	59.19	44.91	39.71	37.72	0.53	0.55	0.58	0.61	0.63
rNiCo-10	148.04	119.65	107.17	93.14	89.70	0.64	0.68	0.70	0.75	0.78
rNiCo-20	257.90	213.31	189.78	171.11	167.71	0.66	0.71	0.75	0.79	0.81
rNiCo-30	308.14	245.54	210.72	177.48	169.82	0.67	0.76	0.83	0.88	0.94

Springer

Content courtesy of Springer Nature, terms of use apply. Rights reserved.

Share

More

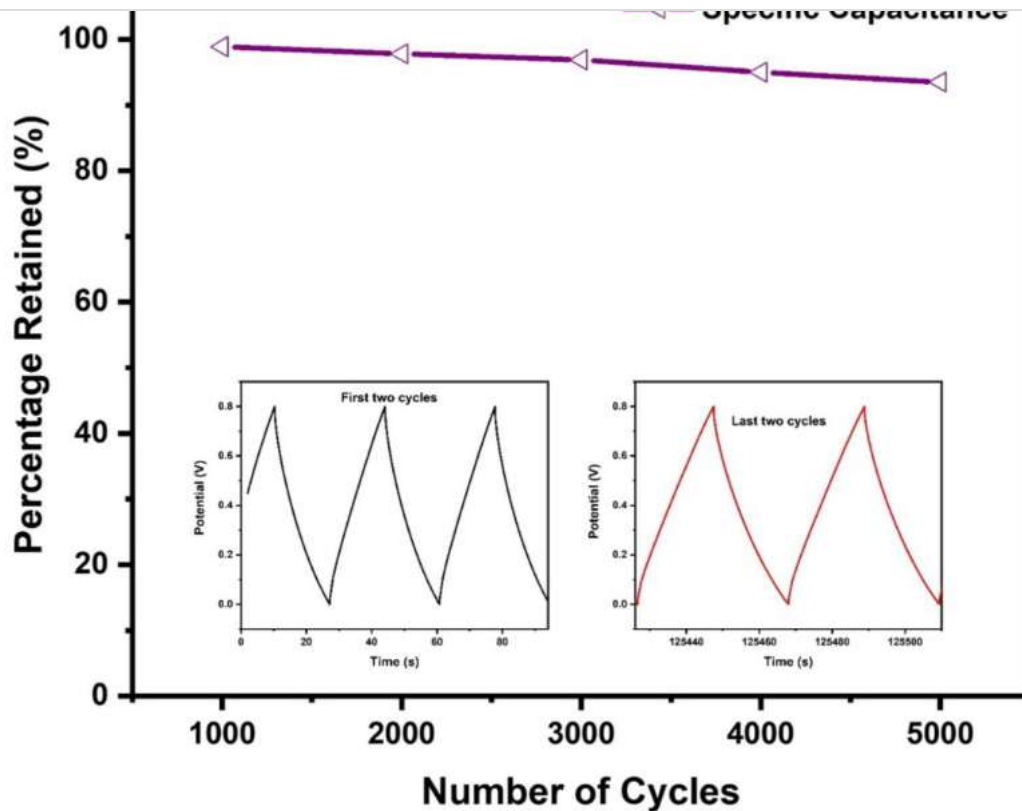


Fig. 8 Cyclic stability curve of rNiCo-30 nanocomposite for 5000 of charge-discharge cycles

capacity of the electrode is directly proportional to the discharge current. The energy density and power density calculated at different current densities are summarized in Table 3.

Furthermore to prove the cycling stability rNiCo-30 electrode, GCD test has been achieved for 5000 cycles at current density  $3 \text{ Ag}^{-1}$  in Fig. 8. The capacitance retention is reached up to 93.5% indicating that rNiCo-30 electrode owing to excellent rate of reversibility and cycling stability. It is also believed that addition of rGO significantly enhanced the mechanical stability and electrical conductivity of the electrode. These results indicate that the rNiCo-30 electrode prove excellent cyclic stability and good rate capability. Figure 9 represents the plot diagram of specific capacitance, energy density and power density values at different current densities.

### 3.5.3 Electrochemical Impedance Spectroscopy (EIS)

Electrochemical Impedance Spectroscopy (EIS) is a significant parameter to evaluate the conductivity of the electrode/electrolyte interface area [37]. Figure 10 shows the EIS Nyquist plot of all respective electrodes. The inset in Fig. 10 displays corresponding equivalent circuit model. The Nyquist plot includes series resistance ( $R_s$ ) at high frequency which was determined by intrinsic resistance and contact resistance of the electrodes. Semicircle at mid frequency region corresponding to charge transfer resistance ( $R_{ct}$ ) of the electrodes. The right semicircle at low frequency section reflects the Nernst diffusion ( $Z_w$ ) which corresponds to the diffusion resistance of the  $\text{Na}_2\text{SO}_4$  electrolyte solution. The smaller  $R_s$  and  $R_{ct}$  values are favorable for fast electron transmission and large diffusion of  $\text{Na}_2\text{SO}_4$  ions into the electrode surface. The value of  $R_s$  is found to be 2.3, 2.5,

Springer

Content courtesy of Springer Nature, terms of use apply. Rights reserved.

Share

More

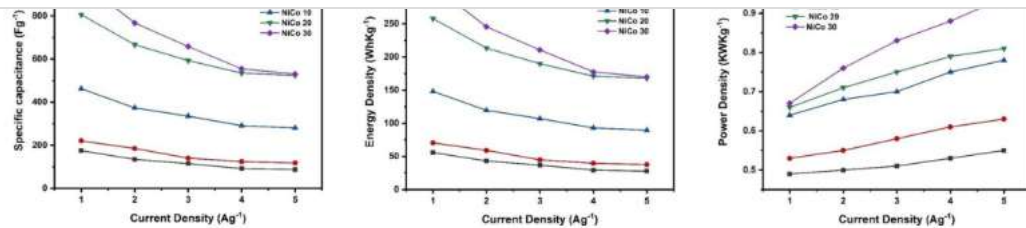


Fig. 9 (a) specific capacitance values at different current densities, (b) energy density values at different current densities and (c) power density values at different current densities

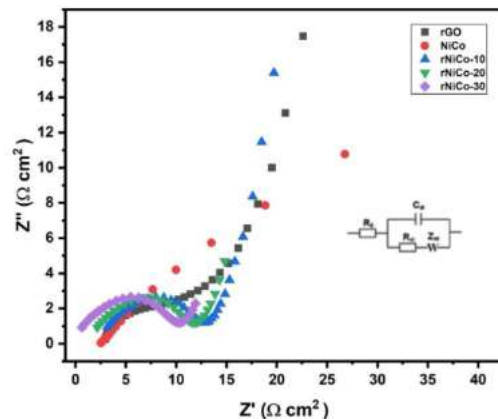


Fig. 10 Shows the Nyquist plot of rGO, NiCo, rNiCo-10, rNiCo-20 and rNiCo-30 electrodes

2.0, 1.4 and 1.1  $\Omega\text{cm}^2$  for rGO, NiCo, rNiCo-10, rNiCo-20 and rNiCo-30 respectively. It is observed that decrease in  $R_s$  value of the rNiCo nanocomposites compared to bare NiCo may be attributed to the superior electrical conductivity provided by the reduced graphene oxide. Further it is observed that the diameter of the semicircle for rNiCo-30 electrode is smaller than the other electrodes, signifying the low charge transfer resistance ( $R_{ct}$ ) of the material. The low value of  $R_s$  and  $R_{ct}$  is found for rNiCo-30 electrode specifies that good ion response with superior electronic conductivity of the material. Also it is believed that graphene provide a short ion transfer path and high charge transfer speed of the electrode. Hence the above studies indicate that rNiCo-30 composite is a promising candidate for energy storage devices.

## 4 Conclusions

In summary, rNiCo was successfully synthesized through an eco-friendly reagent assisted with CTAB by simple hydrothermal method. XRD results clearly shows that graphene oxide surface have been effectively deposited on both sides of NiCo nanoparticles. From HR-SEM and HR-TEM analysis, homogeneous distribution of rGO could provide large surface area and more opening sites for electrochemical reactions. BET studies indicates that all the samples exhibits mesopores structure and more accessible active sites for excellent electrochemical studies. The observed results from CV, GCD and EIS proposes that rNiCo-30 electrode provides high electrochemical surface area and multiphase active sites to achieve remarkable specific capacitance and excellent cyclic stability. From the above results, rNiCo act as one of the most promising materials and has a broader application in the energy storage devices.

**Acknowledgements** The authors acknowledge Centennial Physics Ph.D Instrumentation Centre, Department of Physics, Loyola College, Chennai-600 034.

## Declarations

**Conflict of interest** ☒ The authors declare that they have no known competing financial interests or personal relationships that could have appeared to influence the work reported in this paper.

## References

1. V. Samson, S. Bharathi Bernadsha, P. Albin John, D. Paul Winston, J. Divya, M. Abraham, Raj, J. Madhavan. "rGO Sheets/ ZnFe2O4 Nanocomposites as an Efficient Electro Catalyst Material for  $\text{I}^2/\text{T}$  Reaction for High Performance DSSCs." *Journal of Inorganic and Organometallic Polymers and Materials* (2022):1-7
2. A. Singh, S.K. Ojha, K. Animesh, Ojha. "Facile synthesis of porous nanostructures of NiCo2O4 grown on rGO sheet for high performance supercapacitors. *Synth. Met.* **259**, 116215 (2020)
3. J. Schummer. "From Nano-Convergence to NBIC-Convergence: "The best way to predict the future is to create it"."

Springer

Content courtesy of Springer Nature, terms of use apply. Rights reserved.

Share

More

4. D. Van Lam, M. Sohail, J.-H. Kim, H.J. Lee, S.O. Han, J. Shin, D. Kim, H. Kim, and Seung-Mo Lee. "Laser synthesis of MOF-derived Ni@ Carbon for high-performance pseudocapacitors. *ACS Appl. Mater. Interfaces* **12**(35), 39154–39162 (2020)
5. J. Gu, L.S.Y. Zhang, Q. Zhang, X. Li, H. Si, Y. Shi, C. Sun, Yi Gong, and Yihe Zhang. "MOF-derived Ni-doped CoP@ C grown on CNTs for high-performance supercapacitors. *Chem. Eng. J.* **385**, 123454 (2020)
6. C.-H. Wang, D.-W. Zhang, S. Liu, Y. Yamauchi, F.-B. Zhang, Yusuf Valentino Kaneti. "Ultrathin nanosheet-assembled nickel-based metal-organic framework microflowers for supercapacitor applications." *Chem. Commun.* **58**, 7 (2022): 1009–1012
7. A. Allah, J. Enaïet, Y.V. Wang, T. Kaneti, A.A. Li, Farhali, Mohamed Hamdy Khedr, Ashok Kumar Nanjundan et al. "Auto-programmed heteroarchitecturing: Self-assembling ordered mesoporous carbon between two-dimensional Ti3C2Tx MXene layers." *Nano Energy* **65** (2019): 103991
8. M. Isacfranklin, G. Ravi, R. Yuvakkumar, P. Kumar, D. Velauthapillai, B. Saravanakumar, M. Thambidurai, Cuong Dang. "Urchin like NiCo2O4/rGO nanocomposite for high energy asymmetric storage applications." *Ceram. Int.* **46**, 10 (2020): 16291–16297
9. Y. Luo, H. Zhang, D. Guo, J. Ma, Q. Li, L. Chen, T. Wang, Porous NiCo2O4-reduced graphene oxide (rGO) composite with superior capacitance retention for supercapacitors. *Electrochim. Acta* **132**, 332–337 (2014)
10. S. Zhang, H. Gao, J. Zhou, F. Jiang, Z. Zhang, Hydrothermal synthesis of reduced graphene oxide-modified NiCo2O4 nanowire arrays with enhanced reactivity for supercapacitors. *J. Alloys Compd.* **792**, 474–480 (2019)
11. G. He, L. Wang, H. Chen, X. Sun, X. Wang. "Preparation and performance of NiCo2O4 nanowires-loaded graphene as supercapacitor material." *Mater. Lett.* **98**, 164–167 (2013)
12. J. Pokharel, A. Gurung, A. Baniya, W. He, K. Chen, R. Pathak, Buddhi Sagar Lamsal, Nabin Ghimire, and Yue Zhou. "MOF-derived hierarchical carbon network as an extremely-high-performance supercapacitor electrode." *Electrochim. Acta* **394**, 139058 (2021)
13. T. Liu, S. Zhou, X. Yu, C. Mao, Y. Wei, X. Yu, L. Chen, X. Zhao, G. Tian, L. Chen. "Hexadecyl trimethyl ammonium bromide assisted growth of NiCo<sub>2</sub>O<sub>4</sub>@ reduced graphene oxide/nickel foam nanoneedle arrays with enhanced performance for supercapacitor electrodes." *RSC advances* **12**, no. 7 (2022): 4029–4041
14. Z. Wei, J. Guo, M. Qu, Z. Guo, H. Zhang. "Honeycombed-like nanosheet array composite NiCo2O4/rGO for efficient methanol electrooxidation and supercapacitors." *Electrochim. Acta* **362**, 137145 (2020)
15. L. Ma, X. Shen, Hu Zhou, Z. Ji, K. Chen, G. Zhu. "High performance supercapacitor electrode materials based on porous NiCo2O4 hexagonal nanoplates/reduced graphene oxide composites." *Chem. Eng. J.* **262**, 980–988 (2015)
16. S. Liu, C. An, X. Chang, H. Guo, L. Zang, Y. Wang, H. Yuan, Lifang Jiao. "Optimized core-shell polypyrrole-coated NiCo2O4 nanowires as binder-free electrode for high-energy and durable aqueous asymmetric supercapacitor." *J. Mater. Sci.* **53**, 4 (2018): 2658–2668
17. J. Yan, Q. Wang, T. Wei, Z. Fan, Recent advances in design and fabrication of electrochemical supercapacitors with high energy densities. *Adv. Energy Mater.* **4**(4), 1300816 (2014)
18. S. Liu, J. Wu, J. Zhou, Guozhao Fang, and Shuquan Liang. "Mesoporous NiCo2O4 nanoneedles grown on three dimensional graphene networks as binder-free electrode for high-performance lithium-ion batteries and supercapacitors." *Electrochimica Acta* **176** (2015): 1–9
19. capacitance supercapacitors. *Electrochim. Acta* **111**, 937–945 (2013)
21. Y. Qiu, X. Li, M. Bai, H. Wang, D. Xue, W. Wang, J. Cheng. Pseudocapacitive behaviors of mesoporous nickel-cobalt oxide nanoplate electrodes in different electrolyte systems. *New J. Chem.* **41**(5), 2124–2130 (2017)
22. S. Khalid, C. Cao, A. Ahmad, L. Wang, M. Tanveer, I. Aslam, M. Tahir, Faryal Idrees, and Youqi Zhu. "Microwave assisted synthesis of mesoporous NiCo<sub>2</sub>O<sub>4</sub> nanosheets as electrode material for advanced flexible supercapacitors." *Rsc Advances* **5**(42), 33146–33154 (2015)
23. R. Basu, Prabir, S. Mahesh, S.J. Harish, P. Sagayaraj. "One-pot hydrothermal preparation of Cu<sub>2</sub>O-CuO/rGO nanocomposites with enhanced electrochemical performance for supercapacitor applications." *Appl. Surf. Sci.* **449**, 474–484 (2018)
24. L. Ma, X. Shen, Hu Zhou, Z. Ji, K. Chen, G. Zhu. "High performance supercapacitor electrode materials based on porous NiCo2O4 hexagonal nanoplates/reduced graphene oxide composites." *Chem. Eng. J.* **262**, 980–988 (2015)
25. J. Shi, X. Zhou, Y. Liu, Q. Su, J. Zhang, G. Du. One-pot solvothermal synthesis of ZnFe2O4 nanospheres/graphene composites with improved lithium-storage performance. *Mater. Res. Bull.* **65**, 204–209 (2015)
26. D. Nathan, Muthu Gnana, Theresa, and S. Jacob Melvin Boby. "Hydrothermal preparation of hematite nanotubes/reduced graphene oxide nanocomposites as electrode material for high performance supercapacitors. *J. Alloys Compd.* **700**, 67–74 (2017)
27. S.J. Uke, N. Gajanan, A.B. Chaudhari, Bodade, P. Satish, Mardikar. "Morphology dependant electrochemical performance of hydrothermally synthesized NiCo2O4 nanomorphs. *Mater. Sci. Energy Technol.* **3**, 289–298 (2020)
28. V. Paranthaman, K. Sundaramoorthy, B. Chandra, S.P. Muthu, P. Alagarsamy, R. Perumalsamy. "Investigation on the performance of reduced graphene oxide as counter electrode in dye sensitized solar cell applications." *physica status solidi (a)* **215**, no. 18 (2018): 1800298
29. E. Jekar, and Saeed Shahrokhian. "Synthesis and characterization of NiCo2O4 nanorods for preparation of supercapacitor electrodes. *J. Solid State Electrochem.* **19**(1), 269–274 (2015)
30. J. Xiao, S. Yang. "Sequential crystallization of sea urchin-like bimetallic (Ni, Co) carbonate hydroxide and its morphology conserved conversion to porous NiCo<sub>2</sub>O<sub>4</sub> spinel for pseudocapacitors." *RSC advances* **1**, no. 4 (2011): 588–595
31. N. Zhao, H.F.M. Zhang, J. Ma, W. Zhang, C. Wang, H. Li, Xinfiao Jiang, and Xiaoqiang Cao. "Investigating the large potential window of NiCo2O4 supercapacitors in neutral aqueous electrolyte." *Electrochim. Acta* **321**, 134681 (2019)
32. L. Yu, J. Liu, W. Yin, J. Yu, R. Chen, D. Song, Q. Liu, R. Li, J. Wang. Ionic liquid combined with NiCo2O4/rGO enhances electrochemical oxygen sensing. *Talanta* **209**, 120515 (2020)
33. P. Shewale, Shivaji, Kwang-Seok, Yun. "NiCo2O4/RGO Hybrid Nanostructures on Surface-Modified Ni Core for Flexible Wire-Shaped Supercapacitor." *Nanomaterials* **11**, no. 4 (2021): 852
34. W. Zhang, W. Xin, T. Hu, Q. Gong, T. Gao, G. Zhou. One-step synthesis of NiCo2O4 nanorods and firework-shaped microspheres formed with necklace-like structure for supercapacitor materials. *Ceram. Int.* **45**(7), 8406–8413 (2019)
35. G. Umeshbabu, Ediga, Rajeshkhanna, G. Ranga Rao, Urchin and sheaf-like NiCo2O4 nanostructures: synthesis and electrochemical energy storage application. *Int. J. Hydrog. Energy* **39**(28), 15627–15638 (2014)
36. P. Shewale, Shivaji, Kwang-Seok, Yun. "NiCo2O4/RGO hybrid nanostructures on surface-modified Ni core for flexible wire-shaped supercapacitor." *Nanomaterials* **11**, no. 4 (2021): 852

 Springer

Content courtesy of Springer Nature, terms of use apply. Rights reserved.

Page 13

Share

More

- "Design of copper (II) oxide nanoflakes decorated with molybdenum disulfide@ reduced graphene oxide composite as an electrode for high performance supercapacitor." *Synth. Met.* **278** (2021): 116843
38. P. Selvamani, J. Stephen, L. Judith Vijaya, B. John Kennedy, N. Saravanakumar, Clament Sagaya Selvam, and P. Joice Sophia. "Facile microwave synthesis of cerium oxide@ molybdenum disulphide@ reduced graphene oxide ternary composites as high performance supercapacitor electrode. *J. Electroanal. Chem.* **895**, 115401 (2021)

Springer Nature or its licensor holds exclusive rights to this article under a publishing agreement with the author(s) or other rightsholder(s); author self-archiving of the accepted manuscript version of this article is solely governed by the terms of such publishing agreement and applicable law.

 Springer

Content courtesy of Springer Nature, terms of use apply. Rights reserved.

Page 14

[Share](#)[More](#)

accessing, sharing, receiving or otherwise using the Springer Nature journal content you agree to these terms of use ("Terms"). For these purposes, Springer Nature considers academic use (by researchers and students) to be non-commercial.

These Terms are supplementary and will apply in addition to any applicable website terms and conditions, a relevant site licence or a personal subscription. These Terms will prevail over any conflict or ambiguity with regards to the relevant terms, a site licence or a personal subscription (to the extent of the conflict or ambiguity only). For Creative Commons-licensed articles, the terms of the Creative Commons license used will apply.

We collect and use personal data to provide access to the Springer Nature journal content. We may also use these personal data internally within ResearchGate and Springer Nature and as agreed share it, in an anonymised way, for purposes of tracking, analysis and reporting. We will not otherwise disclose your personal data outside the ResearchGate or the Springer Nature group of companies unless we have your permission as detailed in the Privacy Policy.

While Users may use the Springer Nature journal content for small scale, personal non-commercial use, it is important to note that Users may not:

1. use such content for the purpose of providing other users with access on a regular or large scale basis or as a means to circumvent access control;
2. use such content where to do so would be considered a criminal or statutory offence in any jurisdiction, or gives rise to civil liability, or is otherwise unlawful;
3. falsely or misleadingly imply or suggest endorsement, approval, sponsorship, or association unless explicitly agreed to by Springer Nature in writing;
4. use bots or other automated methods to access the content or redirect messages
5. override any security feature or exclusionary protocol; or
6. share the content in order to create substitute for Springer Nature products or services or a systematic database of Springer Nature journal content.

In line with the restriction against commercial use, Springer Nature does not permit the creation of a product or service that creates revenue, royalties, rent or income from our content or its inclusion as part of a paid for service or for other commercial gain. Springer Nature journal content cannot be used for inter-library loans and librarians may not upload Springer Nature journal content on a large scale into their, or any other, institutional repository.

These terms of use are reviewed regularly and may be amended at any time. Springer Nature is not obligated to publish any information or content on this website and may remove it or features or functionality at our sole discretion, at any time with or without notice. Springer Nature may revoke this licence to you at any time and remove access to any copies of the Springer Nature journal content which have been saved.

To the fullest extent permitted by law, Springer Nature makes no warranties, representations or guarantees to Users, either express or implied with respect to the Springer nature journal content and all parties disclaim and waive any implied warranties or warranties imposed by law, including merchantability or fitness for any particular purpose.

Please note that these rights do not automatically extend to content, data or other material published by Springer Nature that may be licensed from third parties.

If you would like to use or distribute our Springer Nature journal content to a wider audience or on a regular basis or in any other manner not expressly permitted by these Terms, please contact Springer Nature at

[springer.nature.com](#)

Share

More 

---



Home More ▾

Bharathi, is this publication from your current lab?

Link this publication to your lab to increase the visibility of your work.

Yes

No

Preprint File availablerGO Sheets / ZnFe<sub>2</sub>O<sub>4</sub> Nanocomposites as an Efficient Electro Catalyst Material for I<sub>3</sub><sup>-</sup> / I<sup>-</sup> Reaction for High Performance DSSCs

November 2021

DOI: [10.21203/rs.3.rs-1083138/v1](https://doi.org/10.21203/rs.3.rs-1083138/v1)License · [CC BY 4.0](#)

 Anto Feradrick Samson V · Bharathi Bernadsha S · Albin John P Paul Winston · [Show all 7 authors](#) · Madhavan Joseph

Research Interest Score	1.6
Citations	1
Recommendations	1
Reads <span> ⓘ</span>	39

[Learn about stats on ResearchGate](#)

Preprints and early-stage research may not have been peer reviewed yet.

## Description and figures

In this paper, Reduced Graphene Oxide (rGO) / ZnFe<sub>2</sub>O<sub>4</sub> (rZnF) nanocomposite is synthesized by a simple hydrothermal method and employed as a counter electrode (CE) material for tri-iodide redox reactions in Dye sensitized solar cells (DSSC) to replace the traditional high cost platinum (Pt) CE. X-ray diffraction analysis (XRD) and High resolution Transmission electron microscopy (HR-TEM), clearly indicated the formation of rZnF nanocomposite and also amorphous rGO sheets were smoothly distributed on the surface of ZnFe<sub>2</sub>O<sub>4</sub> (ZnF) nanostructure. The rZnF-50 CE shows excellent electro catalytic activity toward I<sub>3</sub><sup>-</sup> reduction, which has simultaneously been confirmed by cyclic voltammetry (CV), electrochemical impedance spectroscopy (EIS) and Tafel polarization measurements. A DSSC developed by rZnF-50 CE ( $\eta = 8.71\%$ ) obtained quite higher than the Pt ( $\eta = 8.53\%$ ) based CE under the same condition. The superior performances of rZnF-50 CE due to addition of graphene in to Spinel (ZnF) nanostructure results in creation of highly active electrochemical sites, fast electron transport linkage between CE and electrolyte. Thus it's a promising low cost CE material for DSSCs.

Available via license: [CC BY 4.0](#)

Share

More

Public File ①

rGO Sheets / ZnFe<sub>2</sub>O<sub>4</sub> Nanocompo...Cs.pdfAvailable via license: [CC BY 4.0](#)  
Content may be subject to copyright.

Page 1

# rGO Sheets / ZnFe<sub>2</sub>O<sub>4</sub> Nanocomposites as an Efficient Electro Catalyst Material for I<sub>3</sub><sup>-</sup> / I<sup>-</sup> Reaction for High Performance DSSCs

**Anto feradrick Samson V ( )**

Department of Physics, Loyola College

**Bharathi Bernadsha S**

Department of Physics, Loyola College

**Albin John P Paul Winston**

Department of Physics, Loyola College

**Divya D**

Department of Physics, Loyola College

**James Abraham**

Department of Physics, Loyola College

**Victor Antony Raj M**

Department of Physics, Loyola College

**Madhavan J**

Department of Physics, Loyola College

---

## Research Article

**Keywords:** DSSCs, Counter electrode, rGO / ZnFe<sub>2</sub>O<sub>4</sub>nanocomposite, Pt-free CEs**Posted Date:** December 1st, 2021**DOI:****License:** This work is licensed under a Creative Commons Attribution 4.0 International License.

Share

More

## Abstract

In this paper, Reduced Graphene Oxide (rGO) / ZnFe<sub>2</sub>O<sub>4</sub> (rZnF) nanocomposite is synthesized by a simple hydrothermal method and employed as a counter electrode (CE) material for tri-iodide redox reactions in Dye sensitized solar cells (DSSC) to replace the traditional high cost platinum (Pt) CE. X-ray diffraction analysis (XRD) and High resolution Transmission electron microscopy (HR-TEM), clearly indicated the formation of rZnF nanocomposite and also amorphous rGO sheets were smoothly distributed on the surface of ZnFe<sub>2</sub>O<sub>4</sub> (ZnF) nanostructure. The rZnF-50 CE shows excellent electro catalytic activity toward I<sub>3</sub><sup>-</sup> reduction, which has simultaneously been confirmed by cyclic voltammetry (CV), electrochemical impedance spectroscopy (EIS) and Tafel polarization measurements. A DSSC developed by rZnF-50 CE ( $\eta = 8.71\%$ ) obtained quite higher than the Pt ( $\eta = 8.53\%$ ) based CE under the same condition. The superior performances of rZnF-50 CE due to addition of graphene in to Spinel (ZnF) nanostructure results in creation of highly active electrochemical sites, fast electron transport linkage between CE and electrolyte. Thus it's a promising low cost CE material for DSSCs.

## 1. Introduction

In recent years, fossil fuels becoming increasingly scarce and global warming gained momentum from rising carbon dioxide emission that imply the need to go for alternates which can replace the fossil fuel and mitigate the pace of global warming. Natural resources such as solar energy, wind energy, hydroelectric energy, geothermal and thermal energy can be harnessed as alternate energy reserves [1,2]. The incident radiation or light energy of the sun is converted to electrical energy or electricity. The Photo Voltaic systems are employed for this conversion process. Dye Sensitized Solar Cells (DSSC) are identified as significant options due to low manufacturing cost, environmental friendly, non-pollution and high energy conversion under low light conditions [3,4]. The major components of DSSC are photo anode, dye, electrolyte and catalytic Counter Electrode (CE). CE is an indispensable key component in the working of a DSSC to improve conversion efficiency, act as a catalyst for the tri-iodide reduction and also collects the electron from the external circuit and injecting it to the electrolyte. Traditionally Platinum (Pt) is widely used as standard CE material for the DSSC due to its good conductivity, catalytic capacity, low charge transfer resistance and higher activity in visible and infrared regions. However Pt it's costlier, possesses highly corrosive nature in the liquid electrolyte which may lead to serious drawbacks in the large scale production [5]. Therefore, developing materials which reduce the use of Pt in DSSC is the need of the hour. So far, other alternative materials like carbon allotropes (activated carbon, CNTs and graphene), conducting polymers (CP) and transition metals have also been introduced to substitute Pt CEs. However the conversion efficiency of those electrodes is still low compared to Pt as a result of low electron conductivity and poor catalytic activity. Recently, it's reported that graphene-based nanocomposites designed to own high chemical stability, significant electro catalytic activity towards iodine triiodide electrolyte, large surface area and more activated electrochemical functionalized sites. Also, there are reports on spinel type rGO based hybrid materials (MFe<sub>2</sub>O<sub>4</sub> and MCo<sub>2</sub>O<sub>4</sub> (M=Ni, Co, Zn, Mg)) examined as a CE material for DSSCs owing to their chemical properties, low cost, high stability

Page 2/10

Page 3

Share

More

(ZnFe<sub>2</sub>O<sub>4</sub>) nanocomposites consisting of reduced graphene oxide (rGO) are suitable with excellent electro catalytic activity [8,9]. Moreover, graphene possesses π-π conjugation structure, which endowed them with excellent electrical property and superior chemical stability in electrochemical environment. properties. In this favor, we have prepared rGO/ZnFe<sub>2</sub>O<sub>4</sub> nanocomposites by facile one-pot hydrothermal method with a different weight ratio of GO sheets. The influence of structural and electrochemical performances of the nanocomposites is investigated. Finally, Dye Synthesized Solar Cells are made employing as synthesized CEs and the results are compared to that of the cells fabricated with Pt CE.

## 2. Experimental

### 2.1 synthesis of rZnF nanocomposites

The Preparation of graphene and reduced graphene oxide (rGO) procedure were followed as reported by Muthu et al (2017) [13]. For rGO/ZnFe<sub>2</sub>O<sub>4</sub> nanocomposites, 25 mg of GO were dispersed in 40ml of DI water by ultrasonication for 30 minutes, on the side 1:2 ratio of Zinc (III) nitrate hexahydrate (Zn(NO<sub>3</sub>)<sub>6</sub>H<sub>2</sub>O) and iron III nitrate nonohydrate (Fe(NO<sub>3</sub>)<sub>3</sub>·9H<sub>2</sub>O) were mixed 40ml of DI water mixed by stirring. Then 5M of NaOH solution added until the pH value exceeds above 10. The above solution mixture was slowly added to as previously prepare GO suspension. Then the solution was taken in autoclave and heated at 180°C for 12 Hrs. After that the precipitate was collected by centrifuge several times and dried at 80°C for 12 Hrs. The obtained sample named as rZnF-25. For rZnF-50 prepare by adapting the same procedure additionally double amount of adding GO. For comparison pure ZnFe<sub>2</sub>O<sub>4</sub> (ZnF) also prepared by without adding GO.

### 2.2 Fabrication of DSSCs

The CEs paste is prepared by 100mg as prepared sample was ground well in mortar, then adding (N, N-dimethylformamidel solution) NMP and PVDF to form a slurry sticky paste, Then the slurry was coated in FTO subtract by using doctor blade method with a contact area of 1.5 cm<sup>2</sup> and sintered 500°C for 30 minutes. The Pt CE was prepared by drop coating method using H<sub>2</sub>PtCl<sub>6</sub> solution with a contact area of 1.5 cm<sup>2</sup> and sintered 500°C for 30 minutes. After natural cooling to room temperature all prepared CE was ready for both electrochemical and photovoltaic studies. simultaneously, the same procedure followed by the preparation of photo anode using commercially available TiO<sub>2</sub> paste. Then the prepared photo anode soaked into 0.5M of N719 dye solution for 12 hours and dried at 60°C. Liquid electrolyte (I<sub>3</sub><sup>-</sup> / I<sup>-</sup>) mediator prepared by 0.5 M of KI and 0.05 M of I were dissolved in acetonitrile solution. The gap between photo anode and CEs were filled with the above electrolyte solution.

The Photo conversion Efficiency and Fill Factor were calculated by the following equations

Page 3/10

Page 4

Share

More

$$\text{Fill Factor} = \frac{J_{mp} \cdot V_{mp}}{J_{sc} \cdot V_{oc}}$$

Where the  $J_{mp}$  and  $V_{mp}$  are the current density and voltage at the maximum power point

### 2.3 Characterization measurements

Electrocatalytic activities of the CEs, Cyclic Voltammetry (CV) were examined 0.5 M of KI and 0.05 M of I<sub>2</sub> iodine/triiodide electrolyte in the potential range 0.1 to 0.6V at the Scan rate of 50mVs<sup>-1</sup>. Tafel polarization curves of the symmetrical cells composing of two identical electrodes in the same electrolyte were recorded between (0.1 to 0.6 V) on the same workstation. Electrochemical impedance spectroscopy (EIS) of the symmetric cells were recorded at zero bias potential and 10 mV amplitude over 0.01≈10<sup>5</sup> Hz. The photovoltaic (J-V) measurements of the device were at room temperature using a Keithley 2400 high current source power meter under the light illumination of 500 W Xenon lamp (AM1.5G).

## 3. Results And Discussions

### 3.1 X-Ray Diffraction

XRD pattern of GO, rGO, ZnF, rZnF-25and rZnF-50 are Shown in Fig.1 (a,b). Graphene oxide characteristic peak at 9.8° following to the plane (001) indicates the successful preparation of graphene oxide from graphite power. For rGO, small broad peak observed at 24.4° corresponds to (002) plane has confirmed the conversion of rGO from GO. The peaks at 29.78°(220), 35.15°(311), 37.90°(222), 42.73°(400) 53.28°(422), 56.71°(511) and 62.36°(440) confirm the formation of high crystallinity cubic spinel structure of ZnF, which were very well synchronized with the JCPDS (card No.01-077-0011).For nanocomposites, there is no disordered graphene oxide peaks were seen, which is due to the considerable amount of adding graphene in the composites and also the diffraction of disordered graphene planes is weak as compare to fine crystalline ZnF planes [14]. This confirms the graphene oxide is successfully dispersed on the surface of ZnF nanoparticles and does not make any structural changes in the planes. The average particle size is calculated using Scherer's equations and the value is found to be 26.1, 17.8 and 15.3 nm for ZnF, rZnF-25 and rZnF-50 respectively. Also In this study, addition of graphene plays a key factor for adjusting the size of the particles. Lattice parameter of cubic crystal lattice (a=b=c) was calculated using the formula, the obtained lattice parameter is listed in Table 1.

$$a = d (h^2 + k^2 + l^2)^{1/2} \text{ \AA} \dots \dots \dots (1)$$

**Table 1. Obtained parameters from X-Ray Diffraction**

Share

More

Lattice parameter( $a \pm 0.001$ ) Å	8.373	8.362	8.357
--------------------------------------	-------	-------	-------

### 3.2 HR-TEM

Additionally, Fig 2 (a&b) shows the HR-TEM images of rGO and rZnF-50 samples respectively. The sheet-like rGO sheets are found to exhibit wrinkled morphology with high transparency representing single layer graphene. In Fig 2(b) it can be seen that the amorphous rGO sheets were smoothly distributed on the surface of ZnF nanostructure, which is expected to provide low charge transfer resistance and efficient channel path for conductivity of the material [13]. Fig. 2(c) shows the SAED pattern of rGO, which confirms the amorphous nature of the graphene sheets. In Fig 2(d) SAED pattern of rZnF-50, consist of several concentric diffraction rings and spots and thus indicating high crystallinity nature of the sample. The well-resolved lattice fringes are observed in the magnified HRTEM images Fig 2(e). The fringes with inter planar spacing of 0.25 nm and 0.24 nm correspond to the (002) plane of rGO and (311) plane of ZnF, respectively. From HR-TEM analysis, the particle size is found to be 29.7, 20.2 and 18.8 nm for ZnF, rZnF-25 and rZnF-50 respectively. The decreasing in particle size benefitted the quick spread of electrolyte and fast charge transport. The obtained particle size from TEM results are in good agreement with XRD results.

### 3.3 FT-Raman

FT-Raman spectra of graphene oxide, rZnF-25 and rZnF-50 nanocomposites are shown in Fig 3. Generally, Ferrite cubic spinel structure which gives rise to 39 normal Raman modes in which  $2A_{1g}$ ,  $1E_g$ ,  $3F_{2g}$  are Raman active modes. The Raman spectra of rZnF-25 and rZnF-50 samples reveals four Raman active modes. The band at 648, 371, 297 and 198  $\text{cm}^{-1}$  were belonging to the vibration modes of  $A_{1g}$ ,  $F_{2g}$ ,  $E_g$  and  $T_{2g}$  respectively. The vibration mode  $A_{1g}$  and  $F_{2g}$  represent Fe-O and M-O stretching at the tetrahedral sites, additionally  $E_g$  and  $T_{2g}$  modes present corresponds to the asymmetric stretching of oxygen atoms with respect to the metal ion at the octahedral site respectively [15]. The corresponding graphene oxide peaks such as 1340  $\text{cm}^{-1}$  and 1590  $\text{cm}^{-1}$  were represents **D-Band**, breathing point of Phonon  $A_{1g}$  symmetry and **G-band**,  $E_{2g}$  Phonon of  $\text{Sp}^2$  C-atoms respectively. Generally, the value of the intensity ratio of the D band to the G band ( $I_D/I_G$ ) is used to estimate the degree of disorder and the defects of carbon material. The obtained ratio is 0.98, 1.17 and 1.26 for rGO, rZnF-25 and rZnF-50 respectively.  $I_D/I_G$  values were higher than that rGO confirms a low graphitic degree, more defects or edges, and disordered structures were introduced in rZnF-25 and rZnF-50 samples which could be beneficial for triiodide reduction process [8].

### 3.4 Electrochemical Measurements

Page 5/10

Share

More 

---

## AQUEOUS ADULTERANTS REMOVAL BY PHOTOCATALYSIS CdO/CuO METAL OXIDE NANOCOMPOSITE

M. MAHENDIRAN<sup>1</sup>, J. J. MATHEN<sup>4</sup>, S. BHARATHI BERNADSHA<sup>3</sup>,  
K. MOHAMED RACIK<sup>2,3</sup>, J. MADHAVAN<sup>3</sup>, M. JOE RAJA RUBAN<sup>2,3</sup>,  
M. VICTOR ANTONY RAJ<sup>2,3\*</sup>

*For innumerable purposes industries water is indispensable. In the recent days adulterants removal from the water is furthered by photocatalytic activity (PCA). The photocatalytic activity of CdO/CuO nanocomposite proposes it as a significant catalyst. The nanocomposite reacts with dye molecule and purifies the adulterants present in the contaminated water. Hydrothermal method is adapted to synthesize CdO/CuO nanocomposite. The synthesized CdO/CuO nanocomposite powder is characterized by XRD analysis. Photoluminescence spectra are useful data for revealing the trapping, relocation, and transfer of carriers. The enhancement of the PCA of the obtained catalyst is the focus of this work. The CdO/CuO nanocomposite gives the efficiency above 90 percent.*

**Keywords:** CdO/CuO; Nanocatalyst; Contaminated water; Photocatalytic activity; Metal oxide;

### 1. Introduction

Safe and clean water providing system is an inevitable element of humanity's development and sustainability. The Photocatalytic Activity (PCA) attracts the researchers over the world, to reduce the colored organic dye present in the water. It is also useful to resolve the problem and to overcome the issues related to the energy and the environment [1]. The globe encounters pollution which affects environmental cycle especially water and air propelled by various pollution emitting industries [2]. At present, the effective elimination of several noxious residues from the drainages of the companies remains a big challenge. Dyes which are not ecofriendly but sold in market become contaminants.

The hazardous inorganic pollutants (phenols) like organic impurities (dyes and metal ions) are those elements present in wastewater [3, 4]. The different

---

<sup>1</sup> Department of Physics, DRBCCC Hindu College, Pattabiram, Chennai

<sup>2</sup> LIFE, Loyola College, Chennai, India.

<sup>3</sup> Department of Physics, Loyola College(University of Madras), Chennai, India.

<sup>4</sup> Department of Physics, St. Thomas College, Palai, Kerala, India

Corresponding author: vicvad2003@yahoo.co.in\*



potential organic pollutant elements are Methyl Orange, Rhodamine B, Methylene Blue and Orange II diazo inorganic pollutants which are to be removed or reduced. Methyl Orange is emerging contaminants organic in nature, which is mostly used as a dye material [5, 6]. The uncontaminated habitat and freshwater body is needed for the health of the humanity and living beings in water. Hence, the elimination of organic contaminants from wastewater is necessary for a conducive environment. The eradication of dye molecule from the contaminant water involves the breaking of complete conjugated unsaturated bonds in molecule. The photocatalytic activity (PCA) degrades the dye contents through decolorization or decontamination from the contaminant water. Thus it is demonstrated to be the excellent increasing efficient method. The nanocomposite has an incomparable role to play in heterogeneous catalysis and it produces harmless materials from the dangerous pollutants.

## 2. Materials and Method

The CdO/CuO nanocomposite is synthesized by a facile and trouble-free, hydrothermal method. For this, 0.2M of Cd (CH<sub>3</sub>COO)<sub>2</sub>·2H<sub>2</sub>O (Cadmium acetate dihydrate) and 0.76g of Copper Acetate Dihydrate (Cu (CH<sub>3</sub>COO)<sub>2</sub>·2H<sub>2</sub>O) are mixed in 70mL water which is deionized 0.5g sodium hydroxide was mixed with double refined water of 20mL and it is then mingled in drops to the solution under continuous stirring for 30 min. The contents of the perfect solution is then shifted to an autoclave and placed in an oven at 140° C for 12h. Through the gradual cooling process, the solution reaches its normal temperature. Using water that is doubly deionized and ethanol the commodity attained is washed five times and it is dried at 80° C for 12 (twelve) hours. The white powder stranded at the base is collected and annealed at 500° C for 3hours. Eventually, black colored nanocomposite of CdO/CuO nanoparticles is successfully obtained.

## 3. Results

### 3.1 Size and Strain Analysis

To find the purity of the crystalline phases of CdO/CuO nanocomposite X-ray diffraction (XRD) measurement results are plotted in Fig. 1. The obtained peaks in XRD results can be attributed to the cubic phase of CdO (cadmium oxide) (JCPDS card no: 05-0640) monoclinic phase of CuO (copper oxide) (JCPDS NO. 36-1451). The XRD crests of the CdO/CuO nanocomposite reveals that the relatively strong diffraction symbolizes CdO/CuO nanostructures possess good crystallinity. Surprisingly, impurity is not identified in the X-ray diffraction pattern. The XRD pattern of CdO/CuO shows a sequence of high and low intensity peaks. The Scherrer's equation measure the crystal size (average) as:

$$D = \frac{k\lambda}{\beta \cos\theta} \quad (1)$$

D - average crystallites size; K-shape factor (0.94);  $\beta$  – FWHM;  $\theta$  -Bragg's angle; wavelength of X-ray  $\lambda=1.54\text{\AA}$ . 41nm is the determined average crystallite size of CdO/CuO nanocomposite. Williamson–Hall analysis is simplified into integral breadth method that differentiates size, strain induced crests broadening by considering the crests width as  $2\theta$  function. According to study of this W-H exploration the crest width at half maximum intensity ( $\beta_{hkl}$ ) is a function of crystallites size and the lattice strain equation [7];

$$\beta_{hkl} = \beta_{crystallite} + \beta_{strain} \quad (2)$$

The broadening accredited to lattice strain in the powders is calculated using equation (3)

$$\beta_{strain} = 4\epsilon \tan\theta \quad (3)$$

Rearranging the equation (2) gives

$$\beta_{hkl} \cos\theta = \frac{k\lambda}{D} + 4\epsilon \sin\theta \quad (4)$$

Fig. 2 exhibits the linear fit curve of  $4 \sin\theta$  vs  $\beta_{hkl}\cos\theta$ . Average size (crystal) and dislocation are calculated in the extrapolation and slope obtained as 43 nm and 0.0031 respectively. Thus, mean size of the crystals is determined by W-H method in line with the result obtained in Scherrer's method.

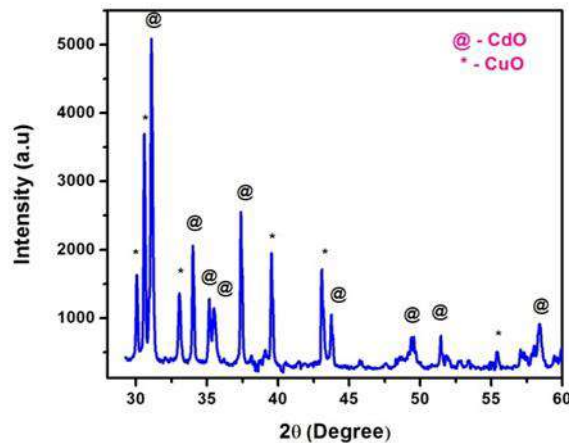


Fig. 1: X-Ray Diffraction of nanocomposite CdO/CuO

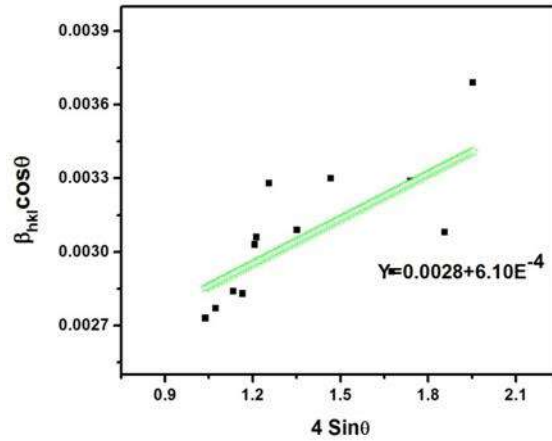


Fig. 2: W-H plot of nanocomposite CdO/CuO

### 3.2 Morphology Analysis

The HR-SEM, HR-TEM images EDAX and spectrum SAED of CdO/CuO nanocomposite are plotted in Fig. 3 (a, b, c and d). HR-SEM reveals the individual spherical Nano flake with a high compact structure. The structure could improve the photocatalytic (PC) properties by easing the charge carrier's transport. The obtained average diametrical size is about 35-55 nm. HR-SEM results and Scherrer formula, Williamson-Hall plot method confirms the particle size achieved from. The EDAX analysis exposes that the elements of CdO/CuO nanocomposite are present in the synthesized powder sample. The major elements present are cadmium Cd (76.16 wt%), copper Cu (12.35wt%) and oxygen O (11.49 wt%). EDAX spectrum is free of unwanted peaks which confirm that the composite sample is impurity absent. TEM analysis and SAED pattern clearly exhibit that a spherical rod is formed and concentric rings match well with CdO/CuO nanocomposite.

### 3.3 Optical Studies

Fig. 4 indicates the UV-Vis spectrum of CdO/CuO nanocomposites. This shows a maximum absorption crest at 327 nm which is a violet shift in the electromagnetic region.  $E_g$  is obtained from Tauc plot (Fig. 5).

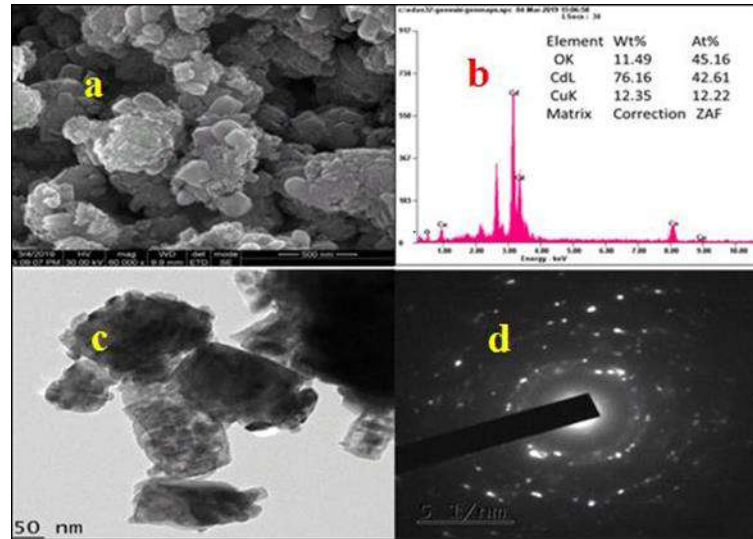


Fig. 3: Images of a) HRSEM, b) TEM, c) EDAX and d) SAED pattern of nanocomposite CdO/CuO

Based on direct allowed transition type, the optical energy band gap of the sample was found using Tauc's relation [14]. Tauc plot graph is drawn with energy ( $h\nu$ ) against  $((\alpha h\nu)^2$  in Fig. 5. Deducing the linear portion of the contour to zero absorption, the  $E_g$  of 3.72 eV is obtained. Excitation of electrons are speeded up by the decrease of energy band gap (between VB and CB) exploiting low energy which will make available more electron hole pairs and improve the removal of the dyes through PC activities.

### 3.4 Photoluminescence Analysis

Photoluminescence spectra reveal the relocation, trapping, and exchange of electron carriers. PL emission is highly dependent on the re-combination of free carriers (Fig. 6) [15]. The emission crest at 420 nm has been ascribed to the changeover between defects (interface traps) at grain boundaries and the valence bands lattice defects that are related to vacancy of oxygen [19-21]. The green emission crest at 529 nm rises due to recombination of photo-generated hole ( $h^+$ ) and singly ionized oxygen. The spectra consist of an acute and strong emission band at 486 nm. The near band-edge narrow UV crest located at 408 nm can be attributed to direct radiative recombination of excitons and the UV-visible crest at 420 nm and 446 nm appeared as a result of charge carrier relaxation.

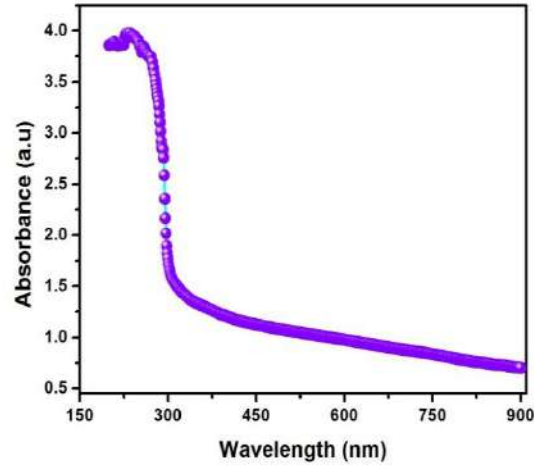


Fig..4: UV-Visible Spectrum of CdO/CuO



Fig. 5: Tauc Plot of CdO/CuO

It happens due to the occurrence of surface related trap states. In case of excitonic PL signals, the lower peak intensity shows the reduction of charge carrier recombination. There is a high possibility for diminishing of peak intensities due to the presences of very small CuO content in CdO nano flake sample, by charge carrier separation, can largely suppress photo-induced electron-hole recombination [22].

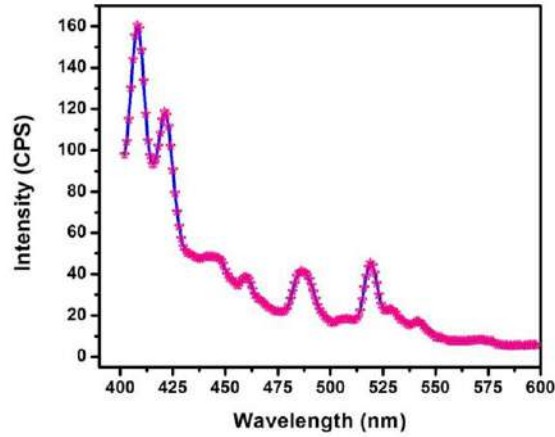


Fig. 6: Photoluminescence (PL) spectrum of nanocomposite CdO/CuO

### 3.5. Measurement of Photocatalytic Activity (PCA)

Fig. 7 shows the experiment of PCA. Methyl orange organic dye is taken for the study of PCA of the synthesized sample. To prepare contaminated water, methyl orange dye is taken as 0.001g and deliquesces in deionized prepared solution is dissolved in catalyst of 0.1g and this mixture is kept in a tightly closed dark room and uniformly stirred for 30 min using magnetic stirrer. After 15 min the solution is kept under the ultraviolet light source (100W mercury lamp) and the suspension was continuously stirred manually. At the interval of 5 min the irradiated solution is removed from the suspension. The complete decolorization is observed at 75 min. The absorption spectrum of the cleared solution is recorded. The collected sample solutions are characterized by UV studies. Degradation extent is determined in terms of the changes in intensity at the  $\lambda_{\max} = 462\text{nm}$  for methyl orange.

The decolorization range is estimated by the equation (5).

$$\text{Percentage of Methyl Orange Degradation} = \frac{C_i - C_f}{C_i} \times 100 \quad (5)$$

Where,  $C_i$  is the initial concentration absorption of each dye,  $C_f$  is the final concentration absorption of each dye.

Fig. 8 illustrates the wavelength vs absorbance of CdO/CuO nanocomposite. The crystalline size, morphology, optical energy gap increase the absorption strength and superior partition of photogenerated electron-hole pairs. Hence, photocatalytic (PC) achievement also enriched (Fig. 9).

This result confirms the contriving mechanism of the methyl orange (MO) degradation process on the surface of the CdO/CuO nanocomposite. Semiconductor nanocomposite is formed by the combination of two metal oxides

which have properly selected values for electronic band potential. The mixed nanocomposite consists of two main semiconductors, one is CdO with an energy band gap of 2.5 eV and other is 1.7eV. The Semiconductor nanocomposite copper oxide has a band gap which is very narrow. This narrow band gap shifts the absorption band along the visible light direction and also separates photogenerated electron-hole ( $e^-+h^+$ ) charge carriers, thus slowing recombination. Zinc oxide and copper oxide are applied over the surface which paves way in increased contact surface of the catalyst with dye nanoparticles, resulting in oxygen diffusion and transport of dye in mass quantity photochemical reaction. The modification of zinc oxide with the addition of copper oxide (CdO) increases the wavelength ( $\lambda$ ) range which increases the efficiency of energy used in the visible light range. The CdO/CuO hetero structure helps in separation of generated electron-hole ( $e^-+h^+$ ) pairs in the presence of photon. Electrons ( $e^-$ ) move from valence band to conduction band while leaving holes positive ( $h^+$ ). Because Copper oxide holds (CuO) a higher energy band to zinc oxide (ZnO) band and hence conduction band and valence bands lie above in CuO (which thermodynamically promote the exchange and transfer of excited electrons and holes between them), this behavior results in increased ZnO quantum efficiency which is the result of separation of carriers in different semiconductors, effectively inhibiting the recombination of electron-hole ( $e^-+h^+$ ) pairs. After the separation of electrons ( $e^-$ ) and holes ( $h^+$ ), reactions of formation of hydroxyl radicals ( $OH^\cdot$ ) occur, which react with organic or contaminate substances in water ( $H_2O$ ) that can be degraded to  $CO_2$  and  $H_2O$ .

The reaction of photocatalytic mechanism involves a few steps like ionization of water, light excitation, absorption of oxygen ion and superoxide protonation. When a photon is subjected to illuminate a metal photo catalyst it will create an electron hole pairs. At the surface of photon or light got excited photocatalyst reduction and oxidation takes place. Then the catalyst particle absorbs photon and creates a positive charged  $h^+$  reacts with  $H_2O$  molecule to produce radicals. Catalysis reacts with dissolved oxygen to generate  $O_2^\cdot-$  radical ions that are able to degrade methyl orange (MO). Photogenerated electrons ( $e^-$ ) can react with molecular oxygen ( $O$ ) to formless noxious superoxide anion ( $*O_2^-$ ) radicals through a minimal process whereas the  $h^+$  reacts with  $H_2O$  or hydroxyl ions ( $OH^-$ ) to form the most reactive hydroxyl ( $*OH$ ) radicals through the oxidative process. The electron-hole pairs react with superoxide anions to generate hydrogen peroxide ( $H_2O_2$ ). The one metal oxide combine with another metal oxide has produced more dynamic photocatalytic centre which assist the photocatalytic degradation performance.

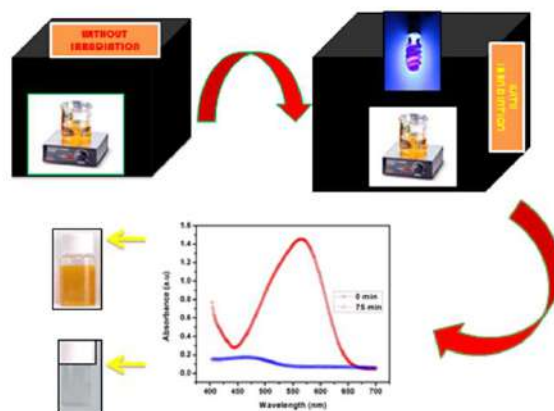


Fig. 7: Schematic diagram of photocatalytic experiment

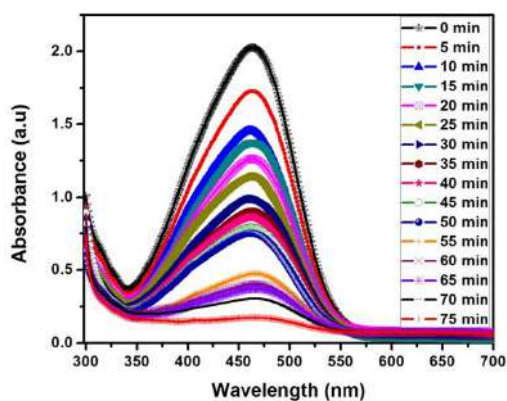


Fig. 8: Absorption graph of CdO/CuO nanocomposite

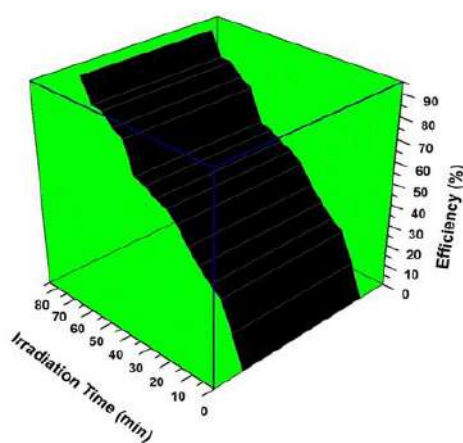


Fig. 9: Decolorization efficiency of CdO/CuO nanocomposite



#### 4. Conclusion

The quality of the crystallite CdO/CuO nanocomposite plays the major role in removing the adulterant from the water. Removing adulterant from the water will make clean environment. The crystal size and morphology of catalyst is examined by X-ray Diffraction HR-SEM and TEM analysis. The nanocomposite's crystallite size is 41nm determined using X-ray diffraction analysis. HR-SEM and TEM studies show the morphology as rod spherical and rod flake respectively. Band gap of the composite are found by UV-Vis spectrometer. The band gap of the nanocomposite has been found as 3.72eV. PL analysis gives the defects of the crystallite. This combination gives favorable PCA performance which is 90%. This promises the obtained composite is suitable for removing the adulterant from the water.

#### REFERENCES

- [1]. *C. G. Tian, Q. Zhang, A. P. Wu, M. J. Jiang, Z. L. Liang, B. J. Jiang and H. G. Fu*, "Environmental Photocatalysis" in Chem. Commun. **vol 48**, no 23, Nov2012, pp2858–2860.
- [2]. *C. Tongqin, L. Zijiong, Y. Gaoqian, J. Yong, Y. Hongjun*, "Enhanced photocatalytic activity of ZnO/CuO nanocomposites synthesized by hydrothermal method." in Nano-Micro Lett., **vol 5**, Sep 2013, pp 163–168.
- [3]. *S.Siuleiman, N. Kaneva, A. Bojinova, K. Papazova, A. Apostolov, D. Dimitrov*, "Photodegradation of Orange II by ZnO and TiO<sub>2</sub> powders and nanowire ZnO and ZnO/TiO<sub>2</sub> thin films." in Colloids and Surfaces A: Physicochem. Eng. Aspects, **vol 460**, Oct 2014, pp 408-413.
- [4]. *Devan RS, Patil RA, Lin JH, Ma YR.*, "One-Dimensional Metal-Oxide Nanostructures: Recent Developments in Synthesis, Characterization, and Applications" in Adv Funct Mater **vol 22**, no 33, Jun 2012, pp 26-70.
- [5]. *Wang G, Ling Y, Li Y*, "Graphene-Based Glucose Sensors: A Brief Review" Nanoscale **vol 4** no 66, Nov 2012, pp82-91.
- [6]. *Yang, Lixia, Z Li, H Jiang, W Jiang, R Su, S Luo, and Y Luo.* "Photoelectrocatalytic oxidation of bisphenol A over mesh of TiO<sub>2</sub>/graphene/Cu<sub>2</sub>O." in Applied Catalysis B: Environmental **vol 183**, Apr 2016, pp75-85.
- [7]. *Z, J.; Hu, Y.; Jiang, X.; Chen, S.; Meng, S.; Fu, X.* "Design of a direct Z-scheme photocatalyst: preparation and characterization of Bi<sub>2</sub>O<sub>3</sub>/g-C<sub>3</sub>N<sub>4</sub> with high visible light activity." in J. Hazard. Mater. **vol 280**, Sep 2014, pp 713-722.
- [8]. *M. Mahendiran, J.J. Mathen, Mohamed Racik, J. Madhavan, M. VA Raj* "Investigation of structural, optical and electrical properties of transition metal oxide semiconductor CdOZnO nanocomposite and its effective role in the removal of water contaminants." in J. of Phy and Chem of Solids, **vol 126**, Mar 2019, pp 322-334.
- [9]. *S. Harish J. Archana M. Sabarinathan M. Navaneethan K.D. Nisha S. Ponnusamy C.*

- Muthamizhchelvan H. Ikeda D.K. Aswal Y. Hayakawa* "Controlled structural and compositional characteristic of visible light active ZnO/CuO photocatalyst for the degradation of organic pollutant." in *Applied Surface Science* **vol 418**, Part A, no 1 October 2017, pp 103-112.
- [10]. *Anand, A. Persis Amaliya, M. AsisiJanifer, S. Pauline* "Structural, morphological and dielectric studies of zirconium substituted CoFe<sub>2</sub>O<sub>4</sub> nanoparticles." in *Modern Electronic Materials* Dec 2017, pp 168–173.
- [11]. *R.M. Mohamed, F.A. Harraz, A. Shawky*, "CuO nanobelts synthesized by a template-free hydrothermal approach with optical and magnetic characteristics." in *Ceram. Int.* **vol 40** Jan 2014, pp 2127-2133.
- [12]. *Sneha G. P, J P. Corbett, M Wojciech. Jadwisienczak, E Martin. Kordesch* "Structural characterization and X-ray analysis by Williamson–Hall method for Erbium doped Aluminum Nitride nanoparticles, synthesized using inert gas condensation technique." in *Physica E: Low-dimensional Systems and Nanostructures* **Vol 79**, May 2016, pp 98-102.
- [13]. *S. Sumithra, N.V. Jaya*, "Band gap tuning and room temperature ferromagnetism in Co doped Zinc stannate nanostructures." in *Physica B* **vol 493**, Jul 2016, pp 35-42.
- [14]. *S.D. Tiwari, K.P. Rajeev*, "Signatures of spin-glass freezing in NiO nanoparticles." in *Phys. Rev. B* , **vol 72**, Sep 2005, pp 104433.
- [15]. *H. Li, L. Zhu, M. Xia, N. Jin, K. Luo, Y. Xie*, "Synthesis and investigation of novel ZnO–CuO core-shell nanospheres." in *Mater. Lett.* **vol 174**, Jul 2016, pp 99-101.
- [16]. *J.Y. Yu, S.D. Zhuang, X.Y. Xu, W.C. Zhu, B. Feng, J.G. Hu*, "Photogenerated electron reservoir in hetero-p–n CuO–ZnO nanocomposite device for visible-light-driven photocatalytic reduction of aqueous Cr (VI)." in *J. Mater. Chem. A* **vol 3**, 2015, pp 1199.
- [17]. *P. Lu, W. Zhou, Y. Li, J. Wang, P. Wu*, "Abnormal room temperature ferromagnetism in CuO/ZnO nanocomposites via hydrothermal method." in *Appl. Surf. Sci.* **vol 399**, Mar 2017, pp 396-402.
- [18]. *Ashar A, Iqbal M, Bhatti IA, Ahmad MZ, Qureshi K, Nisar J, et al.* . "Hydrothermal synthesis of molybdenum trioxide, characterization and photocatalytic activity." in *J Alloy Comp* **vol 678**, feb 2016, pp126-36.
- [19]. *Yang, C. Cao, X. Wang, S. Zhang, L. Xiao, F. Su, X. Wang.* . "Complex-directed hybridization of CuO/ZnO nanostructures and their gas sensing and photocatalytic properties." in *J. Ceram Int.* **vol 41**, Jan 2015, pp1749-1756.
- [20]. *Sahay, Sundaramurthy R, J. Kumar, Thavasi P. S., Mhaisalkar V, S. G. Ramakrishna, S.* . "Synthesis and characterization of CuO nanofibers, and investigation for its suitability as blocking layer in ZnO NPs based dye sensitized solar cell and as photocatalyst in organic dye degradation." in *J. Solid State Chem.* **vol 186**, Feb 2012, pp 261-267.
- [21]. *Yang, X.; Shao, C. Guan, H. Li, X. Gong*, "Novel nanocomposites and nanoceramics based on polymer nanofibers using electrospinning process—a review." in the *J. Inorganic. Chem. Commun.* **vol 7**, Aug 2004, pp 176-178.

- [22]. *Samadi, M.; Shivaee, H. A.; Zanetti, M.; Pourjavadi, A.; Moshfegh,* "Visible light photocatalytic activity of novel MWCNT-doped ZnO electrospun nanofibers." in the *J. Mol. Catal.A: Chem.* **vol 359**, Jul 2012, pp 42-48.

# Multiplicative Labeling Based on Maximum Degree for Some Simple Connected Graph

S. RAGULSANKAR<sup>1</sup>, V. RAJESWARI<sup>2</sup>

<sup>1</sup> Research Scholar Department of Mathematics, Don Bosco College, Dharmapuri

<sup>2</sup> Assistant Professor, Department of Mathematics, Don Bosco College, Dharmapuri.

**Abstract**— A Graph  $G$  with  $p$  vertices and  $q$  edges is said to be multiplicative labeling based on maximum degree graph if the vertices are assigned distinct number  $1, 2, 3, \dots, p$  such that the labels induced on the edges by the product of the end vertices divided by its maximum degree are distinct. We prove some of the graphs such as Crown Graph, Path Graph, Star Graph, Equal Bi-Star Graph are multiplicative labeling based on maximum degree graph.

**Indexed Terms**— Maximum degree, Crown graph, Path graph, Star graph, Equal Bistar graph

## I. INTRODUCTION

In this paper only finite, simple, connected and undirected graphs are considered. A graph labeling of  $G[2]$  is an assignment of labels to vertices or edges or both by following certain rules. Labeling of graph plays an important role in application of graph theory in neural, coding, circuit analysis etc.

## II. DEFINITIONS

### 2.1 MULTIPLICATIVE LABELING BASED ON MAXIMUM DEGREE GRAPH (MLBMD GRAPH)

Let  $G(V, E)$  be a graph with  $p$  vertices is said to be multiplicative labeling based on maximum degree if we define a bijective mapping  $f: V(G) \rightarrow \{1, 2, \dots, p\}$  such that label induced on the edges is given by  $g: E(G) \rightarrow N$  such that  $g(uv) = \left\lfloor \frac{f(u)f(v)}{\Delta} \right\rfloor$ , where  $\lfloor \cdot \rfloor$  denoted the integer part,  $\Delta$  denotes the maximum degree of  $G$ . A graph which admits above labeling is called multiplicative labeling based on maximum degree graph (MLBMD graph)

### 2.2 GRAPH

A Graph  $G$  is a pair  $G = (V, E)$  consisting of a finite set  $V$  and a set  $E$  (infinite graphs are also studied, but we consider only finite graphs). The elements of  $V$  are

called vertices (points, nodes, junctions or 0-simplices) and elements of  $E$  are called edges (line, arcs, branches or 1-simplices). The set  $V$  is known as the vertex set of  $G$  and  $E$  as edge set of  $G[3]$ .

### 2.3 CROWN GRAPH

The crown graph [2][4]  $C_n^+ = C_n \odot K_1$  is obtained by joining a pendant edge to each vertex of cycle  $C_n$ .

### 2.4 PATH GRAPH

A path [1][4] is a simple graph whose vertices can be arranged in a linear sequence in such a way that two vertices are adjacent if they are consecutive in the sequence and are nonadjacent otherwise.

### 2.5 STAR GRAPH

Star graph [5][6] is a special type of graph in which  $n-1$  vertices have degree 1 and a single vertex have degree  $n-1$  this looks  $n-1$  vertex is connected to a single central vertex. A star graph with total  $n$ - vertex is termed as  $S_n$ .

### 2.6 EQUAL BI-STAR GRAPH

The Equal Bi-star  $EB_{m,m}$  is the graph obtained by joining the apex vertices of two copies of star  $K_{1,m}$  and  $K_{1,m}$  by an edge.

## III. MAIN RESULTS

### 3.1 THEOREM:

The Crown Graph  $C_n^+$  is a MLBMD Graph.

#### PROOF:

Let  $\{p_1, p_2, \dots, p_n, p_{n+1}, p_{n+2}, \dots, p_{2n}\}$  be the points of  $C_n^+$

The Crown Graph  $C_n^+$  has  $2n$  points and  $2n$  edges.

The points labeling is constructed as

$f: P(C_n^+) \rightarrow \{1, 2, \dots, 2n\}$  given by

$f(p_i) = i, i = 1, 2, \dots, (n+1)$

$f(p_{n+2}) = 2n$

$f(p_{i+n+2}) = f(p_{i+n+1}) - 1, i = 1, 2, \dots, (n-2)$

From the above labeling pattern on points, the edge labeling is given by

$g(p_i p_j) = \left[ \frac{f(p_i) f(p_j)}{3} \right]$  where 3 is maximum degree of  $C_n^+$  and  $[ ]$  denotes the integer part.

Hence Crown Graph  $C_n^+$  is a MLBMD graph.

3.1.1 EXAMPLE:

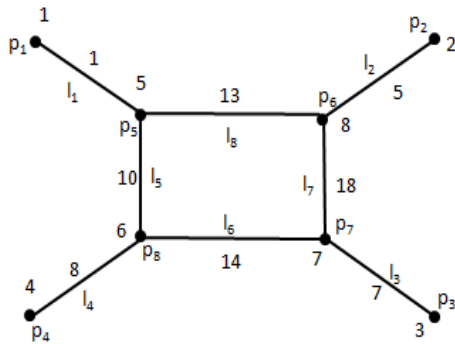


Fig :1 -  $C_4^+$

3.1.2 EXAMPLE:

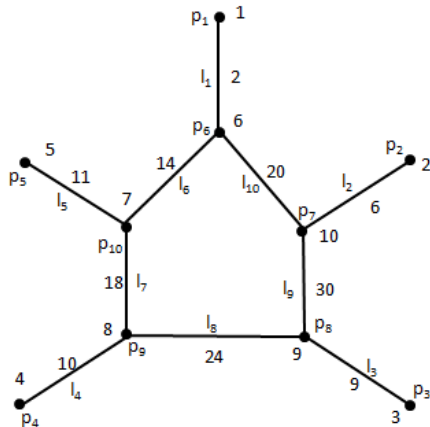


Fig: 2-  $C_5^+$

3.2 THEOREM:

The Path Graph  $P_n$  is a MLBMD graph.

PROOF:

Let  $\{ p_1, p_2, \dots, p_n \}$  be the points of  $P_n$

The Path Graph  $P_n$  has  $n$  points and  $(n-1)$  edges

The point labeling is constructed as

$f: P(P_n) \rightarrow \{1, 2, \dots, n\}$  given by

CASE: 1 (when  $n$  is even)

$$f(p_{2i-1}) = i, \quad i = 1, 2, \dots, \left[ \frac{n}{2} \right]$$

$$f(p_{2i}) = \frac{n}{2} + i \quad i = 1, 2, \dots, \left[ \frac{n}{2} \right]$$

CASE: 2 ( When  $n$  is odd)

$$f(p_{2i-1}) = i, \quad i = 1, 2, \dots, \left( \frac{n+1}{2} \right)$$

$$f(p_{2i}) = \left( \frac{n+1}{2} \right) + i, \quad i = 1, 2, \dots, \left( \frac{n-1}{2} \right)$$

From the above labeling pattern on points ,the edges are labeled by

$g(p_i p_j) = \left[ \frac{f(p_i) f(p_j)}{2} \right]$  where 2 is maximum degree of  $P_n$  and  $[ ]$  denotes the integer part.

Hence Path Graph  $P_n$  is a MLBMD Graph.

3.2.1 EXAMPLE:

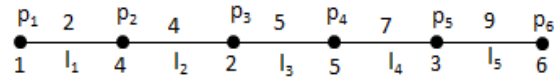


Fig: 3-  $P_6$

3.2.2 EXAMPLE :

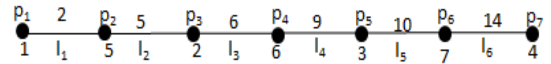


Fig:4 - $P_7$

3.3 Theorem:

The Star Graph  $S_n$  is a MLBMD graph.

PROOF:

Let  $\{ p, p_1, p_2, \dots, p_n \}$  be the points of  $S_n$

The star Graph  $S_n$  has  $n+1$  points and  $n$  edges

The Point labeling is constructed as

$f: P(S_n) \rightarrow \{1, 2, \dots, (n+1)\}$  given by

$$f(p) = n$$

$$f(p_n) = n + 1$$

$$f(p_i) = i \quad i = 1, 2, \dots, (n-1)$$

From the above labeling pattern on points the edge labeling is given by

$g(p_i p_j) = \left[ \frac{f(p_i) f(p_j)}{n} \right]$  where  $n$  is the maximum degree of  $S_n$  and  $[ ]$  denotes the integer part.

Hence star Graph  $S_n$  is a MLBMD graph.

3.3.1EXAMPLE:

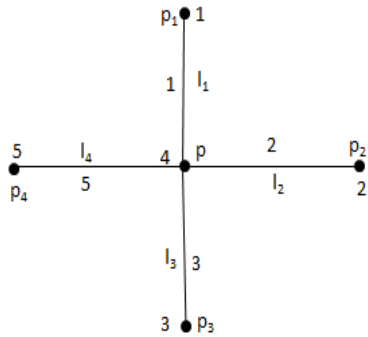


Fig: 5 - S<sub>4</sub>

3.3.2EXAMPLE :

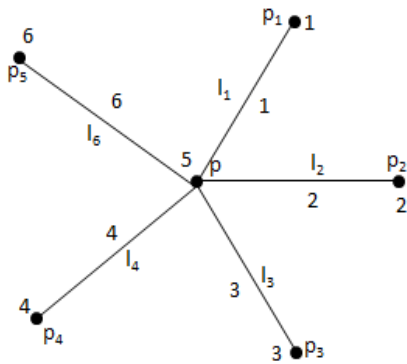


Fig: 6 - S<sub>5</sub>

3.4 THEOREM:

The Equal Bi-Star EB<sub>m,m</sub> Graph admits a MLBMD graph

PROOF:

Let {p<sub>0</sub>,p<sub>1</sub>,p<sub>2</sub>,...,p<sub>m</sub>} and {s<sub>0</sub>,s<sub>1</sub>,s<sub>2</sub>,...,s<sub>m</sub>} be the points of EB<sub>m,m</sub>

The Equal Bi-Star Graph EB<sub>m,m</sub> has 2(m + 1) points and (2m + 1) edges

The point labeling is constructed as

$f: P(EB_{m,m}) \rightarrow \{1,2, \dots, 2(m + 1)\}$  given by

$$f(p_0) = m + 1$$

$$f(p_i) = i \quad i = 1,2, \dots, m$$

$$f(s_0) = m + 2$$

$$f(s_j) = 2m + (j - 1) \quad j = 1,2, \dots, m$$

From the above labeling pattern on points, the edge labeling is given by

$g(p_i p_j) = \left\lfloor \frac{f(p_i) f(p_j)}{(m+1)} \right\rfloor$  where (m+1) is maximum degree of Equal Bi-Star EB<sub>m,m</sub> and  $\lfloor \cdot \rfloor$  denotes the integer part.

Hence Equal Bi-Star EB<sub>m,m</sub> Graph is a MLBMD graph.

3.4.1 EXAMPLE:

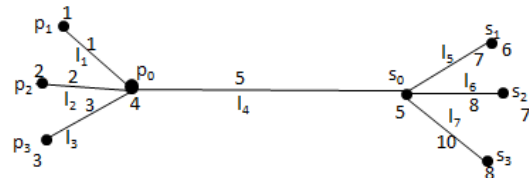


Fig:7- B<sub>3,3</sub>

3.4.2 EXAMPLE:

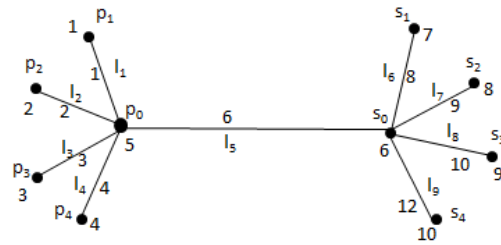


Fig:8-B<sub>4,4</sub>

REFERENCES

- [1] Bondy J.A and Murty U.S.R, "Graph Theory", Springer, ISBN: 978-1-84628-969-9.
- [2] Gallian, J.A., "A Dynamic Survey of Graph Labeling", electronic journal of combinatorics [2010].
- [3] Suresh Singh G, "Graph Theory", PHI Learning Private Limited New Delhi, ISBN-978-81-203-4105-0.
- [4] V. Rajeswari, K. Thiagarajan, Ponnammal Natarajan "Maximum Degree based Vertex Graceful Labeling Graph with Odd Labeling on Edges", Smart Innovation, Systems and Technologies Volume 159 ISSN 2190-3018, ISSN 2190-3026(electronic), ISBN 978-981-13-9281-8, ISBN 978-981-13-9282-5(eBook), <https://doi.org/10.1007/978-981-13-9282-5> Page No: :261-267

- [5] [www.javatpoint.com/graph-theory-types-of-graphs](http://www.javatpoint.com/graph-theory-types-of-graphs).
- [6] [www.geeksforgeeks.org/check-star-graph](http://www.geeksforgeeks.org/check-star-graph).